High-Efficiency Luminescent Solar Concentrators for Photovoltaic Applications

Thesis by
David R. Needell

In Partial Fulfillment of the Requirements for the
Degree of
Doctor of Philosophy

CALIFORNIA INSTITUTE OF TECHNOLOGY
Pasadena, California

2022
Defended September 9th, 2021

David R. Needell
ORCID: 0000-0001-8343-5883

Acknowledgments

In the tempestuous winter of 1997, my parents led our family out from the suburbs and into the front-range forests of Colorado. There they built what would become our home, one in which each electron used for lighting or movie watching or cooking sourced directly from the high-altitude sunshine—an off-the-grid 4.5kW photovoltaic array generously lending us the power. As years flew by, my curiosity grew. I began to wonder how all our energy needs could be powered by such seemingly miraculous monolithic slabs, resting at their 30° incline in the Rocky Mountain foothills. What must be happening inside these panels? How can light magically transform into electrons? How does a solar panel give rise to an electromotive force, propelling charge through conduits and into our home? It would take me a couple decades to satisfactorily answer these questions for myself (and even still, myriad questions continue to surface). But the world that my mother and father crafted out in rural, middle-of-nowhere Colorado taught me certain truths, among others: *(i)* the sun is our, as a species and planet's, most fundamental energy resource, and *(ii)* true curiosity and love for nature can last a lifetime.

As such, I would first like to acknowledge my father, William M. Needell. His imagination and resourcefulness will never cease to amaze and inspire me. My mother, Deborah L. Needell, deserves equal credit; for without her guidance, empathy, and shared love of storytelling, I would never have been able to embark on this beautiful journey into science. And while growing up in a "little house on the prairie" holds certain irrevocable perks, if it was not for the company of Emma A. Needell, probability is high that eremitism may very well have gotten the best of me (us). Thank you Emma for your limitless enthusiasm for my work, camaraderie throughout this oscillatory adventure, and sincere willingness to listen time and again to my ramblings concerning light-matter interaction.

At best, a doctorate of science leads one to consider new questions and concepts with ever-increasing specificity. At worst, the pursuit likens to spelunking—venturing deeper into narrower and darker caverns of a particular project or topic, uncertain of what could be lurking in the void. And so, I give my deepest appreciation and acknowledgment to Harry A. Atwater. For, like exploring the labyrinthine tunnels with a fearless leader, Harry's scientific guidance, natural inquisitiveness, and unmistakable enthusiasm for photonics led me through this PhD. Harry showed me what it means to wake up every morning yearning to learn more about our universe.

Luckily, if we continue this spelunking allegory one paragraph further, I never found myself trapped in the PhD cave desolate and bereft of direction. To that, I must thank all of my colleagues, friends, and role models who ventured into these tunnels with me. To Megan E. Phelan, thank you for your enthusiasm, support, and true friendship these past several years—be it hot chocolate at Red Door, steak in Ávila, or ba-nano pancakes on a hot plate. To Haley C. Bauser, thank you for being my research partner from the beginning, even when a project seemed hopeless (e.g., that one time our sample shunted to the point of failure right before our scheduled outdoor field testing) or just too exhausting (e.g., the countless hours manning a technology showcase booth at all of the ARPA-e summits). Rebecca Saive, your intellectual curiosity and meticulous investigations into science continue to inspire my own work; thank you for all of your emotional and scientific support over the years. And to the numerous other graduate students, staff, and faculty at Caltech, University of Illinois at Urbana-Champaign, NREL, and AMOLF: thank you for the collaborations, discussions, support, and inspiration over the years. It has been a true privilege to have worked alongside people similarly entranced by the intrinsic beauty of our universe.

And last but certainly not least, I give a heartfelt thank you to all the people that helped transform Southern California from an unknown city into a vibrant home, chiefly: José V. García, Varun S. Wadia, Jake R. Sally, Thomas Russell, Andrew J. Taylor, James Holper, Janis Hesse, Nathan Gray. And, of course, to my life partner Cam M. Gray. It is through your kindness, our midnight discussions, and all the laughs and adventures we have shared these past years that I now make it to the end of the cave and out—at least, before plunging into another. I could not imagine a more stable equilibrium than the one you and I have made together, with the help of our cat Poppy of course.

My sincerest and warmest appreciation to all the people who have shared their time and energy with me.

Abstract

Despite an overwhelming abundance of crude solar energy, current photovoltaic systems worldwide harness less than 1% of this available power. As such, emerging solar generation technology must be developed to further spur global adoption—whereby increased sunlight to power conversion efficiency alongside decreased system costs constitute the primary methods to accomplish this goal. The luminescent solar concentrator (LSC) offers a unique approach to collecting and redirecting large areas of incident light onto small-area solar cells. Relying upon photoluminescent materials (i.e., luminophores) suspended within a dielectric waveguide, the LSC absorbs high energy irradiance and re-emits photons at down-shifted energies into optical waveguide modes.

This thesis presents analytical, computational, and experimental work to illustrate the technical power conversion efficiency limits for LSC-based photovoltaic devices. We begin with a technical description of two LSC numerical models—a stochastic Monte Carlo ray-trace and a deterministic closed-form approach. We apply these models to quantify the effects of system and component parameters on power conversion efficiency for a number of end-use applications. To validate our modeling and unveil current practical material limits, we fabricate CdSe/CdS and $CuInS_2$/ZnS core/shell quantum dot waveguides hosting embedded InGaP and GaAs photovoltaic cells, respectively. From these measurements, we observe close model-to-experiment matching and report a world-record LSC power conversion efficiency reaching approximately 10% under 1-sun illumination at modest incident to outgoing radiance areas.

Herein we consider four distinct applications for the LSC: *(i)* single junction LSC devices for terrestrial-based energy generation, *(ii)* building-integrated LSC form factors for on-site electricity, *(iii)* multijunction LSC modules for utility-scale installations at high power conversion efficiency, and *(iv)* ultra-light structures for on-board power in aerospace settings. We organize each chapter according to its end-use application.

Contents

List of Figures

List of Tables

Published Content and Contributions

[1] **Needell, D. R.**; Nett, Z.; Ilic, O.; Bukowsky, C. R.; He, J.; Xu, L.; Nuzzo, R. G.; Lee, B. G.; Geisz, J. F.; Alivisatos, A. P.; Atwater, H. A. Micro-Optical Tandem Luminescent Solar Concentrator. In *2017 IEEE 44th Photovoltaic Specialist Conference (PVSC)*; IEEE, 2017; pp 1737–1740. https://doi.org/10.1109/PVSC.2017.8366508.

D.R.N. participated in the conceptualization of the project, development and validation of the computational model, execution of the simulations, analysis of the results, and writing of the manuscript.

[2] **Needell, D. R.**; Ilic, O.; Bukowsky, C. R.; Nett, Z.; Xu, L.; He, J.; Bauser, H.; Lee, B. G.; Geisz, J. F.; Nuzzo, R. G.; Alivisatos, A. P.; Atwater, H. A. Design Criteria for Micro-Optical Tandem Luminescent Solar Concentrators. *IEEE J. Photovoltaics* 2018, 8 (6), 1560–1567. https://doi.org/10.1109/JPHOTOV.2018.2861751.

D.R.N. participated in the conceptualization of the project, development and validation of the computational model, execution of the simulations, analysis of the results, and writing of the manuscript.

[3] **Needell, D. R.**; Bauser, H.; Phelan, M.; Bukowsky, C. R.; Ilic, O.; Kelzenberg, M. D.; Atwater, H. A. Ultralight Luminescent Solar Concentrators for Space Solar Power Systems. In *2019 IEEE 46th Photovoltaic Specialists Conference (PVSC)*; IEEE, 2019; pp 2798–2801. https://doi.org/10.1109/PVSC40753.2019.8981161.

D.R.N. participated in the conceptualization of the project, development and validation of the computational model, execution of the simulations, analysis of the results, and writing of the manuscript.

[4] Theingi, S.; **Needell, D. R.**; Bauser, H. C.; Phelan, M. E.; Nemeth, W.; Findley, D.; Su, H.; Koscher, B. A.; Nett, Z.; Ilic, O.; Bukowsky, C. R.; Nuzzo, R. G.; Alivisatos, A. P.; Geisz, J. F.; Stradins, P.; Atwater, H. A. Luminescent Solar Concentrator Tandem-on-Silicon with above 700mV Passivated Contact Silicon Bottom Cell. In *2019 IEEE 46th Photovoltaic Specialists Conference (PVSC)*; IEEE, 2019; pp 0747–0749. https://doi.org/10.1109/PVSC40753.2019.8980809.

D.R.N. participated in the conceptualization of the project, analysis of the experimental results, and editing of the manuscript.

[5] Lunardi, M. M.; **Needell, D. R.**; Bauser, H.; Phelan, M.; Atwater, H. A.; Corkish, R. Life Cycle Assessment of Tandem LSC-Si Devices. *Energy* 2019, 181, 1–10. https://doi.org/10.1016/j.energy.2019.05.085.

D.R.N. participated in the conceptualization of the project, construction of the model inputs, analysis of the results, and editing of the manuscript.

[6] **Needell, D. R.**; Bukowsky, C. R.; Darbe, S.; Bauser, H.; Ilic, O.; Atwater, H. A. Spectrally Matched Quantum Dot Photoluminescence in GaAs-Si Tandem Luminescent Solar Concentrators. *IEEE J. Photovoltaics* 2019, 9 (2), 397–401. https://doi.org/10.1109/JPHOTOV.2019.2892075.

D.R.N. participated in the conceptualization of the project, development and validation of the computational model, execution of the simulations, analysis of the results, and writing of the manuscript.

[7] Bauser, H. C.; Bukowsky, C. R.; Phelan, M.; Weigand, W.; **Needell, D. R.**; Holman, Z. C.; Atwater, H. A. Photonic Crystal Waveguides for >90% Light Trapping Efficiency in Luminescent Solar Concentrators. *ACS Photonics* 2020, 7 (8), 2122–2131. https://doi.org/10.1021/acsphotonics.0c00593.

D.R.N. participated in the conceptualization of the project and editing of the manuscript.

[8] Phelan, M.; **Needell, D. R.**; Bauser, H.; Su, H.; Deceglie, M.; Theingi, S.; Koscher, B.; Nett, Z.; Bukowsky, C. R.; Ilic, O.; Stradins, P.; Geisz, J.; Nuzzo, R.; Alivisatos, A. P.; Atwater, H. A. Outdoor Performance of a Tandem InGaP/Si Photovoltaic Luminescent Solar Concentrator. *Sol. Energy Mater. Sol. Cells* 2021, 223 (October 2020), 110945. https://doi.org/10.1016/j.solmat.2020.110945.

D.R.N. participated in the conceptualization of the project, development and validation of the computational model, fabrication of the samples, execution of the simulations and experimental testing, analysis of the results, and writing of the manuscript.

[9] **Needell, D. R.**; Phelan, M. E.; Hartlove, J. T.; Atwater, H. A. Solar Power Windows: Connecting Scientific Advances to Market Signals. *Energy* 2021, 219, 119567. https://doi.org/10.1016/j.energy.2020.119567.

D.R.N. participated in the conceptualization of the project, analysis of the results, and writing of the manuscript.

[10] Bauser, H. C.; **Needell, D. R.**; Atwater, H. A. AlSb as a Material for High Index Contrast Nanophotonics. *Opt. Mater. Express* 2021, 11 (5), 1334. https://doi.org/10.1364/OME.422163.

D.R.N. participated in the conceptualization of the project, analysis of the results, and writing of the manuscript.

[11] van der Burgt, J. S.; **Needell, D. R.**; Veeken, T.; Polman, A.; Garnett, E. C.; Atwater, H. A. Unlocking Higher Power Efficiencies in Luminescent Solar Concentrators through Anisotropic Luminophore Emission. *ACS Appl.*

Mater. Interfaces 2021, 13 (34), 40742–40753. https://doi.org/10.1021/acsami.1c12547.

D.R.N. participated in the conceptualization of the project, development and validation of the computational model, execution of the simulations, analysis of the results, and writing of the manuscript.

[12] Potter, M. M.; Phelan, M. E.; Balaji, P.; Jahelka, P.; Bauser, H. C.; Glaudell, R. D.; Went, C. M.; Enright, M. J.; **Needell, D. R.**; Augusto, A.; Atwater, H. A.; Nuzzo, R. G. Silicon Heterojunction Microcells. *ACS Appl. Mater. Interfaces* 2021, 13 (38), 45600–45608. https://doi.org/10.1021/acsami.1c11122.

D.R.N. participated in the conceptualization of the project and writing of the manuscript.

[13] Bauser, H.; Bukowsky, C. R.; Phelan, M.; Weigand, W.; **Needell, D. R.**; Holman, Z. C.; Atwater, H. A. Luminescent Solar Concentrators with High Concentration Using Photonic Crystal Waveguides. In *High Contrast Metastructures X*; Fan, J. A., Chang-Hasnain, C. J., Zhou, W., Eds.; SPIE, 2021; Vol. 11695, p 13. https://doi.org/10.1117/12.2576720.

D.R.N. participated in the conceptualization of the project.

[14] Tham, R. W.; **Needell, D. R.**; Atwater, H. A. Two-Dimensional Transition Metal Dichalcogenide Heterobilayer Emitters for Luminescent Solar Concentrator Photovoltaics. In *2021 IEEE 48th Photovoltaic Specialists Conference (PVSC)*; IEEE, 2021; pp 0372–0376. https://doi.org/10.1109/PVSC43889.2021.9518444.

D.R.N. participated in the conceptualization of the project, development and validation of the computational model, execution of the simulations, analysis of the results, and writing of the manuscript.

[15] Phelan, M. E.; Potter, M. M.; Balaji, P.; Jahelka, P. R.; Bauser, H. C.; Glaudell, R.; **Needell, D. R.**; Enright, M.; Augusto, A.; Nuzzo, R.; Atwater, H. A. Fabrication Techniques for High-Performance Si Heterojunction (SHJ) Microcells. In *2021 IEEE 48th Photovoltaic Specialists Conference (PVSC)*; IEEE, 2021; pp 0330–0334. https://doi.org/10.1109/PVSC43889.2021.9518579.

D.R.N. participated in the conceptualization of the project and writing of the manuscript.

[16] Enright, M.J.; Jasrasaria, D.; Hanchard, M.M.; **Needell, D.R.**; Phelan, M.E.; Weinberg, D.; McDowell, B.M.; Hsiao, H.W.; Akbari, H.; Kottwitz, M.; Potter, M.M.; Wong, J.; Zuo, J.M.; Atwater, H.A.; Rabani, E.; Nuzzo, R.G. Role of Atomic Structure and Exciton Delocalization on Photoluminescence in NIR Emissive InAs/InP/ZnSe Quantum Dots. *Under Review* 2021.

D.R.N. participated in the conceptualization of the project, execution of the simulations, analysis of the results, and writing of the manuscript.

[17] Bauser, H.C.; Phelan, M.E.; Foley, M.; Weigand, W.; **Needell, D.R.**; Holman, Z.C.; Atwater, H.A. Highly Efficient, Spectrally-Selective Reflectors in the Visible Spectrum via Amorphous Silicon Carbide High Contrast Gratings. *In Progress*, 2022.

D.R.N. participated in the conceptualization of the project.

[18] **Needell, D.R.**; Potter, M.M.; Phelan, M.E.; Jahelka, P.R.; Bauser, H.C.; Korus, D.; Velarde, A.; Balaji, P.; Augusto, A.; McDaniel, H.; Geisz, J.F.; Nuzzo, R.G., Atwater, H.A. Performance Limits and Applications of Area-scalable Luminescent Solar Concentrator Photovoltaic Devices. *In Progress*, 2022.

D.R.N. participated in the conceptualization of the project, development and validation of the computational model, fabrication of the samples, execution of the simulations and experimental testing, analysis of the results, and writing of the manuscript.

[19] **Needell, D.R.**; Su, H.; Phelan, M.E.; Bauser, H.C.; Enright, M.J.; Geisz, J.F.; Nuzzo, R.G.; Atwater, H.A. Active-Passive Hybrid Photovoltaic Concentrators. *In Progress*, 2022.

D.R.N. participated in the conceptualization of the project, development and validation of the computational model, fabrication of the samples, execution of the simulations and experimental testing, analysis of the results, and writing of the manuscript.

[20] **Needell, D.R.**; Phelan, M.E.; Korus, D.; Bauser, H.C.; Kelzenberg, M.D.; Loke, S.; Theingi, S.; McDaniel, H.; Stradins, P.; Geisz, J.F.; Nuzzo, R.G.; Atwater, H.A. Luminescent Solar Concentrators Flown in Lower Earth Orbit. *In Progress*, 2023.

D.R.N. participated in the conceptualization of the project, development and validation of the computational model, fabrication of the samples, execution of the simulations and experimental testing, analysis of the results, and writing of the manuscript.

CHAPTER 1

Introduction & Background

In 2020, the world consumed over 23,000 TWh of electricity[1]. In it, nonrenewable energy sources (e.g., coal, oil, natural gas) made up over 80% of the generated electrical energy—shown in Figure 1.1(a)[2]. With such a significant portion supplied by these fuel sources—sources which produce carbon dioxide emissions as a byproduct of their combustion—recent ecological and climate studies prognosticate a range of baleful environmental outcomes[3–6].

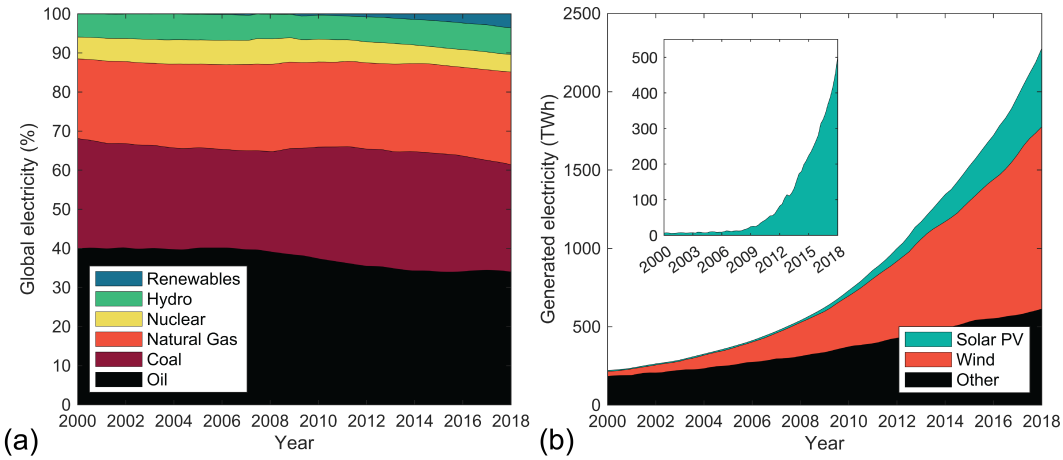

Figure 1.1: An analysis of the global energy portfolio since the beginning of the millennium for (a) all energy sources (renewable and nonrenewable) in terms of the percentage of total generated energy and (b) renewable generation technology in terms of the produced electricity (TWh). Figures adapted from BP's Annual Review of World Energy Report[7].

But despite such a bleak environmental outlook, we would be remiss not to clarify the unmistakable growth that renewable energy sources (e.g., solar photovoltaics, solar thermal, wind, tidal) have undergone; whereby, for example, we readily observe how this renewable energy portfolio has grown by nearly an order or magnitude in generation capacity since the turn of the century[7]. Illustrated in Figure 1.1(b), solar photovoltaic energy—i.e., the conversion of incident sunlight (photons) into useful electricity (electrons)—at present constitutes about 20% of our renewable generation

source[7]. Despite tremendous growth of photovoltaic energy production shown by Figure 1.1(b) inset, the total amount of solar radiance that reaches earth, integrated over an entire year, far outweighs the current worldwide production.

To illustrate this point more quantitatively, let us for example consider some arbitrary photovoltaic generation system (some "blackbox" device that churns out a number of electrons given a number of incident photons). For ease of arithmetic, let us assume that this device produces a single useful electron for every ten incident photons—that is, very roughly speaking, that the overall power conversion efficiency of such a photovoltaic is 10%. Finally, again for argument's sake, let us imagine building enough of these blackbox devices so as to cover 0.50% of the available land area of earth (total land area being almost 150 million km^2, 0.50% of this being about 750 thousand km^2, which equates roughly to the land area of Texas). Assuming all the produced electrons can either immediately be of practical use or stored for later use, we now want to estimate how long it would take to generate the global energy demand of 2020—recalling it to be approximately 23,000 TWh. While the sun delivers just over 1300 watts per square meter of power on the atmosphere, let us assume that half of this is either attenuated or scattered by the atmosphere and cloud coverage. Therefore, we can easily calculate how such a system would generate the worldwide energy demand in about half a day[8]. However over-simplified this gedanken experiment, the raw energy availability of the sun imbues us with the opportunity to eliminate our societal dependence on fossil fuels.

Despite such crude abundance however, there still exist significant hurdles that limit the adoption and integration of photovoltaic systems into the existing energy infrastructure. Appreciably, sunlight is an intermittent resource. Be it in space (geographical) or time (daily, seasonal), irradiance conditions vary considerably and, accordingly, yield intermittent patterns in photovoltaic electricity production[9]. Beyond hurdles related to receiving photons, the costs for building and implementing photovoltaic systems (e.g., raw materials acquisition and transport, processing, manufacturing, installation) arbitrates the economic competitiveness against the incumbent nonrenewable sources. In order to account for both the electrical power generation and full economic scope of a particular system, we can define the levelized cost of energy (LCOE) as a singular Figure of merit to holistically compare different energy generation systems[10]. As defined by Equation 1.1, the levelized cost of energy weighs the total cost of the system (conventionally expressed in ¢) against the amount of energy generated over the system lifetime (expressed units of kWh).

$$\text{LCOE} \equiv \frac{\text{Lifecycle cost}}{\text{Lifetime energy production}} = \frac{C_0 + \sum_{n=1}^{N} C_n}{\sum_{n=1}^{N} E_n} \tag{1.1}$$

where C_0 and C_n give the system costs (¢) for the initial installation and operating costs of every year (n) for N years, respectively. E_n gives the amount of energy generated (kWh) for a given year, n, whereby current standards assume system lifetimes, N, to be greater than or equal to 25 years. As seen from the levelized

cost of energy, developing a photovoltaic system more competitive to incumbent, nonrenewable technologies reduces to: *(a)* driving down system costs, and/or *(b)* optimizing performance to enable increased energy harvesting.

The myriad strategies to accomplish these tasks predicates how solar photovoltaic energy technology has evolved over time. For example, Figure 1.2(a) highlights the production capacity evolution of three distinct classes of photovoltaic materials—single crystalline silicon, poly- or multi-crystalline silicon, and thin-film based devices (e.g., gallium arsenide, copper indium gallium selenide). From this we can observe how silicon-based photovoltaic systems have and continue to occupy the vast majority of installed generation capacity. To clarify (at least qualitatively) why silicon rose and continues to rise in photovoltaic market share, we must recall the first practical demonstration of a working solar cell in 1953 at Bell laboratories[11]. This early fabrication relied upon a monocrystalline silicon cell and, later as the semiconductor industry grew exponentially with the advent of the integrated circuit, the price of silicon processing decreased with economies of scale. As such we find, illustrated in Figure 1.2(b), how the cost reductions of the silicon solar cell, combined with the tremendous power conversion efficiency improvements, correlate to the historical market ubiquity—where today silicon-based photovoltaic cells account for up to 93% of all systems[12].

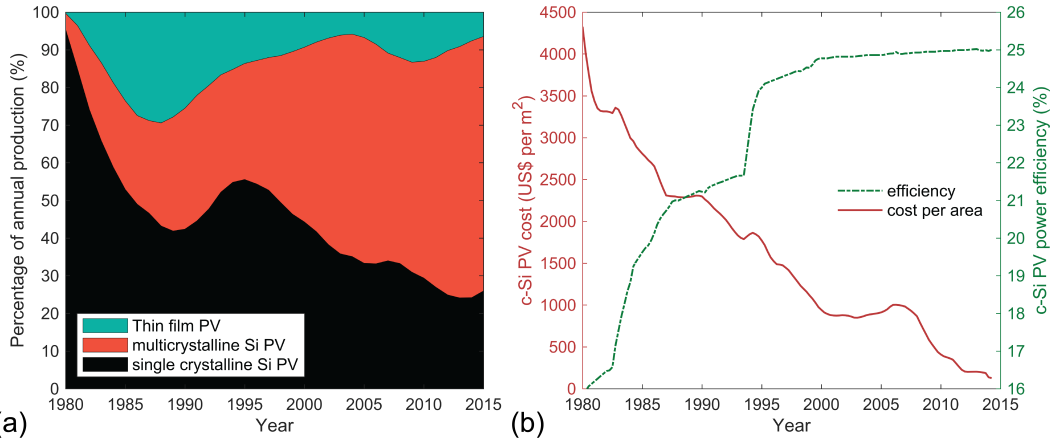

Figure 1.2: An analysis of installed photovoltaic system trends from 1980 until 2015. (a) The three categories of solar technologies and how they contribute to the overall annual energy production over time. (b) The cost (left y-axis, red solid line) of crystalline (single and multi-) silicon photovoltaic cells per area (US$ per m^2), averaged over several leading manufacturers, adapted from Kavlak et al[13]. The record monocrystalline silicon (c-Si), single junction sunlight to electrical power efficiency (right y-axis, green dashed line) certified at the National Renewable Energy Laboratory, adapted from published research cell efficiency charts[14]. Combined, the cost decrease and performance increase help explain the ubiquity of silicon-based photovoltaic technology in the energy market.

1.1 Solar Photovoltaic Energy Generation

Despite the ubiquity of crystalline silicon solar cells, Figure 1.2(b) depicts a critical concern for such devices: a power conversion efficiency plateau. In it, there appears a practical limit to the performance of the silicon cell to convert incident photons to useful electrons—shown to saturate at approximately 25%, where we find that the past two decades of research and development in silicon cells have cumulatively seen less than 1% absolute efficiency improvement. To unveil the origins of this performance ceiling and moreover how to push beyond it, we must first begin by discussing the photonic and electronic material properties fundamental to the photovoltaic effect. To do so, we start with an overview of the basic principles behind how such devices convert incident photons into electrons that can provide useful work. We then discuss the thermodynamic principles that set the conversion efficiency limits for all solar cells under equilibrium, wherein we introduce a breakdown of each energetic loss mechanism that sets such a limit. We finally provide a synopsis of current methods to overcome various losses in order to saturate experimental device efficiencies to their theoretical limit. This discussion of overcoming such losses leads us naturally to strategizing next-generation devices and, more specifically, to the topic of this thesis.

1.1.1 The Fundamentals of Photovoltaic Devices

To quantify the limits of photovoltaic devices, we must first understand the interaction between incident photons—that is, localized electromagnetic oscillations of energy quanta inversely proportional to the wavelength of oscillation, $E = hc/\lambda$ (h, c, and λ being Plank's constant, the speed of light, and the wavelength respectively)—and electrons within solid materials (i.e., crystalline or amorphous). Originally theorized in 1905 by Albert Einstein[15], the photoelectric effect quantifies how photons of sufficient energy can, upon interaction with certain solid-state materials, excite valance electrons out from their localized orbitals and into a delocalized state. This photon-electron interaction, together with the development of solid-state quantum mechanics, provided the basis for rich scientific discoveries in condensed matter physics—among many others, the theory and experimental realization of solar photovoltaic cells.

When a material sufficiently cools in temperature such that there exist local equilibria positions for each atom, a repeated pattern or structure forms (i.e., a crystalline lattice). The atomic constituents determine the interatomic spacing between nearest neighbor atoms. Applying the Pauli exclusion principle, where no two or more identical fermions (e.g., electrons) can occupy the same quantum state (e.g., energy and spin) within the same quantum system, we can qualitatively derive a fundamental property of crystalline solids—the electronic bandgap. As the atoms settle into their minimum energy positions in the lattice, valance band electronic wavefunctions begin to spatially overlap. By the exclusion principle, certain energy levels become forbidden according to this interatomic spacing, and we observe the formation of an electronic energy bandgap (E_g) between localized (valance band)

and delocalized (conduction band) electrons.

As illustrated in Figure 1.3(a), we arbitrarily categorize a class of solid-state materials as semiconductors, defined principally by their electronic bandgap in a crystalline structure of lattice parameter (i.e., nearest neighbor distance), a. This taxonomical class of solids exhibits bandgap energies that typically fall within a few electron volts (eVs)—as opposed to insulators whose electronic bandgaps extend beyond several electron volts, while conductors exhibit negligibly small bandgaps. This energy bandgap quantifies the difference between upper-most, electron-filled energies within the valence band (electrons localized to a single nucleus or multiple nuclei) and lower-most, electron-empty energy levels within the conduction band (whereby excited electrons become delocalized to any one nucleus).

Figure 1.3(b) shows an example of a measured energy band diagram of crystalline silicon and conceptualizes the distinction between electronic valence and conduction bands. As shown, the wavenumber (i.e., the number of electron wavepacket oscillations per unit distance in a certain direction) can extend in different spatial directions of the lattice. As wavenumbers are therefore expressed in units of inverse length (usually cm^{-1}), we often describe their behavior in this reciprocal space. Figure 1.3(b) highlights how, by varying this wavenumber in reciprocal space (illustrated in the bottom left corner), the valence and conduction band energy levels shift; however, we define the principal electronic bandgap of a solid material as the difference between the highest valance energy band level in reciprocal space (in this case occurring at the Γ point) and the lowest conduction level (near X). Therefore, for the case of crystalline silicon, we find a minimum bandgap energy of approximately 1.1eV, whereby the distinction between valence and conduction band wavenumbers illustrate how such a material forms an indirect bandgap (separated by a momentum vector).

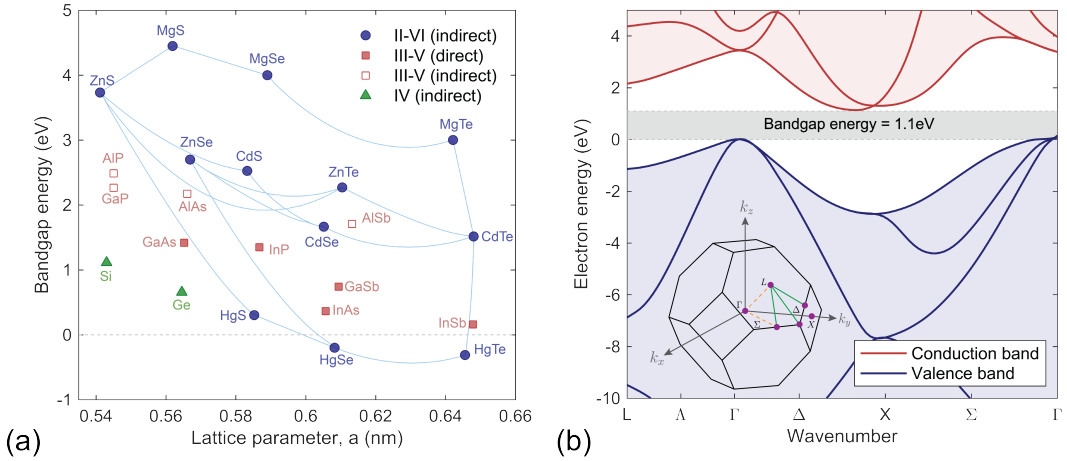

Figure 1.3: An overview of semiconductors showing (a) commonly used types with their accompanying energy bandgaps, lattice parameter, a, and associated alloy pathways, adapted from Yang et al.[16], and (b) a measured crystalline silicon energy band diagram, adapted from Chelikowsky & Cohen[17]. In this, the lowest conduction band and highest valence band energies form an indirect gap from one another, requiring a change of electronic wavenumber (i.e., momentum).

pn Junctions, Light Interaction, and Carrier Dynamics

The goal for any photovoltaic device is to generate a current of electrons propelled through some external load by an electromotive force. As we define electrical power as the electronic current multiplied by the voltage (i.e., the electromotive force), the solar cell must therefore achieve both high current and voltage in order to attain high photon to electrical power conversion efficiency. We previously introduced the concept of how sufficiently energetic photons can excite electrons from the valance band into the conduction band—leaving behind a vacancy in its photoexcited wake (termed a hole). While this excitation produces a delocalized electron that can in principle propagate freely through the semiconductor lattice, the solar cell device must issue some sort of electromotive force in order to separate the electron-hole pair (exciton) from recombining.

The electromotive force that drives this separation, known as the photovoltaic effect, results from an interface (junction) between two semiconductor materials: one with added impurities which donates electrons (e^-) at energy levels in between the valence and conduction bands (termed "donor" states), the other with impurities offering electron vacancies (i.e., holes, h^+) again with mid-level energies (termed "acceptor" states). When two semiconducting materials with opposite doping concentrations are brought into direct contact—or when donor and acceptor dopants are diffused from opposing sides of a single host material—the mid-level donor state (n-type) valance electrons fill the acceptor state (p-type) holes. This process is driven by the fact that there exists, before reaching thermodynamic equilibrium, a difference in the Fermi energy levels (that is, the relative concentration of electrons and holes) across the junction. After equilibration, when the Fermi energy achieves a constant value across the entire device, an electric potential barrier, V_b, forms according to the concentration gradient across this region. Due to the filling of mid-level energy states, we refer to this as the "depletion" region.

Figure 1.4 conceptualizes this pn junction and a real-space energy band diagram across it. For a p-type material, the Fermi energy (the point of equal energy occupancy probability for electrons and holes via our Fermi-Dirac statistics) lies closer to the valence band owing to a higher occupancy of holes in intragap energies. For n-type material, the Fermi level conversely shifts closer to conduction band edge, given that there exist more mid-level electrons. For a pn junction under no illumination and in thermodynamic equilibrium, there exists a single Fermi energy across this junction, yielding a band diagram shown in Figure 1.4(a). Here we can readily observe the band bending (i.e., energy barrier, $E = qV_b$) across the depletion region.

Under no external voltage biasing and no illumination source, the electric field across the depletion region separates excitons generated via the thermal background (at finite temperature) in opposite direction. We label this p-type to n-type flow the drift current. However, there also exists a concentration gradient of electrons and holes across the junction given by the difference of donor/acceptor doping levels. Therefore, via the second law of thermodynamics, there exists a flow opposite the drift, called the diffusion current. In thermodynamic equilibrium, these two currents

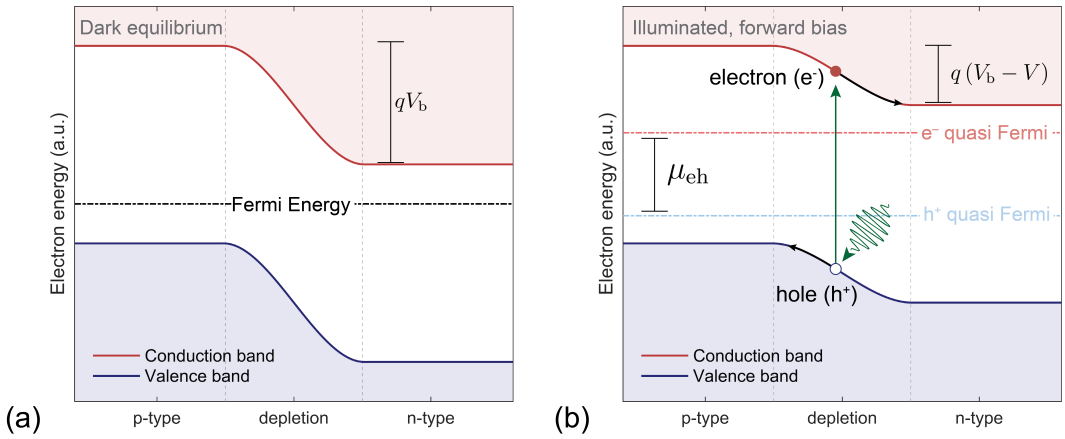

Figure 1.4: A visualization of the *pn* homojunction as it pertains to solar cells, where (a) depicts the steady-state, equilibrium condition under no illumination or biasing with some electric potential barrier, V_b, and (b) provides a qualitative understanding of the junction and charge carrier dynamics under a forward voltage bias, V, with incident photons of energy greater than the semiconductor's bandgap. At forward biases below the open-circuit voltage (V_{oc}), the electric potential barrier weakens in magnitude, thereby perturbing the system out of equilibrium. As a consequence, diffusion of majority carriers on each side competes against photogenerated excitons that separate due to the electric field across the depletion region (electrons pushed to the *n*-type side and holes to the *p*-type). The excitonic chemical potential difference (electromotive force) is given by the quasi-Fermi level split.

exactly cancel each other and we arrive at the band diagram shown in Figure 1.4(a).

When we expose a solar cell to a source of photons (e.g., the sun), the total number of photogenerated excitons under no external voltage biasing sets the maximum amount of light-induced photocurrent, I_L, of the device. As such, drift dominates over diffusion current—as few charge carriers can diffuse across the junction relative to the large number of photogenerated excitons separated by the intrinsic electric field. We label this maximum current as the short-circuit condition, I_{sc}, given that this large current forms when we directly connect the opposite sides of the junction together with little to no resistance across it (i.e., shorting the junction). Here we note that the number of photogenerated excitons depends upon both the incident irradiance (intensity and spectra); the area of solar cell (A_{cell}); the cell absorbance, reflectance, and transmittance properties; and the exciton separation and collection efficiencies. In order to eliminate areal dependence, we define the short-circuit current density (J_{sc}) by dividing the short-circuit current with respect to the overall illuminated cell area. We can characterize the cell excitonic collection efficiency with respect to the incident photon energy, termed the internal quantum efficiency. Further, we can combine the absorbance/reflectance/transmittance spectra with the cell internal quantum efficiency into a single Figure of merit, given as the external quantum efficiency of the cell with respect to photon energy. Near-unity external quantum efficiency signifies a high excitonic generation and collection probability for a photon of energy hc/λ.

In contrast to the short-circuit condition, if we apply an external voltage bias (V) opposite the intrinsic potential barrier, we can shift the *p*- and *n*-type bands

with respect to one another by the amount qV as shown in Figure 1.4(b). Owing to the electric potential barrier decrease across the junction, a split of the Fermi level issues—where quasi-Fermi levels for electrons and holes separately emerge given the imbalance between drift and diffusion currents. The magnitude of this splitting (i.e., the relative difference between the electron and hole quasi-Fermi energies) reveals the chemical potential, μ_{eh}, of the exciton. As expected, while an increase in forward bias voltage increases the chemical potential of the photogenerated exciton, drift current decreases relative to diffusion, which increases exponentially with decreased barrier height. Therefore at sufficient biases or loads, termed the open-circuit voltage (V_{oc}) condition, there exists an exact balance between drift and diffusion such that no net current flow exists across the device. At biases beyond the V_{oc} (for the case of external voltage sources), radiative and non-radiative electron-hole pair recombination continues to increase exponentially and, as a result, such biases create current flow in what is called the forward direction.

Equation 1.2 defines the relationship between current density and applied voltage bias, V, for a solar cell. Here, we show how the net current results from light induced drift photocurrent, J_{L}, in the reverse direction (i.e., affixing a negative sign to this term) and charge recombination due to diffusion current in the forward direction (positive).

$$J = J_0 \left(e^{\frac{qV}{nkT}} - 1 \right) - J_L, \tag{1.2}$$

where J_0 is known as the dark saturation current, q electron charge, n ideality factor of the diode, k Boltzmann constant, and T cell temperature. From Equation 1.2, we can see how the dark saturation term, J_0, gives the amount of diffusion current that exists under ambient background illumination in thermodynamic equilibrium at temperature, T. J_0 can therefore be viewed as the measure of nonradiative and radiative recombination of excitons in the absence of high-intensity illumination since, at thermal equilibrium, total absorption must equal total emission via the Kirchoff law of thermal radiation. By setting V or J to zero, we can uncover J_{sc} and V_{oc} from Equation 1.2, respectively. Doing so, we find:

$$J_{\mathrm{sc}} = -J_L \tag{1.3}$$

$$V_{\mathrm{oc}} = \frac{nkT}{q} \ln \left(\frac{J_L}{J_0} + 1 \right). \tag{1.4}$$

For V_{oc} in Equation 1.4, we can identify two sources of dark current contribution. First, there exists a certain amount of thermally generated excitons (at the surrounding temperature, T) owing to a small amount of high-energy photons that exist in the Blackbody background, which excite charge carriers from the valence to conduction band, J_0^r. Second, material defects of the semiconductor lattice—which can yield interband energy states—also give rise to excitons within the cell that can contribute to this dark current, which we refer to as the non-radiative term, J_0^{nr}. We can choose to view these two terms (the radiative and non-radiative dark currents) either as exciton generation or annihilation. Thus, we can re-write our cell V_{oc} given these two contributions to dark saturation current in the context of

radiative efficiency:

$$\begin{aligned} V_{\text{oc}} &= \frac{nkT}{q} \ln\left(\frac{J_L}{J_0^r + J_0^{nr}} + 1\right) \\ &\approxeq \frac{nkT}{q} \ln\left(\frac{J_L}{J_0^r + J_0^{nr}}\right) \\ &\approxeq \frac{nkT}{q} \ln\left(\frac{J_L}{J_0^r}\right) + \frac{nkT}{q} \ln\left(\frac{J_0^r}{J_0^r + J_0^{nr}}\right) \\ &\approxeq \frac{nkT}{q} \ln\left(\frac{J_L}{J_0^r}\right) + \frac{nkT}{q} \ln\left(Q_{\text{ERE}}\right), \end{aligned} \tag{1.5}$$

where Q_{ERE} defines the external radiative efficiency of the solar cell. We will see later on in this thesis how the V_{oc}, more specifically the radiative efficiency, plays an important role in enhancing solar cell performance.

Electrical power is given as the electron current flow times the voltage bias (chemical potential) across the junction. Because of the diode response of a solar cell in Equation 1.2, there exists a point of maximum power at a specific current and voltage $(J_{\text{mp}}, V_{\text{mp}})$. The fill factor (FF) of a solar cell compares this point of maximum power to the upper limit open-circuit voltage and short-circuit current points. The power conversion efficiency (η_{pce}) of the solar cell is therefore the ratio of output power density of the solar cell to total input power of the light source (integrated over the irradiance, I, of the source with respect to wavelength and solid incident angle, Ω), as described in Equations 1.6 and 1.7:

$$\eta_{\text{pce}} = \frac{P_{\text{out}}}{P_{\text{in}}} = \frac{J_{\text{mp}} \cdot V_{\text{mp}}}{P_{\text{in}}} = \frac{J_{\text{sc}} \cdot V_{\text{oc}} \cdot \text{FF}}{P_{\text{in}}} \tag{1.6}$$

$$P_{\text{in}} = \int_{\lambda} \int_{\Omega} I(\lambda, \Omega) \ \text{d}\Omega\text{d}\lambda. \tag{1.7}$$

As shown in Figure 1.5(a), the current-voltage (JV) relationship gives the power conversion efficiency, non-idealities of the diode behavior (series/shunt resistances), V_{oc}, J_{sc}, and FF. Figure 1.5(b) provides the measured terrestrial (AM1.5) and extraterrestrial (AM0) irradiance spectra from our sun alongside a theoretical blackbody spectrum at 6000K for reference—with several common semiconductor energy bandgaps.

Detailed Balance Efficiency Limit for Single Junction Cells

Because the bandgap energy, E_g, of the depletion region determines the maximum number of photogenerated excitons in the solar cell (short-circuit current), it follows that this energy also relates to the maximum power conversion efficiency obtainable. As described, the J_{sc} results from this number of photogenerated excitons with no external biasing. In materials with smaller bandgaps, a larger portion of incoming photons can excite electrons and, therefore, such materials can typically achieve higher short-circuit currents. Due to smaller energy gaps between the conduction and valence band edges, however, lower bandgap cells cannot attain as large of

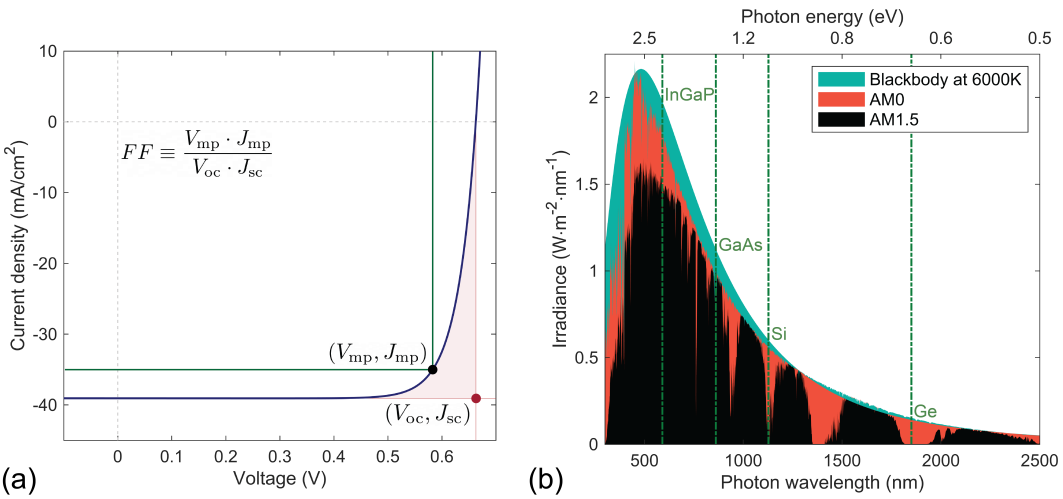

Figure 1.5: (a) An example of a current-voltage (JV) curve for a typical crystalline silicon solar cell[18]. FF defines the area fraction between the inner rectangle formed by the voltage/current maximum power points, (V_{mp}, J_{mp}), and the outer formed by the open-circuit voltage and short-circuit current, (V_{oc}, J_{sc}). (b) The incident light spectra from our sun, showing the blackbody spectrum at 6000K, the measured irradiance at the outer atmosphere (AM0), and the measured irradiance at the surface (AM1.5). Decreased intensity gaps occur as a result of atmospheric light scattering for certain wavelengths. Four commonly used semiconductor materials for solar cells are shown for reference.

quasi-Fermi energy level splittings (i.e., lower chemical potential, μ_{eh} of the photogenerated exciton). Thus, smaller bandgap materials yield decreased open-circuit voltages. Thus, there exists an optimization between J_{sc} and V_{oc} with respect to the electronic bandgap.

Introduced in the early 1960s[19], the theoretical maximum power conversion efficiency of a photovoltaic cell occurs by assuming every incident photon with energy greater than or equal to the cell bandgap produces precisely one exciton within the *pn* junction that can be separated and collected. We can then apply the concept of detailed balance, where we require that exciton pairs be eliminated (radiatively as photons or nonradiatively as phonons) at the same rate as they are generated (via incident illumination or operating temperature blackbody background). This must be the case under thermodynamic equilibrium, otherwise we would observe a charge build up which would contradict our state of equilibrium. By use of the well-known Planck distribution spectrum, Equation 1.8 quantifies this detailed balance limit of power conversion efficiency, $\eta_{\text{det.bal.}}$, with respect to the energy bandgap.

$$\eta_{\text{det.bal.}} = \frac{P_{\text{out(det.bal.)}}}{P_{\text{in(det.bal.)}}} = x_g \int_{x_g}^{\infty} \frac{x^2}{e^x - 1}\, \mathrm{d}x \Big/ \int_0^{\infty} \frac{x^3}{e^x - 1}\, \mathrm{d}x\,, \tag{1.8}$$

where $x_g = E_g/kT_s$ where T_s is the blackbody temperature of the sun. In this limit, we assume the chemical potential of the photogenerated excitons to equal the maximum quasi-Fermi energy level split, given by the semiconductor bandgap. Further, as shown in the denominator of Equation 1.8, we assume all incident photons to strike at normal incidence with respect to the cell planar surface.

While the simplest form of the detailed balance limit shown by Equation 1.8 reaches a maximum efficiency of approximately 44% near a bandgap energy of 1.12 eV, this limit does not take into account deleterious loss mechanisms such as: *(i)* the amount of available incident power and solid angle subtended from the sun, *(ii)* the transmission of radiative recombination out of the cell, *(iii)* the exciton separation and collection efficiencies of the junction, and *(iv)* incomplete photon absorption by the cell for above bandgap energies. For example, including the subtended solid angle from the solar disc and relevant terrestrial AM1.5g spectrum (i.e., the amount of light that reaches the surface of earth on a clear, sunny day), the maximum efficiency occurs when $E_g = 1.1$ eV and decreases to approximately 32.9%[20]. For the case of crystalline Si cells, when including nonradiative recombination pathways and optical absorption/reflection losses, this limit further decreases to 29.8% assuming a standard cell thickness of 100μm[21]. Figure 1.6(a) displays the original detailed balance efficiency limit as a function of bandgap energy, and illustrates how this limit decreases with subsequent revisions that take into account non-idealities. Figure 1.6(b) conceptually shows the four primary recombination types that limit overall power conversion efficiency.

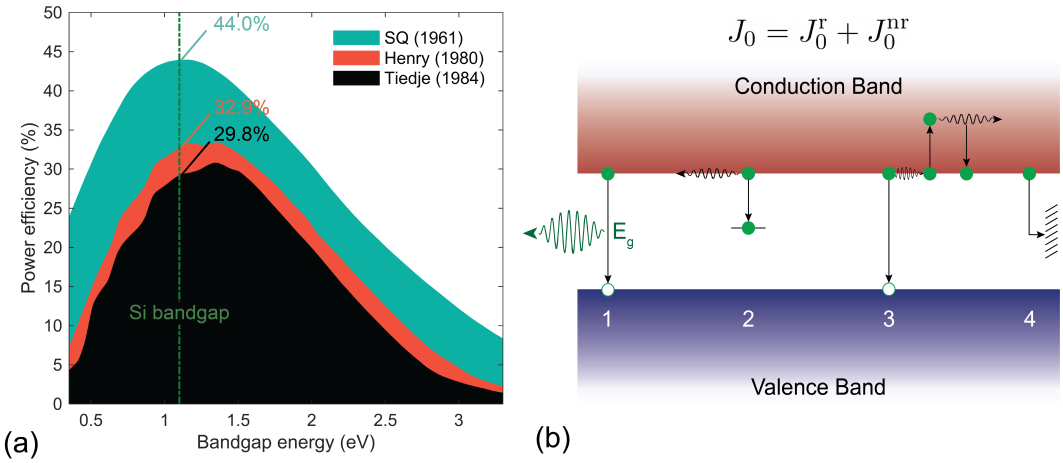

Figure 1.6: (a) Detailed balance models for single junction, 1-sun illumination of a solar cell assuming: (1) blackbody spectrum, no optical absorption/reflection losses, and perfect carrier extraction; (2) AM1.5 spectrum and limited solid angle, no optical losses, and no nonradiative recombination; and (3) AM1.5 spectrum with subtended solid angle, optical losses, radiative and nonradiative recombination. (b) A conceptual diagram comparing the four general categories of recombination within a solar cell: (1) radiative with an emitted photon of energy less than or equal to E_g; (2) Shockley-Reed-Hall for an emission of a phonon and filling of an intermediate energy state (e.g., dopant/defect); (3) Auger recombination where demotion of a conduction band electron to the valence band transfers its energy to a conduction electron, promoted to higher energies, and ultimately thermalizing back to the conduction band edge through phonon emission; and (4) defect state filling at the surface/edge of the semiconductor crystalline lattice and release of a phonon. Adapted from Tous[22].

1.1.2 Technical and Economic Constraints on Solar Devices

As previously discussed in Figure 1.2(a), crystalline silicon cell costs (i.e., processing, manufacturing) have decreased by more than 99% since the early 1980s. Owing to this appreciable decrease, the balance of system (BoS) and "soft" costs[1] currently constitute more than half of the overall system costs, shown in Figure 1.7(a)[23] . With this recent shift in solar energy economics, current research efforts focus away from the minimization of photovoltaic fabrication costs and instead toward designs that can enable markedly lowered BoS and soft costs. With such a paradigm shift, two strategies to further photovoltaic system adoption emerge: *(i)* performance-enhancing designs to enable greater power output per area—thereby requiring fewer installations per unit energy generated—while keeping cell and raw material costs low, and *(ii)* integration of solar designs into existing architectural structures and façades that absorb installation costs, while keeping cell performance high.

While the detailed balance limit sets a maximum on the theoretical efficiency possible for a single junction cell under 1-sun (i.e., a solar cell with a single bandgap energy, E_g), there exist various strategies that can extend power conversion efficiencies beyond this limit. As Figure 1.7(b) illustrates, despite certain unavoidable thermodynamic losses (e.g., entropy due to the conversion of a photon to an electron), such inefficiencies total to approximately 14%[24]. The most significant loss for single junction cells results from highly excited photogenerated carrier relaxation down to the electronic conduction band edge (i.e., thermalization). By the same token, cells with too large of bandgaps suffer from incomplete absorption of the solar spectrum due to the transmission of incident photons with energies below that of the required bandgap. Combined, these two mechanisms account for greater than 40% efficiency loss for a standard silicon solar cell of bandgap energy 1.1 eV. Further, when excitons radiatively recombine and emit as photons into free space, there exists an entropy penalty owing to the angular spread of luminescence relative to the incident solar disc. This penalty accounts for approximately 10% absolute power conversion efficiency loss.

Given these loss mechanisms, there exist myriad methods to overcome the single junction, 1-sun detailed balance limit. On one hand, in an effort to reduce the losses of exciton thermalization and incomplete light absorption, multijunction photovoltaic module designs employ more than one cell material type and, thereby, more than one bandgap. By arranging cells with higher bandgaps in descending vertical order, photons cascade through traditionally monolithic structures, being absorbed and collected by the cell corresponding to its energy. Separately, cells (single- and multijunction) can employ concentrating optics to increase light trapping and reduce the entropic penalties for radiatively recombined excitons. Together with multijunction devices and concentration mechanisms, top research cell efficiencies have recently demonstrated performances that extend up to 47.1% under standard testing conditions[25,26]. Despite such achievements, broad photovoltaic implementation for high-efficiency cells remains limited. For the case of multijunction modules, cell

[1]BoS costs include racking and mounting of panels (i.e., arrays of cells) and supporting structures. Soft costs include all other related costs minus photovoltaic cell fabrication/materials and structural hardware (e.g. permitting, inspection, interconnection, etc.).

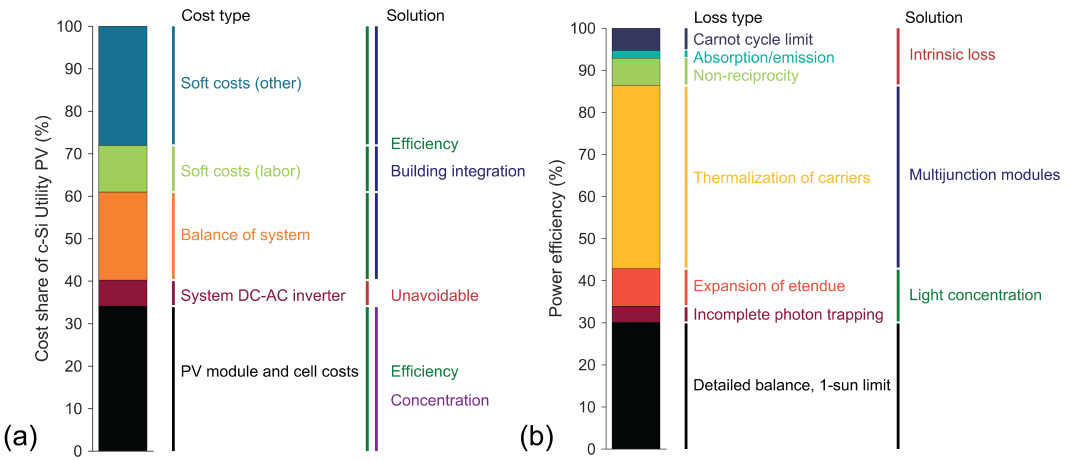

Figure 1.7: (a) A cost breakdown of a standard crystalline silicon (c-Si) solar cell. The BoS and soft costs add up to roughly 60% of the total, adapted from Fu et al.[23]. (b) Sources of cell efficiency loss, showing the dominate mechanisms owing to either incomplete photon absorption, thermalization of high-energy photogenerated carriers, and entropy penalties for radiatively recombined excitons. Adapted from Polman & Atwater[24].

material and processing costs traditionally outweigh the efficiency enhancement, resulting in a substantial increase in the LCOE[27] . Similarly, along with the additional optical materials expense for traditional concentrator technology, such devices can only operate for certain angles of incidence and often exhibit detrimental device heating[28].

As an alternative to enhanced module efficiency, building integrated photovoltaic systems could provide a separate pathway to enable decreased overall LCOE[29,30]. With such modules, the visual aesthetics of the cell aim to blend photovoltaic devices into building façade components—e.g., shingles in a rooftop[31] or glass panes in a window[32–34]. In certain form factors, building integrated BoS costs can reduce to approximately 14% its typical value[35]. Outfitting the functionality of a building component with solar photovoltaic generation can reduce BoS costs. However, owing to increased reflectance or transmittance properties of the device to blend into architectural form factors, the power conversion efficiency typically suffers. Despite over 40 years of research and development for building integrated systems, only recently has there existed a need for this technology given the shifting cost breakdown of the standard utility-scale solar module[36].

1.2 The Concentration of Sunlight

For both high-efficiency, multijunction modules and low-cost, building-integrated cells, concentration of incident light onto a small-area solar cell presents an intriguing method to further technological adoption. In both cases, concentration can enable increased light trapping efficiency and, as discussed, issue higher performances owing to a reduction in the angular spread of radiatively recombined excitons. In the former case of high-efficiency multijunction designs, light concen-

tration reduces the required cell area, thereby decreasing the amount of expensive high-bandgap cell material costs. For the latter case of low BoS cost building integration, concentration allows for non-traditional geometries and structures that serve to further blend the cell into a building component—often obscuring the cell entirely from view. Therefore, cost and power efficient light concentration mechanisms that maintain functionality irrespective of the incident radiance angle could enable higher implementation across a wide variety of markets.

Historically, we can categorize light concentration into two distinct optical varieties: passive (e.g., geometric) and active (e.g., luminescent). In passive light concentration, systems (e.g., Fresnel lenses) focus irradiance of an aperture area, A_{in}, onto a smaller output area, A_{out}, with no photon energy change. In contrast, active concentration converts incident light that impinges upon A_{in} with energy, E_{in}, to a lower energy, E_{out}, in order to redirect downshifted radiance to the output collector, A_{out}. To understand how we can achieve angle-independent light concentrators, we must first consider the case of passive concentration.

1.2.1 Passive Concentration: the Geometric Solar Concentrator

For geometric concentration systems, there exists an optical, or series of optical, setup(s) such that incident photons, entering at A_{in} and within an acceptance cone defined by θ_{in}, concentrate onto an exit aperture, A_{out}, within an exit cone of θ_{out}. Figure 1.8(a) displays a general passive concentration device. The radiance of the light (L) and the projected area and solid angle yield the total photon flux for both the input (Φ_{in}) and output (Φ_{out}) apertures. We can define an arbitrary photon flux (Φ_i) through a certain area (A_i) for some surface, i, as:

$$\Phi_{\text{i}} = \int L_{\text{i}} A_{\text{i}} \cos\theta \ \mathrm{d}\Omega = 2\pi \int_0^{\theta_{\text{i}}} L_{\text{i}} A_{\text{i}} \cos\theta \sin\theta \ \mathrm{d}\theta. \tag{1.9}$$

In the limit of maximum concentration, where we assume conservation of flux throughout the system (i.e., conservation of energy) as well as the stearance of photons (i.e., conservation of optical étendue), incident radiance (L_{in}) matches output radiance (L_{out}). In this limit, assuming the concentrator system is made of a medium with refractive index, n, we obtain the general concentration limit for passive concentrators given by Equation 1.10. Here we define concentration factor (C) as the ratio of illumination flux per area on the exit to entrance apertures. In the limit of angularly independent photon acceptance at the exit aperture, that is $\theta_{\text{out}} = 90°$, Equation 1.10 simplifies to the well-known limit for passive concentrators[37]:

$$\begin{aligned} C &\equiv \frac{\Phi_{\text{out}}/A_{\text{out}}}{\Phi_{\text{in}}/A_{\text{in}}} = \frac{n^2 L_{\text{out}}^2 \sin^2\theta_{\text{out}}}{L_{\text{in}}^2 \sin^2\theta_{\text{in}}} \\ &\leq \frac{n^2 \sin^2\theta_{\text{out}}}{\sin^2\theta_{\text{in}}}, \quad \text{for } L_{\text{in}} = L_{\text{out}} \\ &\leq \frac{n^2}{\sin^2\theta_{\text{in}}}, \quad \text{for } \theta_{\text{out}} = 90°. \end{aligned} \tag{1.10}$$

Assuming an index of 1.5 and an acceptance cone matching that of the solar disc half angle for our sun (approximately 0.25°[38]), passive concentrators can theoretically reach concentration factors over 100,000 as shown in Figure 1.8(b).

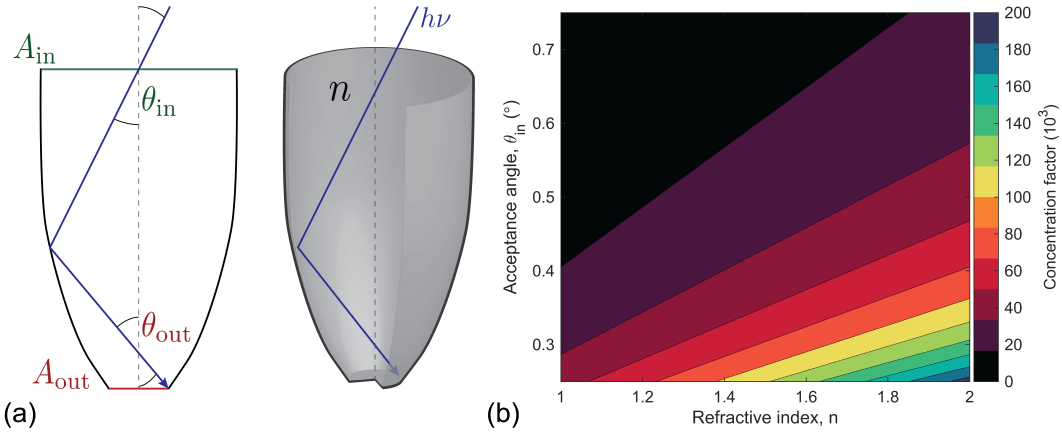

Figure 1.8: (a) A 2D and 3D illustration of an arbitrary passive concentration system, visually defining the entrance and exit apertures and acceptance angles as well as the index of refraction for the system. (b) The maximum achievable concentration ratio for passive concentrators given from Equation 1.10.

As seen in Figure 1.8(b), maximum concentration only occurs for narrow acceptance angles. As an example, if we assume a relatively broad acceptance angle of 50° and a refractive index of 1.5, we observe a concentration factor less than 4. Thus, current state of the art geometric concentrators with narrow acceptance angles require tracking technology in order to achieve sustained performance throughout the day[39]. With this constraint, BoS costs can often outweigh the increased efficiency enhancements illustrated in Figure 1.7, yielding a higher overall LCOE[40].

1.2.2 Active Concentration: the Luminescent Solar Concentrator

Similar to passive systems, active or luminescent solar concentrators (LSCs) redirect incident light entering the optical system at area, A_{in}, with an acceptance cone, θ_{in}, onto an output collector of area, A_{out}. Unlike its passive counterpart, LSCs rely upon embedded photoluminescent (luminophore) particles within an optical waveguide structure as the primary means of light trapping. As incident photons impinge upon the LSC, dispersed luminophores selectively absorb higher energy, shorter-wavelength light, λ_{in}, and re-emit photons of lower energy, longer-wavelength, λ_{out}. LSCs naturally concentrate this luminophore radiation, or photoluminescence, through occupation of total internal reflection (TIR) modes/angles within the optical waveguide. Thus, we can characterize the outgoing angular spread, θ_{out}, as the photoluminesced angles that lie outside the TIR escape cone. For traditional LSC form factors, cells with bandgaps comparable to the average photoluminescent energy border the optical waveguide, converting the trapped radiation into photogenerated excitons[41–68]. Figure 1.9 illustrates the fundamental concentration mechanism for an LSC device, where for example we orient the solar

cell parallel to the rectangular waveguide perimeter edge (i.e., $\hat{z}$-axis parallel).

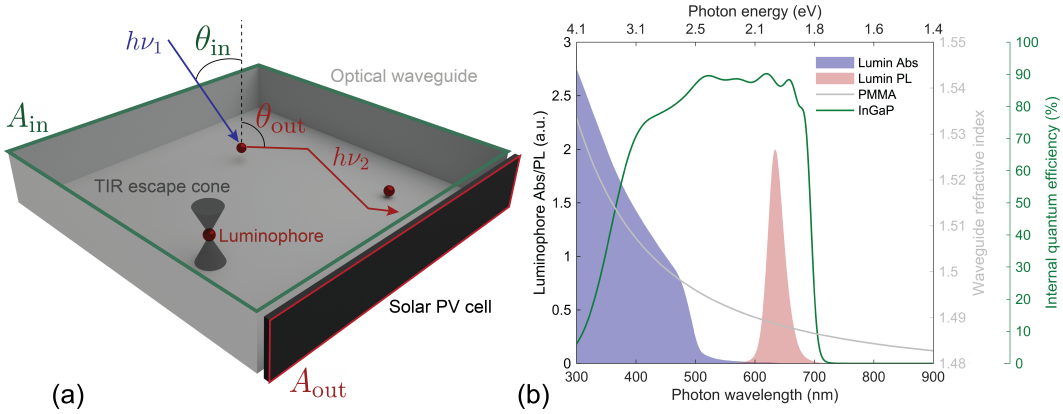

Figure 1.9: (a) A simplified rendering of an LSC employing a traditional edge-lined photovoltaic cell geometry. Light impinges upon the top aperture of area, A_{in}, at an angle, θ_{in}, and with energy, $h\nu_1$. Luminophores embedded within the optical waveguide absorb a portion of these incident photons within the luminophore absorption regime and re-radiate as photoluminescence at energies, $h\nu_2$, at angles outside the TIR escape cone, denoted here by θ_{out}. TIR re-directs these radiated photons to impinge upon the optically coupled cell area, A_{out}. (b) An example CdSe/CdS quantum dot luminophore absorption and photoluminescence spectra with respect to photon wavelength and energy, against an example InGaP solar cell internal quantum efficiency and commonly used (poly)methyl methacrylate (PMMA) refractive index (real part).

LSC Device Components

As shown in Figure 1.9, we can conceptually discretize active concentrator operating mechanisms as: *(i)* conversion of incident photons into photoluminescence via the active luminophore material, *(ii)* trapping of this radiation into TIR guided modes or angles within the optical waveguide(s), and *(iii)* exciton photogeneration within the output solar cell collector via this trapped photoluminescence. Given this process, we begin our analysis of LSC operating mechanisms and limits by first considering the photoluminescent material properties and characteristics of commonly employed luminophores.

The term luminophore describes a broad class of particles that absorb photons at a particular range of energies, λ_{in}, and re-emit at downshifted photoluminescence at λ_{out}. Depending on the physical processes responsible for emission, we broadly categorize luminophores into two distinct types. In type-A materials, lower energy radiation occurs within the same physical structure as the light absorbing process. For this class of luminophores, energy downshifting, termed the Stokes shift (σ), can occur for example from vibrational relaxation[69] or quantum confinement[70]. Type-A luminophores, shown generally in Figure 1.10(a), require large Stokes shifts and narrow emission profiles in order to minimize the overlap between absorption and photoluminescence. Figure 1.10(c) shows a variety of type-A luminophore absorption/emission spectra.

In contrast, type-B luminophores qualify a class of materials where the absorption and photoluminescence processes are decoupled. Such luminophores consist of two or more structures, where the absorber layer shuttles the photogenerated exciton to the emitter layer at a lower energy level, resulting in a tunable Stokes shift given the choice and size of absorber and emitter materials[71]. Figure 1.10(b) depicts a typical type-B luminophore absorption and PL spectra, where the emitter material sets the amount of re-absorption. The luminophore extinction coefficient, ε_{lum}, defined as the ratio of absorber to emitter photon absorption (α_1/α_2), quantifies the likelihood for photoluminescence re-absorption within the LSC. Figure 1.10(d) provides sample spectra for various type-B luminophores.

Whether type-A or B, the photoluminescence quantum yield (PLQY) of the luminophore species determines the likelihood of exciton radiative recombination. For PLQYs below unity, incident light absorption (i.e., $h\nu_1$) and photoluminescence re-absorption (i.e., $h\nu_2$) can yield nonradiative recombination and, subsequently, transformation into heat within the luminophore particle and LSC waveguide system. However, upon radiative emission by the luminophore species, photons can occupy certain angles within the optical waveguide (in the ray-optical regime) or modes (wave-optical), θ_{out}, with respect to the waveguide top surface normal. For an LSC structure with no external trapping mechanisms, the difference in index of refraction between the waveguide and surrounding medium naturally reflects a portion of emitted photons that lies outside the waveguide escape cone. For an index n_{wg} surrounded by air ($n_{\text{air}} \approxeq 1$), we define the escape cone angle, θ_{c}, according to Snell's law of refraction.

$$\begin{aligned} & n_{\text{wg}} \sin\theta_{\text{c}} = n_{\text{air}} \sin 90^\circ \quad \text{(Snell's law)} \\ \implies \quad & \theta_{\text{c}} = \sin^{-1}\left(\frac{1}{n_{\text{wg}}}\right). \end{aligned} \tag{1.11}$$

From θ_{c}, we can calculate the solid angle of the resulting escape cone, Ω_{c}, and thus the fractional amount of luminophore radiation, $F = \cos\theta_{\text{c}}$, that occupies TIR angles for a rectangular slab waveguide assuming an isotropic luminophore emission profile and no reabsorption/re-emission events. For example, the case when $n = 1.5$, the optical waveguide traps approximately 74.5% of luminophore-emitted radiation[82]. Upon emission into a TIR angle or mode, the optical waveguide medium (often a glass or polymer) guides photons to impinge upon a coupled photovoltaic cell, provided no attenuation or bulk/surface scattering of the trapped radiance.

The ratio of incident solar illuminated area, A_{in}, to total cell surface area, A_{out}, defines the geometric gain of the LSC system. By considering the radiative efficiency (i.e., PLQY) of the luminophore with respect to wavelength of light, $\eta_{\text{plqy}}(\lambda)$; LSC incident photon waveguide absorbance given the luminophore material(s), $\eta_{\text{abs}}(\lambda,\theta,\varphi)$; photoluminescence reabsorption via non-ideal luminophore spectra, $\eta_{\text{self}}(\lambda,\theta,\varphi)$; radiance trapping and waveguiding efficiency, $\eta_{\text{trap}}(\lambda,\theta,\varphi)$; and incident photon reflection by the waveguide top surface, $R(\lambda,\theta,\varphi)$; we can quantify the upper limit of the LSC optical efficiency, η_{opt}, at an incoming photon

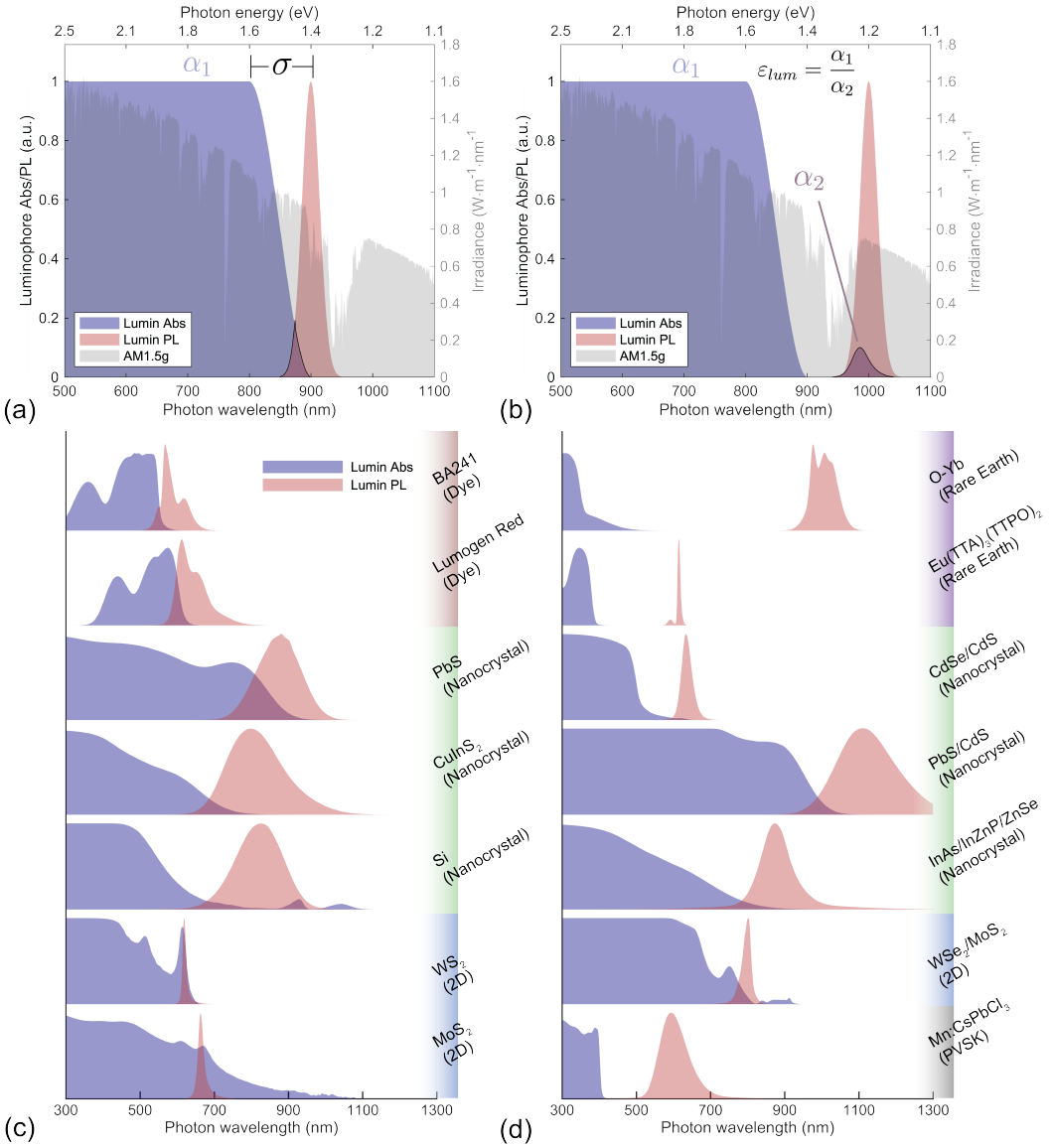

Figure 1.10: Classification of luminophore type-A (a) and -B (b) absorption and photoluminescence (PL) spectra with respect to photon wavelength (nm). Luminophore band-edge absorption (α_1), Stokes shift (σ), re-absorption (α_2), and extinction coefficient (ε_{lum}) determine the concentration performance of the LSC. (c) and (d) survey various examples of type-A and -B luminophores including luminescent dyes[72,73], nanocrystal structures[74–77], two-dimensional materials[78,79], rare-earth doped molecules[80], and perovskite compounds[81]. Adapted from Meinardi et al[29].

wavelength, polar, and azimuthal angles for an LSC:

$$\begin{aligned}\eta_{\text{opt}}(\lambda,\theta,\varphi) = \; & \eta_{\text{plqy}}(\lambda)\cdot\eta_{\text{abs}}(\lambda,\theta,\varphi)\cdot\eta_{\text{self}}(\lambda,\theta,\varphi) \\ & \cdot\eta_{\text{trap}}(\lambda,\theta,\varphi)\cdot(1-R(\lambda,\theta,\varphi))\,.\end{aligned} \tag{1.12}$$

While we can take into account the photon polarization in addition to the wavelength and incident angles, solar irradiance is unpolarized. For such concentrators, we can quantify the geometrical concentration factor, C, as proportional to the system

geometric gain by the optical efficiency of the LSC, shown here in Equation 1.13:

$$C_{\mathrm{LSC}}(\lambda,\theta,\varphi) \equiv \mathrm{GG} \cdot \frac{\Phi_{\mathrm{out}}}{\Phi_{\mathrm{in}}} = \mathrm{GG} \cdot \eta_{\mathrm{opt}}(\lambda,\theta,\varphi), \tag{1.13}$$

where Φ_{in} and Φ_{out} give the incident and outgoing light fluxes, respectively. Equation 1.13 exactly matches the concentration factor definition in the passive case; however for the case of active concentrators, we do not assume equal radiance in and out. As a result of detrimental escape cone loss and non-unity PLQY—thereby poor LSC optical efficiencies—many such concentrator designs incorporate alternative structures, geometries, and luminescent mechanisms in order to increase the overall radiated trapping fraction, F, and efficiency, η_{trap}. Some of these escape cone loss minimization strategies include: applying external trapping layers with photonic bandgaps[83–88], alternative waveguiding geometries and structures with higher natural trapping fractions[89,90], asymmetrical luminophore materials for anisotropic photoluminescence emission into guided angles/modes[91,92], and nanophotonic designs for induced luminophore anisotropy[93–95]. Figure 1.11 overviews several of these mechanisms for increased waveguiding efficiency and how they impact photoluminescence angles/modes that fall outside of the escape cone.

Optical Étendue for LSCs

As referenced in Figure 1.7, there exist numerous strategies to enhance the performance of a photovoltaic cell through amplification of the V_{oc}. As introduced, the concentration of incident photons represents one of these pathways to increased performance, so long as this asymmetrically affects the incoming photons (i.e., J_{sc}) and not the thermal radiation background (i.e., J_0). In fact, we can quantify the effects of concentrating and angle-restricting optics on the V_{oc} in terms of the incoming and outdoing photon entropy of the system. Specifically, we can apply the concept of optical étendue to define the entropy related to the angular distribution of the emitted ($\varepsilon_{\mathrm{out}}$) versus incoming beams of photons ($\varepsilon_{\mathrm{in}}$).

Let us assume, without loss of generality, a terrestrial-based photovoltaic system whose incoming photons originate entirely via direct normal incidence from the solar disc—for now, let us ignore the second-order contribution of thermal background radiation at ambient temperature to incoming irradiance. Given the average distance between the earth and sun (approximately 150 million miles) and the sun's radius (about 800 thousand miles), as described in section 1.2.1, we can approximate the solar disc half angle to be roughly $0.25°(\theta_{\mathrm{in}})$. We can define optical étendue as the product of illumination area (A_{in}) by the solid angle subtended by the light source (Ω). For the case of direct radiation from our sun, we can therefore express étendue as:

$$\begin{aligned} \varepsilon &\equiv A_{\mathrm{in}} \iint_{\Omega} \sin(\theta)\, \mathrm{d}\theta\, \mathrm{d}\phi \\ \varepsilon_{\mathrm{in}} &= A_{\mathrm{in}} \int_0^{2\pi} \int_0^{\theta_{\mathrm{in}}} \sin(\theta) \mathrm{d}\theta \mathrm{d}\phi \\ \varepsilon_{\mathrm{in,sun}} &\approxeq 6 \times 10^{-5} \cdot A_{\mathrm{in}}. \end{aligned} \tag{1.14}$$

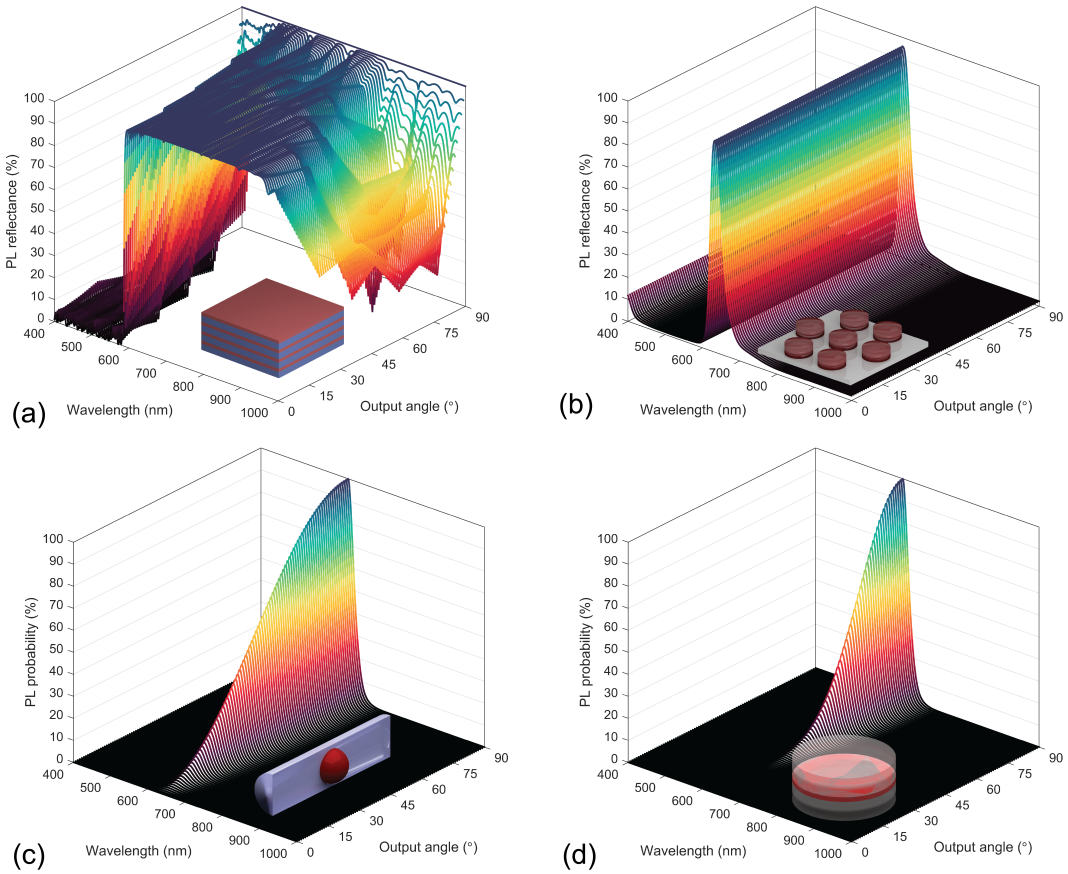

Figure 1.11: Two strategies commonly employed to increase photoluminescence (PL) trapping within LSC optical waveguides through a reduction of escape cone loss, where (a),(b) make use of external optical structures to reflect back escape cone emission, and (c),(d) illustrate anisotropically-emitting luminophore structures to minimize the amount of radiation entering the escape cone. (a) An aperiodic, dielectric stack short-pass filter design, plotting photoluminescence reflectance (%) vs. output polar angle (°) and wavelength (nm), optimized for a CdSe/CdS quantum dot emission pattern. (b) A high contrast grating metasurface structure employing a hexagonal array of sub-wavelength periodicity aluminum antimonide on glass, again optimized for a CdSe/CdS luminophore[96,97]. (c) A quantum nanorod structure relying on a CdS cylindrical shell and a CdSe quantum dot core[91], whose simulated anisotropic emission pattern follows a sine squared, dipole-like function. (d) A CdSe/CdS quantum dot luminophore layer placed between two cylindrical pillars of a high index, dielectric layer for resonant coupling[93], showing a power function radiation distribution for example.

Given Equation 1.14, we can quantify the relationship between incoming and outgoing étendue with respect to the LSC system; furthermore, we can re-write the expression for V_{oc} in terms of this étendue ratio[98]:

$$\begin{aligned} V_{\mathrm{oc}} &= V_{\mathrm{oc}}^{\mathrm{max}} + V_{\mathrm{oc}}^{\text{étendue}} + V_{\mathrm{oc}}^{\mathrm{ERE}} \\ &= V_{\mathrm{oc}}^{\mathrm{max}} + \frac{nkT}{q} \ln\left(\frac{\varepsilon_{\mathrm{in}}}{\varepsilon_{\mathrm{out}}}\right) + \frac{nkT}{q} \ln\left(Q_{\mathrm{ERE}}\right). \end{aligned} \tag{1.15}$$

Where, as described in Equation 1.4, Q_{ERE} gives the external radiative efficiency

of the cell or module (e.g., LSC system) and V_{oc}^{max} defines the upper limit of open-circuit voltage given by the limiting case of spectral absorption up to the system electronic bandgap, thermalization loss of high energy carriers to this band edge, and the Carnot loss given by the ratio of source (i.e., our sun) to the sink (i.e., the cell) temperatures. For the case of an LSC, the maximum open circuit voltage term in Equation 1.15 is complicated by virtue of the system employing at least two bandgaps (luminophore(s) and photovoltaic cell).

As seen by Equation 1.15, the ratio of incoming and outgoing étendue plays an important role in the open-circuit voltage limit. For most photovoltaic systems, we strictly assume $\varepsilon_{in} \leq \varepsilon_{out}$ in order to satisfy the second law of thermodynamics (i.e., the photon angular distribution must increase or, ideally, remain constant over time). For solar cells unable to limit the outgoing or restrict the incoming étendue, V_{oc} values fall well below the maximum. Geometric concentrators, discussed in section 1.2.1, can recover this limit by restricting the acceptance light cone and focus to a smaller output area. A separate method for eliminating the étendue open circuit voltage loss is to angularly restrict the outgoing cell photoluminescence.

The Thermodynamic Luminescence Concentration Limit of LSCs

Following our discussion of the optical étendue limit of a solar cell, we can now investigate the thermodynamic consequences for the LSC—a device which can, in principle, break conservation of optical étendue owing to the heat generation through the photoluminescence Stokes shift. For the case of the geometric concentrator, the flux per area ratio between the output and input apertures defines the concentration; however, unlike the case for a geometric concentrator, the radiance ($L_{in/out}$) at these apertures differs as a consequence of the spectral downshifting by the luminophores.

If we assume a photon energy, E_{in}, corresponding to the case when photon energy matches the luminophore absorption bandgap, and E_{out} to be the emission energy of the luminophore (where we have that the Stokes shift, σ is given as $E_{in} - E_{out}$), we can approximate the radiance of an input/output photon within the LSC by Planck's formula. For the case of a photon luminescence event with energy $E_{in/out}$, we have:

$$L_{in/out} = \frac{2}{h^3 c^2} \frac{E_{in/out}^3}{\exp\{\left(E_{in/out} - \mu_{in/out}\right)/kT_0\} - 1}, \tag{1.16}$$

where h, k, and c correspond to the Planck and Boltzmann constants, and the speed of light, respectively. T_0 gives the operating temperature of the LSC, and $E_{in/out} - \mu_{in/out}$ the amount of energy that the luminophore species dissipates into heat through either the absorption or photoluminescence process, respectively. In this case, $E_{in/out}$ denotes the absorption/emission for a photon of certain energy, and $\mu_{in/out}$ describes the portion of original energy converted to the luminophore excited state. The creation of heat in this LSC system can be thought of as an increase in the entropy due to the absorption or emission process, where the value depends directly on the Stokes shift, σ, of the luminophore[99]. In thermal equilibrium, when $\mu_{in} = \mu_{out}$ or conceptually when the rate of absorbed photons equals that of emitted

photons, we obtain the concentration factor limit:

$$\begin{aligned} C &\equiv \frac{\Phi_{\text{out}}}{\Phi_{\text{in}}} \cdot \text{GG} \\ &= \frac{L_{\text{out}}}{L_{\text{in}}} \quad \text{for } \mu_{\text{in}} = \mu_{\text{out}} \\ &= \frac{E_{\text{out}}^3}{E_{\text{in}}^3} \cdot \frac{\exp\{(E_{\text{in}} - \mu)/kT_0\} - 1}{\exp\{(E_{\text{out}} - \mu)/kT_0\} - 1} \\ &\leq \frac{E_{\text{out}}^3}{E_{\text{in}}^3} \cdot \exp\{\sigma/kT_0\}. \end{aligned} \tag{1.17}$$

From Equation 1.17 we find that the LSC thermodynamic concentration limit depends exponentially on the Stokes shift of the luminophore. That is, we can arbitrarily reach smaller and smaller outgoing optical étendue for ever-increasing Stokes shifts. However, the practical limits of optical efficiency, detailed by Equation 1.12, has prevented any measured LSC system from approaching such an exponential concentration. In addition, this limit, originally derived by Yablonovitch[99], does not reveal how this concentration translates into photovoltaic power conversion efficiency (i.e., V_{oc} or J_{sc}). It is therefore important to understand and quantify the intrinsic loss mechanisms within the LSC and how they prevent active concentrators from converging upon the maximum thermodynamic limiting case. In later chapters, we will also describe this limit in the context of étendue and open-circuit voltage.

LSC Loss Mechanisms and Performance Parameter Space

Measured output/input flux ratios for both simulated and fabricated devices exhibit far less light concentration than the exponential limit shown by Equation 1.17. To understand why, we begin by observing that dispersed luminophores typically cannot photoluminesce at above-unity PLQYs or emit into smaller and smaller outgoing angles (i.e., exhibit experimentally observable decreasing solid angles of emission). Second, not all incoming radiance can be absorbed by the dispersed luminophores, owing to non-zero top surface reflectance, incomplete absorbance by luminophores via insufficient volume concentration, or limited spectral absorbance coverage of the luminophore species itself. Upon absorption, the PLQY sets the probability of photon re-emission by the luminophore ensemble. Upon emission, optical waveguide trapping efficiency, reabsorption and scattering probability, waveguide light attenuation, and non-unity cell external quantum efficiencies limit the amount of concentration for an LSC system[100]. Figure 1.12 depicts each of the possible loss and collection mechanisms characteristic of LSCs where we show each loss mechanism in the ray-optical regime.

In this thesis, we explore the power conversion efficiency thermodynamics, geometrical designs, performance-limiting cases, module architectures, and experimental realization of LSCs for various photovoltaic applications. To do this, we first establish the analytical and computational models we use to evaluate the optical and power conversion efficiency performance of an LSC. Chapter 2 details the tools

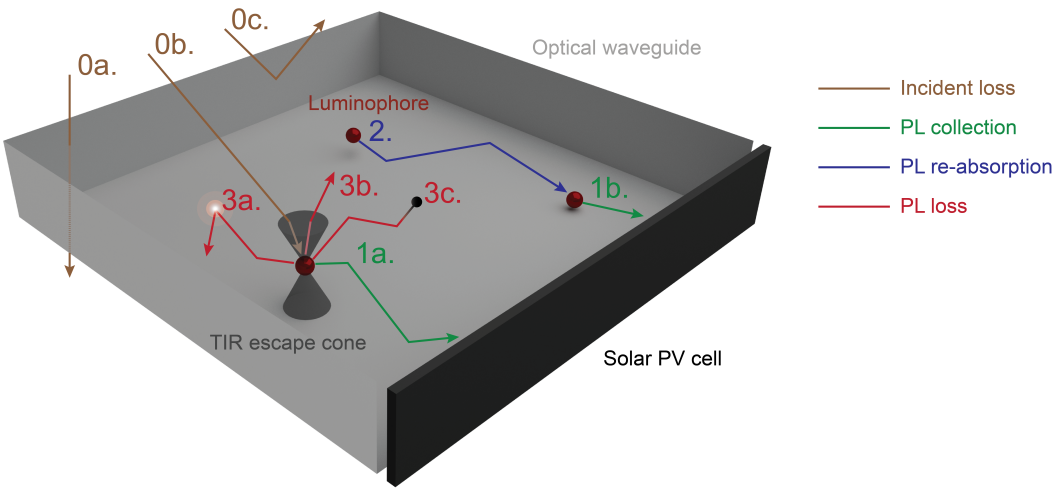

Figure 1.12: Loss and collection mechanisms of LSCs for a general cell, waveguide geometry, and luminophore material. 0a,b,c (brown arrows) indicate potential losses that can occur upon incoming irradiance. These include transmission of light through the LSC (0a), parasitic absorption by the luminophore via non-unity PLQY for incoming irradiance (0b), and top surface reflection (0c). 1a,b (green arrows) depict the two pathways that photoluminescence can be collected by the photovoltaic cell, corresponding to direct absorption by the cell or via waveguide TIR modes/angles, respectively. Additional loss mechanisms can occur at the cell through non-radiative recombination of the exciton (i.e. non-unity quantum efficiencies). 2 (blue arrow) shows the possibility for radiated photons to become re-absorbed by other luminophores within the optical waveguide, where each of the pathways shown here apply to that luminophore absorption event as well. 3a,b,c show the optical losses by the waveguide itself. These include photons that couple into the escape cone upon emission (3a), scatter through bulk or surface imperfections (3b), and become attenuated by the waveguide (3c).

that we employ throughout the entirety of this thesis in order to quantify these Figures of merit. Chapter 3 develops the analytical, computational, and experimental work to quantify the limits of single junction LSC photovoltaic devices under typical 1-sun illumination conditions on Earth. Chapter 4 then investigates how these single-junction limits apply to the case for building-integrated applications, whereby we include a discussion on the technoeconomic metrics. Chapter 5 explores the concept of multijunction LSC devices, aimed to push beyond the single-junction limits for a variety of junction motifs. Finally, given the results of single- and multijunction LSCs, chapter 6 turns to the limits of energy generation per unit mass in the context of LSCs for aerospace applications.

CHAPTER 2

Luminescent Solar Concentrator Modeling Techniques

As introduced in chapter 1, the process of actively concentrating incident photons of given flux, Φ_{in}, at a top surface waveguide area, A_{in}, to an output flux, Φ_{out}, at a total photovoltaic cell collection area, A_{out}, relies upon a large number of parameters. Shown by Equation 1.12, we express optical efficiency as the product of individual constituent efficiencies that interact with the incident and outgoing radiances. We should also note that, as discussed by previous work[100], higher efficiency of an individual constituent can adversely affect another.

Aside from the LSC optical efficiency, we must also consider the photovoltaic cell collection efficiency (i.e., external quantum efficiency) and the diode behavior in order to fully quantify the LSC power conversion efficiency. The parameter space of an LSC can thus be categorized by the waveguide components (e.g., photoluminescence generation, trapping, collection) and the photovoltaic cell exciton dynamics (e.g., electronic bandgap, photoluminescence absorbance, carrier collection), as seen in Figure 2.1. As shown, we subcategorize parameters of the waveguide and cell for a general LSC device.

Given the myriad LSC form factors and materials, the task of modeling the optical and power conversion efficiencies can be accomplished through, and often requires, a variety of techniques. For example, given the waveguide thickness of the LSC and luminescent medium, LSCs can be analyzed in the ray-optical regime (i.e., thickness $\gg$ photoluminescent wavelength)—treating photons as point particles that obey certain properties according to their wavelength, polarization, and path of propagation—or in the wave-optical regime (i.e., thickness $\approx$ photoluminescent wavelength)—where we treat photons as electromagnetic waves that occupy discrete modes within the waveguide. Tremendous research efforts in this community exist concerning the accuracy, run-time (i.e., computational cost), and form factor versatility of LSC models. Here, we identify and compare several techniques to model LSCs. We discuss in detail two custom-built models to evaluate LSC optical and power conversion efficiency that provide the basis for computational analysis in this thesis.

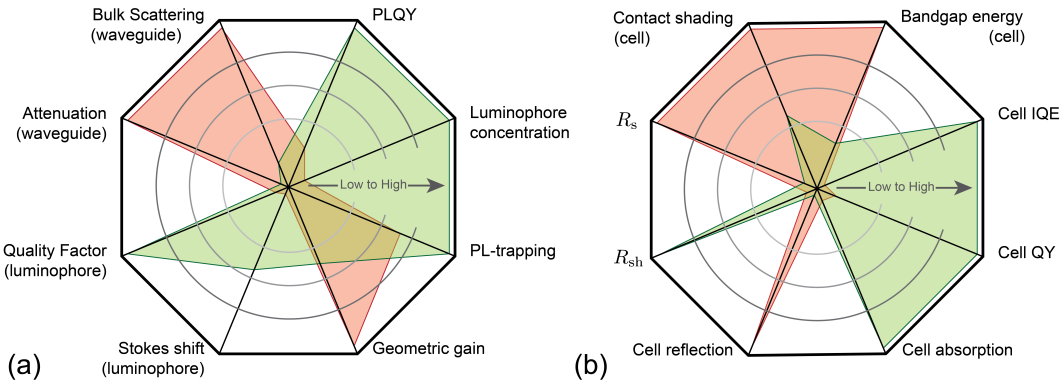

Figure 2.1: The waveguide (a) and photovoltaic cell (b) parameter space for an arbitrary LSC device. Here, the green and red polygons correspond to LSC devices with relatively high and low power conversion efficiencies, respectively. The primary parameters of the waveguide component (a) of an LSC include the scattering of photoluminescence by the waveguide, luminophore radiative efficiency (i.e., PLQY), concentration of embedded luminophores, trapping of emission within TIR modes or angles, geometric gain of the system, luminophore absorption, emission downshifting (i.e., Stokes shift), photoluminescence reabsorption (i.e., extinction factor), and optical waveguide attenuation. Primary factors of performance for the cell component (b) include the shading of incident photons by top metal contacts, electronic energy bandgap of the cell material, quantum and radiative efficiencies of the junction, photoluminescence absorption/reflection, and series/shunt resistances—which indicate the diode response of the cell.

2.1 Active Concentrator Modeling Principles

For traditional LSC applications, the waveguide scale (thickness, length, and width) enables the use of models based on the ray-optical approach. In this regime, we can readily apply a stochastic computational framework (e.g., a Monte Carlo ray-trace) to predict optical performance for a variety of geometries and structures to within a high degree of accuracy[101]. However, as we will see, computational run-time and rapid optimization can often limit the applicability of traditional ray-trace algorithms. As a result, we also discuss the possibility of implementing a closed-form, deterministic analytical technique to model LSC behavior. Recently, developments of high photoluminescence trapping structures on the wave-optics scale necessitate the implementation of analytical or finite-difference, time-domain partial differential equation solvers in order to uncover LSC device performance.

2.1.1 Model Run-time, Lengths Scales, Accuracy, and Versatility

Given the wide variety of optical and power conversion efficiency models, Table 2.1 overviews several examples with respect to the model run-time (in $\mathcal{O}$ notation), applicable length scales, primary outputs, quoted accuracy, robustness of the parameter space (as shown in Figure 2.1), and versatility across LSC applications.

As shown in Table 2.1, each model yields certain advantages for a particular

Model type	Run-time	Length scale	Output	Accuracy	Parameters	Versatile
Monte Carlo ray-trace	$\mathcal{O}\left(N^2 \lg(N)\right)$[102]	$\gg \mathcal{O}(\lambda)$	$\eta_{\text{pce}}, \eta_{\text{opt}}, C_{\text{LSC}}$	High	All	Yes
Quality factor[39]	$\mathcal{O}(1)$	All	$\eta_{\text{opt}}, C_{\text{LSC}}$	High	Limited	No
Single frequency[103]	$\mathcal{O}(1)$	$\gg \mathcal{O}(\lambda)$	$\eta_{\text{opt}}, C_{\text{LSC}}$	Low	All	No
Thermodynamic rate[104]	$\mathcal{O}(1)$	All	$\eta_{\text{pce}}, \eta_{\text{opt}}, C_{\text{LSC}}$	Low	Limited	No
Photon flow[53]	$\mathcal{O}(1)$	$\gg \mathcal{O}(\lambda)$	$\eta_{\text{opt}}, C_{\text{LSC}}$	Low	Limited	No
Edge Collection[105]	$\mathcal{O}(1)$	$\gg \mathcal{O}(\lambda)$	η_{opt}	Low	Limited	No
Probability chain[87]	$\mathcal{O}(1)$	$\mathcal{O}(\lambda)$	η_{opt}	High	Limited	No
FDTD[106]	$\mathcal{O}(N^3)$[107]	$\mathcal{O}(\lambda)$	η_{opt}	High	Limited	Yes

Table 2.1: A number of active concentrator modeling techniques. We compare model types according to the run-time, length-scale, performance outputs, literature-verified accuracy, LSC parameter versatility as identified in Figure 2.1, and whether or not the model can be applied to alternative geometries, form factors, and applications.

setting. For example, in the case of a ray-optical limit LSC, studies often rely upon the Monte Carlo ray-trace method in order to accurately model system geometries. However, as evident in the polynomial computational run-time, the high cost of ray-tracing prompts the use of analytical solvers for certain cases—particularly in that of rapid optimization studies. Substantial research efforts continue to be directed toward identifying highly efficient, versatile models on the ray-optical length scale in constant run-time.

On the other end of the spectrum, relatively few models exist to simulate the performance of wave-optical LSCs. The most common techniques include the finite-difference time-domain (FDTD) solver and Markov chain approximations[87,108]. As LSC researchers have historically fabricated devices within ray-optical regimes, most models focus on the photon interactions based on the laws of ray tracing[49]. However, as photonic LSC devices continue to emerge[95,108], models to predict device performance and optimal design must follow suit.

2.2 Stochastic Modeling Tools

Numerous fields of study apply the method of repeated random sampling to approximate a numerical solution to a deterministic problem (i.e., the Monte Carlo method). The original Monte Carlo concept itself dates back to the work of Stainslaw Ulam and John von Neumann on neutron diffusion in fissionable materials[109]. In it, Ulam and Neumann retooled statistical analysis, such that by applying a large sampling and computationally observing the output behavior (one based upon probabilities of the given system), one could arrive at a numerical solution. This approach extends across a wide-range of scientific fields—even branching into modern graphical/rendering software. In the mid 1960's, Leslie Polgar and John Howell Implemented the

first known version of the Monte Carlo method applied to ray-optical situations (and thus the first ever Monte Carlo ray-trace model) in an application to understanding thermal-radiative properties in various conical cavities[110]. The approach used by Polgar and Howell closely matches the core concept applied today in ray-trace algorithms. Namely, the model depends upon far-field material properties such as reflectance, absorptance, and transmittance in order to predict the paths of injected photons.

2.2.1 The Monte Carlo Ray Trace Method

To evaluate the optical and power conversion efficiencies of an LSC module comprised of varying system configurations and parameters (as discussed in Figure 2.1), we employ a custom Monte Carlo ray-trace model. In it, we stochastically trace individual photons throughout each layer of the LSC architecture (e.g., the luminophore-doped waveguide, top/bottom selective reflector layers, edges or perimeter interactions, solar photovoltaic cells), where we initialize a two dimensional grid mesh across the waveguide top surface area that serves as the injection matrix for incident photons. The size of each mesh pixel, as shown in Figure 2.2 as m_x and m_y, sets this photon areal density. We simulate photons within the wavelength range of particular relevance—however, for most solar applications, 300 to 1500 nm accounts for the first order device effects given the Blackbody spectrum of our sun. In order to achieve accurate LSC modeling results[111,112], we initialize $\mathcal{O}\left(10^7\right)$ individual photons for every simulation.

Upon initialization, we record the previous and current photon positions within the device (r_x, r_y, r_z), original and current photon wavelengths (λ_0, λ), and velocity (v_x, v_y, v_z). Photons travel through the model in discrete step vectors (ℓ) where we set $\ell = 5\mu$m—where for most applications such a large step is sufficient to approximating the dynamics of the photoluminesced photon given layer thicknesses. The normalized velocity vector determines the photon trajectory throughout the device. To approximate the probability of luminophore absorption within the waveguide layer, we apply the Beer-Lambert law given a particular optical density of absorbers. For the remainder of this thesis, we will therefore denote luminophore concentration within a waveguide through the use of this optical density measurement, defined as the total absorption of incident light at a particular wavelength through a single pass of the waveguide structure. We note that by applying the optical density as the metric for luminophore concentration, we can easily apply our model to experimental setups through direct measurement. Equation 2.1 details the Beer-Lambert law in the context of this ray-trace model, giving the waveguide luminophore absorptance probability (P_A) with respect to the step size, optical density (OD) at a reference wavelength (λ_0), waveguide thickness (T), and wavelength-dependent luminophore absorption profile $(\alpha(\lambda))$ normalized at the reference wavelength, λ_0:

$$P_A = 1 - 10^{-\mathrm{OD}_{\lambda_0} \cdot \alpha(\lambda) \cdot (\ell/T)}. \tag{2.1}$$

To determine the probabilities of reflectance and transmittance at a given material interface (e.g., waveguide top surface to surrounding air), we apply the Fresnel and

Snell laws of reflectance and refraction, respectively. As described in Equation 2.2, we supply the model with specific refractive indices of the interface (n_1, n_2) given the LSC materials (e.g., glass substrate/superstrate, polymer waveguide, surrounding medium), photon polarization (s, p), and incident polar angle (θ) as calculated from the velocity vector to determine the reflectance/transmittance probabilities (P_R, P_T). While the Fresnel reflectance law assumes azimuthal (φ) independence, we can modify the code to specify wavelength-selective reflectors that intentionally break this symmetry—as is the case with high contrast grating metasurfaces[96]:

$$P_R^{s,p} = \left| \frac{\pm n_1 \cos\theta \mp n_2 \sqrt{1 - \left(\frac{n_1}{n_2}\sin\theta\right)}}{n_1 \cos\theta + n_2 \sqrt{1 - \left(\frac{n_1}{n_2}\sin\theta\right)}} \right|^2 . \tag{2.2}$$

Upon absorption by the luminescent species within the waveguide, we calculate the probability of re-emission as downshifted photoluminescence via the luminophore radiative efficiency (i.e., PLQY). If radiated, we determine the new wavelength given the emission profile of that luminophore and assign its new unit velocity vector direction according to its far-field radiation profile (e.g., isotropic or anisotropic). Upon interaction with the solar cell, we first apply the known cell reflectance and transmittance with respect to angle of incidence (θ, φ) and photon wavelength (λ) to determine absorption and exciton photogeneration. If absorbed, we apply the known cell internal quantum efficiency at that particular wavelength to estimate carrier collection. For most system configurations, we assume a finite area (e.g., 2.5%) of the solar cell to be specularly reflective given metal contacts for carrier extraction. Similarly, we simulate the use of external photoluminescence trapping structures—like that of Figure 1.11(a,b)—through the simulated or measured reflectance, $R(\lambda, \theta, \varphi)$, and transmittance, $T(\lambda, \theta, \varphi)$, characteristics.

For each photon striking the LSC top surface area, we mark the photon as collected via the coupled photovoltaic cell(s) or lost due to a particular mechanism. If collected, we weigh the photon's original incident wavelength by the irradiance spectrum for that setting (e.g., AM0 for space applications, AM1.5g for terrestrial) and multiply by the mesh unit area to approximate the resulting cell photocurrent. For strings of cells, we typically assume parallel interconnects, where photocurrents are summed over each cell. If photons are lost either as heat or escape the device structure into free space, we tag that particular mechanism for later analysis (as shown in Figure 1.12).

Once all photon wavelengths and grid meshes terminate, we apply open-circuit voltage and fill factor functions (modeled or measured) for a particular cell to calculate the resulting power conversion efficiency of the LSC module. Alternatively, we can apply a detailed balance model for open-circuit voltage and fill factor approximations via the cell radiative efficiency as defined by Equation 1.15[98,113]. Chapters 3 and 5 describe the detailed balance of an LSC device. In certain situations, we also calculate optical efficiency by comparing the collected cell photocurrent to a reference value according to the specific irradiance conditions. Figure 2.2 conceptualizes the ray-trace algorithm features in the context of LSCs. Appendix A overviews

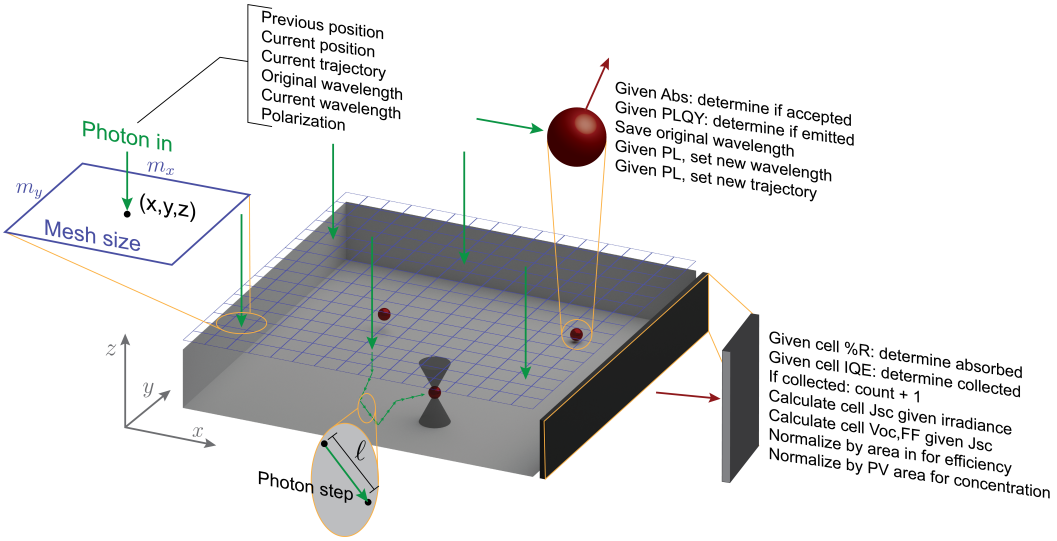

Figure 2.2: A conceptualization of the Monte Carlo ray-trace algorithm as applied to an LSC device architecture. Here we show the grid of injected photons, each mesh of area m_x by m_y, photons tracked throughout the architecture, photon unit step size (ℓ), and processes of photon-luminophore and photon-cell interactions. While in reality the photons consist of spatially localized electromagnetic waves, the ray-trace approximates their behavior as straight lines given the scale of the system.

the pseudo-code and provides a version of the implemented Monte Carlo ray-trace Matlab/C code for reference.

As introduced by Table 2.1, a critical advantage of the Monte Carlo over other computational choices lies in the model versatility and accuracy. Moreover with LSCs, there exists a wide range of form factors—e.g., shapes, sizes, and materials of the waveguide; luminophores and photovoltaic cell types; applications and incident photon spectra; single- vs. multijunction modules. Given this range, Monte Carlo simulations predict device performance to a fine degree of accuracy, as we will quantify in the following section.

2.2.2 Monte Carlo Ray Trace Validation

In order to apply this Monte Carlo model to a variety of LSC parameter sweeps, we must first identify the accuracy of this model against measured base cases, for both single junction photovoltaic cells and known LSC variations. To do this, Table 2.2 compares the measured performance of a given device (single junction cell or LSC module) against the Monte Carlo ray-trace output. In each case, the optically coupled photovoltaic external quantum efficiency and diode behavior are taken into account in order to accurately apply this model to estimate the short-circuit current density, open-circuit voltage, and fill factor. For each case shown, we find matching within experimental error between the measured and simulated performances.

While we find excellent agreement between the ray-trace algorithm and a variety of base cases, as shown in Table 2.1, there exist numerous disadvantages for such

Device	Measured Performance	Modeled Performance
Record GaAs Single junction[25]	$\eta = 29.1 \pm 0.6\%$	$\eta = 28.8\%$
PERC Si Single junction[114]	$\eta = 19.2 \pm 0.5\%$	$\eta = 19.4\%$
Pass. Contact Si[114]	$\eta = 20.4 \pm 0.5\%$	$\eta = 20.3\%$
Double-dye, LSC[65,115]	$\eta = 7.1 \pm 0.4\%$	$\eta = 7.1\%$
High Concentration LSC[116]	$C_{\text{LSC}} = 30.3 \pm 1$	$C_{\text{LSC}} = 31.0$
Record LSC Device†	$\eta = 9.86 \pm 0.8\%$	$\eta = 10\%$

Table 2.2: Evaluation of the Monte Carlo implemented model against various literature and experimental benchmarks. The first three rows compare the simulation to single junction solar cells under AM1.5g 1-sun illumination. The double-dye, LSC includes a four GaAs, edge-lined waveguide employing two types of organic dye luminophores (LumogenRed, Fluorescence Yellow), where we model exact specifications from Sloof et al.[65,115]. The high concentration LSC derives from a study performed by Bronstein et al.[116] measuring LSC concentration factors consisting of a micro-silicon photovoltaic cell within a thin waveguide ($30\mu m$) of CdSe/CdS quantum dots. Finally, the last comparison (denoted by †) consists of a single-junction, GaAs solar cell (1.4mm square) coupled to a $CuInS_2$/ZnS quantum dot waveguide with no external trapping structures, measured and discussed in chapter 3.

stochastic modeling tools. Notably, the model run-time and physical scale can often limit these simulations both in their ability to perform rapid optimization routines and restrict the applicability to a specific class of LSC devices. As such, we now turn our attention to the pursuit of analytical, closed form solutions—the primary goal being to identify a simulation tool that operates in constant time and can be applied to a variety of LSC parameters within a high degree of accuracy. In the following section, we explore two formulations for a deterministic LSC model, and discuss how it can inform our design and fabrication of high efficiency LSCs.

2.3 Deterministic Modeling Tools

As discussed, while stochastic Monte Carlo methods enable highly accurate and versatile modeling capabilities, they can not only limit the ability to perform rapid optimization but also our understanding of photon dynamics within the luminescent medium and fundamental performance limits. For example, one aspect of LSC photon collection not readily understood by most ray-tracing techniques lies in the appearance of non-uniform waveguide collection with respect to translational, optical excitation[117]. Given the statistical nature of ray-trace models, often a deeper understanding of how photoluminesced photons concentrate onto the solar cells can elude analyses.

In this section, we overview a particular LSC analytical tool, commonly cited in the community, for example, and clarify the limits to which this method can

be applied. Next we introduce a novel tool based upon the photoluminescence solid angle between the emitting luminophore and collecting cell, link how this new expression can fold into the existing method, and overview the results of this model with respect to optical collection efficiency.

2.3.1 Deterministic Methods and Techniques

Evidenced by Table 2.1, the search for accurate, versatile, and constant run-time LSC models—as well as for other photonic applications—remains an active area of research. Within this field, the "quality factor" model developed in 2016 by Klimov et al.[39] provides a unique perspective into the performance of active concentrators. In it, the model suggests that the concentration factor limit for such devices is crucially linked with what the authors term luminophore quality factor—what we refer to in this thesis as the extinction coefficient, ε_{lum}, or the probability of photoluminescence reabsorption. The strength of this model lies in both its constant run-time, length scale applicability, and high accuracy against Monte Carlo validation for specific instances of LSC geometries.

To begin, the quality factor model issues a core assumption in order to uncover concentration factor limits of LSCs. Namely, we begin by assuming that waveguide losses stem solely from luminophore reabsorption events. As shown in Figure 1.12, we can broadly categorize photoluminescence loss into: (1) photons re-emitted back into free space and (2) photons that lead to nonradiative recombination (heat) by a particular system constituent. In the former, apart from initial surface reflection or incomplete absorption by the luminophores, emission back into free space occurs whenever photons exit the waveguide through TIR escape cone angles (ray-optical) or modes (wave-optical). In this case, radiation can either be scattered by the waveguide host material or become re-absorbed by luminophores and, subsequently, re-emitted into angles/modes falling within this cone. Therefore, as we will observe, this model does not take into account scattering within the waveguide structure—which, for most practical cases, is a second order effect compared to luminophore reabsorption.

In the latter loss mechanism (non-radiative absorption of a photon), heat can be generated by the LSC system in three, distinct processes. Namely: *(i)* non-radiative attenuation by the waveguide bulk or top/bottom surfaces, *(ii)* parasitic reabsorption of trapped photons by the luminophore species, owing to finite extinction factors (ε_{lum}) or insufficiently large Stokes shifts (σ), and *(iii)* absorption by the optically coupled solar cell(s) and exciton nonradiative recombination for below unity quantum and collection efficiencies. For this model by Klimov et al., we assert that waveguide attenuation is a second order effect compared to reabsorption by the luminophore—which can be true provided high quality host materials. We also ignore the effects of non-ideal cell quantum efficiencies, given that our primary concern lies with the optical efficiency by which the waveguide can deliver radiance to its output aperture area, A_{out}.

We can write the total count of photoluminesced photons after a certain number

of n reabsorption events within the waveguide via a geometric series. Specifically, given our assumptions above, we can express the LSC optical efficiency (η_{opt}) as a factor of the absorption (η_{abs}) and collection (η_{col}) efficiencies, where we define the collection efficiency as a convolution of the PLQY (η_{plqy}), trapping (η_{trap}), and waveguiding (η_{wg}) efficiencies. In this last term, η_{wg} represents the fraction of initial absorption/emission photons that reach the solar cells. The inductive step of this model asserts that, for a given n^{th} reabsorption event by a luminophore, the collection efficiency becomes:

$$\eta_{\text{col}}^{n} = \left(\eta_{\text{plqy}} \cdot \eta_{\text{trap}} \left[1 - \eta_{\text{wg}}^{(1)}\right]^{n-1}\right) \cdot \eta_{\text{col}}^{(1)}, \tag{2.3}$$

where $\eta_{\text{wg}}^{(1)}$ is first-generation (initial absorption) fraction of incident light to be collected by cells in the absence of luminophore re-emission—that is, the upper limit of waveguiding efficiency for a particular geometry. Therefore, the factor $\eta_{\text{wg}}^{(1)}$ also takes into account the amount of incident absorption by the LSC waveguide given the optical density of luminophores. Finally, we can sum all contributions to absorption/emission events to yield:

$$\eta_{\text{col}} = \sum_{n=1}^{\infty} \eta_{\text{col}}^{n} = \frac{\eta_{\text{col}}^{(1)}}{1 - \eta_{\text{plqy}} \cdot \eta_{\text{trap}} \left(1 - \eta_{\text{wg}}^{(1)}\right)}. \tag{2.4}$$

In this form, we know that the collection efficiency of the very first absorption event, $\eta_{\text{col}}^{(1)}$, simplifies to the PLQY and trapping efficiencies. Thus, the final unknown term in Equation 2.4 is given by the factor $\eta_{\text{wg}}^{(1)}$. We can observe its importance in this analytical model by re-writing as the overall LSC optical efficiency:

$$\eta_{\text{opt}} = \frac{\eta_{\text{abs}} \cdot \eta_{\text{plqy}} \cdot \eta_{\text{trap}} \cdot \eta_{\text{wg}}^{(1)}}{1 - \eta_{\text{plqy}} \cdot \eta_{\text{trap}} \left(1 - \eta_{\text{plqy}} \cdot \eta_{\text{trap}} \cdot \eta_{\text{wg}}^{(1)}\right)}. \tag{2.5}$$

Besides the unknown factor, $\eta_{\text{wg}}^{(1)}$, we can directly measure each term of the optical efficiency shown in Equation 2.5—absorption, PLQY, and average trapping efficiencies. However, this final term, $\eta_{\text{wg}}^{(1)}$, cannot be directly measured as it accounts for the dynamics of photons within the waveguide system with respect to the collecting cell areas. In the original model, Klimov et al. estimate this term on a previous calculation of waveguiding efficiency based upon the work of Weber and Lambe[42], citing the perimeter edge length, L, and luminophore reabsorption edge, α_2, as the sole variables.

The accuracy of this example quality factor model therefore depends entirely on the expression for waveguiding efficiency of an initial absorption event. With appropriate choices for this term with respect to the LSC form factor, one can obtain reasonably accurate optical efficiencies[39]. However, while useful in certain situations, this model cannot operate without this initial explicit input. It is therefore of significant interest to describe the photoluminescence dynamics within a waveguide from first principles in a closed form setting.

2.3.2 The Solid Angle Model of Luminescence

Let us consider a single luminophore absorption event of an incoming photon within an optical waveguide of thickness, T, of a certain dielectric material of refractive index, n, located at some point, $\vec{r}$. For LSC applications, we aim to determine the likelihood that, upon radiative emission, the photon is collected by some intended absorber (e.g., a solar cell). Therefore, let us assume an arbitrary absorbing material located at one of the four waveguide edges of length, l, where we place our origin, $\mathcal{O}$, in the center of this edge. For simplicity, we will assume that all other edges are completely absorptive. Finally, let us define the probability of photoluminescence collection by this absorber as $I(\vec{r})$, where we assume some dependence of this collection according to the distance, $\vec{r}$, between the cell and emitter center positions. Figure 2.3(a) depicts the general setup of the luminophore/waveguide/absorber system.

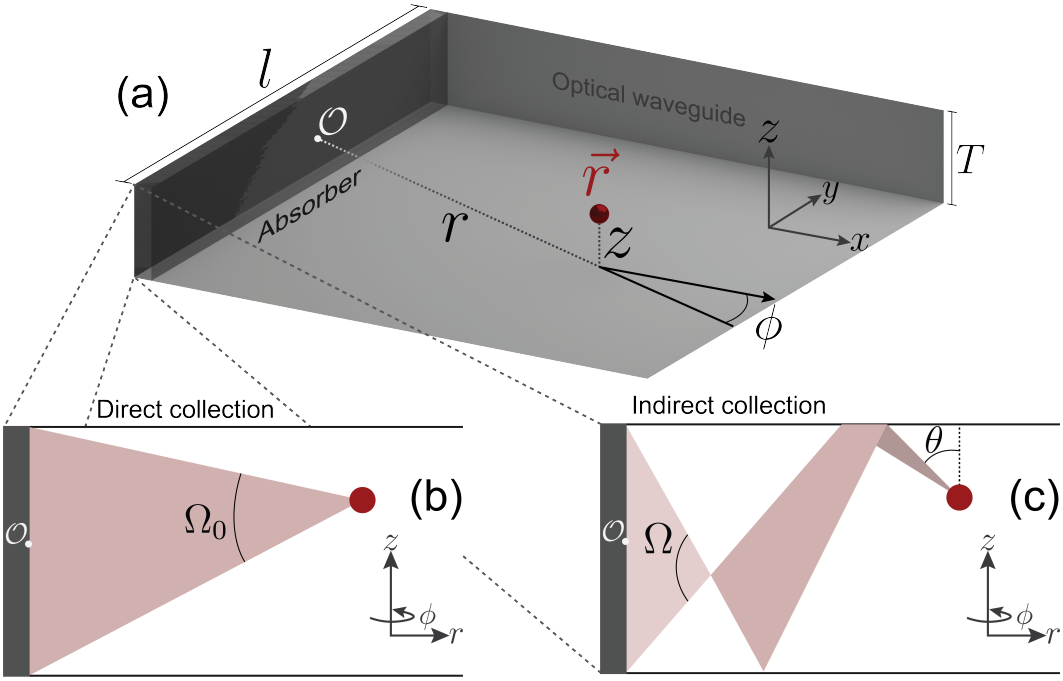

Figure 2.3: A general absorber/emitter setup for an LSC system, where we restrict our scope to a single luminescence event. (a) A 3D conceptualization of the problem, identifying the origin, $\mathcal{O}$, for the given solid angle calculation, and emitter position, $\vec{r}(r, \phi, z)$, in cylindrical coordinates for mathematical ease. (b) and (c) illustrate a simplified 2D setup for the direct and indirect (guided) photon collection solid angle cases Ω_0 and Ω, respectively.

To quantify this probability, we must first identify the pathways by which photons can reach this cell. Within a waveguide of thickness $T \gg \lambda_{\text{pl}}$, where λ_{pl} is the emitted photon wavelength, we can distinguish two pathways for collection. First, emitted photons within a solid angle can impinge upon the absorber with no waveguide edge interactions (i.e., can strike the absorber directly). Second, emitted photons can radiate at waveguide TIR angles and reach the absorber after a certain number of top/bottom edge boundary reflections. For the case of waveguide

thicknesses $T \approx \lambda_{\text{pl}}$, we must consider discrete TIR modes rather than the nearly continuous set of angles.

As described, emitted photons can reach the absorbing cell via two pathways (direct and guided). In the general case where we place a rectangular cell absorber in the waveguide center, photoluminescence can impinge upon either the absorber top/bottom or side surfaces. However, in this edge-lined case, we need only consider interaction with the cell edge surface that directly faces the waveguide. Thus, we can re-write our photon collection probability as:

$$\begin{aligned} I_{\text{edge-lined}}\left(\vec{r}\right) &= I^{\text{top}}\left(\vec{r}\right) + I^{\text{side}}\left(\vec{r}\right) = \cancelto{0}{I^{\text{top}}}\left(\vec{r}\right) + I^{\text{side}}\left(\vec{r}\right) \\ &= I_0^{\text{side}}\left(\vec{r}\right) + \sum_{\theta \in \varsigma_{\text{tir}}} I^{\text{side}}\left(\vec{r}, \theta\right), \end{aligned} \tag{2.6}$$

where we have that I_0 describes the probability of direct photon collection for either the top or side surface and θ is a TIR angle in the set of angles, ς_{tir}, that impinge upon the absorber surface. For the edge-lined cell case, all TIR angles will impinge upon the cell after a certain number of top/bottom reflection events, provided the emission direction is toward that edge. As such, the discrete sum of angles becomes an integral for TIR emitted, edge-facing photons—i.e., with $\theta \in (\theta_c, \pi - \theta_c)$, where θ_c is the critical angle given by Equation 1.11. We now can define each probability term as the solid angle of that collection method (direct or guided) given the total sum of available 4π steradians solid angles per collection mode. Re-writing $I(\vec{r})$ with respect to this integral of solid angles, we have:

$$I_{\text{edge-lined}}\left(\vec{r}\right) = \frac{\Omega_0^{\text{side}}\left(\vec{r}\right)}{4\pi} + \frac{\displaystyle\int_{\theta_c}^{\pi-\theta_c} \Omega^{\text{side}}\left(\vec{r}, \theta\right) \mathrm{d}\theta}{\displaystyle\int_{\theta_c}^{\pi-\theta_c} 4\pi \mathrm{d}\theta}, \tag{2.7}$$

where Ω_0^{side} and Ω^{side} give the solid angle for photons at a location, $\vec{r}$, to the area of an edge-lined absorbing cell for the direct and indirect (i.e., guided) cases, respectively. As shown in Figure 2.3(b),(c), we can identify this solid angle given the collection surface dimensions, luminophore position, and the photon path-lengths. For directly incident pathways, this solid angle can be calculated, in cylindrical coordinates for convenience, as[118]:

$$\begin{aligned} \Omega_0^{\text{side}}\left(r, \phi, z\right) &= 4\sin^{-1}\left(\sin\left(\alpha_0^{\text{side}}\left(r, \phi, z\right)\right) \cdot \sin\left(\beta_0^{\text{side}}\left(r, \phi, z\right)\right)\right) \\ &= 4\sin^{-1}\left(\sin\left(\tan^{-1}\left(\frac{l\left|\cos\phi\right|}{2\sqrt{r^2+z^2}}\right)\right) \cdot \right. \\ &\qquad \left. \sin\left(\tan^{-1}\left(\frac{T\left|\cos\left(\tan^{-1}\left(z/r\right)\right)\right|}{2\sqrt{r^2+z^2}}\right)\right)\right). \end{aligned} \tag{2.8}$$

We can derive a similar expression for the Ω^{side} solid angle function as well. Accounting for how the emitted angle affects the overall radial distance, r, we can

write the solid angle for indirect, guided pathways as:

$$\begin{aligned}\Omega^{\text{side}}(r,\phi,z,\theta) &= 4\sin^{-1}\left(\sin\left(\alpha^{\text{side}}(r,\phi,z,\theta)\right)\cdot\sin\left(\beta^{\text{side}}(r,\phi,z,\theta)\right)\right)\\ &= 4\sin^{-1}\left(\sin\left(\tan^{-1}\left(\frac{l\,|\cos\phi|}{2\sqrt{\frac{r^2}{\sin^2\theta}+z^2}}\right)\right)\cdot\right.\\ &\qquad\left.\sin\left(\tan^{-1}\left(\frac{T\left|\cos\left(\tan^{-1}(z/r)\right)\right|}{2\sqrt{\frac{r^2}{\sin^2\theta}+z^2}}\right)\right)\right).\end{aligned} \tag{2.9}$$

With the analytical expressions for each term of Equation 2.6, we can now develop some intuitive understanding of the photoluminesced photon collection probability for a luminophore at position vector, $\vec{r}$, relative to the edge-lined cell center. Figure 2.4 examines the interplay between some of the system geometrical parameters and this collection probability in the absence of luminophore reabsorption. We assume a 500μm thick waveguide of refractive index $n = 1.50$ and cell edge length 1cm. Seen in Figure 2.4(a), we can probe the vector space by simultaneously varying each position component.

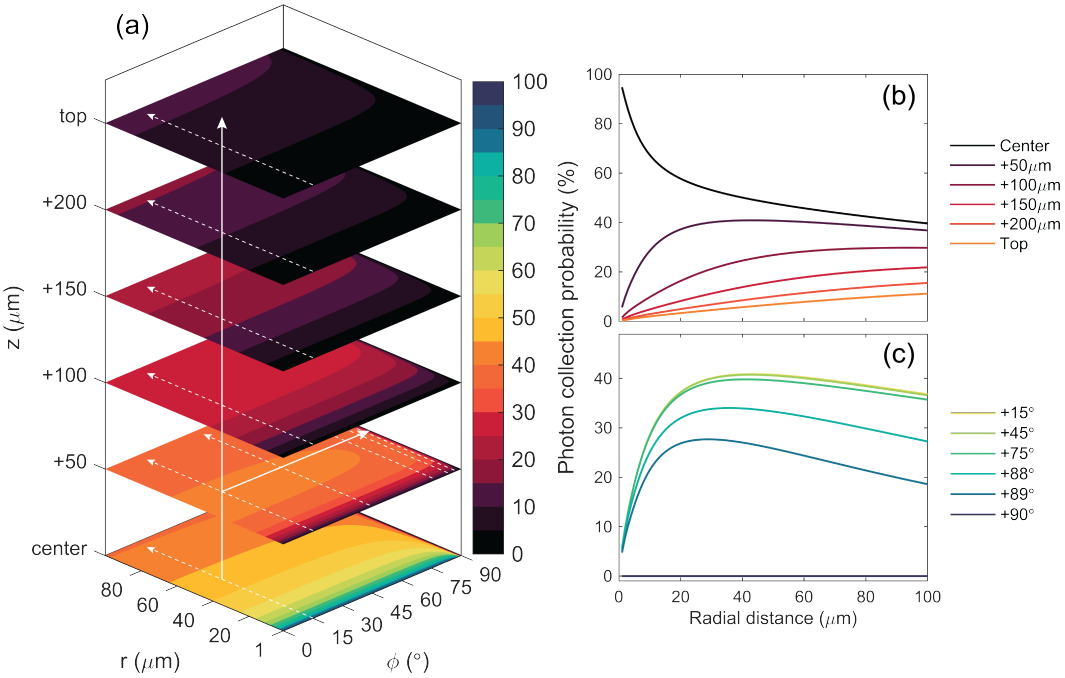

Figure 2.4: Results of the solid-angle model in the ideal case of zero luminophore reabsorption (i.e., $\alpha_2 = 0$). (a) Full, 3D parameter space results of the photon collection probability with respect to the radial distance, r, in micrometers (μm); polar angle, ϕ, in degrees (°); and vertical distance, z, with respect to the cell edge center. (b),(c) show how radial distance and vertical or polar coordinates, respectively, affect the photon collection probability for the case where $\phi = 15°$ or $z = +50\mu m$, respectively.

While Figure 2.4 quantifies the likelihood of photon collection from a fractional solid angle standpoint within a perfect waveguide material, we know from previ-

ous work the detriment photoluminescence reabsorption can have on LSC performance[39,42]. As such, we can modify Equations 2.8 and 2.9 by including a reabsorption term. Specifically, we apply the Beer-Lambert absorption law for a given luminophore extinction coefficient, α_2, to scale the total photoluminescence travel length, d, giving us a multiplicative absorption factor ($\mathcal{A}$) to Ω_0^{side} and Ω^{side} as:

$$\begin{aligned}\mathcal{A} = &\quad \exp\left\{ -\alpha_2 \cdot (d/T) \right\} \\ = &\begin{cases} \exp\left\{ -\frac{\alpha_2 \cdot \sqrt{r^2+z^2}}{T} \right\} & \text{for: } \Omega_0^{\text{side}} \\ \exp\left\{ -\frac{\alpha_2 \cdot \sqrt{\frac{r^2}{\sin^2\theta}+z^2}}{T} \right\} & \text{for: } \Omega^{\text{side}}. \end{cases}\end{aligned} \tag{2.10}$$

By combining the reabsorption factor, $\mathcal{A}$, with the full expression for photon collection probability in 2.7, we can calculate the total waveguiding efficiency, $\eta_{\text{wg}}^{(1)}$, of a given LSC device by integrating the collection probability for a given luminescence event location, $I_{\text{edge-lined}}(\vec{r})$, across all points in a particular waveguide geometry. For discussion, let us assume a square form factor with side length, ℓ, and thickness, T, as shown in Figure 2.3(a). Thus, our final expression for total waveguiding efficiency can be written as:

$$\begin{aligned}\eta_{\text{wg}}^{(1)} = \frac{1}{4\pi} \int_0^{\sqrt{5}/2\ell^2} \int_0^{\pi/2} \int_0^{T} \Bigg\{ &\mathcal{A}(r,z)\, \Omega_0^{\text{side}}(r,\phi,z) + \\ &\frac{\int_{\theta_c}^{\pi-\theta_c} \mathcal{A}(r,z,\theta)\, \Omega^{\text{side}}(\vec{r},\theta)\, \mathrm{d}\theta}{\int_{\theta_c}^{\pi-\theta_c} \mathrm{d}\theta} \Bigg\} r \mathrm{d}z \mathrm{d}\phi \mathrm{d}r,\end{aligned} \tag{2.11}$$

where the integral bounds are determined by transforming from Cartesian to cylindrical coordinates for the square waveguide. For brevity, Equation 2.11 does not include the normalization factor, where we must divide by unity probability at all points within the device volume. We can now see how to write the LSC waveguiding efficiency term—discussed by Klimov et al.[39]—based solely off the device geometry and luminophore reabsorption coefficient, α_2. Given this expression, we can vary the luminophore characteristics to unveil both the limits of waveguiding (and overall optical) efficiency and the effect of luminophore reabsorption. Figure 2.5 shows these results and the impact of α_2 on both the collection probability (a) and overall waveguiding efficiency (b). From previous work[42], we can observe the close matching of this solid-angle luminescence collection model to measurement.

With a closed form model at hand to quantify the overall LSC optical efficiency, we can apply rapid optimization analyses to probe the parameter space for a variety of form factors. Appendix B describes the analytical model implementation in a Matlab/C environment.

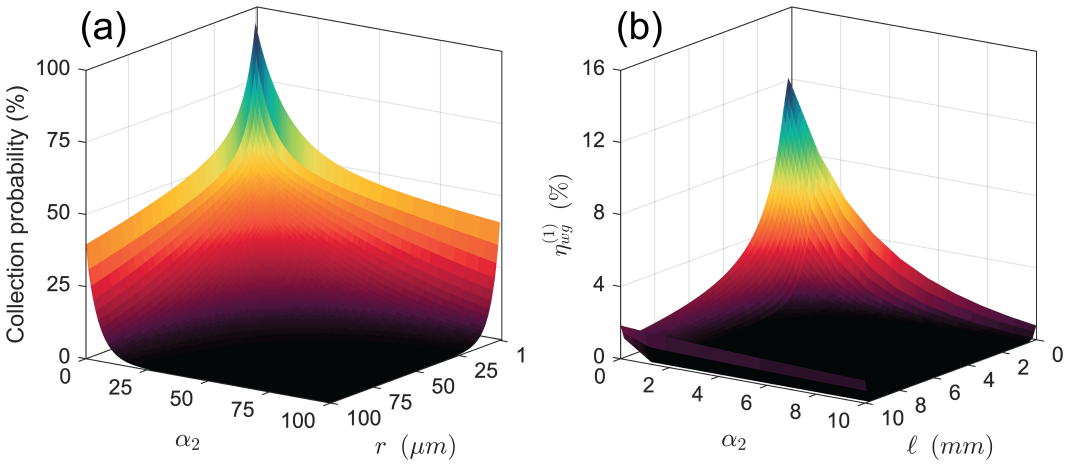

Figure 2.5: The results of a first principles calculation of collection efficiency of a square LSC of side length ℓ. (a) The impact of luminophore re-absorption (α_2 from Equation 2.10) and radial component, r, on the luminophore collection probability, $I_{\text{edge-lined}}$, at a given location $\vec{r} = (r, 0, 0)$. (b) The full waveguiding efficiency, $\eta_{\text{wg}}^{(1)}$, for an LSC of edge length ℓ given by equation 2.11.

2.4 LSC Modeling Techniques Outlook

In this chapter, we have discussed various methods to quantify LSC device performance (in the context of optical and power conversion efficiency). While there exists a variety of closed form models, the accuracy of Monte Carlo ray-tracing routines and their versatility to a wide-range of ray-optical form factors enable such tools to be the most common and widely accepted modeling approach. However, both for rapid optimization and wave-optical regimes, ray-trace methods cannot sufficiently describe all scenarios. Given these limitations, we have introduced here a closed form calculation of photoluminescence waveguide collection probability and, subsequently, overall LSC optical efficiency based in part on the quality factor model by Klimov et al.[39]. The approach of this model in developing an analytical expression for fractional solid angles with respect to emission location applies itself to non-traditional waveguide geometries, wave-optical LSCs, and constant run-time analyses for large parameter sweeps. Future work in this area must compare experimentally the predicated performance by the model for both ray- and wave-optical scales in order to verify its versatility and accuracy.

With the tools discussed in this chapter, we can now turn our attention to quantifying the performance and technoeconomic limits of LSCs. Throughout the remainder of this thesis, we will rely primarily upon the Monte Carlo ray-trace tool to examine device limits and the effects of system constituent non-idealities—enabling us to understand the pathways forward toward higher power conversion efficiencies. As such, we organize each chapter in this thesis by application and intended LSC use that sets the form factor and system input parameters.

CHAPTER 3

Single Junction LSC Devices for Terrestrial Applications

In the spring of 1953, Gerald Pearson, Daryl Chapin, and Calvin Fuller of Bell Laboratories inadvertently fabricated the first ever single junction silicon photovoltaic cell—a cell which, at the time, reached a record 4% power conversion efficiency under typical terrestrial (i.e., 1-sun AM1.5g) conditions[11]. Within two years, William Cherry proposed the first ever large-scale application of photovoltaic cells through integration with orbiting Earth satellites. And in 1958, the Vanguard I space satellite flew into orbit with on-board silicon photovoltaic modules, delivering less than one watt of electrical power. It was not until the early 1970's that photovoltaic cell manufacturing reached low enough costs to enable terrestrial applications. And, as described in chapter 1, the tremendous decrease in cell cost combined with scientific breakthroughs in performance led to single-junction terrestrial photovoltaic systems today totaling more than 500 GW of power—that is, 500 billion times the amount of total power production in about 60 years.

Of particular importance to both the general solar photovoltaic and more niche LSC communities, quantifying the thermodynamic limits of a terrestrial, single junction solar converter enables finer understanding in the potential impact a specific device holds, in addition to the methodology for how to reach these upper-bounds. Having shown the well-known detailed balance limit in Figure 1.6 and Equation 1.8, we can apply a similar analogue to the LSC. Previous studies exist illustrating how such a detailed balance approach could apply to certain geometries of an LSC[119–121]—a device that consists of not one but two distinct electronic bandgap energies (i.e., the luminophore absorber/emitter and photovoltaic cell collector). Here we detail a general approach to quantifying the power conversion efficiency limit of LSCs, taking into account the double bandgap of LSCs as well as the system parameters. Such an analysis identifies both the upper performance limits and the pathways to achieving increased efficiencies.

3.1 Efficiency Limits for Single Junction LSCs Under 1-Sun

To begin, let us assume an arbitrary LSC device that consists of an optical waveguide with refractive index, n, embedded luminophores of absorption and photoluminescence bandgap energies, $E_{\text{lum}}^{\text{abs}}$ and $E_{\text{lum}}^{\text{pl}}$ respectively, and an optically coupled solar cell of bandgap energy, E_{pv}. We can further define the Stokes shift separation, σ, between absorbed and emitted photons of the luminophore as $\sigma = E_{\text{lum}}^{\text{abs}} - E_{\text{lum}}^{\text{pl}}$. As given in Chapter 1 via Equations 1.3,1.4, and 1.6, to clarify the upper performance limits we must characterize the short-circuit current and open-circuit voltage. To quantify the former, we can apply either our deterministic or stochastic modeling techniques given the luminophore and cell bandgap energies—whereby we can also include device-specific parameters (e.g., luminophore PLQY, photoluminescence trapping, waveguide attenuation or scattering, etc.). However, to understand the open-circuit voltage maximum, we must also develop a model for calculating the dark saturation current of the photovoltaic cell when optically coupled to a luminescent waveguide.

Therefore, before we can quantify the AM1.5g 1-sun performance limits for a general single junction LSC device, we must first construct an understanding of the dark current term and, specifically, how inelastic, incoherent concentration of light affects the ratio between dark and light currents.

3.1.1 The LSC Limit in the Context of a Maxwell Demon

Let us, for the moment, consider by way of analogy a famous gedanken experiment originally brought forward by James Clerk Maxwell. Described in a letter around the mid 19$^{\text{th}}$ century to Peter Guthrie Tait[122], Maxwell introduced the concept of a system that could, at first glance, break the second law of thermodynamics via some sort of "demon"—some outside entity that would decrease entropy. In its first form, Maxwell envisioned this foreign entity (the "demon") to distinguish between low and high velocity gas molecules in a box. At time $t = 0$, all particles would exist within a single partition. As time runs forward and the atoms collide with the barrier, Maxwell imagined a "trap door" that the demon could open and close at will. The demon would then quickly open and shut the valve in order to separate low and high velocity gasses. Thus, it would appear that a temperature gradient would spontaneously form—the high and low velocity gas sides becoming hotter and cooler, respectively.

We resolve this apparent contradiction by considering the amount of entropy that the demon must add to the system through the act of opening and shutting the trap door and measuring the gas velocities. Turning our attention back to LSCs, we can similarly frame the upper performance regime for such a device in the context of a Maxwell demon. If we imagine a waveguide that could trap high energy photons but reflect low energy photons, where the trapped particles would forever occupy waveguide modes, then we would effectively recover the photonic analogy

to the Maxwell demon[123]. However, as given by Liouville's theorem—with specific application to the brightness theorem in geometric optics—the intensity (that is, the number of particles passing through a given point per unit momentum, per unit area, per unit solid angle) of a photon beam cannot change[124].

Given that trapping high energy incident light remains the general goal of LSCs, we must carefully understand how it is that we do not violate Liouville's theorem and, in turn, the second law of thermodynamics. Akin to the demon, we must include in our system that the only means by which we can trap high energy light is through the use of waveguide-embedded luminophores. Such particles absorb high energy light and re-radiate lower energy light along with heat. Thus, we resolve our apparent paradox by noting that the downshifting luminophores must play the role of our demon, generating additional entropy within the system. At the uppermost limit of photon concentration, the system equilibrates: where the luminescent waveguide emits high energy photons at the same rate as they are absorbed and downshifted (as shown in Equation 1.17 via $\mu_{\text{in}} = \mu_{\text{out}}$).

To determine the impact that this photon concentration holds over the LSC photovoltaic performance, we begin by quantifying this effect with respect to the dark radiative current term, J_0^{r}, and its relationship with open-circuit voltage. While the concentration of the incident photon beam affects both the light induced photocurrent (J_{sc}) and dark radiative current, the latter results from ambient, background radiation when the LSC system is in thermal equilibrium (and thus we can readily apply the Kirchoff law of radiation). To calculate the photoinduced current at high irradiance levels, to first order, we can ignore the effects of the surrounding ambient blackbody radiation.

In the LSC radiative limit, where we consider the photovoltaic cell dark current to result solely from radiative recombination/generation of excitons (i.e., $Q_{\text{ERE}} = 1$), we can rewrite our open-circuit voltage, given by Equation 1.5, as:

$$V_{\text{oc}}^{\text{rad}} = \frac{kT}{q} \ln\left(\frac{J_{\text{sc}}}{J_0^{\text{r}}}\right), \tag{3.1}$$

where, as before, k, q, and T are the Boltzmann constant, electronic charge, and temperature of the LSC (which we assume to be at 300K for typical terrestrial-based applications).

In thermodynamic equilibrium, the total absorption by the LSC system from the blackbody background ($J_{0,\text{abs}}^{\text{r}}$) must equal the total emission by the LSC into free space ($J_{0,\text{emit}}^{\text{r}}$), as illustrated in Figure 3.1(a). Therefore, when solving for J_0^{r}, we can choose either the absorption or emission picture[125]. Let us therefore assume that $X\%$ of luminophore photoluminescence and $Y\%$ of photovoltaic cell photoluminescence enter the waveguide escape cone and radiate back into free space. Here, $X\%$ can be calculated via the specific luminophore radiance profile and knowledge of the escape cone and $Y\%$ by the waveguide index of refraction and specific cell orientation[82]. Starting with the emission picture, we can distinguish the resulting LSC dark current as the luminophore contribution ($J_{0,\text{emit}}^{\text{r,lum}}$) and photovoltaic cell ($J_{0,\text{emit}}^{\text{r,pv}}$) into free

space:

$$J_0^{\mathrm{r}} = J_{0,\mathrm{emit}}^{\mathrm{r}} = J_{0,\mathrm{emit}}^{\mathrm{r,lum}} + J_{0,\mathrm{emit}}^{\mathrm{r,pv}}. \tag{3.2}$$

Figures 3.1(a),(b),(c) conceptually illustrate this dark current term in both the emission and absorption settings. Given the $X\%$ and $Y\%$ fractions, we can rewrite Equation 3.2 to include the total amount of luminophore and cell emission rather than solely into the escape cone—and thereby back into free space. Doing so, we have:

$$J_0^{\mathrm{r}} = X\% \cdot J_{\mathrm{net,\ emit}}^{\mathrm{r,lum}} + Y\% \cdot J_{\mathrm{net,\ emit}}^{\mathrm{r,pv}}, \tag{3.3}$$

where $J_{\mathrm{net,\ emit}}^{\mathrm{r,lum}}$ and $J_{\mathrm{net,\ emit}}^{\mathrm{r,pv}}$ give the total amount of radiative recombination by the luminophore and solar cell, respectively, and not just the portion that emits back into free space. By Kirchhoff, the total absorption into the luminophores/cell must equal total emission out of the luminophores/cell, respectively. And so we can rewrite Equation 3.3 in the context of absorption—which we more readily can measure:

$$J_0^{\mathrm{r}} = X\% \cdot J_{\mathrm{net,\ abs}}^{\mathrm{r,lum}} + Y\% \cdot J_{\mathrm{net,\ abs}}^{\mathrm{r,pv}}. \tag{3.4}$$

As shown in Figure 3.1(b), we know that the total cell absorption ($J_{\mathrm{net,\ abs}}^{\mathrm{r,pv}}$) must be a sum of both the trapped luminophore photoluminescence (i.e., $1 - X\%$) and photons entering the waveguide and striking the cell directly from the blackbody spectrum at ambient temperature, T—where the geometric gain (GG) gives this amount of ambient background radiation directly striking the cell. For simplicity we assume (given the electronic bandgap of the luminophores and that cell PLQYs are orders of magnitude lower than that of luminophores) that the trapped cell photoluminescence contributes a negligible amount to the total absorption of the luminophores. Therefore, we can write:

$$J_0^{\mathrm{r}} = X\% \cdot J_{\mathrm{net,\ abs}}^{\mathrm{r,lum}} + Y\% \left((1 - X\%) \cdot J_{\mathrm{net,\ abs}}^{\mathrm{r,lum}} + \frac{1}{\mathrm{GG}} J_{0,\ \mathrm{abs}}^{\mathrm{r,pv}} \right), \tag{3.5}$$

where, as shown in Equation 3.5, we distinguish between $J_{\mathrm{net,\ abs}}^{\mathrm{r,lum}}$ and $J_{0,\ \mathrm{abs}}^{\mathrm{r,pv}}$, where the former gives total absorption by the luminophore species, which must equal the total amount of photoluminescence, while the latter indicates irradiance absorbed by the photovoltaic cells exclusively by free space blackbody radiation. We can now define each of these terms given our known absorption profiles and the Planck spectrum:

$$\begin{aligned} J_0^{\mathrm{r}} = \Big[X\% + Y\% \left(1 - X\%\right) \Big] \cdot \int_{\omega} \int_{\Omega} \mathcal{A}_{\mathrm{lum}} \left(\omega, \Omega\right) \cdot \Phi_{\mathrm{bb}} \left(\omega\right) \mathrm{d}\Omega \mathrm{d}\omega \ + \\ Y\% \cdot \frac{1}{\mathrm{GG}} \cdot \int_{\omega} \int_{\Omega} \mathcal{A}_{\mathrm{pv}} \left(\omega, \Omega\right) \cdot \Phi_{\mathrm{bb}} \left(\omega\right) \mathrm{d}\Omega \mathrm{d}\omega, \end{aligned} \tag{3.6}$$

where $\mathcal{A}_{\mathrm{lum}}$ and $\mathcal{A}_{\mathrm{pv}}$ give the absorption profiles of the luminophore and photovoltaic cells, respectively, as a function of photon frequency, ω, and incident solid angle, Ω. Φ_{bb} is the Planck spectra at 300K. With this expression, we can calculate the dark current of our LSC in closed form and, thereby, the radiative-limit open-circuit voltage. Given Equation 3.6, we can conceptually unveil the effects of luminescence

trapping with such an optical waveguide in terms of the spectral shifting of the solar cell radiative recombination of excitons, highlighted by Figures 3.1(d),(e),(f).

As shown in Figure 3.1(d), if we assume general luminophore and cell absorption and emission profiles, we can qualitatively observe the impact of luminophore light trapping on exciton recombination energies. As seen in 3.1(e), partial trapping yields blue-shifted cell emission (higher photogenerated exciton energies), while full trapping (3.1(f)) demonstrates how the effective system open-circuit voltage saturates to the luminophore bandgap for the limit of high geometric gain. In order to include non-radiative effects of the cell (i.e., excitons that do not contribute to meaningful work and are not radiated at bandgap energies), we can apply explicit forms of the external radiative efficiency (Q_{ERE}), as well as approximate fill factor calculations (i.e., series/shunt resistances) to account for non-idealities in carrier transport.

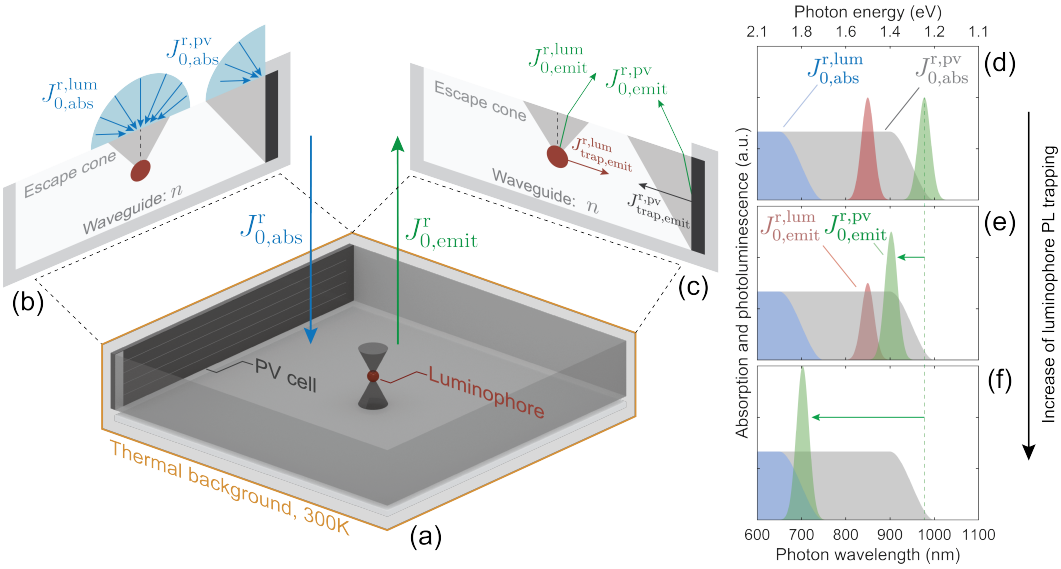

Figure 3.1: A conceptualization of the LSC system when in thermal equilibrium with the ambient Blackbody background at 300K. In this case, we know that absorption into and emission out of the LSC system must be equal as shown in (a). Therefore, we can choose to analyze the system in either the absorption (b) or emission (c) pictures. (d),(e), and (f) conceptually illustrate the spectral consequence to outgoing, free space photoluminescence via the coupled photovoltaic cell—shown here to be oriented as an edge-lining cell for example—as the luminophore photoluminescence trapping increases. (d) depicts the case of no photoluminescence trapping, where the luminophore absorption (blue) and luminescence (red) are shown to be separated by the Stokes shift energy (σ), and there is some spectral width to the cell radiative emission (green) for an arbitrary cell absorption (gray). (e) and (f) show how varying the amount of luminophore photoluminescence trapping affects the spectral location of the cell emission—where, as shown in (f), complete trapping yields the highest open-circuit voltage condition which is given by the luminophore absorption bandgap.

3.1.2 Detailed Balance Limits for Single Junction LSCs

With an explicit form of LSC dark radiative current given by Equation 3.6, we can now predict the detailed balance performance limits. Unlike conventional single junction photovoltaic cells, an LSC consists of two energy bandgaps (luminophore, cell) and a Stokes shift energy that traps luminophore emission to impinge upon the cell. Therefore, we begin our analysis of the detailed balance limit of an LSC by co-varying the luminophore and cell bandgaps. To elucidate the upper limit, we assume: *(i)* a co-planar cell form factor at a geometric gain of 20 for example, *(ii)* unity luminophore PLQY, *(iii)* a constant Stokes shift separation (in wavelength) of luminophore absorption/emission, *(iv)* a high optical density of embedded luminophores within the LSC waveguide such that 99% of incident light up to the absorption bandgap of the luminophores is absorbed, and *(v)* a Heaviside step-function as the collecting photovoltaic cell external quantum efficiency. Importantly, the detailed balance results of this section assume an LSC form factor where the collecting photovoltaic lies parallel along the bottom waveguide surface (normal in the $+\hat{z}$ direction). Section 3.3 discusses the implications for edge-lined versus co-planar orientations of the cell and consequences on area scalability.

Figure 3.2(a) illustrates the luminophore absorption and photovoltaic cell energy bandgaps of the LSC with respect to wavelength against the incident AM1.5g irradiance. As shown, we first vary the luminophore and cell absorption bandgaps separately in order to clarify the full operating space of an arbitrary LSC system. Figures 3.2(b),(c) quantify this detailed balance limit for the cases of luminophore photoluminescence trapping limited by the refractive index contrast between the optical waveguide ($n = 1.50$) and surrounding medium (air) and perfect trapping, respectively. We observe that in either case, there exists an ideal luminophore to cell bandgap offset. For this analysis, we assume a certain Stokes shift of 200nm wavelength for every luminophore instance. Given the 20nm emission full-width at half-maximum, we find ideal cell matching to depend upon both the photoluminescence profile width and the Stokes shift—where in this case the ideal separation we find to be 180nm. Of course, we could have chosen a different emission profile shape and/or a varied Stokes shift. In any case, the ideal matching between the cell and luminophore is given by how the luminescence matches near the band edge of the photovoltaic cell.

For the case of ideal emission trapping in Figure 3.2(c), we find an ultimate LSC power conversion efficiency upper limit approaching 28% given the system geometric gain, optical density, and absorption/emission spectra for the case when luminophore/cell bandgaps near 1000/1200nm, respectively. This limit nearly matches the detailed balance limit for a single junction photovoltaic cell at 1000nm (i.e., 1.24eV); however, as discussed in section 3.1.1, the dark current limit must also take into account the photovoltaic cell photoluminescence that escapes back into free space. Given that we make no assumptions on how the LSC system traps outgoing cell emission, the open-circuit voltage of the ideal LSC falls short of the traditional detailed balance 1-sun limit given the finite geometric gain of 20. However, in the limit where the geometric gain approaches infinity and we retain perfect waveguide trapping, the power conversion efficiency will saturate to the well-known

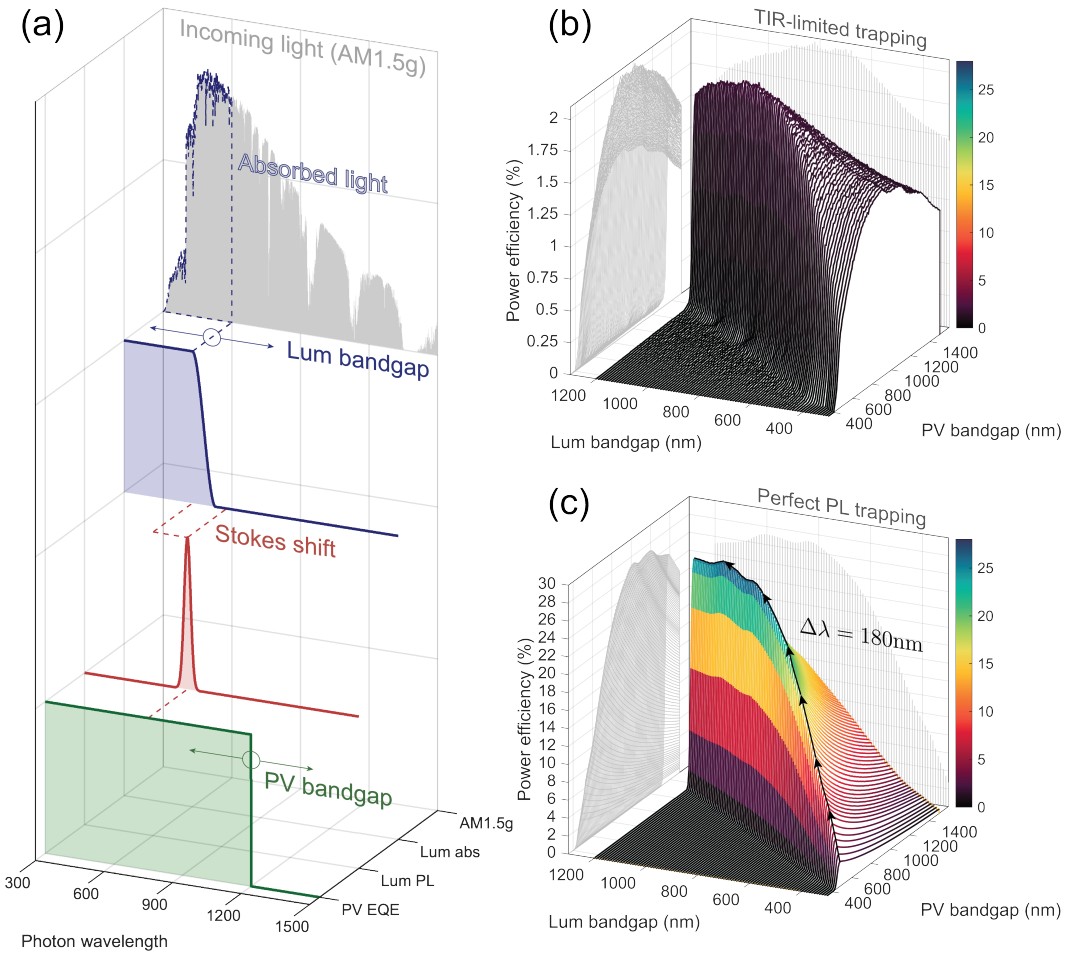

Figure 3.2: A detailed balance analysis for an LSC device, varying simultaneously the luminophore and photovoltaic cell bandgaps. We assume fixed Stokes shift with respect to wavelength offset, ideal cell and luminophore absorption edges as shown in (a), and unity PLQY to probe the upper performance limits for such modules at a system geometric gain of 20 and high luminophore optical density loading to enable complete incident light absorption by the luminophores. (b) The upper limits for LSCs with no luminophore photoluminescence trapping methods other than the contrast in index of refraction between the waveguide and external media (TIR). (c) The upper limits for LSCs in the case for some arbitrary perfect photoluminescence trapping waveguide mechanism. Here we observe a narrow ridge-line that forms, given the luminophore emission profile and Stokes shift.

detailed balance limit for traditional photovoltaic cells.

3.1.3 The Single Junction LSC Parameter Space

Beyond the two bandgap system, we can quantify the impact of optical waveguide luminophore emission trapping and PLQY on the system power conversion efficiency. As discussed in chapter 2 and shown in Figure 2.1, there exists myriad number of device parameters that affect power conversion and optical efficiency performance. However, the photoluminescence trapping and luminophore PLQY

are first order factors for attaining high efficiencies, as shown quantitatively in Figures 3.3(a),(b) respectively. We observe how, in order to achieve high performance LSCs, we must reach near-unity trapping and PLQY efficiencies at optimized luminophore/cell bandgaps. We also observe how, contrary to previous paradigms in the LSC community[126], the photoluminescence trapping plays a more impactful role in attaining maximum power conversion efficiency than PLQY.

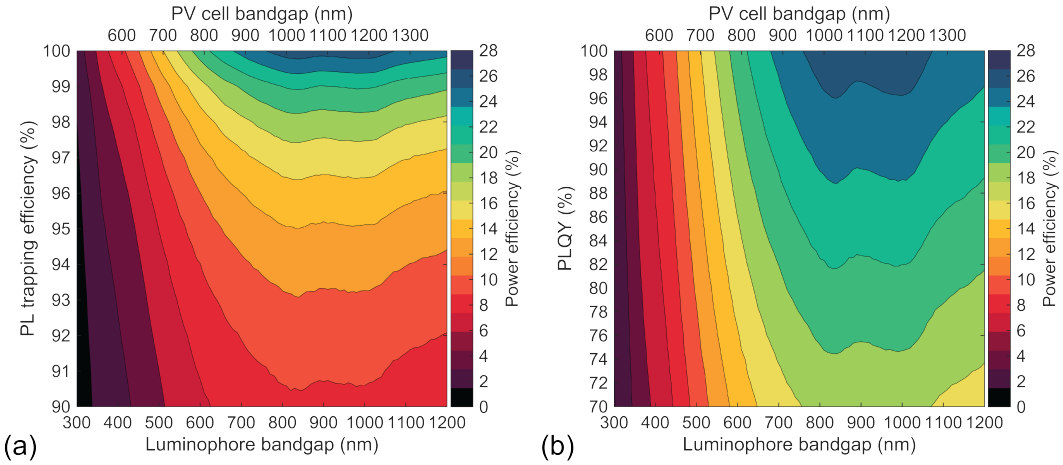

Figure 3.3: The parameter space of an LSC with respect to the system bandgap. Given the optimization between photovoltaic cell and luminophore bandgaps shown in Figure 3.2, we assume a fixed wavelength offset in order to quantify the effects of luminophore photoluminescence waveguide trapping efficiency (a) and PLQY (b). In (a), we assume unity PLQY; whereas in (b), we fix the trapping efficiency to 100%. As seen, a reduction in trapping from unity to 90% yields a power efficiency reduction of approximately 17.5% absolute for the optimal system bandgap case. In contrast, PLQY leads to less than 8.5% absolute for the same range.

Armed with this knowledge of the LSC parameter space with respect to the luminophore and cell bandgap energies, we can now begin to unveil how various system parameters affect performance (e.g., geometric gain and optical density). Given the availability of high radiative efficiency and ideal band alignment of III-V GaAs photovoltaic cells, we now analyze power conversion efficiency for such an LSC. We begin by assuming an ideal, step-like function response of the GaAs cell external quantum efficiency (electronic bandgap at approximately 900nm). Further, to probe the limits for such devices, we also assume a reabsorption free luminophore material[127] with ideal bandgap matching as given by Figures 3.2 and 3.3.

As expected for near zero luminophore reabsorption, Figure 3.4(a) shows how increased optical density (i.e., concentration within the dielectric waveguide) yields increased power conversion efficiency performance regardless of the photoluminescence trapping fraction (η_{trap}) and PLQY (η_{pl}). For all cases, the power conversion efficiency saturates for optical density values greater than 3—corresponding to an average visible transparency of 0.1%. We can further understand the effects of varying the ratio of illuminated waveguide area to total photovoltaic cell area (geometric gain). As we should expect, increasing gain monotonically decreases power conversion efficiency, illustrated in Figure 3.4, as more photons must travel greater lengths

within the optical waveguide to be collected by the planar solar cell. Additionally, at low geometric gains, the photovoltaic cell collects incident irradiance not absorbed by the luminophore species.

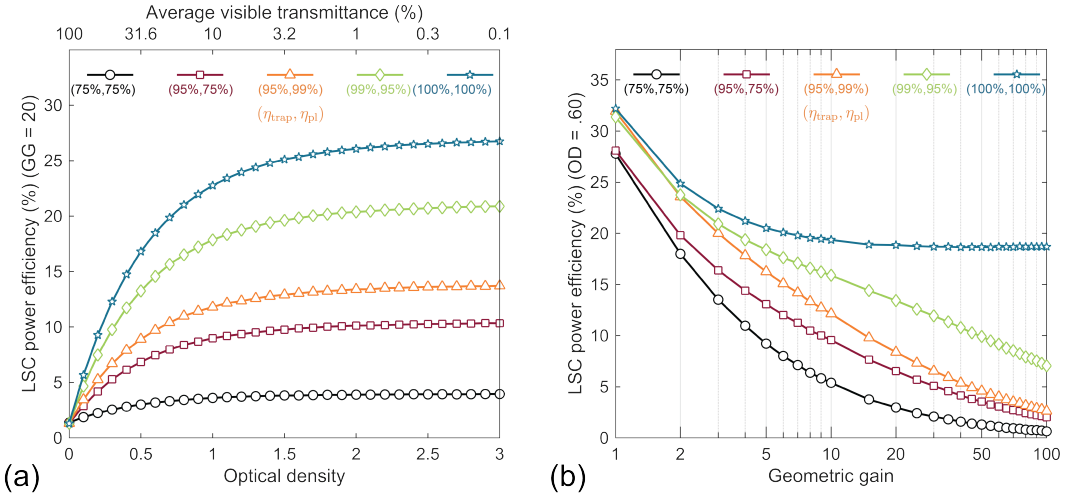

Figure 3.4: The upper performance limits for an ideal (Heaviside) GaAs embedded cell of area 1.4mm x 1.4mm within an optical waveguide of index, $n = 1.5$, varying (a) the luminophore loading (optical density measured at 450nm light) and (b) geometric gain together with the trapping efficiency (η_{trap}) and photoluminescence quantum yield (η_{pl}).

3.2 The Implications of Anisotropic Luminophore Radiance

As we have seen in Figure 3.3(a), trapping photoluminesced photons into the optical waveguide modes most influentially determines the resulting power conversion efficiency of an LSC photovoltaic device. Given this result, we can turn our attention to various methods that serve to increase this trapping fraction. For single junction applications (i.e., LSCs with only one luminophore species), we can optimize external photonic crystal structures exhibiting optical bandgaps to enable high transmittance of short-wavelength, high reflectance of long-wavelength light. However, such structures (e.g., one-dimensional photonic crystals) typically depend on the incident polar angle of light (with respect to the surface normal). Thus, while suitable for a narrow range of incident photon angles, LSCs equipped with these trapping layers suffer from high reflectance for off-angle light—preventing such concentrators from operating at high efficiencies in diffuse light conditions[117].

An alternative approach to inducing high photoluminescence trapping efficiencies is to alter the angular distribution of the luminophore emission profile while maintaining high incident light absorption. Certain luminophores naturally exhibit anisotropic radiation due to geometrical asymmetry, such as quantum rod structures[91,128], specific dye molecules[49], or two-dimensional transition metal dichalcogenide heterobilayers[79]. While there exist various known materials that achieve

anisotropy, relatively fewer studies unveil the effects on power conversion efficiency for LSC devices[129].

3.2.1 1-Sun Limits of Anisotropically Emitting LSCs

Given the LSC power conversion efficiency limits for an ideal GaAs-based device, we can now model an experimentally realized GaAs cell based on the Alta devices record[25]. As shown in Figure 3.5(a), we consider an ideal luminophore absorption bandgap with a Stokes shift less than 200nm and a finite reabsorption band within the photoluminescence wavelength regime. Here we aim to quantify effects of luminophore anisotropic emission on power conversion efficiency, assuming isotropic incident light absorption and a more realistic reabsorption pattern than in Figures 3.2. Figure 3.5(b) shows example luminophore photoluminescence spectra for three radiation profiles: the isotropic, Heaviside, and dipole-like patterns.

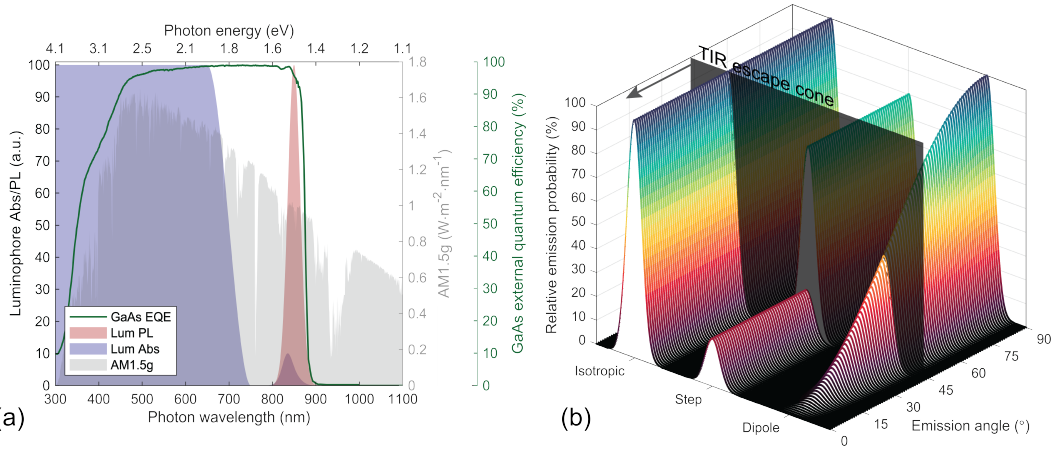

Figure 3.5: (a) The spectral profiles that we assume; whereby we model a luminophore with an absorption edge up to 700nm (left y-axis), a photoluminescence center of 800nm with a full-width at half-maximum of 20nm (left y-axis), and a GaAs cell whose measured external radiative efficiency we show in green (far right y-axis). We plot against the AM1.5g spectrum (right y-axis) for reference. (b) Three examples of luminophore photoluminescence profiles (arbitrary wavelength) given the emission angle relative to the top waveguide surface normal. Here we show the relative emission probability for the case of an isotropic luminophore with equal likelihood of radiance across all angles; a Heaviside function luminophore with a probability, P_{esc}, of emitting into the escape cone and a complementary probability, P_{tir}, of emitting into trapped angles; and a dipole emission pattern showing a continuous anisotropic profile.

Ideal Emitters with Step-like Anisotropy

To begin, we assume a step-like luminescence angular emission distribution, as shown in Figures 3.6(a),(b). We vary the luminescence intensity fraction, P_{tir}, emitted at total internal reflectance angles and assume this angular distribution to be symmetric about the z-axis (i.e., normal to the waveguide plane). By representing

the luminophore anisotropy with a single variable, we uncover the relationship between anisotropic emission, system geometric gain, optical density of embedded luminophore absorbers, and luminophore PLQY. First, we vary the luminescence quantum yield and P_{tir} of the luminophores, assuming a high optical density of three, such that 99.9% of the incident light is absorbed in a single pass for a modest geometric gain of 20. As shown in Figure 3.6(c), the optimal conversion efficiency occurs for unity PLQY and P_{tir}, where for this luminophore/cell system, we observe a global maximum of approximately 29% power conversion efficiency under 1-sun illumination—approaching the detailed balance limit with respect to the luminophore absorption and reabsorption bandgaps, including nonradiative effects within the GaAs cell. We note that by decreasing the Stokes shift to enable a broader spectral coverage of incident light, the power conversion efficiency for this system extends past that shown by Figures 3.2 and 3.4. In contrast to this anisotropic limit, the isotropic case ($P_{\text{tir}} = 75\%$) falls short of 5% power conversion efficiency.

Within Figure 3.6(c), we plot contours of the product (PLQY, P_{tir}) for constant values of 0.60, 0.70, 0.80, 0.90, 0.95, and 0.99, finding qualitative alignment between these contours and the simulation results. This agreement can be understood given that the product of luminescence quantum yield and P_{tir} sets the probability that a trapped photon survives an absorption event by a luminophore and traverses the waveguide to reach the solar cell collector. Whether the photon is lost through nonradiative recombination (for low PLQY) or by escaping the waveguide (low P_{tir}) is irrelevant for the high-level power conversion efficiency. Significantly, achieving higher P_{tir} fractions is more important than increasing the luminescence quantum yield, as seen by previous results in the detailed balance section.

To examine the relationship between photoluminescence trapping, PLQY, geometric gain, and optical density, Figures 3.6(d),(e) show stacked contour maps for total internal reflection limited and ideal trapping cases, respectively. As seen in Figure 3.6(d), there exists a global optimum optical density for all PLQY and geometric gain values of approximately 0.50 for PLQYs between 75% and 100%. As the geometric gain increases for PLQYs at or below 99%, we observe a steep and monotonically decreasing power conversion efficiency at constant optical density. Importantly, we find that for ideal emitters (near-unity PLQY and unity trapping) lower geometric gain limits the maximum concentration of the system thereby constraining the open-circuit voltage to the GaAs electronic bandgap. As the gain increases for these high PLQY and trapping cases, the system tends toward the luminophore absorption bandgap yielding higher overall performance.

We find a similar trend with a global optimum optical density near 1.0 for cases where the PLQY falls below 95%. For higher PLQYs we observe a shift in maximum power conversion efficiency with respect to optical density—in the case of unity PLQY, higher density yields more significant power conversion efficiency. Only in the case of unity trapping and PLQY do we observe power conversion efficiencies that remain constant with increasing geometric gain. Figures 3.6(c) and 3.6(e) demonstrate the importance of achieving both near-unity PLQY and PL trapping.

In order to more closely quantify the role of optical density and geometric gain, Figures 3.7(a),(b) examine how various (PLQY, P_{tir}) pairs impact conversion effi-

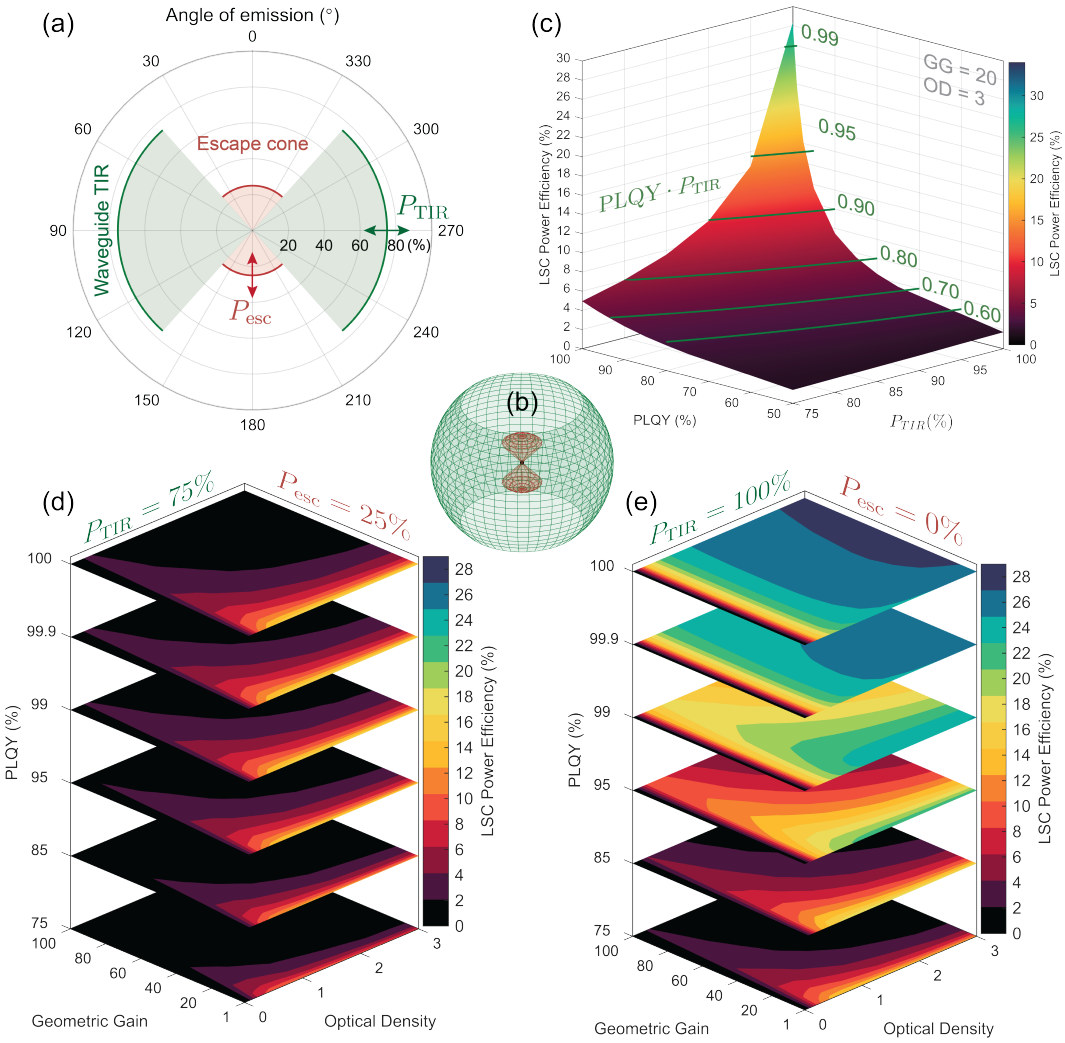

Figure 3.6: (a) 2D polar plot of the step-function emitter profile, illustrating how the total internal reflection (TIR) escape cone (P_{esc}) and TIR trapping probabilities (P_{tir}) affect the overall luminescence angle of emission probability. As shown in (c), we assume symmetry about the polar angle (i.e., about the z-axis). (b) The effects of luminophore anisotropy on the power conversion efficiency of an LSC. Here we vary the PLQY and amount of TIR emitted radiation by the luminophore, assuming a geometric gain (GG) of 20 at a waveguide optical density of 3. The analytical predictions for the efficiency (green contours) show close matching with the Monte Carlo results. (d),(e) Monte Carlo ray-trace simulations for the power conversion efficiency of an LSC with luminophores that emit 75% into TIR angles (i.e., isotropic) vs. 100% (i.e., anisotropic) as a function of geometric gain, optical density, and PLQY, respectively.

ciency. As seen in Figure 3.7(a), the optimal optical density depends strongly upon the waveguide trapping and luminophore radiative efficiency. Since this density determines both the amount of absorbed sunlight and photoluminescence reabsorption within the waveguide, a poor PLQY and P_{tir} results in detrimental nonradiative recombination and high escape cone losses for absorbed incident and re-emitted photons. As the (PLQY, P_{tir}) product increases, the drawback of re-absorption diminishes while the advantage of increased sunlight absorption remains, thereby

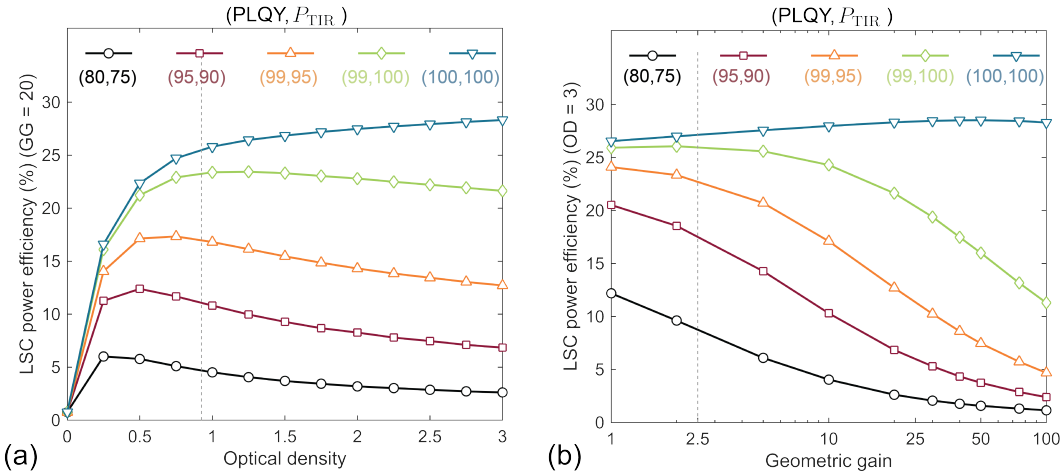

Figure 3.7: (a) LSC power conversion efficiencies as a function of optical densities for several (PLQY,P_{tir}) pairs, illustrating how an increase in the (PLQY,P_{tir}) enables higher efficiencies and shifts the optimum optical loading to higher values. Here we assume a GG of 20. (b) LSC power efficiencies as a function of geometric gain for the same (PLQY,P_{tir}) pairs as (a), assuming an optical density of three. We observe decreasing efficiencies with increasing geometric gain for low PLQY and P_{tir} values due to surface and bulk scattering waveguide losses. At near-unity PLQYs and P_{tir} values, however, increased geometric gain yields open-circuit voltage enhancement due to larger concentration. The dotted lines in both (a) and (b) correspond to the optical density and geometric gain for the previous record LSC with conversion efficiency 7.1%, respectively.

increasing the optimal optical density. Figure 3.7(b) illustrates the difficulty in achieving a high power conversion efficiency for increasingly large waveguide to cell area ratios for products less than unity. In all but the ideal case, efficiency monotonically decreases with increasing geometric gain. Even in this special case of unity PLQY and P_{tir}, increasing the geometric gain beyond a certain value yields higher likelihood of photoluminescence scattering inside the escape cone, resulting in lowered power conversion efficiencies. We find that for power conversion efficiency values above 15% and geometric gains greater than 10, the (PLQY, P_{tir}) product must exceed 85%.

Having identified the effects of an ideal anisotropic system on the power conversion efficiency of an LSC device, one where we can continuously vary the degree of anisotropy, we can now model more realistic anisotropic systems. We can still assume certain idealities with respect to the luminophore absorption/emission spectra and second-order effects such as bulk/surface state waveguide scattering. By modeling certain experimentally-achievable far-field emission profiles, we can better understand how realistic devices can unlock higher performance.

Emitters with Dipole-like Anisotropy

For a more realistic approximation of an LSC employing anisotropic emission, we begin by modeling a system comprised of dipole-like emitters. Figures 3.8(a),(b) illustrate the polar and 3D plots of the far-field dipole emission pattern, where we

again observe symmetry about the z-axis (azimuthal). We find upon integration that approximately 91% of the generated luminescence is emitted into TIR angles assuming a dielectric waveguide of refractive index, $n \approx 1.5$. Varying the PLQY, geometric gain, and optical density, we find that—similar to our previous analysis for non-unity (PLQY, P_{tir}) pairs—there exist global optima optical densities. A PLQY of 95% and gains below 60 yield optimal luminophore concentrations near 0.67. We find a maximum power conversion efficiency of approximately 25% for the case of unity PLQY, optical density of three, and geometric gain of unity. For a gain of 10, a geometry of practical experimental interest, the maximum power conversion efficiency decreases to approximately 18.5% for unity PLQY and an optical density loading of 0.75.

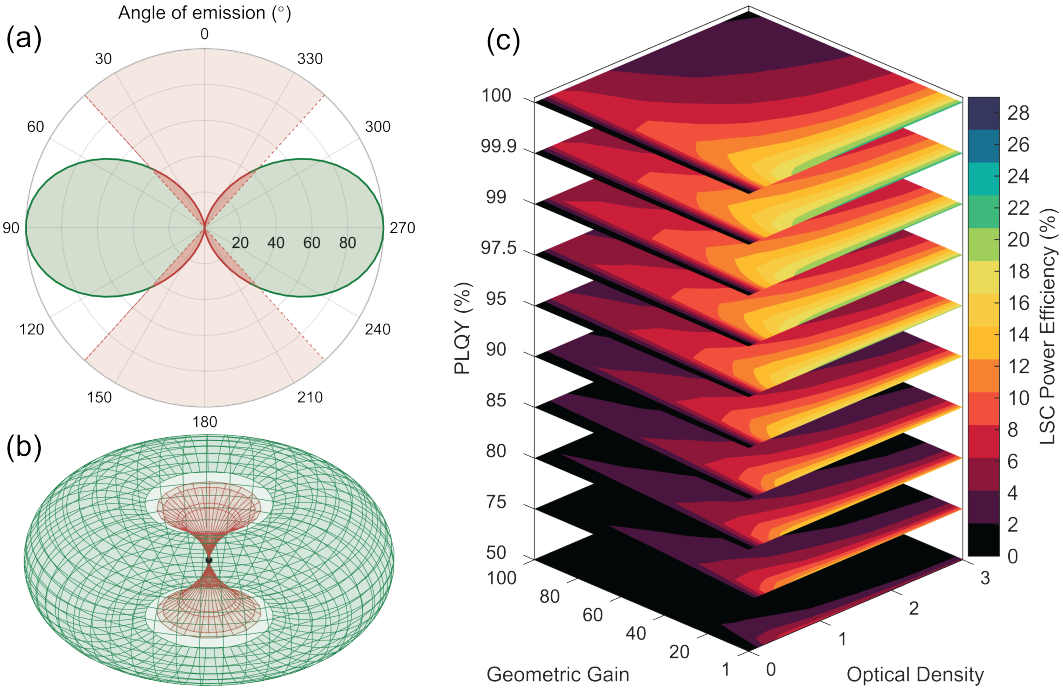

Figure 3.8: Monte Carlo ray-trace results for an ideal dipole-like emission pattern, where (a) shows the polar two-dimensional plot of the simulated PL profile with respect to azimuthal angle and (b) illustrates the polar angle symmetry (i.e., about the z-axis). (c) Power conversion efficiency of the LSC module with respect to geometric gain, optical density, and PLQY.

Emitters with Azimuthal Asymmetry

Thus far, our analysis has employed anisotropic emitters with far-field radiation symmetric about the z-axis (azimuthal). We now turn attention to optical structures that exhibit strong emission in a single direction, breaking this symmetry. In the case of emission systems symmetric about the z-axis, photons perform random walks throughout the waveguide. By contrast, forward emitting luminophores exhibit a decreased mean free path for photon propagation to the collector cells. We simulate forward emitting luminophores consisting of spherical absorbing/emitting nanopar-

ticles embedded within a nanocone. For such forward-emitting luminophores, Figures 3.9(a),(b), and (c) highlight the polar radiation plot, spatial emission profile, and nanocone structure. Integrating the luminescence intensity, we observe that approximately 88% of the irradiance from such structures couples into TIR waveguide angles—slightly less than for the dipole-like emitter.

As shown in Figure 3.9(d), the dependence of forward emitter power conversion efficiency on optical density, geometric gain, and PLQY closely parallels that of the dipole emitter case. However, even though the forward-like case is 33% more likely to emit photons into the escape cone relative to dipole structures, we observe a maximum conversion efficiency of 24%, approximately 96% the dipole emitter limit. We find fewer luminescence re-absorption events for forward emitters compared to their dipole emitter counterparts, suggesting that breaking z-axis symmetry enables shorter luminescence mean free paths within the waveguide. This decreased path length almost completely compensates the increased escape cone loss. Further, we observe that for a geometric gain of 10, the maximum conversion efficiency reaches 17.3% for the case of unity PLQY and optical density of 0.75.

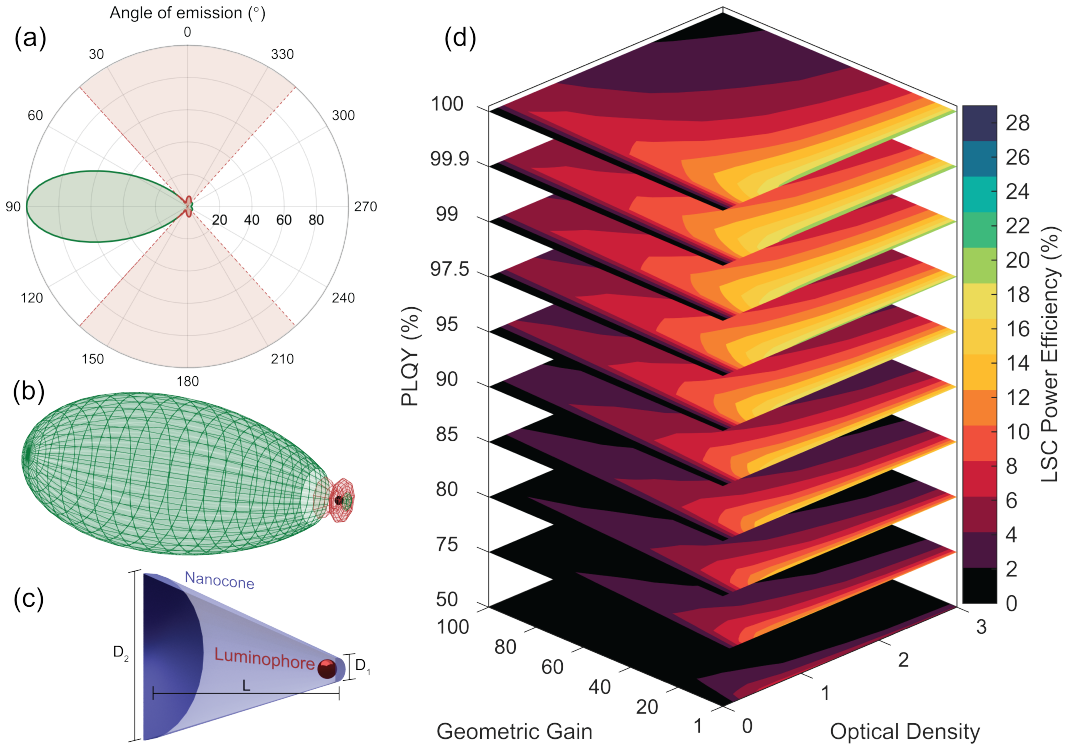

Figure 3.9: Monte Carlo ray-trace results for the forward, nanocone emission pattern, where (a) shows the polar plot of the simulated PL profile with respect to azimuthal angle and (b) illustrates the polar angle asymmetry of the forward emitter, where the structure preferentially emits into angles along a single direction of the horizontal x-axis. (c) A three-dimensional rendering (cross section) of the forward emitting structure, consisting of the luminophore (red sphere) at the narrow end of the cone (D_1) of length L with a final, large diameter of D_2. (d) Conversion efficiency of the LSC module with respect to geometric gain, optical density, and PLQY.

2D Heterobilayer Emitters

Recently, two-dimensional transition metal dichalcogenides (TMDCs) have achieved near-unity PLQYs after chemical treatment, making such materials promising candidates for LSC devices[130]. Particularly, monolayer molybdenum disulfide (MoS_2), tungsten disulfide (WS_2), and tungsten diselenide (WSe_2) exhibit direct electronic band gaps and thus have shown enhanced PLQYs. While monolayer MoS_2, WS_2, and WSe_2 each exhibit significant overlap in their photoluminescence and absorption spectra, heterobilayer TMDCs (e.g., MoS_2/WS_2 and MoS_2/WSe_2) achieve larger Stokes shifts[131]. Moreover, these heterobilayers exhibit anisotropic, dipole-like radiative emission patterns[79] making them of practical interest given our results shown by Figure 3.8.

Here, we investigate, as a proof of concept, two distinct LSC systems: whereby one employs an MoS_2/WS_2 luminophore system, the other MoS_2/WSe_2. Figure 3.10(a) shows the full spectral breakdown of the LSC device, where we plot the MoS_2/WS_2 and MoS_2/WSe_2 absorption and emission spectra (left y-axis) in reference to the optically coupled GaAs cell (far right y-axis). Again, we simulate the Alta devices record GaAs cell while now introducing realistic absorption and emission spectra of the embedded TMDC heterobilayer luminophores. Figure 3.10(b),(c) again show the polar and 3D plots of the far-field dipole emission pattern simulated here.

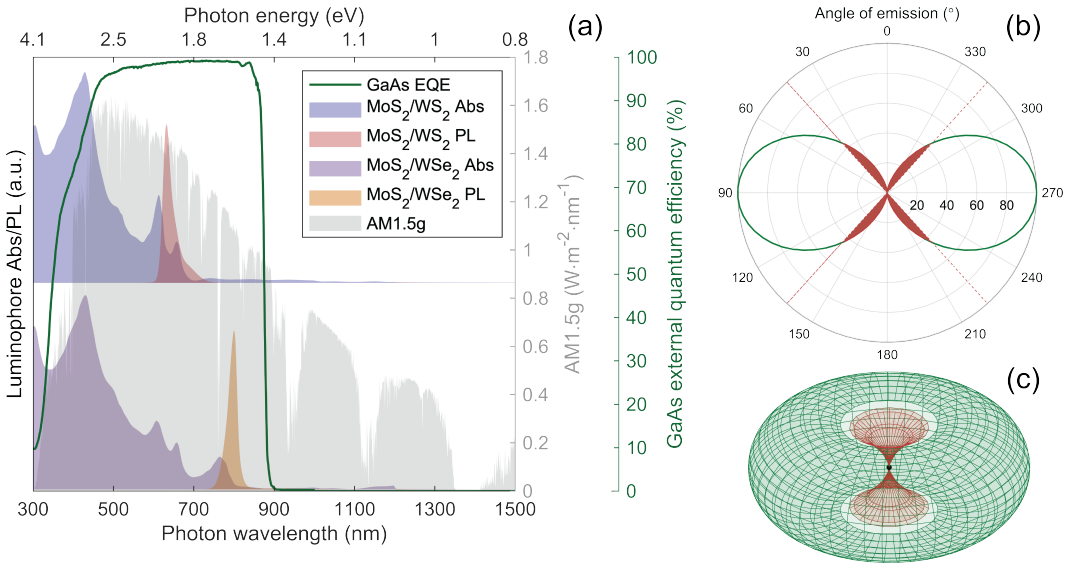

Figure 3.10: (a) Heterobilayer TMDC absorption and emission spectra overlaid against an Alta Devices GaAs solar cell external quantum efficiency and AM1.5G spectra. We supply these spectra directly into the Monte Carlo ray-trace and detailed balance model to predict the LSC device performance. (b) The polar two-dimensional plot of the simulated emission profile with respect to azimuthal angle, where (b) illustrates the polar angle symmetry of the dipole emission.

Both heterobilayer absorption/emission spectra shown in Figure 3.10 originate from previous measurements[79,131]. For both studies, the monolayer TMDCs were

prepared using mechanical exfoliation and measured at ambient temperature. To approximate the full spectral response of each heterobilayer interlayer exciton recombination, we apply a Gaussian fit to extrapolate across the broad wavelength regime from 300 nm up to 1500 nm. For both of the material absorption data, we reference monolayer MoS_2, WS_2, and WSe_2 refractive indices and extinction coefficients measured from 193 nm to 1700 nm at 300K[132]. Applying the transfer matrix method[133] and assuming a monolayer thickness of approximately 0.6nm, we calculate the expected absorption spectra for each of the heterobilayer TMDCs. For means of comparison, we calculate the absorption spectra using the complex dielectric function from a separate study[134]. We find close matching between the resulting absorption spectra from each method.

As shown in Figure 3.11, we evaluate the TMDC based LSC power conversion efficiency as a function of the luminophore PLQY, device geometric gain, and waveguide optical density loading of luminophores (referenced at 450 nm). However, given the limited interlayer exciton PLQY for such heterobilayer materials, we vary the PLQY from 50% to 100%—as done in the cases for computationally modeled forward/dipole emitters. Figures 3.11(a) and 3.11(d) overview the entire parameter space with respect to these three independent variables for the MoS_2/WS_2 and MoS_2/WSe_2 cases, respectively. Highlighted in Figures 3.11(b) and 3.11(e) for each material case, we analyze the LSC power conversion efficiency solely as a function of optical density, assuming a constant system gain of 10 and PLQYs given by each curve (where we choose discrete values of 80%, 90%, 95%, 99%, and 100%). For MoS_2/WS_2, we observe efficiencies starting at 2.9% purely due to bulk waveguide scattering of incident photons. As the optical density of heterobilayer TMDC luminophores increases, the efficiency ranges from 2.0% up to 3.8%. For MoS_2/WSe_2 system we observe similar trends with respect to luminophore concentration. For PLQYs less than unity, higher optical density luminophore loading yield lower power conversion efficiency performance as a result of increased photon reabsorption at photoluminescence wavelengths—thus adding a chance at further non-radiative exciton recombination or emission into the escape cone. As a result, we find that for PLQYs below 99%, there exists a global optimal value of optical density. Further, as a result of relatively higher amounts of absorption/photoluminescence overlap in the MoS_2/WS_2 system than the MoS_2/WSe_2, there exists a stronger dependence on the PLQY for all optical densities.

Figures 3.11c and 3.11f quantify the effects of LSC system geometric gain on the overall power conversion efficiency performance, assuming a constant optical density of three. For all values of PLQY, power conversion efficiency decreases monotonically as the geometric gain increases as seen in our previous analysis in Figure 3.8. However, at unity gain and PLQYs of 80% and 100%, the conversion efficiency ranges from 3.9% to 6.6% and 4.5% to 6.4% in the MoS_2/WS_2 and MoS_2/WSe_2 cases, respectively. We observe that, for gain values less than six and high PLQYs, the WS_2 luminophore-based system can achieve higher conversion efficiencies owing to a lower energy bandgap and, therefore, a more complete spectral coverage of the incident AM1.5G spectrum. However, at larger geometric gains, MoS_2/WS_2 efficiencies decrease more quickly than that of the WSe_2-based system owing to larger Stokes shift between the absorption and photoluminescence peaks.

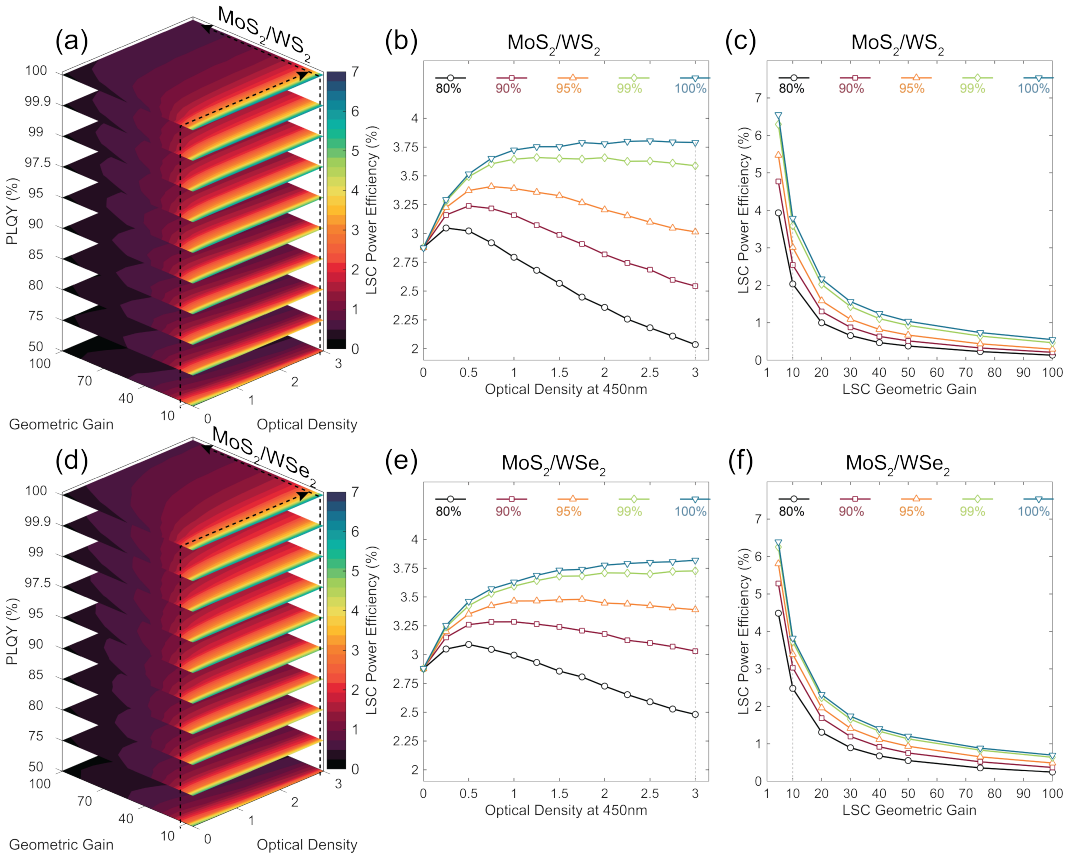

Figure 3.11: Analysis of two-dimensional TMDC-based LSC devices for the MoS_2/WS_2 (a,b,c) and MoS_2/WSe_2 (d,e,f) luminophore cases as a function of device geometric gain, optical density at 450nm, and luminophore (i.e., interlayer exciton) PLQY. (a) and (d) illustrate the full parameter space for these two luminophore sets. (b) and (e) highlight the LSC power conversion efficiency dependence as a function of optical density and PLQY for a set geometric gain of 10. (c) and (f) similarly show this efficiency dependence as a function of geometric gain and PLQY for a set optical density of three.

Enhancing the Previous LSC Record Device

While the dipole and forward emission cases correspond to physically realizable emitters, the LSC structure itself assumes certain idealities. Specifically for the case of Figures 3.8 and 3.9, we have assumed record GaAs cells coupled to ideal luminophore emitters with a narrow photoluminescence profile matched to the GaAs bandgap. Additionally, our simulated LSC waveguide matrix assumes a constant index of refraction across the relevant emitted photon wavelengths. To illustrate how anisotropic emission can significantly benefit less idealized systems, we model the previous record power conversion efficiency luminescent concentrator fabricated by Slooff et al.[65] As shown in Figure 3.12(a), this device employs two luminophore species: LumogenRed and Fluorescence Yellow dyes, with peak optical densities of 0.71 and 2.36 at 450 nm light and luminescence quantum yields of 87% and 98%, respectively. With a square waveguide side length of 5 cm and an overall thickness of 0.50 cm, the fabricated LSC yields an overall geometric gain of 2.5. Figure 3.12(a)

displays the refractive index of the waveguide polymer matrix material, poly(methyl methacrylate) and the external quantum efficiency of the GaAs solar cell. Finally, a diffuse Lambertian-scattering back reflector is coupled to the bottom surface of the waveguide, with approximately 97% averaged reflectance at photoluminescent wavelengths.

We first simulate this luminescent concentrator device assuming no anisotropy of the luminophore radiance profile—validating our model by obtaining a power conversion efficiency equal to the experimental measurement. As a next step, we systematically vary the luminescence fraction emitted into TIR angles in the waveguide. As shown in Figure 3.12(b), the isotropic emission case (i.e., P_{tir} of 75%) attains the experimentally measured conversion efficiency value of 7.1% under 1-sun illumination. However, upon increasing the anisotropic luminescence fraction, we find a monotonic increase in performance up to 9.6% in the ideal case of unity P_{tir}—a relative increase of 35%. The observed power conversion efficiency enhancement resulting from luminophore anisotropy again underscores the crucial role of waveguide trapping.

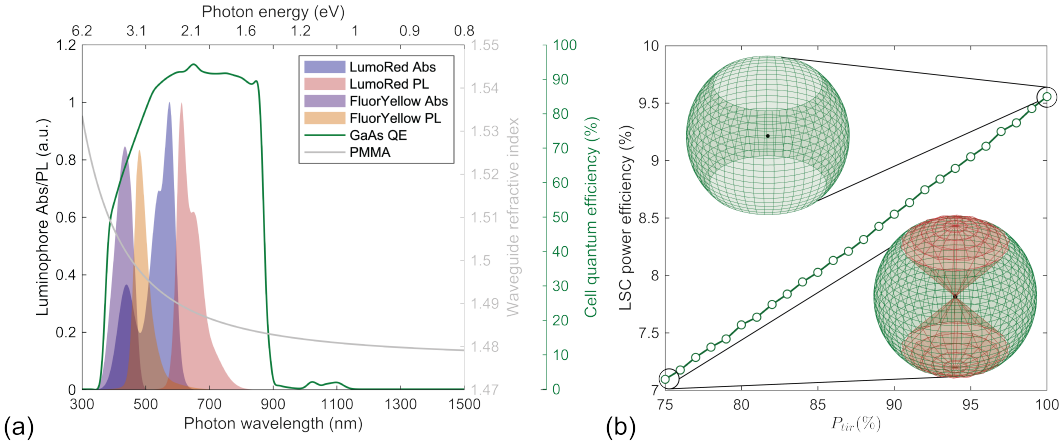

Figure 3.12: (a) The spectral characteristics of the current record LSC device, consisting of two luminophores within the waveguide (LumogenRed, Fluorescence yellow) (left y-axis), four edge-lined GaAs cells (cell quantum efficiency at far right y-axis), and a PMMA waveguide matrix (refractive index at right y-axis). (b) Monte Carlo ray-trace simulations showing the impact of anisotropy on the power conversion efficiency for the current record device. At the isotropic limit (P_{tir} of 75%), we observe close matching between measured and modeled efficiencies (7.1% measured and 7.096% modeled). At the anisotropic limit, power efficiencies reach 9.6%, a relative increase of approximately 35%.

3.2.2 Anisotropic LSC Thermodynamic Losses

As discussed in chapter 2, the Monte Carlo ray-trace model tracks photons collected as well as lost. For the LSC, we can categorize losses into five thermodynamic mechanisms. Figures 3.13(a)–(c) illustrate these losses as a function of the luminophore optical density at an LSC geometric gain of 20, assuming PLQY of 95%. For each of the three emitter types (step, dipole, and forward), losses can be understood as

either: *(i)* non-absorbed incident photons due to sub-bandgap photon energy or low luminophore optical density; *(ii)* thermalization, i.e., energetic relaxation of photogenerated excitons to the luminophore bandgap energy; *(iii)* waveguide escape cone loss; *(iv)* sub-unity PLQY loss; and *(v)* loss from the photovoltaic cell itself, owing to thermalization from the luminophore emission energy to the cell bandgap, sub-unity collection efficiencies (i.e., external quantum efficiencies), fill factor, and cell contact resistance.

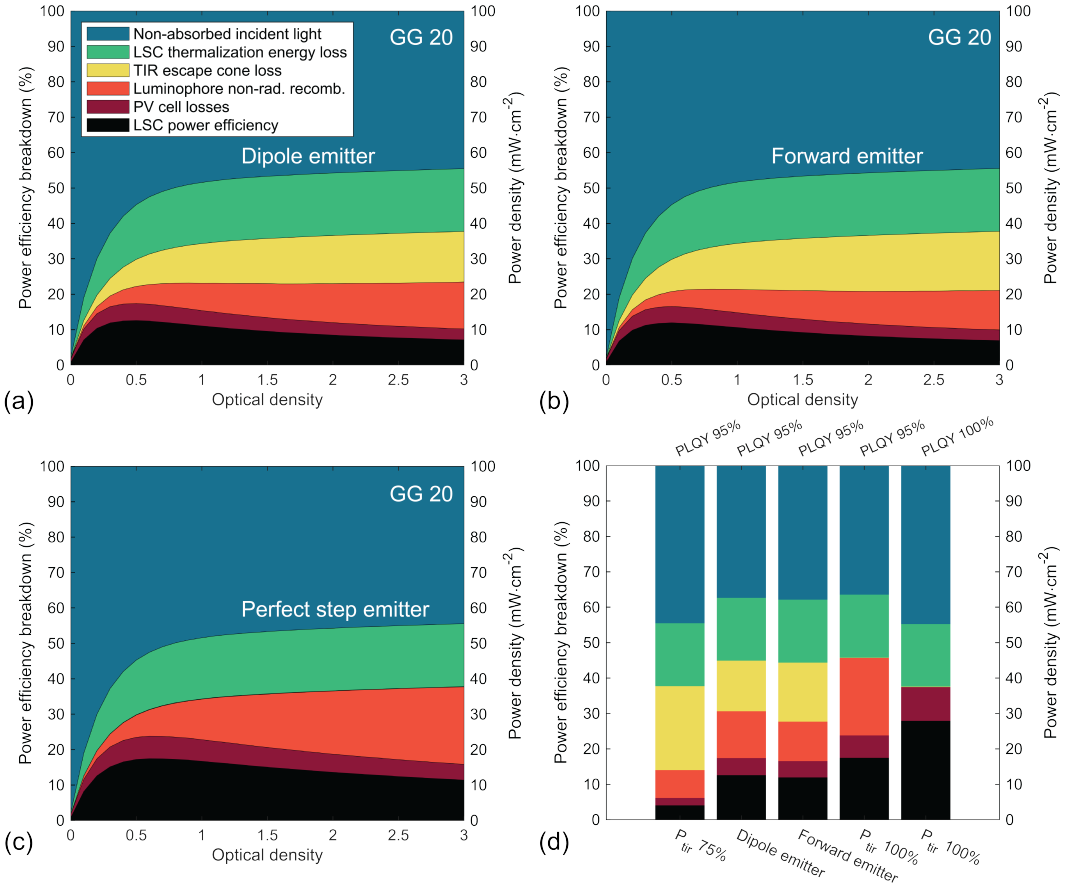

Figure 3.13: The overall power conversion efficiency loss mechanisms of an LSC with respect to the optical density of the luminophores within the optical waveguide for the case of the dipole emitter (a), forward emitter (b), and perfect anisotropic step emitter (c). (a), (b), and (c) assume a PLQY of 95%. Here we define the losses as: *(i)* incident irradiance not absorbed by the LSC, limited by both the absorption spectrum of the luminophore and, for lower optical densities, the amount of in-band luminophore absorption; *(ii)* LSC thermalization energy loss, owing to the thermalization of photogenerated excitons within the luminophore that relax to the photoluminescence band edge; *(iii)* the TIR escape cone loss of the photoluminescence which can result from emission coupling into the cone from an emission event or a scattering event by the waveguide; *(iv)* luminophore non-radiative recombination of photogenerated excitons given non-unity PLQYs; and *(v)* PV cell losses, which include parasitic absorption, given the limited internal quantum efficiency of the coupled cell material and thermalization from the photoluminescence wavelength to the bandgap of the cell. (d) A comparison of five cases at optimal optical density given the emitter and geometric gain of 20 for *(i)* PLQY of 95% and TIR-limited trapping, *(ii)* the dipole emitter at 95% PLQY, *(iii)* the forward emitter at 95% PLQY, *(iv)* PLQY of 95% and perfect trapping, and *(v)* the upper performance-limit of unity PLQY and perfect trapping.

Figures 3.13(a)-(c), illustrate the trade-off between optical density and maximum power conversion efficiency (black). Although a higher optical density minimizes the non-absorbed incident light (blue), waveguide escape cone loss (yellow) and luminophore non-radiative recombination (orange) adversely affect overall performance for the dipole and forward emitters. For the perfect step emitter, we observe increased luminophore optical density yields substantially higher amounts of non-radiative recombination (orange). As expected, we observe lower escape cone loss in the dipole emitter case compared to that of the forward emitter. However, the forward emitter loses comparatively less power through luminophore non-radiative recombination compared to the dipole case given shorter mean free photoluminesced photon path lengths as previously discussed.

Figure 3.13(d) compares four non-ideal systems to an ideal case of unity PLQY and P_{tir}, high optical density of three, and a geometric gain of 20 (yielding a maximum conversion efficiency of approximately 29% as expected for this luminophore and cell system). For isotropic emission (i.e., P_{tir} of 75%) at a PLQY of 95%, the dominant loss mechanism is photoluminescence coupling into the escape cone. We also observe that for dipole, forward, or perfect step emission and PLQY of 95%, the primary loss mechanism is luminophore non-radiative recombination. In the ideal case of complete trapping and perfect luminophore radiative efficiency, the luminescent concentrator power conversion efficiency reaches the detailed balance limit of a photovoltaic system whose bandgap is given by the luminophore absorption spectra rather than the GaAs bandgap. This can be understood given that incident light with energies greater than the bandgap of the cell, but less than the luminophore absorption edge, will not be absorbed by either the luminophore or waveguide matrix—assuming a dielectric waveguide with an arbitrarily large bandgap (i.e., insulator). As demonstrated by previous studies[120,121,129], LSCs can retain the detailed balance limit only if this condition holds where the dark radiative saturation current is not scaled with the short-circuit current.

3.3 Consequences of Geometric Form Factors

As discussed in chapter 1, the traditional LSC form factor consists of photovoltaic cells optically adhered to collect photoluminesced photons at the perimeter edge of a rectangular waveguide. While previous studies unveil the effects of altering the luminescent waveguide geometry (e.g., square, thin rectangular, rod)[66], the arrangement of the collecting photovoltaic remains largely undiscussed in the LSC literature. While sections 3.1 and 3.2 discuss the limits of an LSC employing edge-lined photovoltaic cells, we can also develop deeper insight into the question of how cell placement affects power conversion efficiency and system geometric gain.

3.3.1 The Geometric Gain

Defined in section 1.2.2, the geometric gain relates the total illuminated LSC waveguide area (A_{in}) to the total active photovoltaic cell area (A_{out}). If we generally

assume a square waveguide of edge length, ℓ, of thickness, h, and cells lining each of the four edges, then we observe that the geometric gain simplifies to:

$$\mathrm{GG}_{\text{edge-lined}} = \frac{A_{\text{in}}}{A_{\text{out}}} = \frac{\ell^2}{4\ell h} = \frac{\ell}{4h}. \tag{3.7}$$

As shown by previous luminescent concentrator studies[135,136] and this thesis, power conversion and optical efficiencies monotonically decrease with increasing geometric gain. If we therefore assume the case where such concentrators transition from the lab-scale (e.g., $\ell = \mathcal{O}(\text{cm})$) to the industrial scale (e.g., $\ell = \mathcal{O}(\text{m})$), we must carefully consider how to decouple module power conversion efficiency performance from overall device area. That is, we must issue a luminescent solar concentrator form factor whose geometric gain remains fixed given increasing module sizes (ℓ).

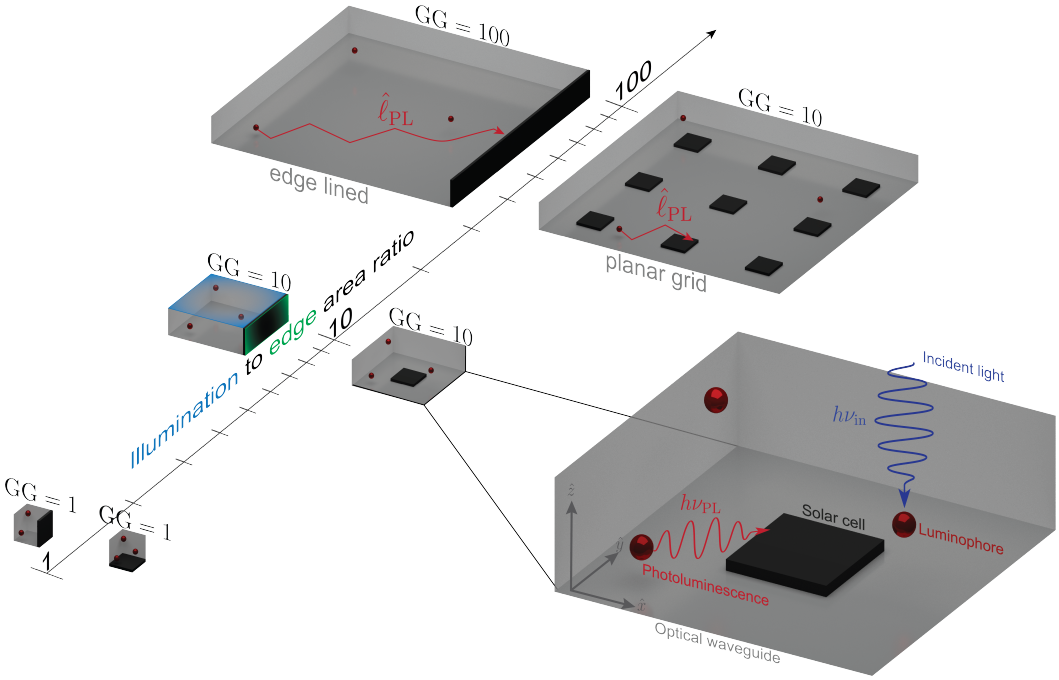

Figure 3.14: The comparison between an edge-lined and planar grid photovoltaic LSC device as a function of the illumination to edge area ratio. (left) a traditional edge-lined LSC, whereby an increase in the illumination to edge area ratio of 1, 10, and up to 100, corresponds to a system geometric gain growth by the same amount. In contrast, (right) a planar grid architecture demonstrates how the fractional areal density of photovoltaic cells sets a constant gain, irrespective of illumination to edge area ratio. At large ratios, modest geometric gain LSCs enable decreased average photon collection lengths. (Zoom-in) A look at a general planar luminescent solar concentrator unit cell, consisting of luminophores dispersed within an optical waveguide, absorbing incident light and re-radiating as down-shifted photoluminescence within the optical waveguide to be collected by the embedded photovoltaic cell.

Among many possible solar cell arrangements within the luminescent waveguide, let us imagine a two-dimensional grid-like pattern of small-area solar cells to lie planar the luminescent waveguide bottom surface, as illustrated in Figure 3.14. As

a proof of concept, we will forego any discussion of the assembly and interconnection for such an array of cells—although various studies have discussed similar, large-area designs and approaches for alternative applications[137–143]. As seen, the total photovoltaic area for such a layout depends solely on the fractional area density of the cell grid, ρ_{grid}. We can now rewrite our expression for geometric gain as:

$$\text{GG}_{\text{planar}} = \frac{A_{\text{in}}}{A_{\text{out}}} = \frac{\ell^2}{\rho_{\text{grid}} \cdot \ell^2} = \frac{1}{\rho_{\text{grid}}}. \tag{3.8}$$

With these two different LSC form factors, we qualitatively observe how the average photoluminescence collection length, $\hat{\ell}$ shown in Figure 3.14, increases monotonically for the case of edge-lined photovoltaic cells and remains constant for a grid array. Despite our choice of orienting the periodic unit cell to lie planar to the bottom waveguide surface, we could have chosen a number of various cell form factors. Therefore, we can quantify the impact orienting the photovoltaic cell within the unit cell waveguide has on collection efficiency.

3.3.2 LSC Form Factors

While the choice to assemble a repeated motif of unit cell LSCs enable module scalability to arbitrary areas, the orientation of the collecting photovoltaic within the LSC unit cell remains an active parameter. Here we evaluate optical efficiency of a unit cell (i.e., the photoluminescence collection efficiency) for six distinct arrangements of the photovoltaic. As seen in Figure 3.15(a), we will assume a CdSe/CdS quantum dot luminophore (measured absorption/photoluminescence) waveguide of poly(lauryl methacrylate). We simulate the optical efficiency via the Monte Carlo ray-trace model, whereby the unit cell consists of a silicon photodiode collector (Luna Optoelectronics PDB-C152SM) at a fixed area at different orientations.

For example, we assume the collecting cell to be arranged: *(i)* vertically in the center of the waveguide (monofacial), *(ii)* vertically along one of the four edges, *(iii)* planar at the top and laterally centered, where the photoactive area of the diode is face downward (inverted), *(iv)* planar in the center of the waveguide and laterally centered, *(v)* planar along the bottom and laterally centered, and *(vi)* planar along the bottom and located parallel to an edge of the waveguide. In all cases, we assume a monofacial photodiode cell with approximately 5% areal coverage due to active area shading. Figure 3.15(b) illustrates the various orientations described here.

From Figures 3.15(c),(d), we observe distinct optical efficiency performance of the LSC unit cell for varying orientations of the collecting photodiode and optical density or geometric gain, respectively. While the planar edge (PE), planar bottom (PB), and planar center (PC) follow similar trends and efficiency values with respect to optical density and geometric gain, these show superior performance to the vertical center (VC) and vertical edge (VE) designs in all geometric gains and optical density values. Due to the planar top (PT) inversion of the active area, low geometric gains prevent significant photoluminescence collection efficiency of the planar top cell. However, for increasing geometric gains, we observe that the planar

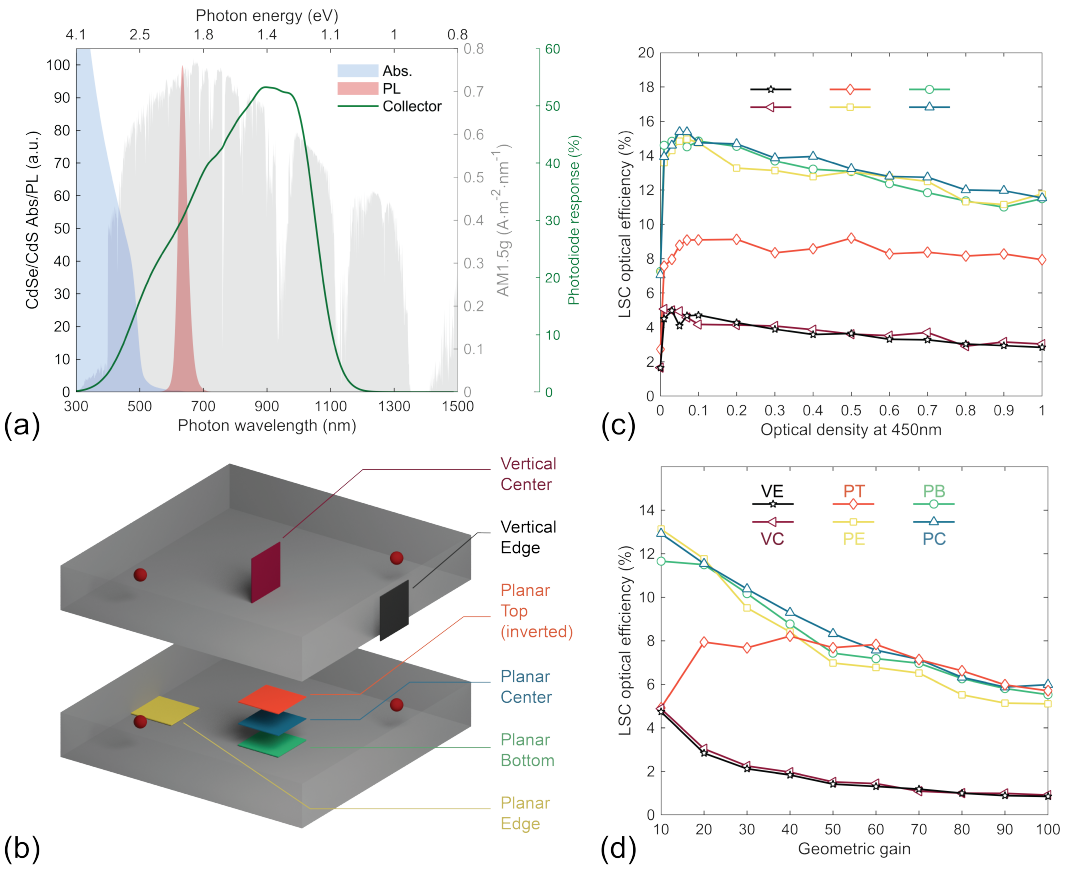

Figure 3.15: A study on the impact of the collecting cell (in this case a silicon photodiode) on the optical efficiency. (a) The modeled spectra for the Monte Carlo ray-trace model, showing a measured CdSe/CdS quantum dot spectra and the photodiode response curve against the irradiance (AM1.5g). (b) An illustration of how we arrange the cells within the LSC unit cell waveguide. For ease of illustration, we arrange the vertically aligned cells (top LSC) and planar aligned cells (bottom LSC) in different waveguides. A single simulation uses a single LSC waveguide with the specified cell orientation. (c),(d) Optical efficiency results for varied cell orientations with respect to the optical density taken at 450nm or unit cell geometric gain, respectively.

top orientation converges to the other planar cases.

With this analysis of the geometrical form factor of the collecting photovoltaic cell within the LSC unit cell, we find strong evidence that suggests planar cells outperform their vertical cell counterparts. This also suggests that photoluminescence collection within the LSC waveguide does not occur isotropically—as we should expect given the escape cone loss. This conclusion implies that we cannot simply treat the waveguide as a photon gas. Armed with this study, we can now turn our attention to fabricating high efficiency LSC devices employing planar cell orientation.

3.4 Solid-State, Single Junction LSC Devices

In order to quantify the current material constraints in achieving a high performance single junction LSC, we fabricate a fully polymerized, solid-state luminescent waveguide with a planar photovoltaic unit cell. To emulate periodic boundary conditions—and therefore an infinite array of cells—we herein place our LSC module within a diffuse trench reflector as discussed and shown in Appendix H. Figure 3.16 schematically depicts the prototype structure, LSC constituents, diffuse trench reflector, and process of fabrication and assembly. We can further measure the spectral characteristics for each of the LSC components (i.e., GaAs external quantum efficiency, $CuInS_2$/ZnS quantum dot absorption/photoluminescence) as well as the angle-averaged reflectance of the trench, where Figures 3.16(3b),(5a),(6a) gives each measured spectra, respectively.

3.4.1 Single Junction Fabrication Procedure

Among many choices of luminophores (as shown for example in Figure 1.10), here we employ a core/shell, $CuInS_2$/ZnS quantum dot. As seen in Figure 3.16(5a), the luminophore absorption extends up to approximately 700nm incident light and exhibits a large Stokes shift at 800nm center wavelength emission. Given these spectral features, a GaAs cell (electronic bandgap of approximately 900nm) matches well to the photoluminescence behavior. We commercially order the $CuInS_2$/ZnS quantum dots (UbiQD Inc.) and collaborate with the staff scientists in order to disperse these dots within a poly(lauryl methacrylate) waveguide layer of approximately 2mm in thickness.

At UbiQD, the waveguide samples are prepared using a cast-in place, capillary injection method in which we introduce a liquid resin between two glass waveguides and polymerize to create a laminate. In the absence of spacers that set the interlayer thickness, a custom-built scaffold is used to suspend and align the top waveguide directly above the bottom, with the entire luminescent layer. We inject resin manually with a syringe and needle to fill the volume between the glass substrate and superstrate, where we cure the resin for 30 mins under a 403nm source (LEDSupply). Glass layers consist of low iron, optical Schott B270i glass (Edmund Optics). We prepare the liquid resin according to the method described in Bergren et al.[144]. We optically characterize the quantum dots within the luminescent waveguide using a commercial absorption spectrometer (Cary 8454) and custom built near infrared emission spectrometer equipped with a 640nm laser (Coherent Cube), an InGaAs photodiode detector (Thorlabs PDF10C), and a lock-in amplifier (Stanford Research Systems SR830 DSP)[144].

Through collaboration with researchers at the National Renewable Energy Laboratory, we grow n-on-p upright GaAs homojunction solar cells by atmospheric pressure organometallic vapor phase epitaxy at 650°C. The Zn-doped absorber layer was approximately 2.5μm thick and the Se-doped emitter layer was 100nm thick. Nearly lattice-matched p-GaInP was used as a back-surface-field while a 25nm-thick

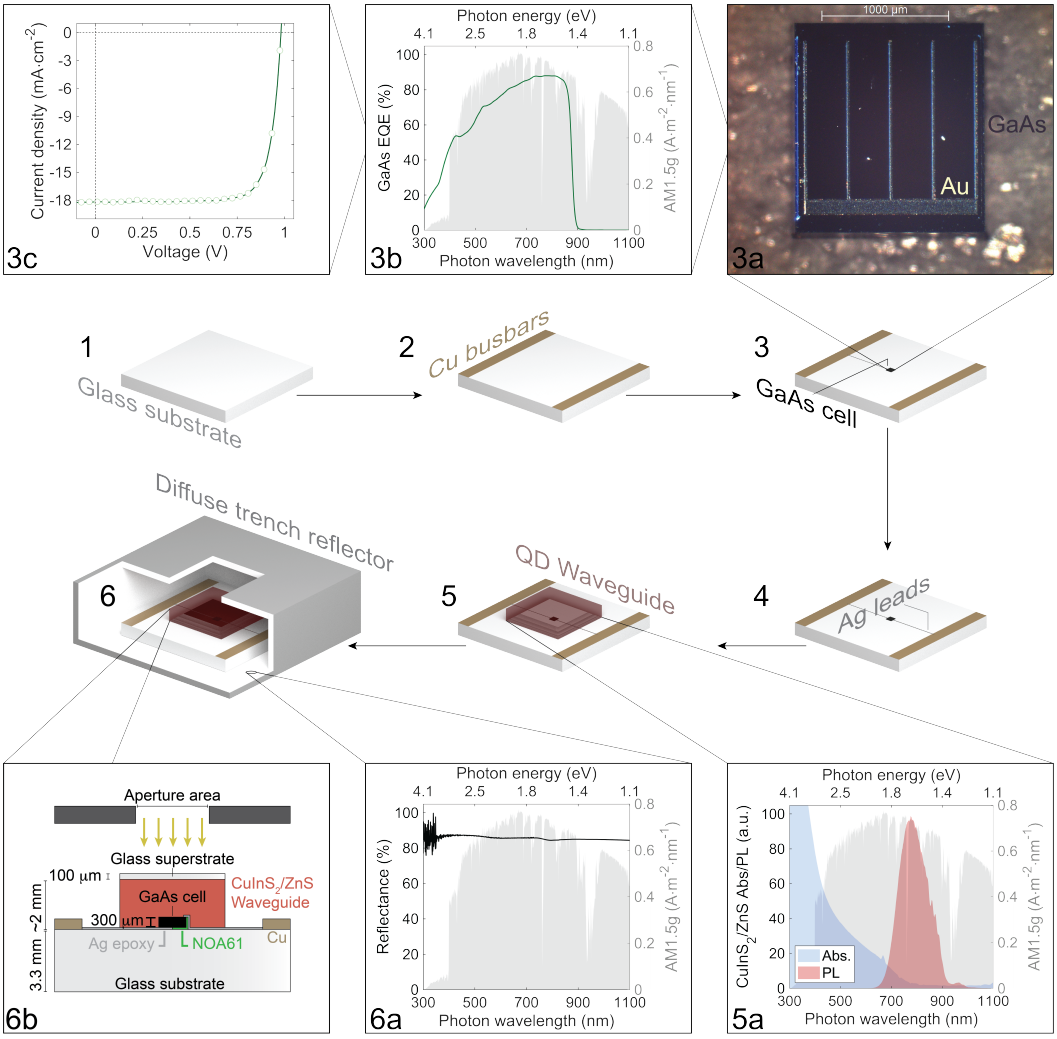

Figure 3.16: The single junction LSC device fabrication process. Starting with: a glass substrate of 2.5cm x 2.5cm area and 3.3mm thickness (1), adhering Cu tape busbars to either side of the glass for electrical power collection (2), anchoring GaAs minicell (1.4mm x 1.4mm x 300μm) to the glass with Ag backside epoxy (3)—where 3a,b,c show an optical microscope image, the measured GaAs external quantum efficiency, and the cell area-normalized JV curve under 1-sun AM1.5g illumination, respectively—attaching Ag epoxy leads and side wall insulation (4), depositing a thick $CuInS_2$/ZnS core/shell quantum dot waveguide (5)—where 5a gives the measured absorption and photoluminescence of the luminophores in powder form—and placement of the LSC device within a diffuse trench reflector to emulate a periodic array of the LSC component for a two-dimensional grid array (6)—where 6b gives a side-view cartoon of the device structure and thicknesses of each layer as well as demonstrating the variable aperture area over the LSC waveguide.

Se-doped AlInP layer served a passivating window. Electroplated gold on the GaAs substrate formed the back contact. Front Pd/Ge/Ti/Pd/Al grids were defined by standard photolithography, deposited using e-beam evaporation, annealed at 120-140°C, and mesa isolated to form 0.02 cm^2 square devices. 80nm of ZnS deposited by thermal evaporation was used as an antireflective coating between the GaAs and the LSC waveguide.. Appendix E details the precise geometry of the mesa etch,

metallization, and anti-reflection coating mask set. Upon deposition of the final layer (anti-reflection), we send the full wafer to be diced by a commercial vendor with an automated dicing scribe tool (American Precision Dicing Inc.).

In order to create an electrically interconnected co-planar cell, we mount the diced 1.4mm x 1.4mm GaAs cells onto glass substrates. We apply copper tape to either side of the glass, shown in Figure 3.16, to act as larger busbars for four-point probe measurements. We apply a thin line of silver epoxy (Creative Materials 114-41) from the center of the glass substrate to the copper busbar, place the GaAs cell onto this thin layer of epoxy (several microns thick), and cure the epoxy in place under 165°C for 45 mins. After curing, we electrically insulate the edges of the GaAs cell with Norland Optical Adhesive (NOA61) in order to prevent shunting and shorting across the heterojunction. We then cure the adhesive under 10 mins of 403nm UV illumination (LEDSupply). Next, we apply a thin line of silver epoxy to the top contact busbar of the minicell out to the opposite copper pad and cure again at 165°C for 45 mins. Figure 3.16 shows the entire cell mounting and interconnection process.

Described in section 3.3 and highlighted in Figure 3.14, the co-planar LSC design holds a distinct advantage over its edge lined counterpart: cells can be placed in repeating unit grids throughout the waveguide substrate, effectively establishing a fixed geometric gain regardless of overall LSC lateral size. Given our engineering limitations in the laboratory, constructing printed minicells in series and parallel over large distances for hundreds of cells requires use of pick-and-place automation and screen-printing technology. Instead, we place the entire LSC module within a diffuse trench reflector as shown in Figure 3.16(6). We custom fabricate the diffuse trench reflector out of aluminum stock material and mill the pieces to the appropriate dimension. Appendix H gives the dimensions and fabrication process for the trench. Matching the area of our glass substrates, we cut a 2.5cm x 2.5cm window within the top half of the aluminum trench in order to allow incident light through to reach the LSC. We sand blast the interior aluminum faces and apply (air gun) barium sulfate paint in excess of 30 layers in order to achieve high reflectance. Figure 3.16(6a) displays the measured spectrum of the trench interior.

3.4.2 Single Junction Results and Analysis

Figure 3.17(a) provides the current density response to varying voltage biases of the device under an aperture corresponding to a relatively small geometric gain of 1.6. We measure the luminophore PLQY at 87% when dispersed in the poly(lauryl methacrylate) waveguide layer at an optical density of 0.88 measured at a reference wavelength of 450nm. At the low geometric gain of 1.6, the LSC achieves approximately 9.86% power conversion efficiency under an AM1.5g solar simulator lamp measured at approximately 83 mW per cm^2 of input power.

Figure 3.17(b) shows the effect of varying geometric gain (performed via an iris aperture directly atop the diffuse trench reflector window) on power conversion efficiency. We observe clear matching between our model and measured data for all

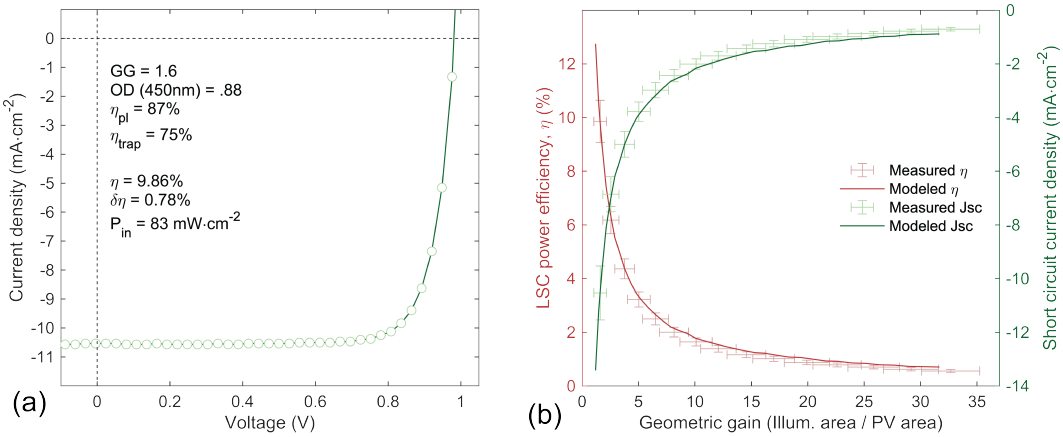

Figure 3.17: For a planar luminescent solar concentrator employing the components detailed in subsection 3.4.1, (a) gives the maximum measured power conversion efficiency, current-voltage analysis at a geometric gain (GG) of 1.6 and measured optical characteristics. (b) Describes the effect of illuminated geometric gain on measured device power conversion efficiency (red bars) and short circuit current density (green bars) against the predicted performance via the Monte Carlo ray-trace model (red/green lines).

geometric gains, within error—the uncertainty given due to the error in measurement of the illumination aperture, cell area, and irradiance given our reference cell, as detailed in Appendix I. As predicted, power conversion efficiency decreases monotonically with increasing geometric gain. This important result clarifies the value of a luminescent solar concentrator whose form factor decouples geometric gain from overall device area.

3.5 Passive/Active Concentrator Devices

Section 1.2 introduced the notion of light concentration, where we spoke clearly of two separate mechanisms. The first mode we discussed, passive concentration, occurs for systems in which the energy of incident light equals the energy of outgoing light. Through relating the total incident to output flux, we found that this method occurs only when we effectively restrict the acceptance angle of the incident ensemble of photons—otherwise we would be breaking the conservation of optical étendue. In contrast, the second mode of light concentration, active concentration, enables us to circumvent this passive conservation law by downshifting the trapped photon energy and, thereby, introduce non-concentrated thermal photons to the system.

Given this physical distinction, active and passive concentrators have historically been viewed as separate branches in optical devices. However, given the evidence we have seen in this thesis, both systems offer unique practical advantages to photovoltaic devices. For the case of the geometric concentrator, given the narrow solar disc half angle, photons that strike the device from this far-away light source can be directed to very small output collector areas at extremely high efficiency—described by Equation 1.10. Unlike the passive concentrator, the LSC can achieve angle-insensitive light concentration owing to its Stokes shift down-conversion. And while

the LSC can only absorb those photons at energies within the absorption region of its active luminophore species, a geometric concentrator remains agnostic to the incident photon energy.

With the complement of advantages between the luminescent (active) and geometric (passive) concentrator, we can design a hybridization of the two distinct concepts into a single device. Figure 3.18 illustrates the rendered and schematic view for such a concentrator. As seen, high energy incident light, irrespective of incidence angle, interacts strongly with the luminescent layer. Assuming high photoluminescence light trapping within the device, this high energy irradiance can be collected by the optically coupled photovoltaic cell. Concurrently, as low energy photons strike the concentrator at near normal incidence, their optical paths are very weakly perturbed by the luminescent layer; such photons can therefore interact with the geometric concentrator component and be focused on the photovoltaic according to the laws of ray-optics.

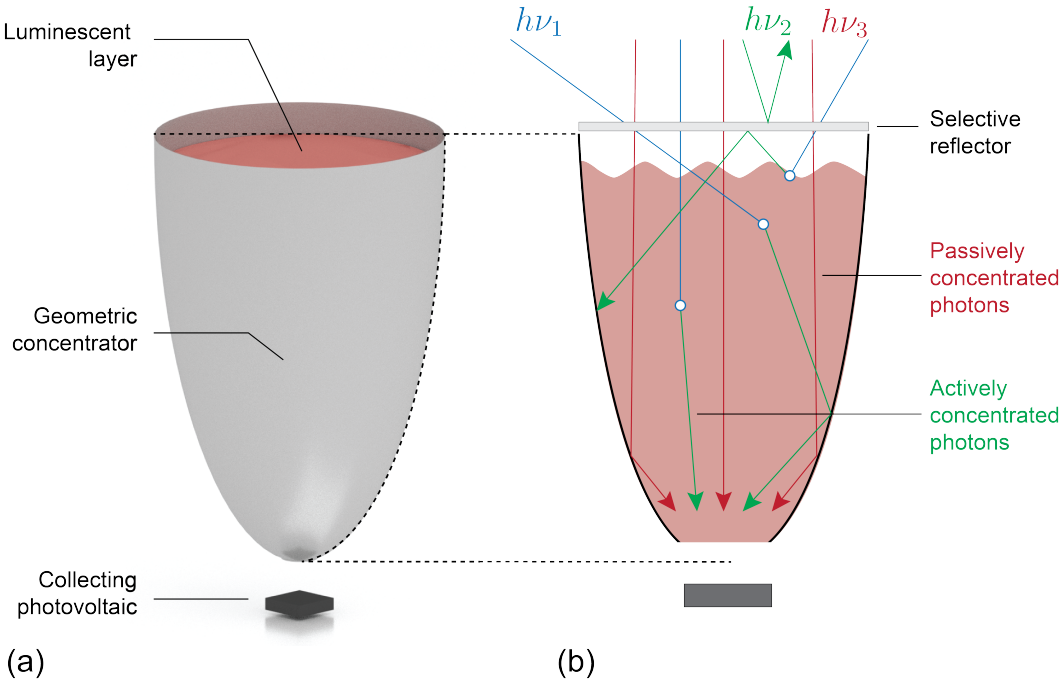

Figure 3.18: The concept for a hybrid passive/active photovoltaic concentrator. (a) The three-dimensional rendering for a compound parabolic concentrator structure that hosts a luminescent waveguide layer within its shell and couples the concentrated light onto a collecting cell. (b) The two-dimensional sketch view of this compound parabolic concentrator structure, where we specifically employ a selective reflector atop the module to trap photoluminesced photons within the concentrator. Here, $h\nu_1 > h\nu_2 > h\nu_3$.

3.5.1 Geometric Concentrator Fabrication

While Figure 3.18 displays a compound parabolic concentrator geometry as its passive component, as a proof of concept we employ a hemispherical shell reflector

design for ease of fabrication. Figure 3.19(b) shows the rendered shell reflector we use as the geometric concentrator. As illustrated, such a device concentrates incident illumination onto a center focal point given the curvature of the shell. Figures 3.19(b),(c) give the dimensions of the fabricated shell reflectors as well as the measured reflectance with respect to incident wavelength, respectively.

To construct this shell reflector, we first saw standard round-bottom vials with a 1.6cm diameter across and 4.4mm diameter depth. We next deposit a high reflectance silver layer via electron beam deposition mounted to a custom chuck holder shown in Figure 3.19(a). This chuck enables more uniform deposition over the shell reflector surface and, therefore, more uniform growth and a higher reflectance. We custom fabricate this chuck holder out of aluminum stock by lathing and milling.

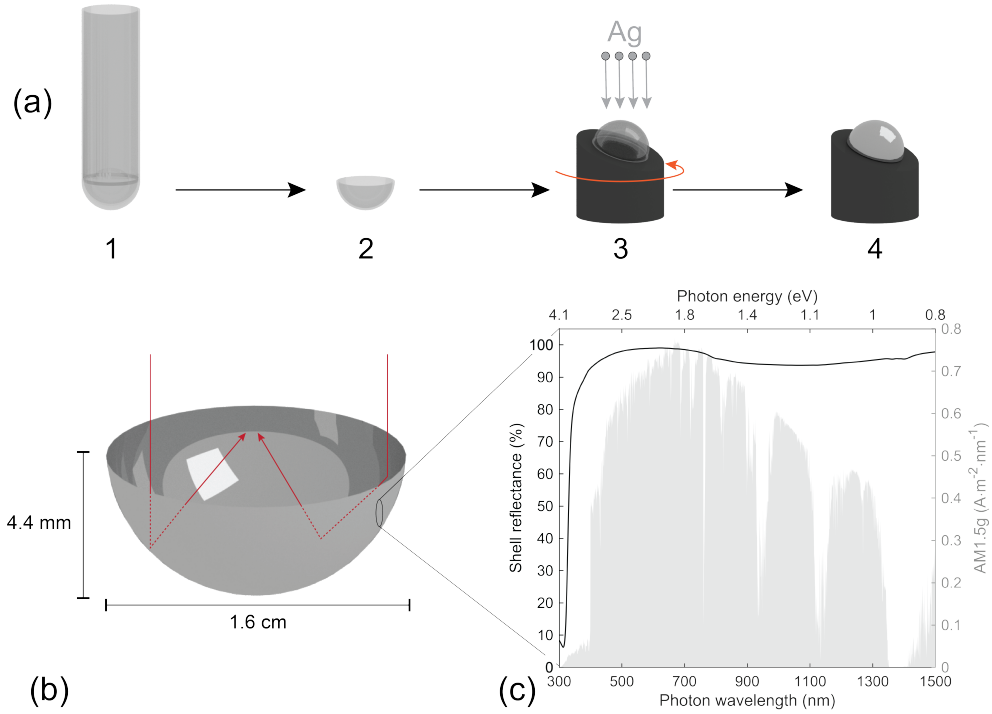

Figure 3.19: (a) The fabrication process for the geometric concentrator component. We begin with a glass vial (1), cut the rounded bottom with a glass saw (2), mount onto an angled check and electron beam deposit about 300nm of silver (Ag) uniformly onto the surface (3), and then remove the hemisphere from the chuck (4). (b) A rendered schematic of the hemispherical reflector serving as a geometric concentrator where, as shown in red arrows, incident photons near normal incidence reflect to the top center of the shell. (c) The measured specular reflectance of the silver-coated hemisphere (black, left y-axis) across the incident AM1.5g spectrum (gray, right y-axis).

3.5.2 Liquid Waveguide Layer Integration

In tandem with the geometric concentrator component (in this study, a hemispherical shell reflector), we disperse a luminophore solution into the shell in order to

absorb and actively concentrate a portion of the irradiance. The architecture of this design, shown in Figure 3.18, affords us the ability to apply a liquid waveguide layer—rather than a polymer-based layer as for typical LSC designs (3.4). Such a liquid-based luminescent component leverages several advantages both in fabrication and operation: *(i)* a single hemispherical shell can be reused for a variety of luminophore types and optical density loading in solution (given we can pipette in/out the luminophore waveguide), *(ii)* as shown by previous work[145], the PLQY of quantum dot luminophores decreases upon polymerization owing to clumping of nearby dots, and *(iii)* the luminophores (in this case various types of quantum dots) that we disperse within a solvent (toluene) can be reused for different shell reflectors or geometric optics components.

For square or rectangular LSC waveguide layers of uniform thickness with respect to the top surface normal (e.g., $+\hat{z}$ direction as shown in Figure 2.3), we indirectly measure the concentration of luminophores dispersed with the (typically polymer) waveguide via the optical density at some reference photon wavelength. Given that the optical density is a measure of the transmittance though a single-pass of the luminescent waveguide, per the Beer-Lambert absorption law given by Equation 2.1, we must be careful with how we apply this parameter to such a hemispherical shell hybrid concentrator device. Namely, given that the shell depth changes in the $+\hat{z}$ direction, we can only define the optical density as it pertains to the hemisphere center—that is, a thickness equaling the shell radius.

Figure 3.20 shows three different types of quantum dot absorption and photoluminescence patterns we can dissolve in three different hybrid concentrator designs. We obtain commercial $CuInS_2$/ZnS in powder form (UbiQD) with measured PLQYs greater than 94% in solution. We also can disperse two other core/shell structures to illustrate the impact that the choice of luminophore has on the concentrator performance, where we collaborate with the Nuzzo Research group at University of Illinois at Urbana Champaign to acquire solutions of CdSe/CdS and InAs/InP/ZnS. In addition, Figure 3.20(b) shows an example of how we determine the optical density per unit length (mm shell depth) with respect to the net quantum dot mass (mg of dots) per solution volume (mL of toluene). We apply an exponential fit to the measured reference points given the Beer-Lambert law.

3.5.3 Full Device Assembly and Analysis

With the hemispherical shell reflector and the luminescent solution, we can quantify the optical and power performance of the full active/passive photovoltaic concentration device. Figure 3.21 illustrates the experimental setup we employ, where (a) and (b) depict the simplified sketches of the system. With this testing apparatus, we can analyze the concentration factor (1.13), power conversion efficiency, and the device response with respect to angle of incidence—where we can measure the bare shell reflector case as a baseline for the geometric concentrator.

For this work, we focus exclusively on the high radiative efficiency $CuInS_2$/ZnS quantum dot luminophore liquid waveguide layer devices, owing to their large spec-

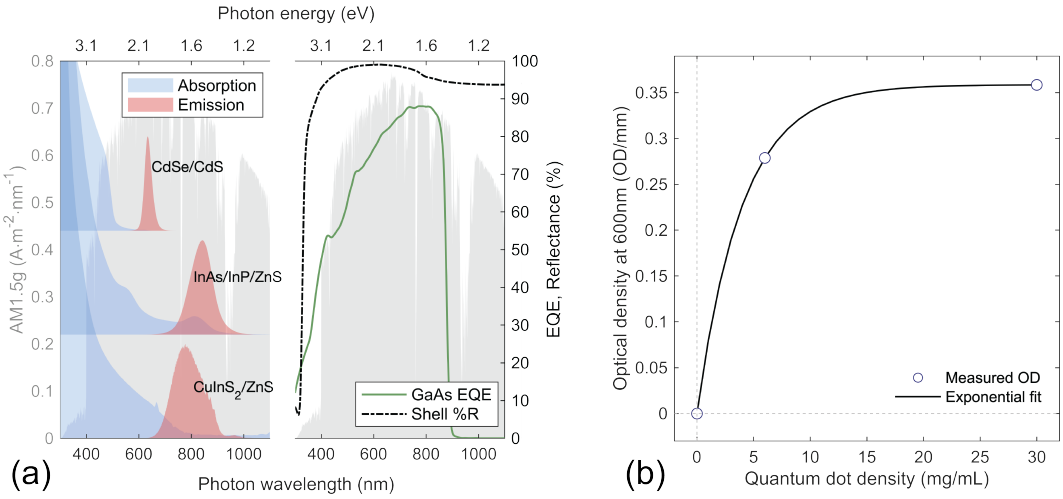

Figure 3.20: The analysis of example quantum dot luminophore systems integrable into the hybrid active/passive photovoltaic concentrator device. (a) Spectral measurements of the absorption/emission pattern for *(i)* core/shell CdSe/CdS, *(ii)* core/shell/shell InAs/InP/ZnS, and *(iii)* core/shell $CuInS_2$/ZnS quantum dot structures. We include the collecting GaAs photovoltaic cell (1.4mm x 1.4mm in active area) and hemispherical shell angle average reflectance with respect to photon wavelength. (b) An example calculation to determine the optical density (at 600nm) of the $CuInS_2$/ZnS quantum dots with respect to the amount of material within solution.

tral coverage and ideal alignment to the GaAs electronic bandgap (approximately 900nm). As shown in Figure 3.22, we quantify the concentration factor with respect to three, separate illumination conditions. In the short-pass case, we apply a blue filter atop the entire device setup—transmittance given by 3.22(b,top). We calculate the concentration factor given the short-circuit current density of the full device with respect to illumination condition 3.22(a,bottom) divided by the reference case 3.22(a,top) where we illuminate an upright GaAs cell given the illumination condition.

Since we supply a high optical density of approximately 0.70 at 600nm within the shell reflector, this illumination condition gives approximately the light concentration owing to the active component. Alternatively, we can allow full AM1.5g 1-sun illumination (100mW$\cdot$ cm^{-2}) to impinge upon our device, and we can further quantify the impact that a photoluminescence trapping filter has on concentration. Figure 3.22(a) shows the results for this case (red) and (b,bottom) the corresponding reflectance curve for the distributed Bragg reflector (Edmund Optics) placed in direct optical contact with the glass superstrate. For 3.22(b), we measure the reflectance with a Cary UV-Vis spectrometer and calibrate the instrument using a NIST-issued specular reflector with known reflectance.

As seen in Figure 3.22(a), we achieve a maximum concentrator factor of 11. For the case of the short-pass and photoluminescence trapping filter, insignificant amounts of incident lower energy photons are blocked by either layer. Thus, in these two cases, concentration results primarily due to the active luminescent waveguide layer. However, as we observe for the case of no-filter under 1-sun, the resulting

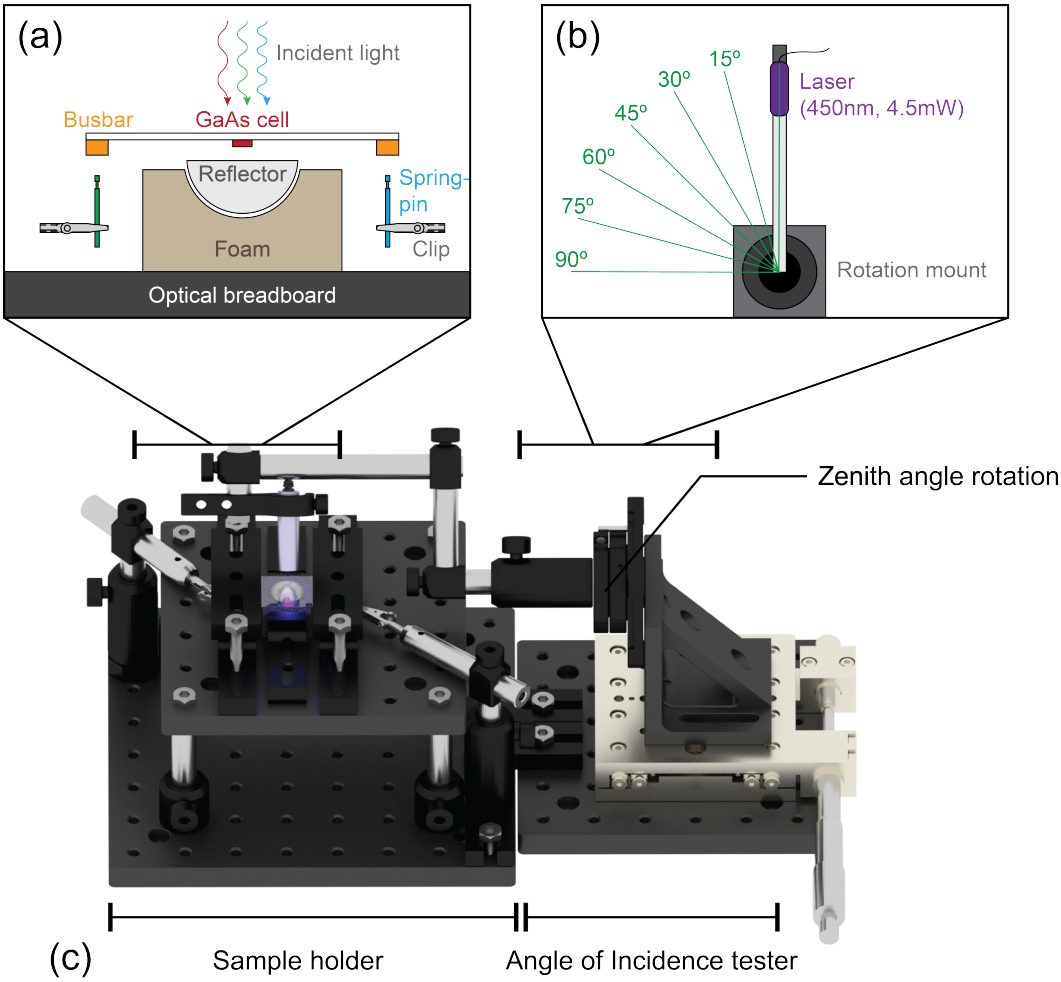

Figure 3.21: The testing setup for a hemispherical active/passive hybrid photovoltaic concentrator. (a) A simplified two-dimensional cartoon of the sample holder. We mount the hemispherical reflector onto a compressible foam cutout. The GaAs cell superstrate (inverted on glass) is held into optical contact with the reflector/liquid luminescent layer by external clamps, and the device busbars press into electrical contact with spring-pin leads held in place by mechanical clips. The entire holder is mounted onto an optical breadboard. (b) The angle of incidence tester in two-dimensions showing the variation of zenith angles with a mounted laser of 450nm, 4.5mW. (c) The full three-dimensional rendering of the sample holder and angle of incidence testing.

concentration factor increases by only 10% relative to the distributed Bragg reflector case. This finding suggests the need for optimization of the geometric concentrator component. For example, the compound parabolic design shown in Figure 3.18 could issue significantly higher factors.

In addition to varying the illumination conditions of the hybrid concentrator device, we can also adjust the optical density of luminophores with the toluene solution in order to gradually transition the concentrator from passive (geometric) to active (luminescent). For an optical density of zero, we regain our geometric concentrator design. We test six different optical density solutions (when measured at the reference wavelength, $\lambda_0 = 600$nm, for the shell radius) and measure the current-

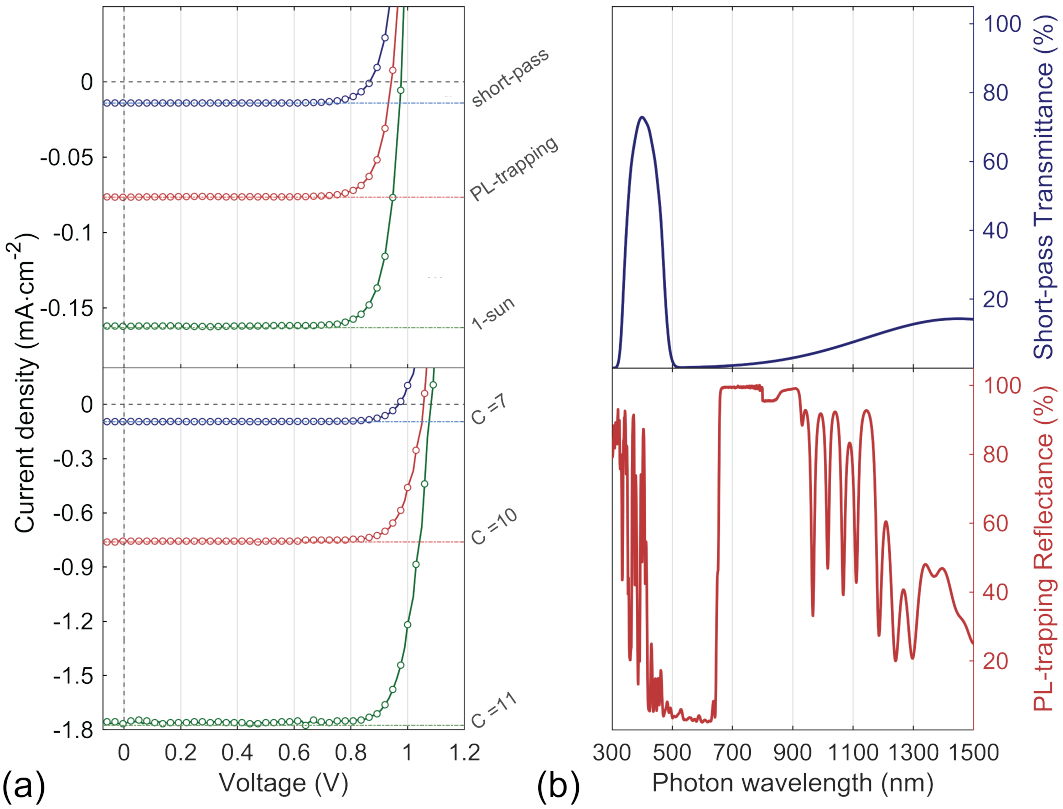

Figure 3.22: The concentration factor results for a hybrid passive/active photovoltaic concentrator. (a) The reference (top) and measured (bottom) current density, voltage plots for varying illumination condition. (b) The measured transmittance (top) and reflectance (bottom) for the short-pass filter and distributed Bragg reflector, respectively.

voltage characteristics. Figures 3.23(a)–(d) show the power conversion efficiency performance of the device with respect to the optical density.

From Figure 3.23, we observe that the power conversion efficiency monotonically decreases for increasing optical density. This result, however, aligns with our intuition from previous results. Namely, that for photoluminescence trapping efficiencies near the total internal reflection limit, overall power conversion efficiency decreases with increasing optical density owing to multiple luminophore re-absorption events (such as in Figure 3.7). However, as is the case for rectangular slab LSC waveguides, we expect to observe increased device performance for near-unity trapping efficiencies.

The hypothesized ability for such a hybrid concentrator to operate in both direct and diffuse (i.e., off-normal angles of incidence) irradiance conditions underlines one of the key motivations. As such, we aim to unveil whether or not such a device outperforms its geometric concentrator counterpart and, if so, to quantify that difference with respect to angle of incidence. Shown in Figure 3.21, we build a zenith angle rotating illumination source in order to determine the difference of performance relative to the normal incidence case.

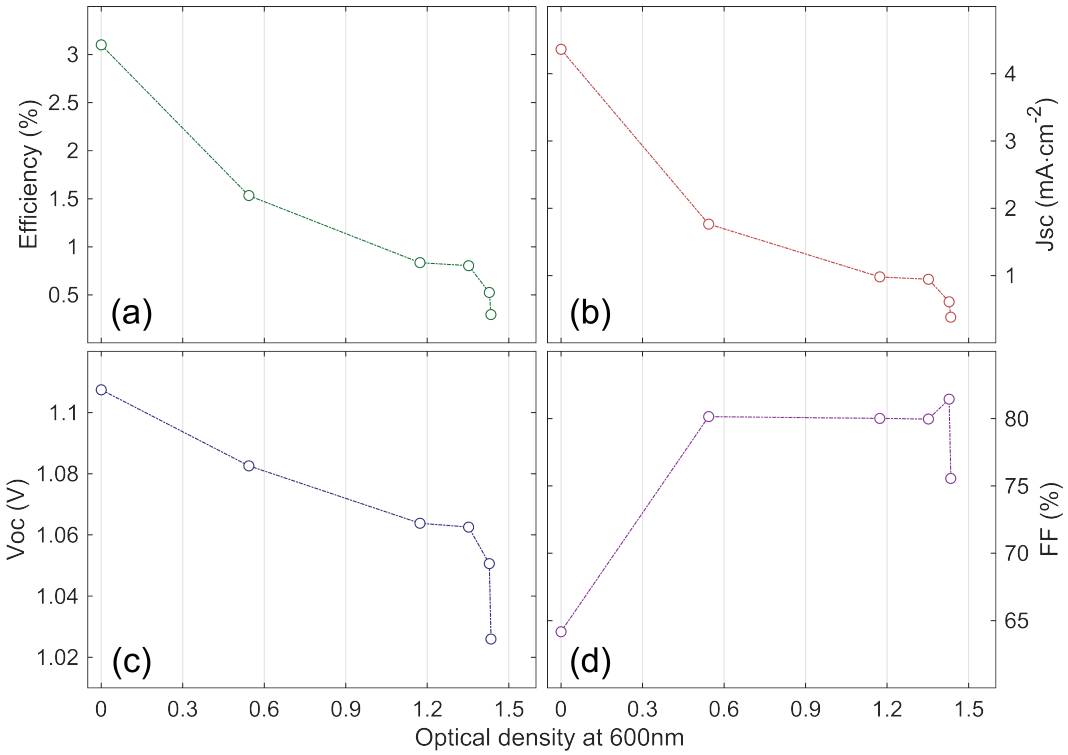

Figure 3.23: The passive/active concentrator device performance for AM1.5g, 1-sun illumination and no additional photoluminescence trapping layers, showing the (a) overall power conversion efficiency, (b) short circuit current density (Jsc), (c) open-circuit voltage (Voc), and (d) fill factor.

Here, we evaluate the power conversion efficiency performance, again relative to an incident angle of zero degrees to the surface normal. Figure 3.24(a) shows the device response for the cases of a bare (no luminescent waveguide) shell reflector and one with an optical density of 0.50. As expected, the geometric concentrator case exhibits a strictly decreasing performance relative to normal incidence photons—matching well to the concentration factor response given by Equation 1.10. In contrast, for the case of the hybrid concentrator, we find a non-intuitive response curve given the angle of incidence. While more precise modeling is needed in order to fully understand the non-trivial device behavior, from a qualitative perspective, off-normal photons that strike the luminescent layer observe a larger travel distance—thereby issuing varied probabilities of absorption and photoluminescence. As this travel distance through the waveguide changes, we should expect to see varying amount of active concentration, shown by the cartoon in Figure 3.24(b). This hypothesis could help to explain the response we observe.

3.6 Single Junction LSC Device Outlook

Here we have closely quantified the performance limits, device trade-offs, and experimental characterization methods for the single junction LSC. In our efforts to

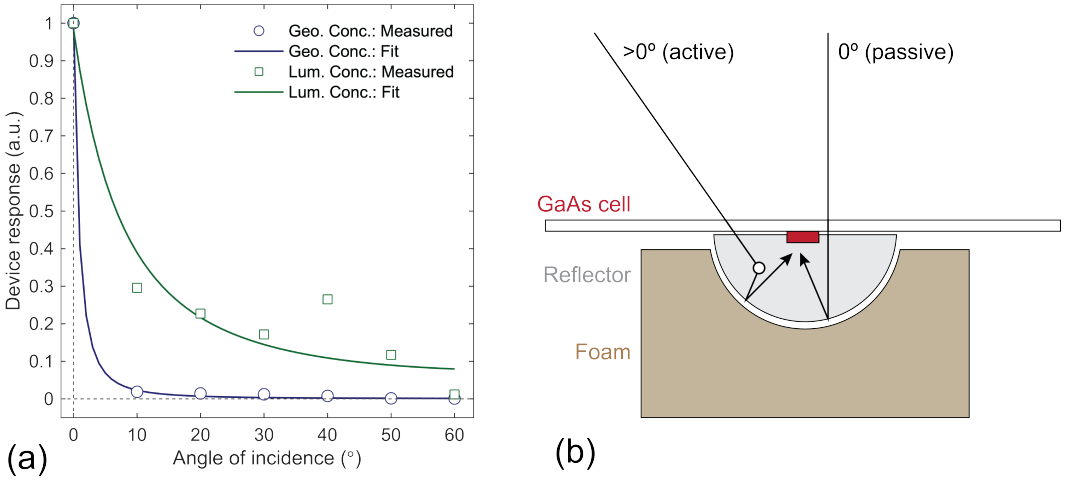

Figure 3.24: (a) The relative power conversion efficiency (device response) of a hybrid active/passive photovoltaic concentrator with respect to the angle of incidence for a 450nm, 4.5mW laser. We include approximate fit responses given the $\sin^{-2}$ curve. (b) An illustration of two possible ray-optical pathways for incident photons where: *(i)* the first strikes at normal incidence and is collected by the GaAs cell via geometric concentration, and *(ii)* the second strikes at off-normal angles and, consequently, exhibit longer travel lengths within the waveguide layer.

unveil a path toward high power conversion efficiency concentrators, we first developed an analytical expression of the dark radiative current term in order to derive a comprehensive theory of LSC open-circuit voltage behavior. We next found the detailed balance limits for a general single junction LSC by varying the electronic bandgap of both the collecting photovoltaic and emitting luminophore. Through our analysis, we determined the photoluminescence trapping efficiency to be among the most influential parameters in achieving high performance—therefore exploring the concept of embedding anisotropic luminophore emitters within the waveguide for increased trapping. To further validate our detailed balance model as well as attempt for a high performance LSC device, we fabricated a single-junction module with $CuInS_2/ZnS$ quantum dot luminophores that reached efficiencies near 10%. Finally, we provided a first-look into a novel concentrator design that joins passive and active components into one device, where we quantified the concentrator performance with respect to optical density and angle of incidence.

As discussed in chapter 1, an emerging area of photovoltaic technology blends the power generation component into building façades for markedly lowered balance of system and soft costs. In this next chapter, we will analyze how LSC devices apply to building-integrated photovoltaic modules and, moreover, the technoeconomic limits that such devices can achieve in this form factor.

CHAPTER 4

Single Junction, Building Integrated LSC Devices

As introduced in chapter 1 and shown qualitatively in Figure 1.7, recent technoeconomic progress in silicon photovoltaic cells has shifted the dominant cost mechanisms away from cell processing and toward installation, hardware, and other soft costs[146,147]. As this cost landscape continues to evolve over time, new methods for markedly lower system costs could surface and, as such, progress photovoltaic technology in myriad directions. One method for reducing system costs blends solar cells directly into building components—that is, building-integrated photovoltaic devices.

In the late 1970s, various initiatives worldwide began to evaluate the potential to integrate photovoltaic devices directly into distributed (i.e., on-site) generation for buildings both residential and commercial[148]. As part of this effort, research and development teams worked to catalyze market deployment for modules blended into form factors such as rooftop shingles, building curtain wall, and semitransparent windows among others. While rooftop photovoltaic systems for residential settings continue to increase in generation capacity[149], commercial high-rise building sidewall surface area offers more than double the total rooftop areas. However, despite this tremendous potential, current building integrated photovoltaic deployment remains vastly underutilized[150,151].

Given this disparity between area availability and building integrated photovoltaic implementation, as well as the recent shift in silicon technoeconomics, Figure 4.1 overviews several power-generating technology intended for partially transparent façade applications. Unlike conventional utility photovoltaic modules, building integrated window designs must respond to aesthetic requirements (e.g., color, average visible light transparency, image clarity) in addition to power production. Consequently, a variety of technologies have been developed over the past several decades to comply with these constraints. Given that a portion of visible light must pass through the window to reach the building occupant(s), a reduced spectrum of light is usable for power conversion. As a result of this reduced amount of usable light, the power production of the device is limited, creating an inherent trade-off between window transparency and power conversion efficiency. Figure 4.1(a) depicts photovoltaic power generation by light absorption and electron-hole pair generation at

the inside surface of the exterior glass pane.

While building integrated photovoltaic windows share a common feature of incident sunlight to electrical power conversion in semi-transparent modules, the underlying generation mechanisms vary, as shown in Figures 4.1(b)-(e). Among others, organic photovoltaic[152–154], luminescent solar concentrator, thin-film[155–160], and perovskite[161–166] all enable partial light absorption and have been researched for power-generating window applications. Figures 4.1(b)-(e) illustrate typical components found for thin film structures for each of these technologies.

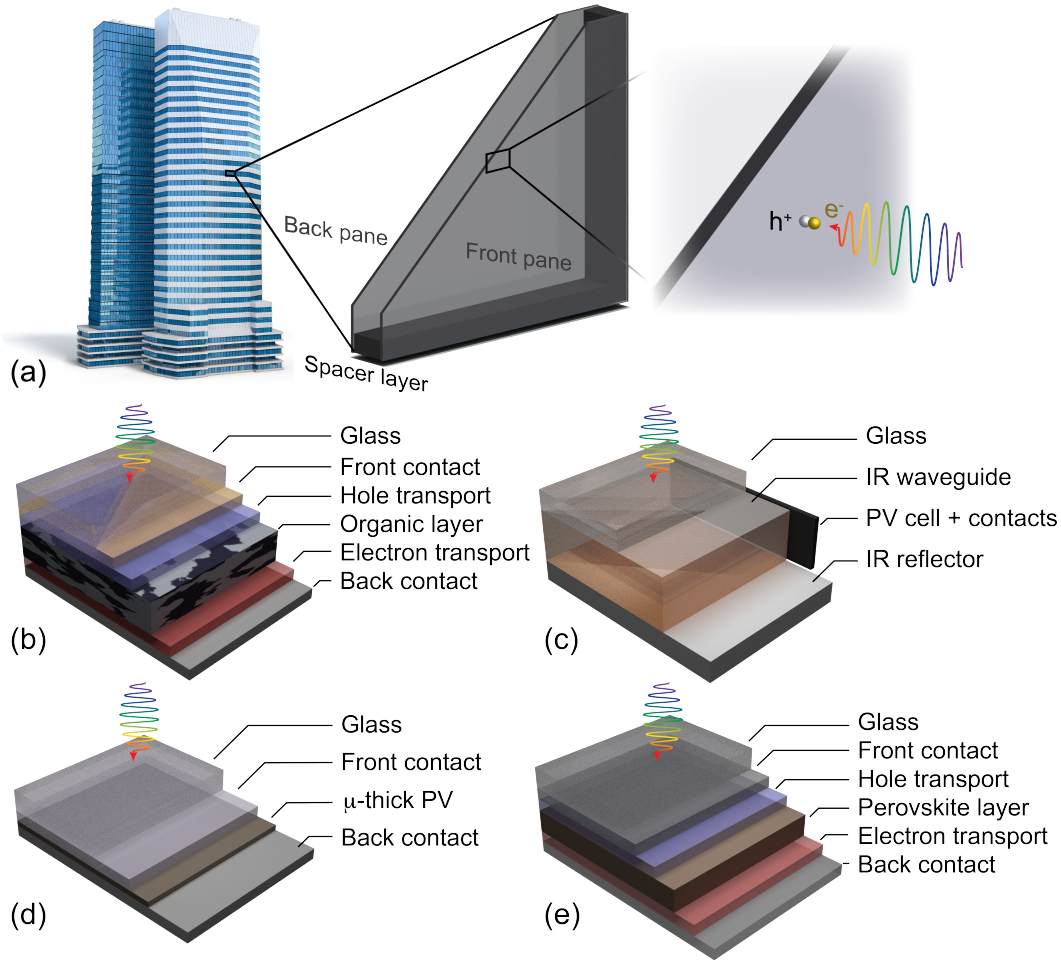

Figure 4.1: An overview of various photovoltaic generation devices and their respective structures for a building integrated window insulated glass unit. (a) An illustration of the structure for a double pane unit with the front layer containing the photovoltaic module—yielding a photogenerated exciton (h^+,e^-). (b), (c), (d), and (e) Renderings of four commonly-employed window devices including organic, LSC, thin-film, and perovskite structures, respectively. Adapted from Needell et al.[167].

While Figure 4.1(c) displays a traditional LSC form factor with an edge-lined photovoltaic orientation, from our discussion in chapter 3.3, we introduce a two-dimensional cell grid layout for a building-integrated photovoltaic application. With

this modified form factor, LSC window areas can scale to match current industry standards ($\mathcal{O}$(m)) without sacrificing power conversion efficiency. Figure 4.2(a) displays the conceptual rendering for an LSC window device employing this cell layout.

4.1 Blending Form with Functionality

As for the case of the terrestrial single junction LSC application, in order to quantify the performance limits for building integrated LSC windows, we assume an ideal absorption and photoluminescence spectra for the luminophore material based on type-B quantum dot heterojunctions within a poly(lauryl) methacrylate waveguide layer. We determine this optimal absorption bandgap from our analysis in section 3.1.

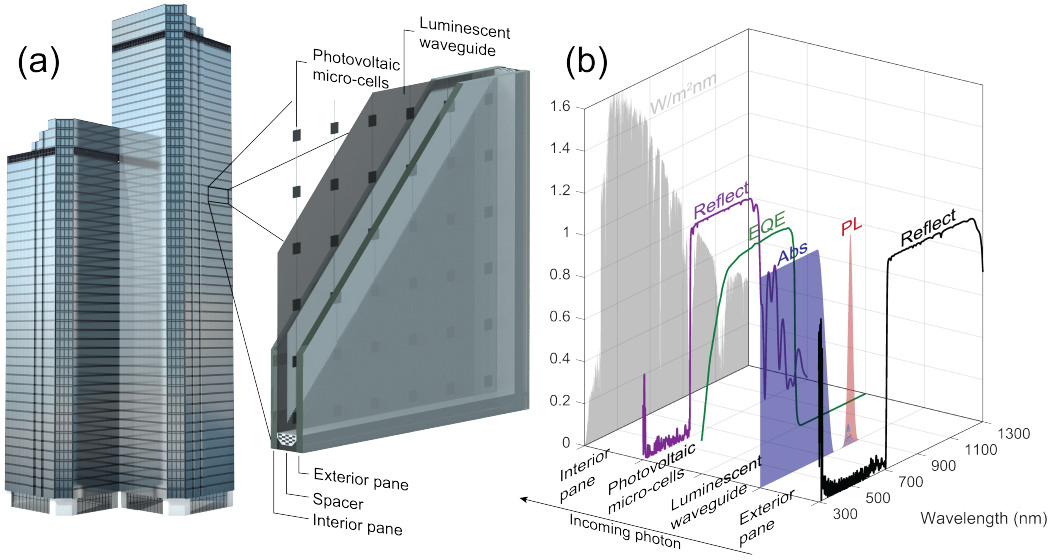

Figure 4.2: The three-dimensional rendering and spectral characteristics of an LSC power-generating window for building integrated photovoltaic applications. (a) The zoom-in on the planar grid structure of the photovoltaic micro-cells (columns in series connection) within the double pane insulated glass unit with a neutral color density luminescent waveguide. (b) The spectral breakdown of each component of the LSC window unit, where an incident photon first interacts with the exterior pane distributed Bragg reflector (black), then the luminescent waveguide absorption and photoluminescence features (blue and red, respectively), where photoluminesced photons can be collected by the planar GaAs micro-cells (green), and further trapped within the window unit by an interior (building-wise) glass pane coated with a distributed Bragg reflector (purple). The relevant AM1.5g irradiance measured in $\mathrm{W{\cdot}m^{-2}\cdot nm^{-1}}$ is shown in gray and projected on the back z-axis.

Figure 4.2(b) displays the broadband absorption and infrared emission spectra of a prototypical quantum dot, employing a Stokes shift of 170nm with an absorption band-edge located at approximately 700nm. As seen in the emission, the peak centers at approximately 870nm, where we assume a finite re-absorption band. To collect photoluminesced photons at this wavelength range, we model GaAs micro-solar cells, whose overall external quantum efficiency is shown in Figure 4.2(b).

We assume a short-pass, long-stop distributed Bragg reflector structure cladding the front and back of the window device, as shown in Figure 4.2(b). We model the photoluminescence-trapping layers via the OpenFilters™ optimization program, assuming 100 layers of alternating high/low refractive index material—where we assume TiO_2 and SiO_2 respectively.

In order to quantify the performance of the LSC window, we assume a less than 90° tilt angle for a southward oriented building at a geometry such that the full AM1.5g 1-sun irradiance strikes the top distributed Bragg reflector surface of the device at normal incidence[168]. Previous studies (e.g., Kuhn et al.[168]) provide more rigorous analyses of the irradiance fluctuations with respect to azimuthal orientation and module tilt for varying geographies. However, for a tilt angle less than 60° for a southward orientation, models indicate that the full irradiance saturates to the 1-sun limit.

We simulate the spectral and electrical behaviors of the optically coupled GaAs photovoltaic component. To model state-of-the-art performance, we employ a square-shaped 800μm x 800μm single junction GaAs heterojunction cell. We account for perimeter edge effects at such small cell sizes by specifying a recombination velocity of 1 x 10^6 cm/s along the device edges[169]. Figure 4.3(a) details the internal quantum efficiency and optical reflectance of the micro-solar cell used in this simulation. To quantify the open-circuit voltage, fill factor, and short-circuit current density characteristics with respect to the amount of sunlight concentration, we apply a Sentaurus program as a direct input into the Monte Carlo ray-trace solver as shown in Figure 4.3(b)—giving us the approximate cell electrical behavior for a continuous fit.

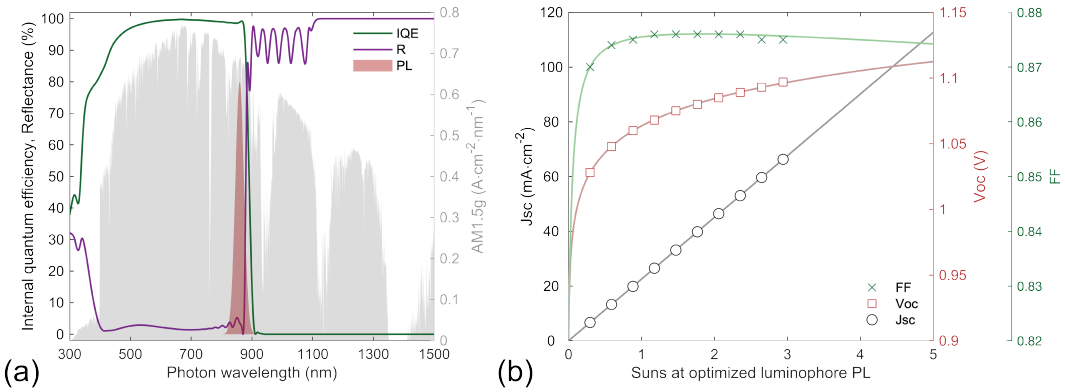

Figure 4.3: The spectral (a) and electrical (b) response of the GaAs 800μm x 800μm cell device. (a) The simulated internal quantum efficiency of photogenerated excitons and front-surface reflectance. We supply the modeled luminophore photoluminescence (PL) curve for reference along with the relevant AM1.5g spectrum. We note that the reflectance oscillations below the energy bandgap originate from the anti-reflection coating thin film interference. (b) The simulated electrical performance (short-circuit current density, open-circuit voltage, fill factor) of the GaAs cell under varying concentrations of the luminophore photoluminescence irradiance.

We design the square-shaped, 800μm x 800μm single junction GaAs micro-cells

with the following layered structure: p-type AlGaAs window (10nm, 4 x 10^{19} cm^{-3}), p-type GaAs emitter (60 nm, 4 x 10^{18} cm^{-3}), n-type GaAs base (1.5μm, 2 x 10^{17} cm^{-3}), n-type GaAs buffer (1.5μm, 1 x 10^{18} cm^{-3}), silver reflector (100nm)[170]. We further model a SiN_x coating (69nm) applied to the top and edges of the device for anti-reflection[171–173]. Given the area of the front surface of the micro-cell, we assume the top contacts to cover approximately 5% of the active area. Interfacial recombination velocity between the base and emitter was specified as 100 cm/s, and edge recombination velocity at the device edges was set to 1 x 10^6 cm/s (bulk lifetime 100ns). We apply the transfer-matrix method as the optical solver for calculating device external and internal quantum efficiency.

4.2 Luminophore Optimization for LSC Windows

With a scalable LSC form factor, we can now evaluate the effects of luminophore spectra on window power conversion efficiency and visual acuity. While we have developed previous analyses regarding the electrical performance of an LSC, here we assume an average visible transparency of 10% in order to appropriately blend into a commercial building insulated glass unit. However, unlike previous analyses, we must also consider the window aesthetics in addition to power generation. Given the importance of luminophore materials for LSC device performance and design, we develop a quantitative roadmap for achieving high power conversion and custom visual features.

4.2.1 Performance of Architectural LSCs

We begin with an analysis of the power conversion efficiency performance of an architectural LSC depicted in Figure 4.2. Here we co-vary the luminophore extinction coefficient (ε_{lum}, defined in Figure 1.10 as the ratio of initial absorption to photoluminescence re-absorption) alongside the luminophore PLQY for a full-width at half-maximum of approximately 50nm with a center at 870nm. Figure 4.4(a) demonstrates how we vary ε_{lum}, where (b) illustrates this effect on the overall power conversion efficiency of the LSC window module. We assume that, for any photon emitted by the luminophore that escapes into free space (interior or exterior the building), the photon is lost.

We can also co-vary the photoluminescence full-width at half-maximum in order to identify the ideal downshifting material characteristics for such a building integrated application. Figure 4.4(c) visualizes how we vary this emission width, whereby we assume an ideal extinction coefficient of 100. 4.4(d) quantifies the power conversion efficiency dependence on these two parameters. For all simulations here, we assume a modest geometric of 20 for the LSC waveguide and an optical density of unity at the absorption bandgap energy (approximately 700nm).

As expected we observe the steepest increase in power conversion efficiency for a low extinction coefficient and near-unity PLQY—owing to high likelihood of photo-

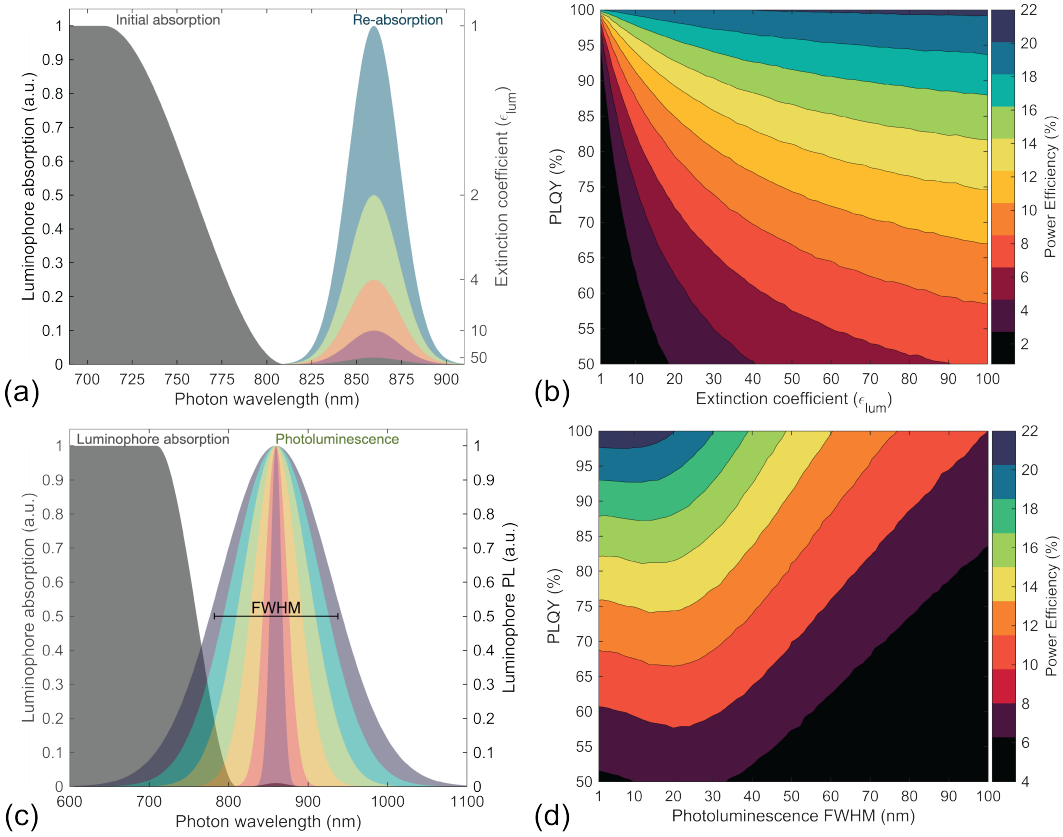

Figure 4.4: The impact of luminophore extinction coefficient (re-absorption) (a,b), photoluminescence full-width at half-maximum (FWHM) (c,d), and PLQY on the overall window power conversion efficiency. (a) The spectral shaping of luminophore re-absorption with respect to varying extinction factor. (b) The power conversion efficiency under 1-sun for varying extinction coefficient and PLQY. (c) The impact of FWHM on the spectral profile of the luminophore photoluminescence curve. (d) The power conversion efficiency for varying FWHM and PLQY.

luminesced photon absorption. As the re-absorption probability decreases (increasing extinction coefficient), the constraints on obtaining high PLQY values to allow high power conversion efficiencies decrease. In the best case, we find a power conversion efficiency beyond 22% at average visible transparencies of 10%. In contrast, for PLQYs below 100%, we find that there exists a global optimum photoluminescence full-width at half-maximum that lies between 15 and 30nm dependent upon PLQY. As the radiative efficiency nears unity, this optimal width decreases. At below unity PLQYs, modest luminescence widths yield lower likelihood in emission energies that coincide with the peak re-absorption. As the peak grows too large, however, the likelihood of emission into energies below the GaAs energy bandgap increases—thereby decreasing power conversion efficiency.

4.2.2 LSC Window Aesthetics

A key metric to evaluate the viability of a building integrated photovoltaic power window system is the visual transparency, acuity, and color tint of the module. To begin, we can characterize the average visible transparency by the spectrum of light that transmits through the LSC by the photopic response of the human eye, P_{eye}, and the incident solar photon flux (i.e., AM1.5g)[149]. Equation 4.1 details this average visible transparency (AVT) where we integrate over the wavelength (λ) of light:

$$\text{AVT} = \frac{\int T_{\text{lsc}}(\lambda) \cdot P_{\text{eye}}(\lambda) \cdot S(\lambda)\ \mathrm{d}\lambda}{\int P_{\text{eye}}(\lambda) \cdot S(\lambda)\ \mathrm{d}\lambda}, \tag{4.1}$$

where T_{lsc} is the spectrally resolved transmittance of the LSC (determined by the luminophore and photoluminescence-trapping layer) and S is the incident AM1.5g spectra.

While we can define the average visible transparency in order to enable inter-technological comparison, the visual acuity of the window lacks such a clear quantitative Figure of merit. Qualitatively, we define the visual acuity to be the clarity of transmitted images through the window—i.e., related to the scattering of incident light. Despite the tremendous importance that previous studies place on this window characteristic[31,143,174,175], quantifying this image clarity aesthetic still remains a challenge (e.g., certain studies refer to the haze of the window[144]). As a result, we print 800μm x 800μm cell patterns at a geometric gain of 20 onto 1m^2 square sheets of variable average visible transparency as shown Figures 4.5(a),(b). We further laminate this sheet onto a double pane insulated glass unit in order to capture the visible aesthetics of such an LSC-based module. We include three distinct transparencies at (a) 56 and 26% and (b) 28% and 26%, where only upon closer view can we identify the micro-cell grid.

The final Figure of merit regarding the aesthetic design concerns the color tinting of the window. Given the near-infrared photoluminescence and, consequently, infrared stop-band of the distributed Bragg reflectors, the luminophore absorption bandgap as well as the optical density within the waveguide affect the resulting color. We can quantify the color via the International Commission on Illumination (CIE) 1931 chromaticity color space diagram, whereby we apply the photopic response of the eye and the red-green-blue color spectrum to calculate the color space coordinates (x,y) of the transmitted light—the transmitted light modeled via the Monte Carlo ray-trace. Figure 4.5(c) demonstrates the effect of increased luminophore optical density (that is, average visible transparency) on the color coordinate. Figure 4.5(d) illustrates how artificially shifting the luminophore absorption bandgap (assuming a constant photoluminescence profile) alters the window hue.

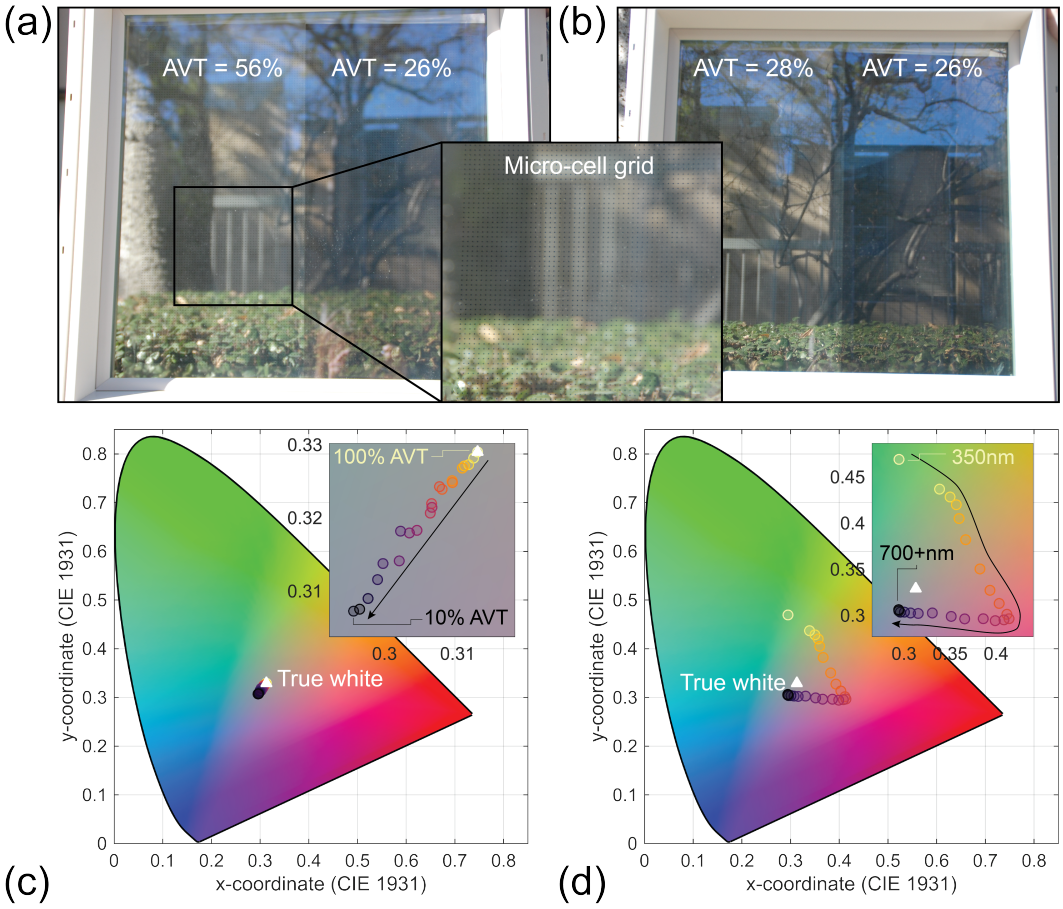

Figure 4.5: (a),(b) Laminate sheets composed of a two-dimensional grid of micro-cell pattern shapes at 800μm x 800μm at a geometric gain of 20. We vary the average visible transmittance of several laminates in order to qualitatively observe the difference in image acuity. (c) The impact of luminophore optical density of luminophores within the LSC waveguide on the (x,y) color coordinates. We observe, as optical density increases, shifting away from true white. (d) The color variability of an LSC module dependent upon the absorption bandgap of the luminophore, where we find a range of colors available in the CIE coordinate space.

4.3 Technoeconomics of Architectural LSC Windows

Beyond the aesthetic tunability of a photovoltaic window, the technoeconomic feasibility of building integrated devices indicates the likelihood of market adoption. As done in other studies for comparable energy generation technology[35,176–179], the cost per watt of generated electrical power enables a system-level comparison between various building integrated photovoltaic devices as well as other markets (e.g., utility or residential). While performance modeling like the Monte Carlo ray-trace can provide high accuracy estimations of overall power conversion efficiency under varying illumination conditions, developing a thorough technoeconomic model for a to-scale product remains a much more uncertain challenge. In order to develop such an analysis, we must therefore clearly state the assumptions and parameters of our model in addition to one possible realization of the roll-to-roll assembly line for an

LSC-based power generating insulated glass unit.

To begin, we must first understand the conceptual breakdown of costs associated with an LSC window production line. We can therefore categorize costs into two distinct categories: *(i)* capital expenditure (CapEx) and *(ii)* operating expenditure (OpEx). The former describes all costs associated with major purchases that will be used over a long period of time. We thereby can approximate CapEx as fixed, one time costs. The latter, OpEx, includes all expenses that require running the day-to-day operations of the production line. We therefore must first assume a certain size and production volume of windows per year (at a typical window size of 1m x 1.5m for example) in order to quantify the size of space and equipment that is needed (i.e., CapEx) and also the amount of goods, energy, and labor needed to deliver this throughput per day (i.e., OpEx). Table 4.1 defines the starting assumptions for this technoeconomic model.

Operating parameters	Value	Units
Production volume	500,000	Windows per year
Daily throughput	2,000	Windows per day
Operational days	250	Days per year
Operating Hours	8	Hours per day (in operation)
Maximum Allowed Line Utilization	85%	unitless
LSC geometric gain	*variable*	unitless
LSC optical density	*variable*	unitless

Table 4.1: The operating parameters we assume for a technoeconomic analysis of a large-scale LSC window production. We note that the geometric gain and optical density of the LSC remain independent variables that we will tune. The former impacts power conversion efficiency and the required amount of cell area per window, while the latter describes both the power conversion efficiency and average visible transparency as well as the volume of luminophores per window.

Given the overall parameters described in Table 4.1, we can now define the precise CapEx and OpEx needed in order to realize these production volume bounds. First, however, we must develop an understanding of the production process for a double pane, insulated (argon gas) glass unit employing an LSC component with a grid of micro-cell GaAs photovoltaic devices connected in series (column) and parallel (top/bottom row) as shown schematically in Figure 4.2(a).

To do so, we model a roll-to-roll process that consists of four sequential steps highlighted in Figure 4.6. To begin, we deposit onto the glass pane (front/exterior surface) high/low refractive index dielectric material in a large-scale sputterer—outfitted with TiO_2 and SiO_2 in alternating layers (4.6(1a)). Parallel to this coat-

ing process, we input wholesale GaAs heterojunction photovoltaic cells at large areas and dice these into the modeled 800μm x 800μm size via a laser cutting tool (4.6(1b)). We use a commercial pick-and-place tool to adhere and arrange the cells in a grid to the glass pane substrate, where we apply a screen printing tool (not shown) to use bump-bonding soldering to series interconnect the micro-cells (4.6(2)). We next deposit the quantum dot waveguide (with dots and monomer solution as material inputs) via a doctor blade tool equipped with an ultra-violet curing chamber (4.6(3)). Finally, we adhere the edges of the LSC-exterior pane with a spacer layer, in-fill with argon gas, and cap the structure with a glass pane superstrate to serve as the interior window pane (4.6(4)).

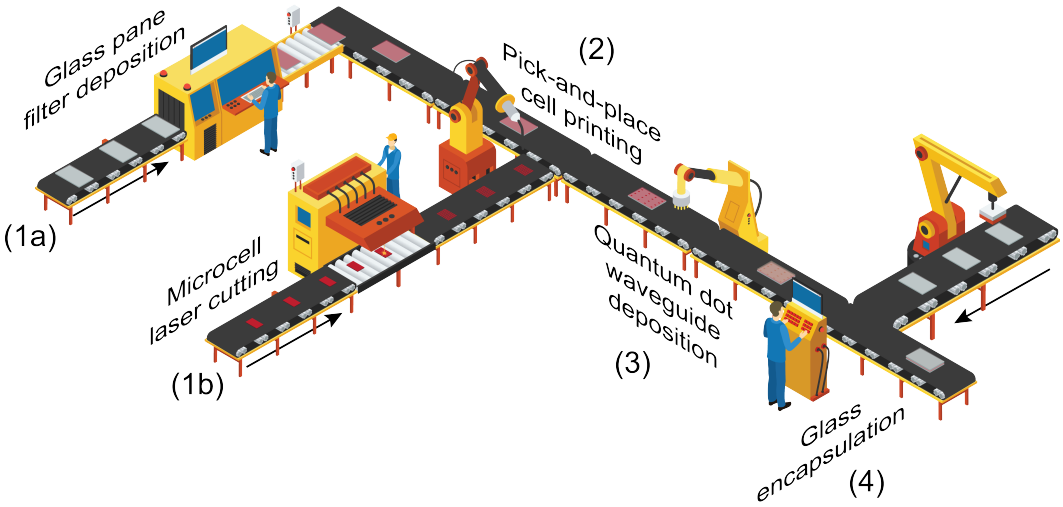

Figure 4.6: The roll-to-roll process of a building integrated LSC photovoltaic window (i.e., double pane insulated glass unit). We conceptually discretize this process into four sequential steps of the fabrication: (1a) distributed Bragg reflector deposition onto the glass pane substrate, (1b) (concurrently with 1a) laser cutting of the GaAs heterojunction cells into micro-sized devices, (2) pick-and-place printing and adhesion of the micro-cells onto the glass substrate as well as electrical interconnection (not shown) via screen printing, (3) quantum dot waveguide deposition of the monomer solution at a particular luminophore optical density and (not shown) ultra-violet curing, and (4) spacer layer adhesion, argon-gas filling, and glass superstrate encapsulation for the final LSC product.

Equipped with this assembly process of the LSC insulated glass unit, we can now define the approximate area and equipment needed to run this line. To begin, we assume for example a plant to be located in Los Angeles, CA—thereby including the overhead of building and permitting costs as well as energy rate. To quantify the depreciation of the physical assembly line tools, we apply a 10% discount rate and assume a 10 year line lifetime. The total manufacturing time throughput is approximately 6.5 hours per batch for each window production line (multiple lines needed to achieve the overall throughput). We further estimate cycle times of: (1a) 0.50 hours per batch for distributed Bragg filter deposition; (1b) 0.50 hours per batch for GaAs micro-cell laser cutting; (2) 5.00 hours per batch for the micro-cell array printing and interconnecting; (3) 0.20 hours per batch for the quantum dot, polymer deposition and curing process; and (4) 0.30 hours per batch for the front

glass encapsulation. All values come from interviews with commercial manufacturers for a given tool assuming to-scale production throughputs.

Table 4.2 details the specific CapEx costs for the assembly line shown in Figure 4.6. We note that we assume electricity costs in Los Angeles to be on average 6¢ per kWh over the entire year. We also include maintenance costs for the facilities to be 3% of the total equipment costs following previous modeling[180].

Process Step	Equipment	Footprint (m^2)	Unit Price ($ per window)
1a	Sputterer[176]	20	6,000
1b	Laser cutter[176]	15	60
1b	PECVD 1[181]	2	1,500
1b	PECVD 2[181]	2	7,325
2	Pick-and-place[181]	10	215
2	Screen printer[181]	5	350
3	Doctor blade[176,182,183]	5	100
4	Laminator[176]	10	450

Table 4.2: The CapEx for an LSC insulated glass unit production line. Here we give the corresponding step for each equipment piece—shown schematically in Figure 4.6—followed by the approximate areal footprint and price per unit. We note that PECVD 1 corresponds to an anti-reflection coating deposition tool, and PECVD 2 corresponds to a side wall passivation layer given the small top surface to side wall area ratio.

Complementary to the CapEx, OpEx defines daily cost drivers. In practice, this corresponds to raw material inputs, electricity use per tool and assembly line, and the cost of labor for each stage of the process. Appendix D provides a more thorough description of the implementation of this technoeconomic analysis, specifically as it relates to the OpEx. However, the primary inputs that determine the overall cost of a single LSC double pane window device derive from the raw materials needed. Therefore, Table 4.3 defines the assumptions and references for the various goods needed to build these devices.

With the assembly process line fully defined, we can now combine the economic model with the performance modeling to quantify the technoeconomic limits for a 1m x 1.5m double pane insulated glass unit with an integrated LSC layer. We input the luminophore optical density (that is, the resulting average visible transparency) of the window and the LSC geometric gain (the density of GaAs micro-cells in a particular window) as the independent variables into this model. Importantly, these two parameters affect both the overall unit cost of a single window as well as the performance. Figure 4.7 illustrates the effects of these two parameters for the case of low (a) and high (b) cell/quantum dot cost limits.

Process Step	Raw material	Cost rates	Units	Materials cost ($/window)
1a	Si target[176]	44.14	$ per kg	0.36
1a	Ti target[176]	22.20	$ per kg	1.04
1a	Glass pane[184]	3.00	$ per m^2	9.09
1b	GaAs cell[27,180]	1920—6400	$ per m^2	*variable*
1b	Ag paste[176,181]	58.77	$ per kg	0.002
1b	Al paste[176,181]	52.00	$ per kg	0.02
1b	Cu tabbing[176,181]	0.0007	$ per m	0.00001
2	Quantum dots†	70—140	$ per m^2	*variable*
3	Lauryl Methacrylate[176]	15.44	$ per kg	4.06
3	Polymer cross-linker[176]	22.84	$ per kg	0.73
3	Dispersing agent[176]	82.31	$ per kg	0.83
3	Photoinitiator agent[176]	65.37	$ per kg	0.01
4	Glass pane[184]	3.00	$ per m^2	9.09
4	Encapsulation[181]	1.54	$ per m^2	4.61

Table 4.3: The OpEx for the LSC window production line. As in Table 4.2, the process step corresponds to each discrete assembly procedure. †: an estimate of the quantum dot cost to scale given interviews with the leading quantum dot manufacturers as of 2020.

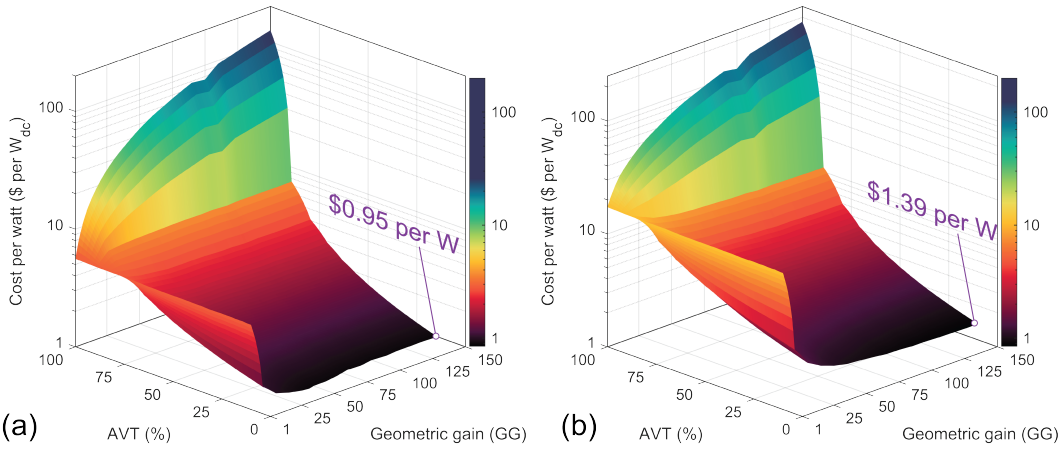

Figure 4.7: The modeled technoeconomic performance ($ per Watt (DC)) of a 1.5m x 1m double glass pane window unit housing an LSC layer. (a) and (b) illustrate the low- and high-cost regimes for the GaAs and quantum dot OpEx raw input costs, respectively.

Shown in Figure 4.7, we find the global minimum cost to be between approximately $0.95 and $1.39 per Watt (DC). With increasing geometric gain, the cell costs decrease for low visible transparency—as more light can be effectively con-

centrated over larger distances. However, at high visible transparencies, increasing geometric gain decreases the system performance. We should note that we do not take into account the costs associated with installing or permitting the window into a commercial building.

4.4 LSC Windows Outlook

In this chapter, we have evaluated the technical performance and technoeconomic limits of a single junction LSC device embedded into an insulated glass unit window for building integrated photovoltaic applications. Through our validated Monte Carlo ray-trace modeling, we unveil a road toward high power conversion efficiency devices, discuss the aesthetic tunability for such modules, and introduce a rigorous technoeconomic analysis and to-scale production line. With our findings, we observe how such building integrated LSC devices could offer significant overall photovoltaic system cost reductions.

Thus far in this thesis, we have assumed a single junction LSC design, limited by a single electronic bandgap to absorb incident photons. Next, we turn our attention to the possibility of optically stacking multiple semiconductor materials in order to subdivide the solar spectrum and, in so doing, push beyond the single junction detailed balance limit.

CHAPTER 5

Multijunction LSC Devices for Terrestrial Applications

Discussed in section 1.1.2 and shown in Figure 1.7, thermalization of high energy photogenerated conduction band electrons accounts for over 40% of the power conversion efficiency loss of a single junction solar cell. Intuitively, introducing more than one electronic bandgap in a multijunction photovoltaic module subdivides the incident light spectrum—whereby high/low energy photons generate near-bandgap excitons in high/low energy bandgap materials, respectively. This notion of cascading photons through a multijunction stack of high to low bandgap materials traces back to the beginning of modern solar cell research in 1955[185–187]. Given the lack of high quality epitaxial growth techniques at the time, however, high efficiency tandem (multi-junction) devices did not come about until around the 1980s.

Beyond stacking monolithic multijunction cells through epitaxial growth processes, subdividing the incident solar spectrum into discrete energy bands through external optics has long been studied in order to overcome the single junction detailed balance limit[188–193]. While such methods require external photonic structures to redirect portions of irradiance to its bandgap-matched solar cell, the process requires no lattice matching. Figures 5.1(a),(b) illustrate these two cases for spectrum splitting photovoltaic modules. Figure 5.1(c) quantifies the detailed balance limit for a multijunction device (either through monolithic stacking or spectral mirrors) as a function of the number of junctions and lowermost bandgap—we also show the case for infinite subdivisions of the spectrum and the maximum concentration for a glass-based geometric concentrator with an acceptance angle equal to that of the solar disc (i.e., 46,200).

Owing to the spectral selectivity of the embedded luminophore material, LSCs provide an alternative approach to multijunction photovoltaic modules to those shown in Figures 5.1(a),(b). A monolithic waveguide stack where each layer comprises a different luminophore—from higher to lower absorption bandgap from top to bottom—offers the advantages of simplified device architecture as in traditional multijunction stack designs (b) with the benefit of avoiding the issue of lattice matching as in spectrally selective mirror designs (a). For this reason, several studies have shown proof of concept fabrication for two-[136,194] and three-layer[195,196] tandem LSCs.

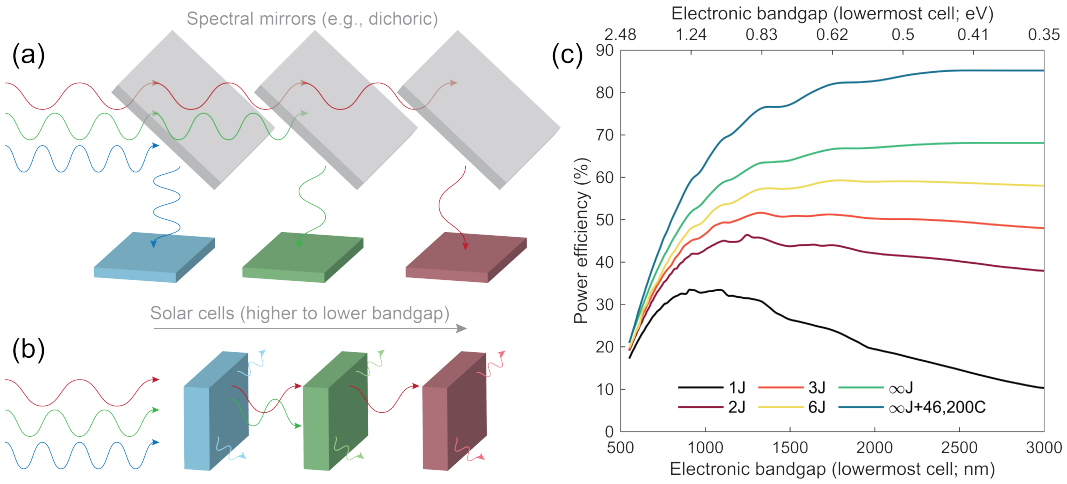

Figure 5.1: An overview of methods and power conversion efficiency limits of multijunction solar devices. (a) The concept of subdividing the incident solar spectrum through spectral mirrors, whose reflectance band red shifts as photons cascade through the module. (b) A depiction of monolithically stacking solar cells of higher to lower energy bandgap. (c) The detailed balance limits for a solar device as a function of the number of junctions (1J, 2J, 3J, 6J, and infinite junctions) and the bandgap energy (nm and eV) of the lowermost cell. We also show the case for maximum geometric concentration assuming a glass index of refraction ($n_{\text{glass}} \approx 1.5$) and an acceptance angle (θ_{in}) equal to the solar disc half angle. Adapted from Green & Bremner[18].

5.1 The Multijunction LSC Device

Evidenced by previous work in multijunction LSC modules, power conversion efficiencies remain limited: where the current record stands at just 3.1% (lower than that for single junction LSCs). Among others, non-unity photoluminescence trapping efficiency within the optical waveguide yields poor spectral splitting and photovoltaic collection; and while external trapping structures can enable higher photon recycling in the single junction case, typical distributed Bragg reflectors used in the LSC community block lower energy photons from reaching the bottom layers in an optically stacked tandem LSC.

As discussed in section 3.2, however, nanophotonic luminophore materials exhibiting anisotropic emission into guided waveguide modes could eliminate dependence on external photonic crystal structures (e.g., distributed Bragg reflectors). As such, we first calculate the detailed balance limit for multijunction LSC modules optically stacked with cascading high to low energy bandgap luminophores (and matched photovoltaic cells) as a function of the number of waveguides (i.e., luminophore/cell systems) and the Stokes shift.

5.1.1 The Detailed Balance Limit for n LSC Stacks

An important evaluation of any photovoltaic device is the detailed balance limit—as discussed in section 3.1. For the case of an optical monolith of LSC devices con-

sisting of cascading luminophore energy bandgaps (high to low), we assume certain idealities about the luminophore absorption, photoluminescence, and cell external quantum efficiency spectra to determine this limit. Starting with the photovoltaic cell coupled at the edge of an LSC, we assume a Heaviside function response of the internal quantum efficiency and assume zero incident reflectance and complete absorption of photons with energy at or above the bandgap. In order to uncover the detailed balance limits with respect to the number of LSC layers that comprise our stack, we assume a lowest photovoltaic bandgap equivalent to a germanium cell (approximately 0.66eV at room temperature).

Similar to the photovoltaic, we assume a luminophore absorption that behaves as a Heaviside function with energy bandgap equal to the photovoltaic cell added by the fixed Stokes shift. We thereby assume a Dirac-delta photoluminescence emission profile for example (the limit as a semiconductor luminophore reaches its zero dimensional case). For all cases, we assume unity photoluminescence trapping and waveguiding efficiency: assuming zero luminophore re-absorption of photoluminescence and perfect collection via the edge-lined photovoltaic cell at a geometric gain of 20. We therefore form one matrix consisting of the luminophore absorption spectra for the given number of LSC layers and one for the photovoltaic cell—offset by the Stokes shift. Equation 5.1 shows the LSC absorption matrix that we assume in this toy model, where $\mathcal{A}_i$ gives the i^{th} LSC layer luminophore absorption:

$$\mathcal{A}_{\text{LSC}} = [\mathcal{A}_1 \mathcal{A}_2 \cdots \mathcal{A}_n] = \left.\begin{bmatrix} 1 & 1 & \cdots & 1 \\ \vdots & \vdots & \cdots & \vdots \\ 1 & 1 & \cdots & 1 \\ 0 & 1 & \cdots & 1 \\ \vdots & \vdots & \cdots & \vdots \\ 0 & 1 & \cdots & 1 \\ 0 & 0 & \cdots & 1 \\ \vdots & \vdots & \cdots & \vdots \end{bmatrix}\right\} \text{wavelength.} \tag{5.1}$$

We calculate the short-circuit current by multiplying the incident solar spectrum by this absorption matrix in Equation 5.1, where the number of junctions determine the step function edge wavelength. The available incident solar spectrum diminishes as photons cascade through the multijunction stack, shown conceptually in Figure 5.2(a) Thereby, as the number of junctions grow, the available amount of photocurrent for any one layer decreases—eventually, for the limit of infinite junctions, the photocurrent of a single LSC tends toward zero. We calculate the open-circuit voltage via equation 1.5, where we assume a radiative efficiency of 2% for all junctions and calculate the dark radiative current term via our expression given by equation 3.6 (assuming a waveguide index of refraction of 1.50 for all layers, complete luminophore photoluminescence trapping, and a geometric gain of 20).

As seen in Figure 5.2(b), we vary both the number of LSCs within the monolithic stack (a) as well as the Stokes shift offset between luminophore absorption and photoluminescence—and, as discussed, photovoltaic cell bandgap. As expected, as the number of layers in the optical stack grows so does the power conversion effi-

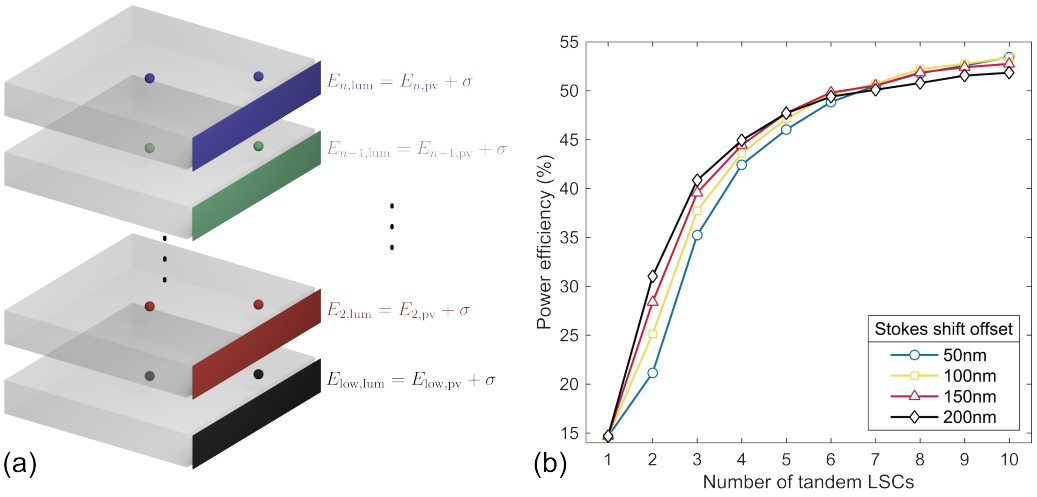

Figure 5.2: The detailed balance limit for tandem (i.e., multijunction) LSC devices monolithically stacked in the vertical direction, where we assume an overall module consisting of n LSCs in highest to lowest energy bandgap ($E_{n,\mathrm{lum}} > E_{n-1,\mathrm{lum}} > \cdots > E_{2,\mathrm{lum}} > E_{\mathrm{low,lum}}$). (a) A conceptual depiction for this LSC tandem stack device, where we assume a certain Stokes shift, σ, offset between luminophore absorption and photoluminescence (assuming a Dirac-delta emission) and a photovoltaic cell bandgap equal to the downshifted photon energy for that particular layer. We assume the lower limit to be a germanium solar cell (bandgap energy of approximately 0.66eV). (b) The detailed balance limiting power conversion efficiencies of a multijunction LSC stack with respect to the number of LSCs in the stack and the Stokes shift of the luminophore species.

ciency under 1-sun illumination. We observe that a Stokes shift increase adversely affects power conversion efficiency for a large number of LSCs in the stack. We can understand this result owing to the fact that a larger Stokes shift restricts the available irradiance spectrum—we are not able to as tightly Riemann integrate the solar spectrum with larger Stokes shifts. On the other hand, at low number of junctions, larger Stokes shifts lead to greater separation between absorption and emission of the luminophore. In turn, we observe that the maximum open-circuit voltage for a given layer is increased in this case and, as such, a low number of junctions with large Stokes shifts outperform their limited Stokes shifted counterparts.

5.2 The Tandem LSC/Si Device

With the wide availability of silicon-based photovoltaic devices, research interest grew in the late 1980s into developing high efficiency two-junction tandem modules with silicon as the low bandgap material[197]. In recent years, owing to the dramatic cost decrease of silicon cells (illustrated in Figure 1.2) and emergence of low-cost materials such as solution-processable perovskite solar cells, renewed interest in silicon-based tandem devices has resurfaced[198–201]. And while there exists significant research efforts that develop methods to minimize traditionally cost-prohibitive top-junction components (e.g., III-V epitaxial growth materials)[202–205], relatively fewer studies apply the concept of decreasing the necessary area of the III-V top junction

through an LSC structure[83–85,117].

Despite this, an LSC offers distinct advantages in an on-silicon tandem configuration, among others: *(i)* the use of high external radiative efficiency III-V cells as the photoluminescence collector (i.e., high open-circuit voltages), *(ii)* decreased materials cost proportional to the geometric gain of the LSC, *(iii)* minimal thermalization (i.e., heat generation) within the III-V cell owing to spectral matching between the luminophore emission and cell bandgap, and *(iv)* simplified tandem assembly through optical stacking of the LSC waveguide atop the underlying silicon cell (for use in a four terminal module). Here we evaluate the detailed balance limits, parameter space, experimental fabrication, and four terminal module performance analysis for an LSC/Si tandem device.

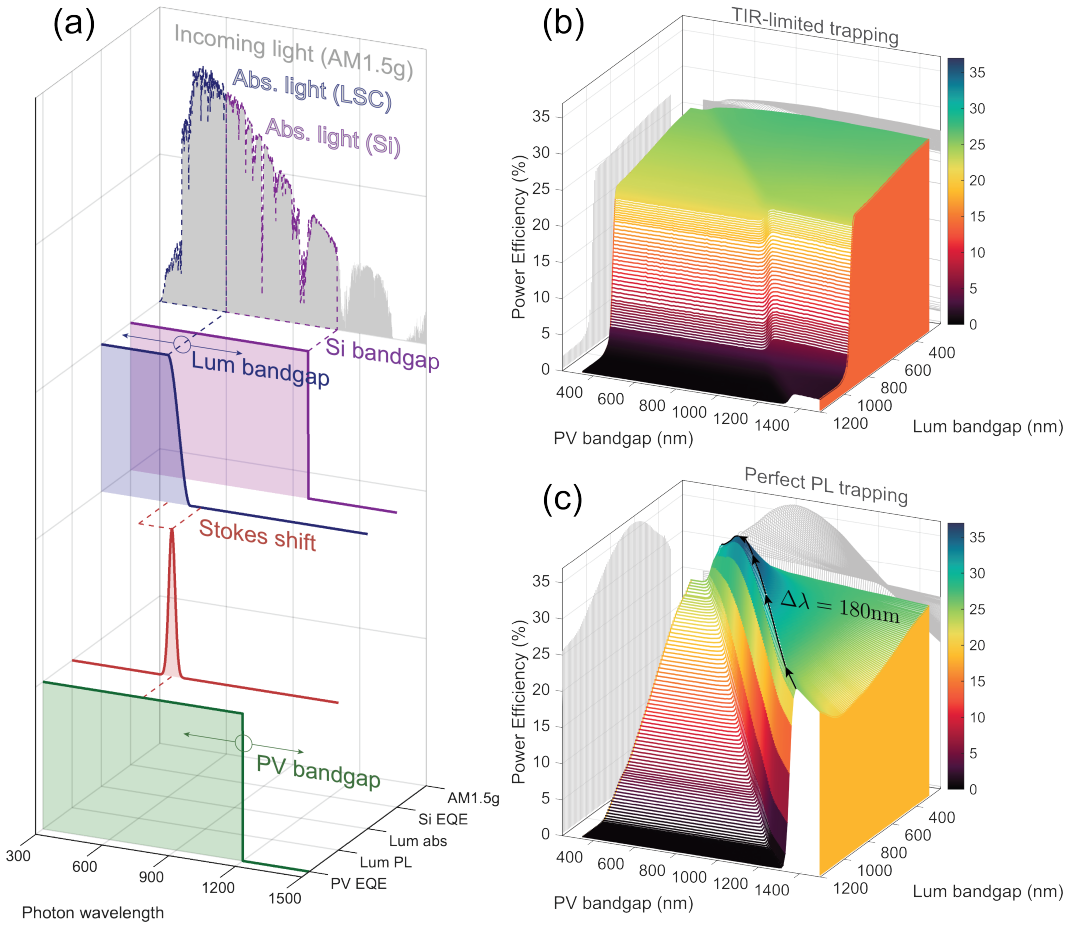

Figure 5.3: The detailed balance limits of power conversion efficiency for a planar grid luminescent solar concentrator at a geometric gain of 20 optically stacked atop an arbitrary silicon photovoltaic cell of bandgap 1100nm (a) We assume high optical loading of luminophores within the waveguide layer to simulate complete incident photon absorption up until the luminophore bandgap edge. (b), (c) The upper performance limits for such a concentrator device in the context of luminophore emission trapping limited by the index of refraction contrast between the waveguide ($n = 1.5$) and air ($n = 1$) and for the ideal case of unity photoluminescence trapping, respectively.

5.2.1 The Detailed Balance Limit for LSC/Si Modules

As in chapter 3, we begin by quantifying the detailed balance limits of an LSC/Si tandem structure, where we independently vary the luminophore and LSC photovoltaic cell bandgap assuming a fixed Stokes shift of 200nm. In contrast to the single-junction case, we model an ideal silicon cell (bandgap of approximately 1100nm) to optically lie underneath the LSC waveguide layer. As before, we model the short-circuit current (i.e., optical efficiency) through the Monte Carlo ray-trace and calculate the open-circuit voltage and cell fill factor through our analytical expression given the dark radiative current of the cell (Equation 3.6) and an assumed external radiative efficiency of 2% for both the silicon and LSC cells. The tandem module spectra are shown in Figure 5.3(a).

We first identify the case limited to total internal reflectance. Figure 5.3(b) illustrates how, under this trapping regime, the top LSC negligibly contributes to the power conversion efficiency of the overall module. In contrast, for the case of perfect photoluminescence trapping within the optical waveguide component shown in Figure 5.3(c), we find a steep ridge-line that arises for the case of an ideal luminophore to photovoltaic cell bandgap matching. We calculate the upper limit for an on-silicon tandem LSC module to be approximately 36.0% at a geometric gain of 20 and a 200nm stokes shift.

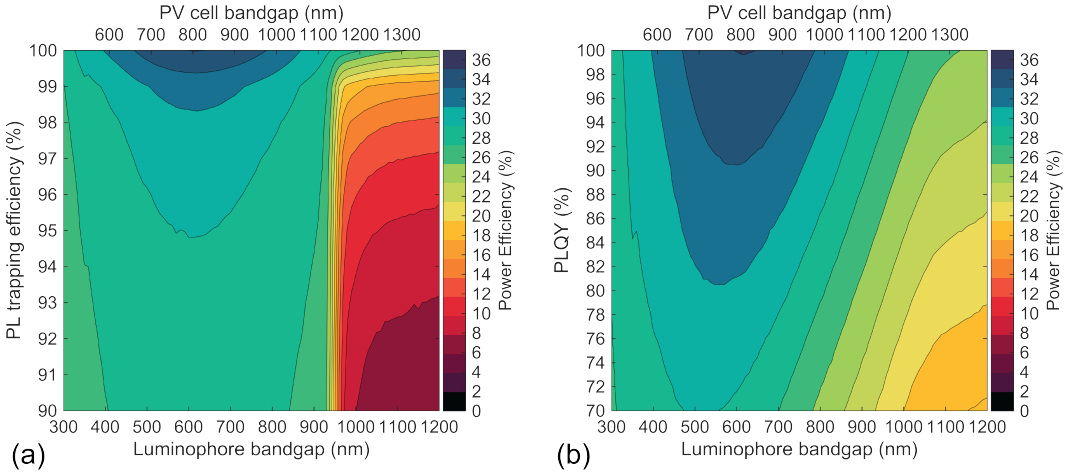

Figure 5.4: (d),(e) Power efficiency analyses given the optimal luminophore to cell bandgap offset (180nm) shown in Figure 5.3(c), varying the photoluminescence trapping efficiency (90% to 100%) and quantum yield (i.e., radiative efficiency) (70% to 100%).

5.2.2 The LSC/Si Parameter Space

Analogous to the single junction LSC case, we can evaluate the performance for an LSC/Si four terminal tandem device beyond this two bandgap system—developing our understanding of luminophore emission trapping and PLQY on the system power conversion efficiency. We find higher sensitivity to waveguide trapping than to PLQY, where we find absolute differences of approximately 7% and 6% (Figure

5.4(a),(b)) at optimized bandgaps, where the former does so for trapping value contrasts between 100% and 90% whereas the latter does so for PLQYs of 100% and 70%. Relative to the single-junction luminescent solar concentrator device, power conversion efficiency of the on-silicon tandem module appears less sensitive to below unity trapping and PLQY values. For below-unity waveguiding efficiency, the silicon subcell can still collect escaped photoluminescence, and thus we would expect greater leniency in the trapping parameter relative to the single junction case.

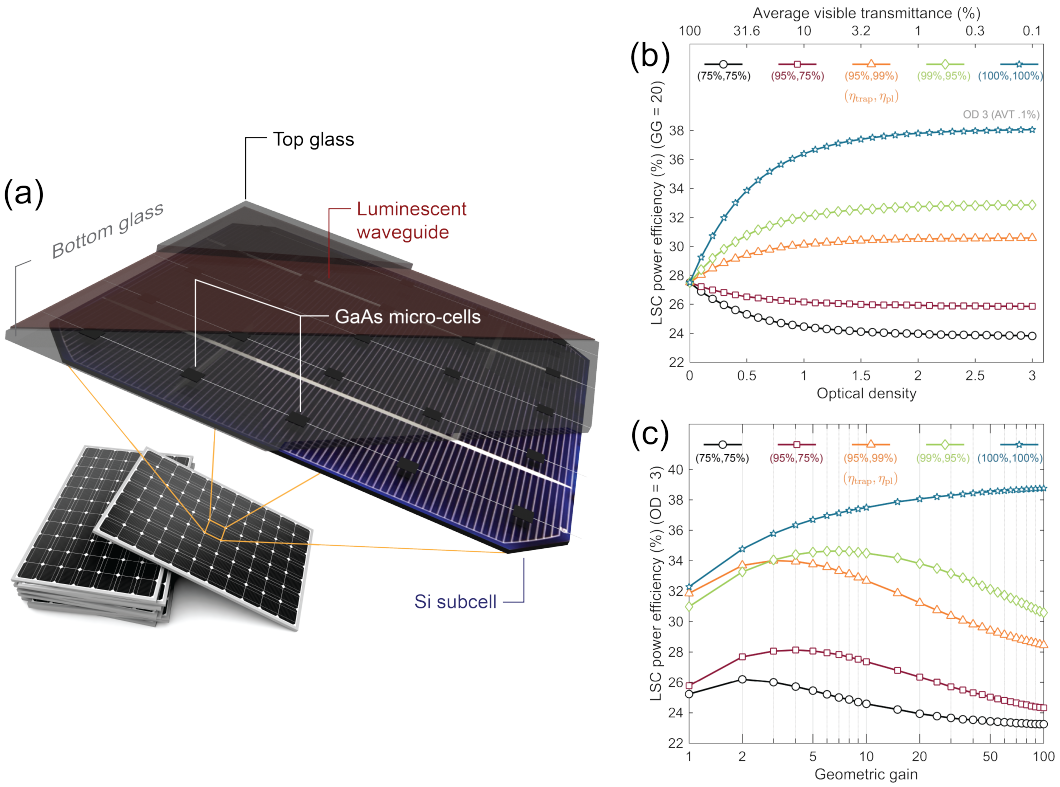

Figure 5.5: A possible application of area-scalable LSC devices into on-silicon tandem, utility-scale photovoltaic structures (e.g., panels), shown conceptually in (a). (b),(c) quantify the upper performance limits for an ideal (Heaviside) GaAs embedded cell of area 1.4mm x 1.4mm within an optical waveguide of index $n = 1.5$. We optically stack this luminescent solar concentrator atop an ideal (Heaviside) silicon cell of area equal to the waveguide. We vary the luminophore loading (optical density measured at 450nm light) and geometric gain together with the trapping efficiency (η_{trap}) and photoluminescence quantum yield (η_{pl}), respectively.

As seen in Figures 5.4(a),(b), a GaAs-based (900nm bandgap) luminescent solar concentrator in optical tandem with a silicon subcell can theoretically achieve greater than 30% module power conversion efficiency. Such a tandem structure that stacks a planar grid of GaAs micro-cells embedded within a luminescent waveguide atop silicon photovoltaics, conceptually rendered in Figure 5.5(a), takes advantage of the high output voltage of the GaAs cell, area-scalability of a planar grid architecture, and the large short-circuit current of the silicon. Figures 5.5(b),(c) show the upper performance limits for an idealized GaAs cell (with step function quantum efficiency)

and optimal luminophore (Stokes shift of 200nm) with respect to the luminophore optical density (b) and geometric gain (c). We find that for poor values of waveguide trapping efficiency and PLQY, increased optical density decreases overall module performance—as fewer photons can reach the underlying silicon subcell. We also find that for ideal cell/luminophore materials and above 75% waveguide trapping and PLQY values, the globally optimal geometric gain is not unity, as larger gains allow for more light to reach the underlying silicon cell without shadow losses.

5.3 LSC/Si Module Fabrication and Analysis

With the computational LSC/Si device limits and parameter space, we now turn our attention to fabrication of tandem structures in an effort to further validate our device modeling and demonstrate the first ever four terminal module of this design. To do this, we develop two separate device structures whose LSC component consists of two distinct luminophore/cell material sets. The first, analogous to the single junction case, consists of a $CuInS_2$/ZnS core/shell quantum dot slab waveguide with a single GaAs mini-cell centered within the LSC and a heterojunction silicon solar cell. The second, in order to shift our top LSC junction to a higher open-circuit voltage, consists of a CdSe/CdS core/shell quantum dot waveguide with a printed array of planar InGaP heterojunction micro-cells. In either case, we describe the fabrication procedure, spectral analyses, and tandem module performance.

5.3.1 GaAs Based LSC/Si Fabrication Procedure

As shown in Figure 5.5, a GaAs-based LSC/Si four-terminal tandem module can in principle achieve beyond 36% power conversion efficiency. While this upper limit motivates further engineering of the luminophore and waveguide materials sets, a proof of concept fabrication serves to demonstrate the technical efficacy to such a tandem photovoltaic structure. Therefore, we begin by fabricating a single GaAs mini-cell oriented planar to a quantum dot waveguide whose photoluminescence closely matches the electronic bandgap of the GaAs heterojunction. As for the single junction case, discussed in section 3.4, we analyze the LSC/Si performance within a diffuse trench reflector in order to emulate larger arrays consisting of this archetypal unit cell.

We disperse commercially available (UbiQD Inc.) $CuInS_2$/ZnS core/shell quantum dot luminophores within a lauryl methacrylate monomer solution and polymerize under ultraviolet exposure (precise recipe discussed in section 3.4). As before, the quantum dots absorb strongly in the short-wavelength regime up until approximately 700nm and exhibit a large Stokes shift to emit around the center wavelength of approximately 800nm. The GaAs cell growth, isolation, dicing, and contacting procedures follow exactly with that described previously.

In order to complete this optically stacked tandem LSC/Si module, we begin with a large area silicon heterojunction cells, where the non-metallized wafers were

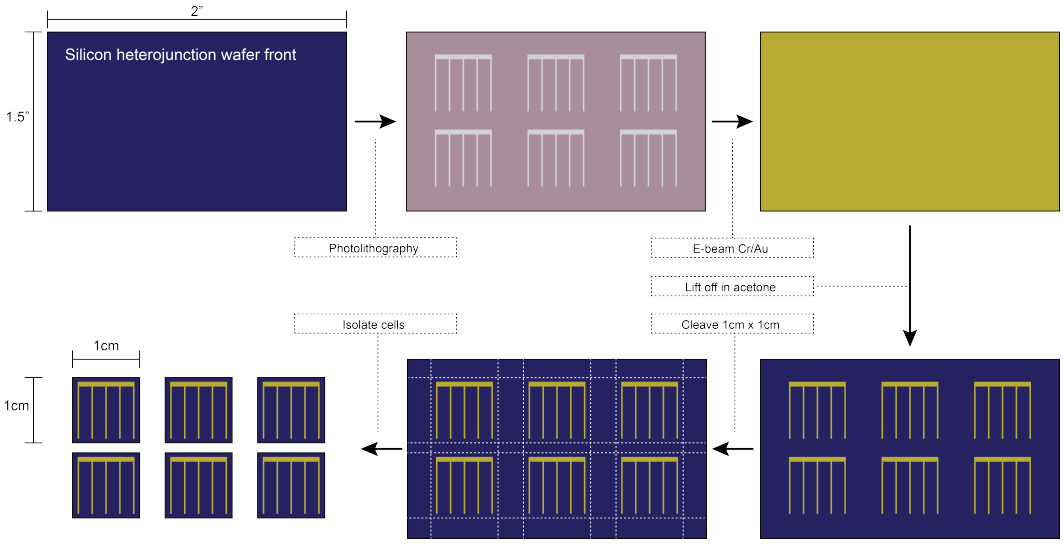

Figure 5.6: The silicon heterojunction metallization and dicing process with input wafers grown from previous studies. The final device size shown here yields six, 1cm x 1cm active cells to be optically placed underneath the LSC top layer for the GaAs-based LSC/Si tandem modules.

fabricated at large-scale (6“ x 6”) using previously established methods[206–213]. We next cleave the wafers into smaller (ca. 1.5“ x 2”) pieces, and metallize the back side of the devices using electron beam evaporation (10nm Cr with 300nm Au). To deposit front contacts, a contact pattern was defined on the front using the following photolithography recipe (AZ P4620, AZ Electronic Materials):

1. Dehydration bake, 110°C for 5 mins,
2. HMDS treatment, room temperature for 5 mins,
3. Spin-coat AZ P4620 at 1000 rpm for 10 sec, 2000 rpm for 30 sec,
4. Soft bake at 65°C for 5 mins, then 95°C for 20 mins,
5. Expose 400 mJ/cm^2 at 365nm,
6. Develop in 3:1 H_2O:AZ400K developer (AZ Electronic Materials) for 2 mins,
7. O_2 de-scum, 3 mins,
8. Hard bake at 70°C for 20 mins (ramp from 35°C to 70°C over 1 hour).

Using e-beam deposition, we deposit metal on top of the patterned photoresist, (10nm Cr with 300nm Au) and liftoff in acetone followed by cleaving, yielding isolated 1cm x 1cm silicon heterojunction devices to serve as the tandem subcell. We finally apply silver epoxy to the top and bottom of the silicon subcell, along with an insulating side-layer of NOA61, and contact onto external busbars to extract the electrical power via four-point probe measurement. Figure 5.6 illustrates the full silicon fabrication process.

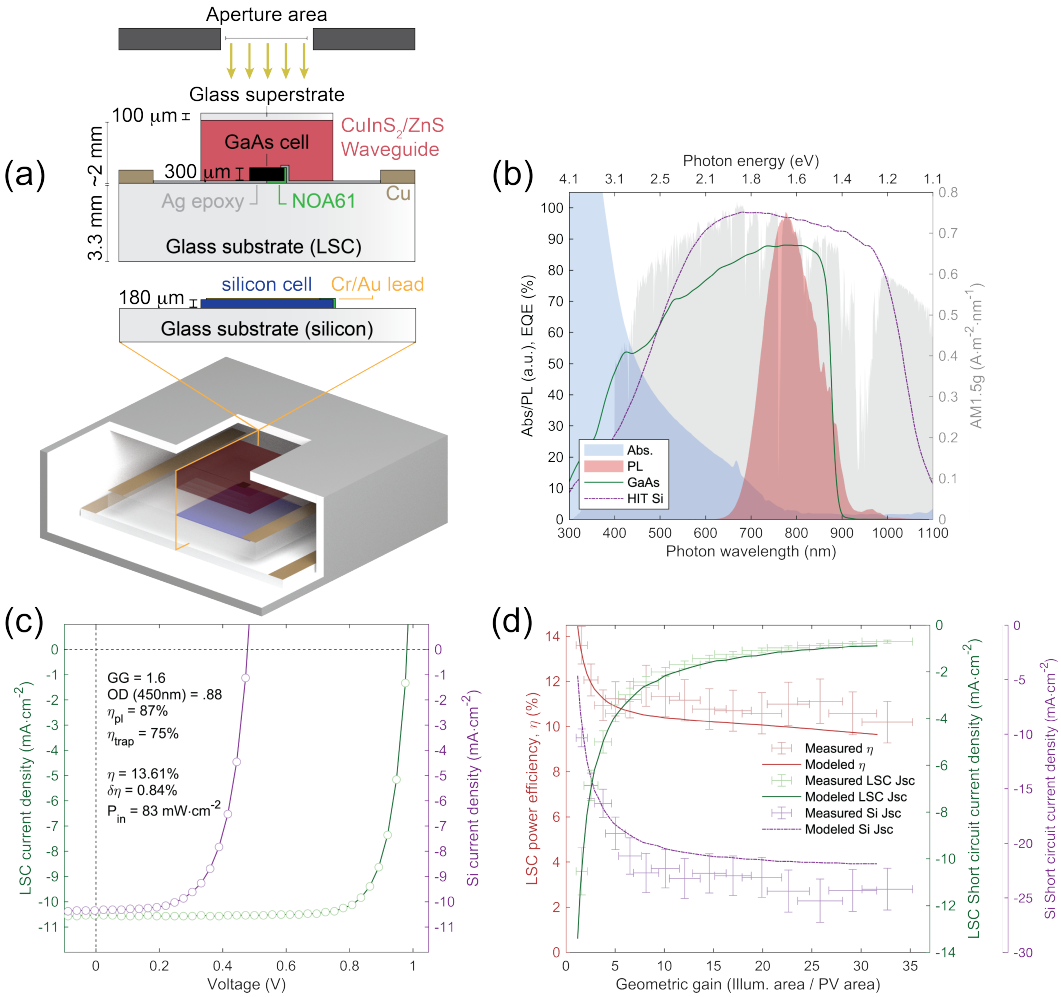

Figure 5.7: A three-dimensional conceptual rendering of the experimental setup (a) with a zoom-in of a simplified profile depiction of the tandem LSC/Si four-terminal device. (b) gives the measured $CuInS_2/ZnS$ quantum dot absorption and emission spectra with respect to photon wavelength/energy along with the fabricated 1.4mm x 1.4mm active area GaAs minicell and the underlying 1cm x 1cm active area silicon heterojunction cell. The gray background area shows the incident AM1.5g irradiance. For a planar luminescent concentrator/silicon device employing these components, (c) gives the maximum measured power conversion efficiency, current density-voltage analysis for both the concentrator and silicon components at a geometric gain of 1.6 and measured optical characteristics. (f) illustrates the effect of illuminated geometric gain on measured device power conversion efficiency (red bars) and short circuit current density (green and purple bars) against the predicted results (red/green/purple lines).

5.3.2 GaAs Based LSC/Si Results and Analysis

With the $GaAs/CuInS_2/ZnS$ LSC and heterojunction silicon components fabricated and stacked optically within the diffuse trench reflector (detailed in appendix H), we can measure the spectral characteristics for each component and the power conversion efficiency of the full device. Figure 5.7(a) depicts a rendered setup of the tandem device alongside a simplified two-dimensional profile view of the LSC/Si

tandem module within the trench reflector. Figure 5.7(b) provides the full spectral characterization for each device component measured by a Cary 5000 UV-Vis spectrometer (luminophore absorption), a custom external quantum efficiency measurement tool, and an inverted microscope.

Figures (c) and (d) provide the power conversion efficiency measurements of the LSC/Si four-terminal tandem module within the diffuse trench reflector, whereby (c) gives the current density ($mA \cdot cm^{-2}$) response for each the LSC and silicon layers with respect to applied voltage bias (V) and (d) gives the overall power efficiency (%) and short-circuit current density ($mA \cdot cm^{-2}$) with respect to the illuminated geometric gain of the system (varying an external iris aperture, as described in appendix H).

Upon exposure under a low geometric gain of approximately 1.6, we find a maximum tandem device efficiency of 13.61% under a reduced AM1.5g spectrum (measured input irradiance of approximately 83 $mW \cdot cm^{-2}$). From Figure 5.7(c) we observe that, unlike the GaAs-based luminescent concentrator that achieves high open-circuit voltage values, the silicon heterojunction subcell demonstrates below 500mV at open-circuit. Such low voltage behavior of the silicon cell is attributed to comparatively high dark radiative currents given the shadow losses from the GaAs component. Figure 5.7(d) illustrates the close model matching to the measured tandem performance for the power conversion efficiency (red), LSC short-circuit current (green), and underlying silicon short-circuit current (purple).

5.3.3 InGaP Based LSC/Si Fabrication Procedure

From Figure 5.4(b), we readily observe how, for PLQY values less than unity, the optimal luminophore-photovoltaic cell bandgap of the LSC component of an LSC/Si tandem module blue-shifts. Qualitatively, as the LSC component decreases in optical efficiency, a luminophore that exhibits a decreased spectral coverage will outperform owing to fewer opportunities for incident photons to nonradiatively recombine in the LSC layer. Therefore, we now turn our attention to an LSC/Si architecture whose luminophore absorption bandgap is blue-shifted with respect to the $CuInS_2$/ZnS and GaAs system. Specifically, we consider the case when we employ CdSe/CdS core/shell quantum dot luminophores (absorption bandgap of approximately 500nm and photoluminescence centered at 635nm) where we couple to an embedded InGaP heterojunction solar cell (electronic bandgap at approximately 700nm). Furthermore, in order to increase the amount of photoluminescence trapping within the LSC layer, we clad the top and bottom waveguide surface with high/low (Ta_2O_5/SiO_2) refractive index aperiodic dielectric stack filters.

Figure 5.8 shows both photographic (a),(b) and rendered schematics (c) of the LSC/Si tandem module with the external photoluminescence trapping layers. Figure 5.8(d) displays a conceptual illustration of the core/shell structure of the CdSe/CdS quantum dot, as well as a transmission electron microscope image of the nanoparticles. In addition to evaluating the effects of a blue-shifted quantum dot layer within the LSC on the power conversion efficiency, we implement a 4x3 array of InGaP

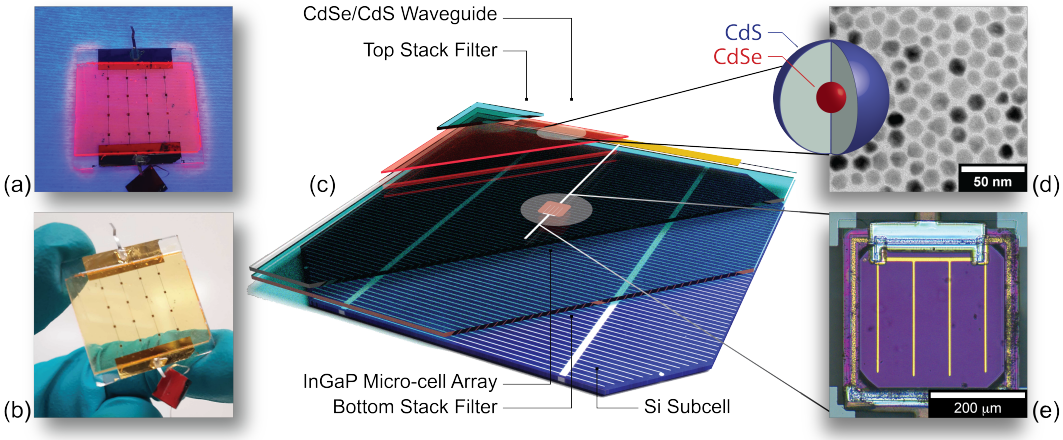

Figure 5.8: The InGaP-based tandem LSC/Si, four terminal module. (a) The top LSC component consisting of a 4x4 InGaP micro-cell array encapsulated within a 30 micrometer (μm) thick CdSe/CdS core/shell quantum dot waveguide under ultraviolet illumination, visibly displaying photoluminescence in the red (635nm). (b) The same top LSC component as (a), under ambient light held for scale. We note that, as viewed in (a) and (b), the right-most column of InGaP micro-cells (4 cells in total) electrically shorted during fabrication process, yielding an effective 4x3 micro-cell array. (c) A rendering of the full tandem LSC/Si module with photoluminescence trapping stack filters coupled to the top and bottom surfaces of the LSC waveguide/InGaP micro-cell array component. (d) The core/shell structure of the CdSe/CdS quantum dot alongside a transmission electron microscope image. (e) A confocal microscope image of the anchored InGaP micro-cell on the LSC glass substrate, with cell dimensions of approximately 400μm x 400μm. Adapted from Phelan et al.[117].

micro-cells (approximately 400μm x 400μm) to lie planar the glass substrate of the LSC waveguide. Such an array demonstrates, as proof of concept, the key fabrication steps in scaling the planar form factor to larger areas, where Figure 5.8(e) provides a confocal microscope image of a single InGaP heterojunction micro-cell. Figure 5.8(b) shows the realized InGaP-based LSC top layer array, where we image the waveguide photoluminescence under UV-light in (a).

InGaP Micro-Cell Array Fabrication

Our collaborators at the National Renewable Energy Laboratory (John Geisz) grow the upright n-on-p InGaP solar cells on GaAs substrates by atmospheric-pressure metal-organic vapor phase epitaxy[214,215]. The Zn-doped absorber layer measures approximately 900nm thick with a 2μm $Al_{.5}Ga_{.5}As$ lateral conduction layer for transparency, allowing for bifacial operation of the device (that is, light collection from the top and bottom faces of the cell within the waveguide). An AlInP layer beneath the $Al_{.5}Ga_{.5}As$ acts as a sacrificial layer for lifting off micro-cells during the transfer printing process to create arrays of interconnected cells.

For the fabrication of micro-cells, our collaborators at the University of Illinois at Urbana Champaign begin by defining the geometry of the negative terminal via photolithography. We subsequently electrodeposit the contact pad consisting of

10nm Ni and 1μm of Au. We define the cell mesa on the GaAs substrate with a two-step wet etch: the first being a 1:100 bromine-hydrobromic (48% HBr, Sigma-Aldrich) acid etch to non-selectively complete the main part of the etch, the second being a saturated HCl etch to selectively remove the remaining InGaP and expose a smooth and undamaged lateral conduction layer. In a similar process we establish the positive contact and isolate the devices via a final HCl etch, exposing the GaAs substrate. To minimize Fresnel reflectance losses, we deposit approximately 50nm of silicon nitride over the device via plasma-enhanced chemical vapor deposition. Figure 5.9(a) displays the measured external quantum efficiency at normal incidence illumination of the isolated InGaP cell.

To transfer the isolated InGaP heterojunction cells from the GaAs wafer and onto our LSC glass substrate (2.5cm x 2.5cm), we spin coat a 150 nm layer of spin-on-glass/epoxy adhesive[216]. We then apply a (poly)dimethylsiloxane stamp to pick up and transfer the micro-cells—isolated by a reactive ion etching process—to the glass substrate to form an array of cells[137,217]. We cure the epoxy layer by sequential heating and ultraviolet exposure. In order to prevent electrical shorting or device shunting, we insulate the cell edges with SU-8 2025. Finally, to complete the cell array and electrically interconnect micro-cells in a series (columns), parallel (rows) fashion, we sputter a layer of 30nn Cr, 150nm Cu, 50nm Al, and 200nm Au in order to fabricate a low mechanical stress and electrical resistance lead.

CdSe/CdS Quantum Dot Waveguide Synthesis

Similar to the $CuInS_2$/ZnS waveguides for the GaAs-based LSC devices, we disperse core/shell CdSe/CdS quantum dots within the monomer lauryl methacrylate (Sigma-Aldrich) and ethylene glycol dimethacrylate (Sigma-Aldrich) cross-linker at a 10:1 ratio. Appendix G details the quantum dot synthesis recipe from our collaborators at University of California, Berkeley as well as the polymerization recipe. To obtain a thinner waveguide relative to the GaAs-based LSCs, we fabricate a 30μm layer through the use of soda-lime glass spacers atop the 2.5cm x 2.5cm glass substrate (hosting the InGaP micro-cell array). We mount a capping, quartz glass superstrate atop the spacers, treated with repel-silane (GE Healthcare). We then apply a capillary force method, injecting the quantum dot/monomer solution between the glass substrate/InGaP array and the glass superstrate. We cure the waveguide solution under 365nm ultraviolet exposure and remove the quartz glass superstrate after curing—as the repel-silane surface treatment prevents strong bonding to the polymer waveguide. Figure 5.9(a) shows the measured absorption and photoluminescence of the CdSe/CdS 30μm polymerized waveguide layer.

Distributed Bragg Reflector Design and Fabrication

In a tandem LSC/Si module, any external trapping filter must provide additional photoluminescence recycling without reflecting away long wavelength photons meant to impinge upon the underlying silicon cell. Out of several methods, including two-dimensional photonic crystals (where the index of refraction is varied in a repeatable

pattern across a two-dimensional substrate[96,97,218]), one of the most common approaches includes a one-dimensional photonic crystal (also termed a Distributed Bragg reflector). Such a crystal alternates high/low refractive index materials (periodically or, in order to suppress certain photon (de)coherence patterns, aperiodically) in a single direction (e.g., vertical with respect to the planar waveguide surface).

Here, we design and optimize a dielectric, aperiodic notch filter stack through a nonlinear optimization routine in combination with a transfer matrix method[219]. As with most optimization routines, the Figure of merit we use to calculate the band-stop mirror quality dictates the success of the optimization. Given the nature of this LSC/Si tandem stack, our Figure of merit consists of three independently weighted factors: *(i)* the transmittance of low-wavelength photons for luminophore absorption within the LSC (up to 500nm), *(ii)* the reflectance of photoluminescence-wavelength photons (i.e., 635±50nm), and *(iii)* transmittance of long-wavelength photons for silicon subcell collection (beyond 685nm). Figure 5.9(a) compares the optimized transfer matrix calculation of our aperiodic dielectric stack filter at normal incidence for averaged s- and p-polarized light against the LSC spectra (luminophore and cell data).

With an optimized aperiodic filter structure, we contract the sputter deposition fabrication (>100 layers) onto a 2.5cm x 2.5cm x 2mm glass substrate with an anti-reflective coating opposite the dielectric stack (Evaporated Coatings Inc., Willow Grove, PA USA). Figures 5.9(c) and (d) compare the modeled to measured stack filter component. We mechanically stack the InGaP array/LSC component directly on the bottom dielectric stack filter and glass substrate. We similarly place a top fabricated structure atop the waveguide to complete our device design as shown schematically in Figure 5.8(c). We place this bottom filter/InGaP micro-cell array/LSC waveguide/top filter structure atop a passivated contact silicon subcell with a window area of 1.6cm x 2.5cm, and embed the entire tandem structure within a mirrored acrylic test bed in order to emulate a larger LSC grid array[89].

Passivated Contact Silicon Subcell Fabrication

Our collaborators at the National Renewable Energy Laboratory fabricate the underlying silicon subcell using a single side textured, rear junction cell with heavily doped n-type and p-type poly-Si/SiO_x passivation layers deposited at the front and the back of an n-type Cz wafer respectively[114,117]. We measure the passivated contact silicon cell under a 1-sun solar simulator, measure again under the CdSe/CdS waveguide, and once more under the LSC/filter structure in order to estimate the cell performance in the tandem configuration. We encapsulate this subcell with a mm-thick layer of (poly)dimethylsiloxane. Figure 5.8(b) shows the measured passivated silicon subcell external quantum efficiency against the transmitted irradiance through the LSC/stack filter top component.

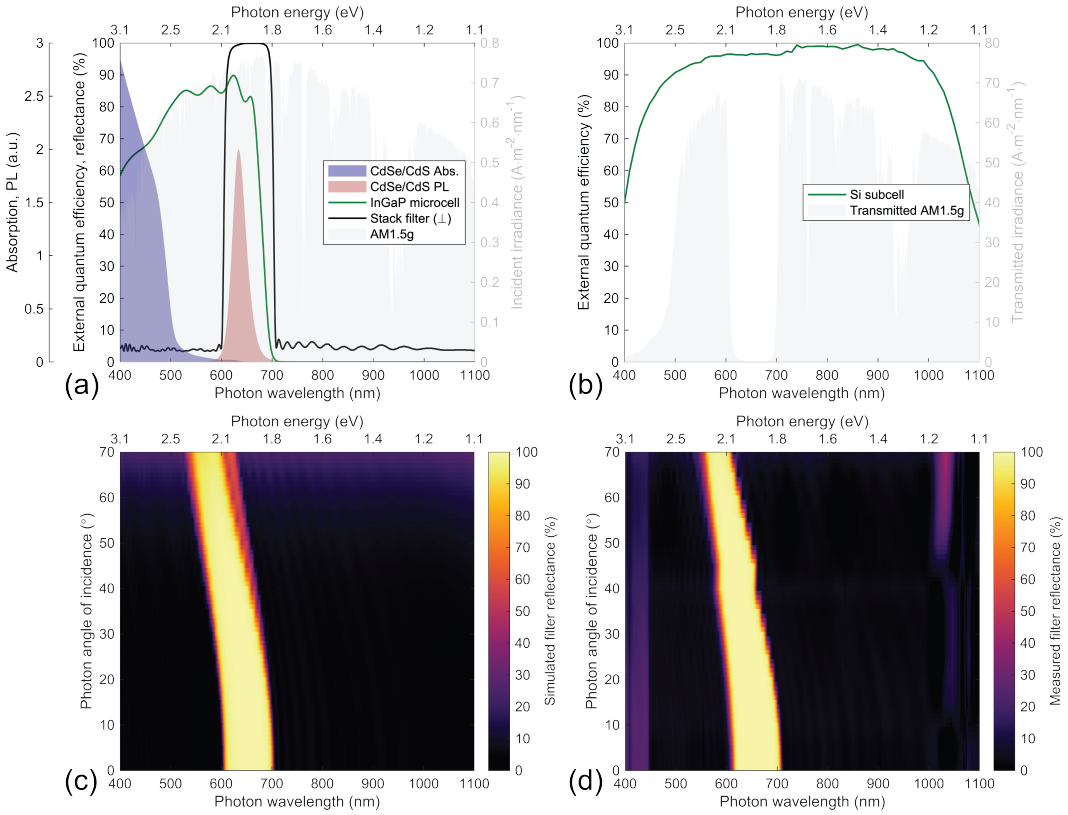

Figure 5.9: The spectral characteristics of the InGaP-based tandem LSC/Si module. (a) The top LSC photovoltaic component, comparing the CdSe/CdS absorption/photoluminescence spectra (far left y-axis), printed InGaP micro-cell external quantum efficiency (left y-axis), aperiodic stack filter reflectance spectrum at normal incidence (left y-axis), and incident AM1.5g spectrum (right y-axis). (b) The bottom passivated silicon component of the tandem LSC/Si module, comparing the cell external quantum efficiency (left y-axis) against the transmitted irradiance through the LSC top component (right y-axis). (c), (d) The simulated and measured dielectric, aperiodic stack filter with alternating layers of Ta_2O_5 and SiO_2, respectively. The realized stack filter (d) is deposited atop an approximately 2mm thick glass substrate. Adapted from Phelan et al.[117].

5.3.4 InGaP Based LSC/Si Indoor Characterization

In order to characterize the external quantum and power conversion efficiencies for both the LSC and underlying passivated contact silicon cell, we first conduct indoor laboratory measurements. For power conversion analyses, we analyze the performance under one-sun solar simulation (experimental setup detailed in Appendix I) for both the LSC and silicon components (given that this structure is a four terminal tandem design). Figures 5.10(a),(b) illustrate the effects from LSC and stack filters on the external quantum efficiency in a layer-by-layer fashion. As the LSC components shape the incident light spectrum, fewer photons are collected by the passivated silicon subcell, as seen in Figure 5.10(b),(d). Solar simulator current density-voltage measurements reveal a short-circuit current of approximately 29 mA·cm^2 and an open-circuit voltage of 700 mV for the bare silicon subcell.

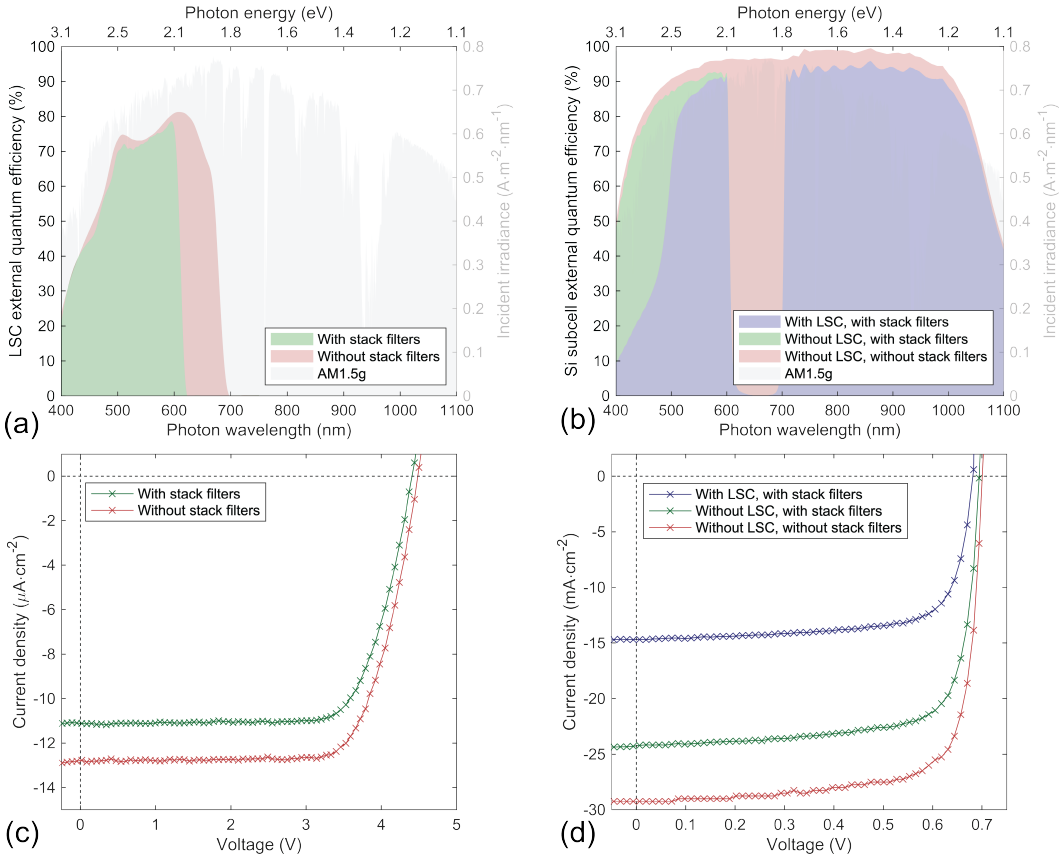

Figure 5.10: The measured electrical performance of the InGaP-based tandem LSC/Si device under artificial, AM1.5g light via a solar simulator. (a) The quantum efficiency analysis for the top LSC component for the cases with and without the top/bottom photoluminescence-trapping stack filters shown in Figure 5.9. (b) The quantum efficiency analysis for the bottom, passivated contact silicon component for the cases with LSC and photoluminescence-trapping stack filters, with solely filters, and finally without the LSC or filters. (c) Current-density, voltage measurements of a sparse InGaP micro-cell array top LSC component (geometric gain of 250) for the cases with and without stack filters, under AM1.5g illumination. (d) Equivalent measurements as in (c) of the Si passivated contact bottom cell. Adapted from Phelan et al.[117].

The LSC analogously demonstrates values of 13 μA·cm^2 and 4.5V for the 4x3 InGaP micro-cell array under the LSC waveguide. With each layer added to the full device, the total output current from the silicon is reduced and open-circuit voltage decreases slightly shown in Figure 5.10(c). The 4x3 InGaP array experiences a current drop off with the addition of the top filter as a result of the reduced quantum efficiency spectrum of the InGaP micro-cell. However, given proper tuning of the notch filter and LSC parameters (e.g., luminophore concentration, geometric gain), increased photoluminescence trapping can offset the drop-off in InGaP micro-cell quantum efficiency, thereby resulting in an enhanced power output of the full device. As highlighted for example in Figures 3.7 and 5.5, too large of LSC geometric gains reduce the probability of photoluminescence collection by the photovoltaic. In this geometry, the system reaches a geometric gain of approximately 250—too large to enable high power conversion efficiencies.

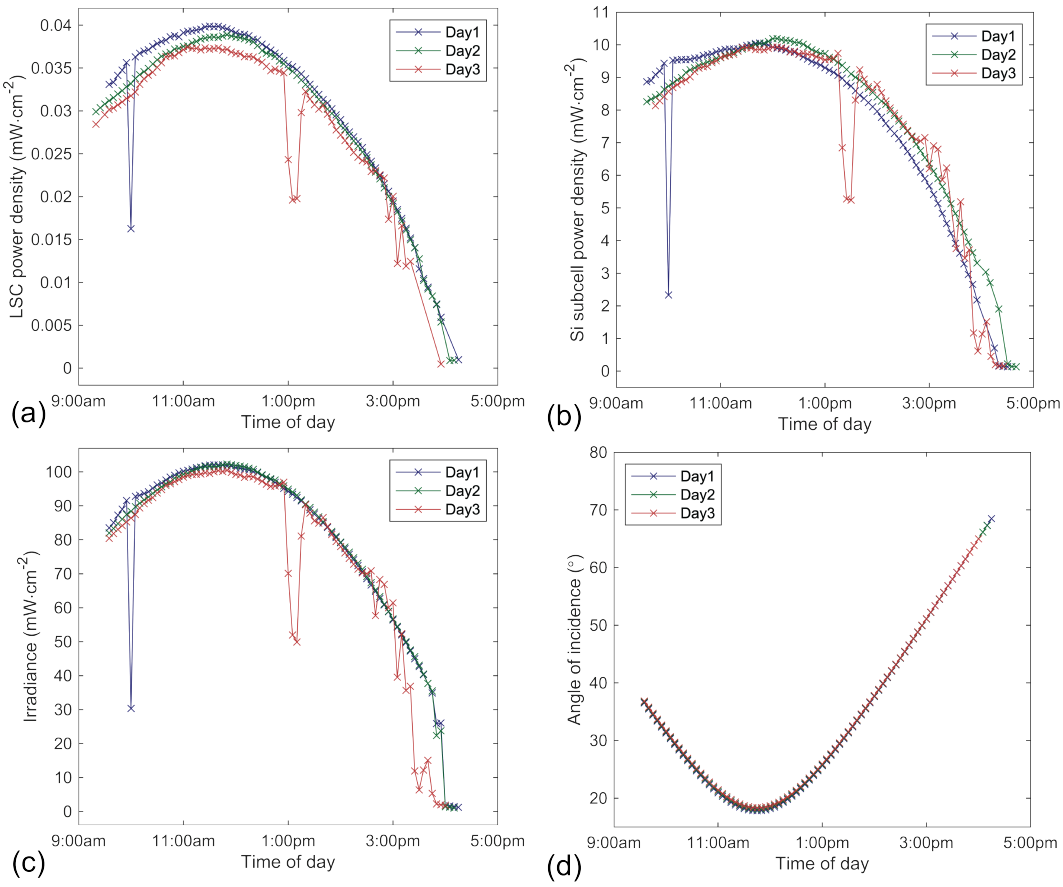

Figure 5.11: Outdoor testing results with respect to time of day at the National Renewable Energy laboratory in Colorado, USA for November 13th, 14th, and 15th 2018. (a) The top LSC component and (b) bottom silicon cell power output in mW per cm^2 over the course of three full days of testing. (c) The solar irradiance (mW per cm^2) and (d) angle of incidence (°) relative to modules top surface for each day of testing, where 90° signifies normal incidence. Dips in the data correspond to brief periods of cloud and/or snow coverage at the testing facility. Adapted from Phelan et al.[117].

5.3.5 InGaP Based LSC/Si Outdoor Testing

While solar simulation testing within a laboratory aids in understanding photovoltaic performance, there is no substitute for outdoor field testing—as this is, of course, the intended operating space for all terrestrial-based solar photovoltaic devices. As such, we now evaluate the power performance of this InGaP-based LSC/Si four terminal module at the outdoor testing facility located in Golden, Colorado at the National Renewable Energy Laboratory—testing during the week of November 11$^{\text{th}}$, 2018. Originally hypothesized as a motivation for LSC devices[42], we aim to understand the angular dependence of light concentration within the LSC in contrast to the underlying silicon subcell and, related, how diffuse vs. direct irradiance conditions affect overall power conversion efficiencies for each component.

We first determine the effects of irradiance and diffuse light illumination on tandem LSC/Si, with modules tilted at a fixed 40° relative to horizontal with con-

tinuous on-site irradiance measurements[220]. As demonstrated in Figure 5.11(a),(b), we measure power output as a function of the time of day and observe an expected maximum performance near 12:00pm. As seen, this power point for both components coincides with maximum solar irradiance, Figure 5.11(c), and an angle nearest to normal incidence of the module when loaded onto the tilted hardware stand, Figure 5.11(d). By 4:00pm, limited incident irradiance and large off-normal angles of incidence result in negligible output power of the module. We observe similar temporal trends for both the underlying silicon and top LSC components. Also shown in Figure 5.11(a), the maximum LSC component power output decreases noticeably throughout the three testing days, a trend not seen in the silicon subcell. We attribute this trend to a degradation mechanism of the LSC waveguiding efficiency, most likely attributed to photodegradation of the luminophore radiative efficiency (i.e., PLQY)[221,222].

Turning our attention now to the component (LSC and silicon subcell) performance under varying diffusivity conditions, we can observe that our outdoor field testing data matches well with previous power conversion efficiency trends measured in prior work[49]. Seen in Figure 5.12(b), the silicon subcell power conversion efficiency monotonically decreases once the amount of direct normal irradiance drops below $50\text{mW}\cdot\text{cm}^{-2}$. In contrast, the top LSC component does not demonstrate a steady decreasing trend as a function of direct irradiance. The spread in normalized efficiency for both the LSC and silicon components in Figures 5.12(a),(b) results, most likely, from day-to-day variations in testing conditions (e.g., cloud and snow coverage). Moreover, we hypothesize that the slight drop in normalized efficiency for the silicon subcell towards maximum direct irradiance, which typically occurs near noon, may result from a modest shift of the solar spectrum in the afternoon. Fernandez, et. al. previously demonstrated how higher angles of incidence—that occur in the afternoon—produce larger attenuation of the UV-visible region of the solar spectrum yielding a red-shifted irradiance (owing principally to Rayleigh scattering by the atmosphere)[223]. Such a red-shifted solar spectrum is better matched to the silicon band edge, potentially leading to a slight increase in performance, as we observe in Figure 5.12(b).

5.3.6 InGaP Based LSC/Si Device Analysis

While indoor and outdoor testing of the InGaP-based LSC/Si four terminal tandem module provides a proof of concept prototype demonstration, we can also analyze the loss mechanisms, photoluminescence travel pathways, and attainable power conversion efficiencies through the use of further spectroscopic measurements and Monte Carlo ray-trace modeling. Bolstering our device analysis with these tools, we can further clarify how to achieve higher overall performance of LSC/Si tandem structures.

The InGaP-based device we fabricate under-performs our previous simulation work of an LSC/Si tandem design composed of these material sets—where such analyses suggest an optimized LSC/Si tandem module could reach power conversion efficiencies near 29% as the LSC approaches its radiative limit[84]. Shown in Figure

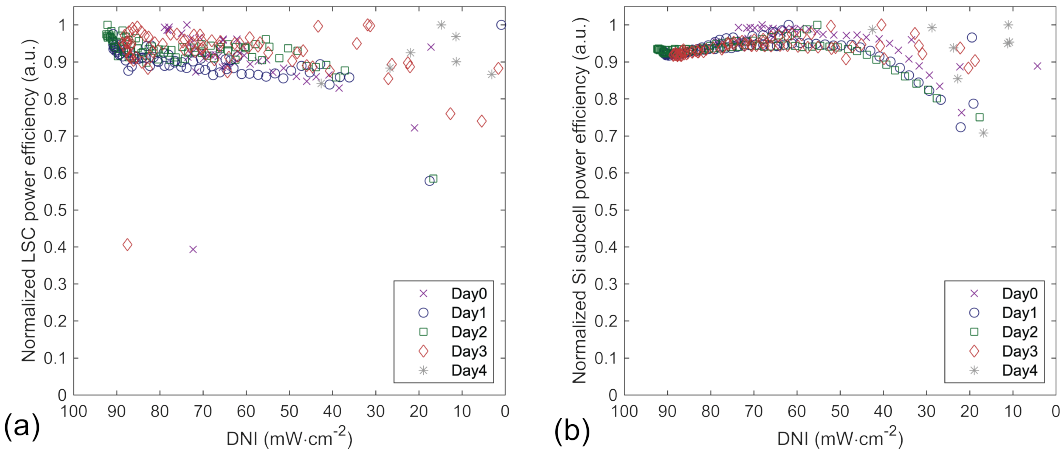

Figure 5.12: Outdoor testing results with respect to the fraction of direct normal irradiance (DNI) by total integrated irradiance at the National Renewable Energy Laboratory in Colorado, USA for November 12th (partial day), 13th, 14th, 15th, and 16th, 2018. Here we show the normalized efficiency with respect to the amount of DNI for the (a) top LSC component and (b) bottom silicon cell. We normalize the power conversion efficiency for each individual day to the highest value for that given day. Days 3 and 4 of (a) correspond to the case with no top photoluminescence-trapping stack filter. Adapted from Phelan et al.[117].

5.11, the passivated contact silicon subcell performed at approximately 10% power conversion efficiency, while the LSC component contributed just 0.04%.

To identify the primary LSC loss mechanisms and optimize our design performance, we can apply our Monte Carlo ray-trace to the LSC/Si tandem module equipped with the spectral measurements of each component (given in Figure 5.9). From our model, we find agreement of a device power conversion efficiency reaching 10%. We therefore can apply this computational tool to pinpoint the exact causes of lowered output current by the top LSC component—as it is in photoluminescence loss that yields such markedly lowered performance. Figure 5.13(a) conceptualizes the most significant loss mechanisms that limit the performance for our tandem structure. Through this modeling, we find that the most significant areas of photon loss stem directly from: *(i)* top filter reflection of incident irradiance, *(ii)* non-radiative recombination of absorbed photons by the CdSe/CdS luminophores (i.e., non-unity PLQY), *(iii)* scattered photons lost through the escape cone of the waveguide/filter component, and *(iv)* parasitic subcell absorption (e.g., defect-site driven non-radiative recombination). Figure 5.13(b) shows these primary loss mechanisms with respect to the incident photon spectrum.

As shown in Figure 5.13(b), LSC non-radiative absorption through below-unity quantum dot PLQYs combined with waveguide escape cone re-emission account for the vast majority of loss for the LSC component. As such, improved photoluminescence collection necessitates increased optical efficiency of the waveguide[126]. In order to spatially resolve the photoluminescence collection efficiency of our LSC waveguide, we map the quantum dot emission by scanning a 490nm wavelength, 10μm spot-size beam[224] across a single InGaP micro-cell LSC. We illuminate the waveguide starting from one corner of the 0.16mm^2 InGaP and extend into a spatial

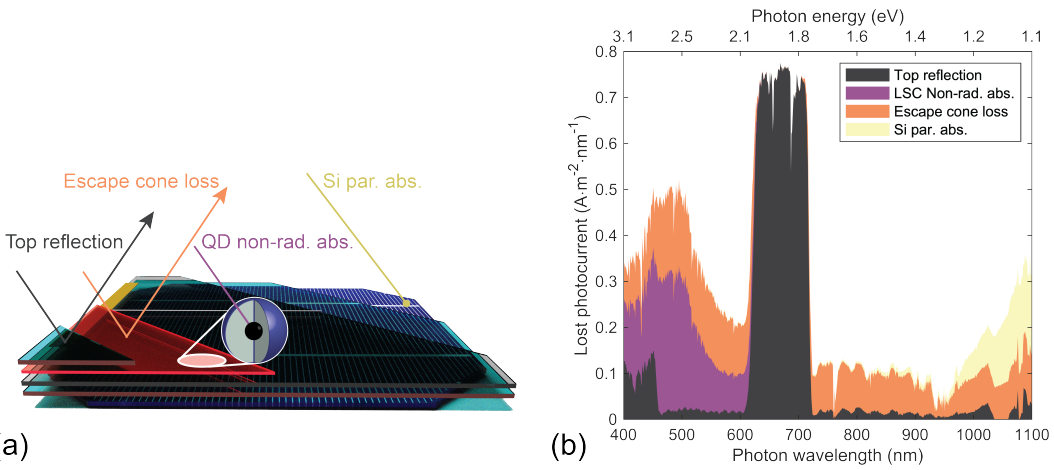

Figure 5.13: Computational results showing the primary loss mechanisms responsible in our InGaP-based tandem LSC/Si system. (a) A rendered schematic depicting the various loss mechanisms, including: top surface reflection of incident sunlight due, primarily, to the top notch filter (dark gray), escape cone loss from the LSC waveguide (orange), CdSe/CdS quantum dot (LSC) non-radiative recombination absorption (purple), and silicon parasitic recombination (yellow). (b) The spectral account for the full tandem LSC/Si loss mechanisms, given as the total lost photocurrent (A per m^2 per nm). Adapted from Phelan et al.[117].

quadrant analyzing a 2.5cm x 2.5cm area—equivalent to a geometric gain of 625—shown in Figure 5.14(a). As seen, the measured photocurrent drops with the spatial separation between the illumination point and the micro-cell corner. An inflection point in the steep drop off located less than 0.2mm from the quadrant origin indicates a combination of photoluminescence and nearby scattered, short wavelength light collected in this small radius. Such an inflection reveals that the mean photon travel distances within the LSC waveguide are significantly limited by a convolution of escape-cone and non-radiative luminophore losses.

Via an understanding of the loss mechanisms in the LSC, we can design an improved tandem device. Figure 5.14(b) projects the modeled power conversion efficiency, as well as the associated photocurrents for each the LSC top component and silicon subcell, possible for various approaches to optimization for the tandem LSC device under normal incidence illumination conditions. One promising method for maintaining quantum dot photostability in an ambient environment and enhancing PLQY performance involves the use of siloxane as a part of the waveguide matrix, which has shown to help quantum dots maintain PLQYs across high temperatures and various moisture due to the strong thermal stability of the bonds in the siloxane[225].

In Figure 5.14(b), we model the following optimizations: *(i)* unity PLQY, improved from the current measured conditions of 60% for the outdoor testing, *(ii)* a defect free waveguide, consisting of a decreased re-absorption probability (i.e., extinction coefficient) of the quantum dots and non-aggregated dispersion of luminophores within the polymer[226]; *(iii)* minimized photoluminescence leakage from the device edges; *(iv)* optimized top/bottom filters to reduce loss from low-

wavelength incident photon reflection and scattered photon transmission through the waveguide escape cone; *(v)* a decreased geometric gain (from 250 to 10) of the LSC for higher micro-cell collection yields, without obscuring long-wavelength photons from reaching the underlying silicon; *(vi)* a re-optimized concentration (i.e., optical density) of luminophores (from 0.33 to 2.4 at 450nm); and *(vii)* a decreased emission full-width at half-maximum[227]. By optimizing each of these components, the tandem device is expected to achieve an ultimate output photocurrent of 10.1mA·cm^{-2} and open-circuit voltage of = 1.48V for the LSC component with 27.2mA·cm^{-2} and 0.65V for the Si subcell. These optimizations are predicted to enable a total module power efficiency of 27.2% under 1-sun illumination.

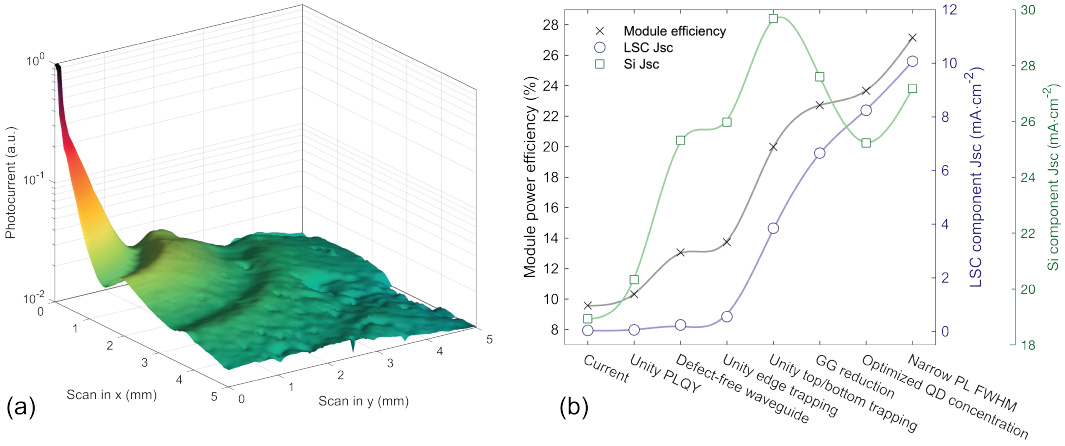

Figure 5.14: (a) The photocurrent mapping of a single InGaP micro-cell embedded within a 30μm waveguide doped with CdSe/CdS quantum dot luminophores, plotted on a log scale. A 490nm laser source scans x- and y-distances up to 5mm from the outside corner of the device active area (the origin corresponding to the cell center). (b) A performance forecast for the tandem LSC/Si module, illustrating approaches for increased module power efficiency (left y-axis, black x-markers) through optimization of the LSC component, alongside the predicted LSC photocurrent (right y-axis, blue circle-markers) and predicted Si subcell photocurrent (far right y-axis, green square-markers). Efficiencies are modeled for 100% DNI under standard AM1.5g conditions. Adapted from Phelan et al.[117].

5.4 Multijunction LSC Device Outlook

Through computational and experimental means, we have explored the concept of optically integrating at least one LSC into a multijunction photovoltaic module. We analyzed the thermodynamic detailed balance for a monolithic stack of n LSC layers as a function of the luminophore Stokes shift, introduced and motivated an LSC/Si device architecture, evaluated the upper power conversion efficiency performance limits with respect to the luminophore and coupled photovoltaic cell bandgap for such a module, and discussed the experimental fabrication and testing of a GaAs- and InGaP-based LSC/Si four terminal device. Through our analysis, we observe the importance of photoluminescence trapping within the waveguide—specifically underscoring the benefits of anisotropically radiating waveguide structures.

As we turn our attention to nanophotonic waveguide and/or luminophore materials that can achieve such anisotropy, a natural consequence for these wave-optical devices is a lowered overall mass per unit area of the device. Given this, we can begin to identify how a single or multijunction LSC could enable unprecedented *specific* powers (that is, generated power per mass). Therefore, we next explore the possibility of optimizing LSC devices for space-based power generation.

CHAPTER 6

Ultra-Light LSC Structures for Aerospace Applications

The prohibitively high manufacturing costs of crystalline silicon wafers in the early 1950s limited the scope of photovoltaic devices—where the first application of silicon solar cells that found a commercial foothold was in early space satellites[11,228]. As this market grew, researchers proposed new concepts about space-based solar photovoltaic arrays. Following William Brown's invention of the rectenna[1] in 1964, Peter Glaser introduced a novel concept for energy harvesting four years later that married the photovoltaic cell and the rectenna[229]. For such a power station, nearly continuous irradiance from the sun with no diffuse component and zero atmospheric scattering/absorption (i.e., 30% greater irradiance levels than terrestrial) could yield unrivaled power production for solar photovoltaic utility applications.

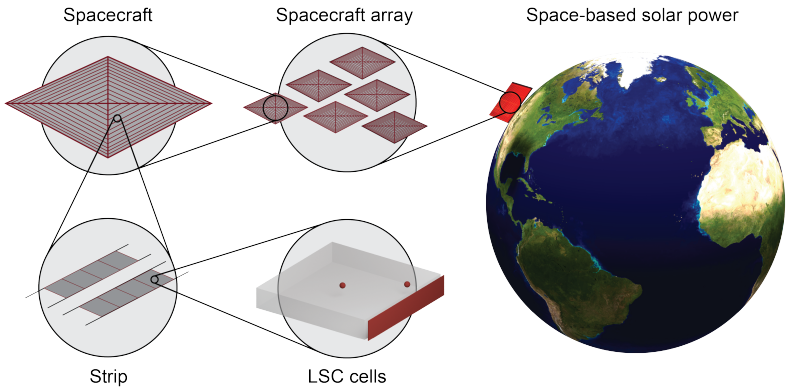

Figure 6.1: The concept of space-based solar power for an example LSC spacecraft deployment. Here, series of individual LSCs (shown as an edge-lined form factor for example) make up an entire strip, where strips makes up a fully deployed (i.e., launched) spacecraft, and we fly spacecrafts in an array in geostationary orbit for 24/7 illumination conditions at AM0 irradiance. Adapted from Kelzenberg et al.[228].

This proposal, which became known as space-based solar power, imagines flying a utility-scale photovoltaic array into geostationary orbit. Upon generation, the

[1]The rectenna consists of a dipole antenna connected to a radio frequency diode, such that incoming radio frequency waves cause a direct current to flow.

electricity radiates through an antenna aimed at a receiving rectenna station on earth—thereby completing a process where the energy flows from photons (sun) to direct current electrons (photovoltaic) to alternating current electrons (antenna) to emitted photons (radio frequency beam) to alternating current electrons (receiving antenna) and finally to direct current electrons (diode). A conceptualization of the space-based solar power array and process is shown in Figure 6.1 Further feasibility studies followed suit[230] and a primary limitation arose relating to the areal mass density for such arrays; as is still the case, launch costs pose a significant barrier to economical energy generation.

6.1 The Space Race for High Specific Power Technology

Despite the high barrier to adoption for space-based solar power, tremendous research efforts have taken place over the past 50 years on developing ultra lightweight and power conversion efficient solar cells. Since, for this industry, both the mass and power generation of the cell dictate the feasibility of the photovoltaic technology, we adopt *specific power* as the primary Figure of merit—defined as the power produced (kW) per mass of the cell (kg). In the early days of space-based solar power, specific powers for solar cells fell below .2kW/kg, where viability calculations indicated that such generation stations needed devices with specific powers in excess of 1kW/kg[230]. Since then, lightweight geometric concentrator solar cells (e.g., stretched lens arrays, parabolic trough reflectors) have shown terrific promise in breaking beyond .3kW/kg[231–235] and emerging thin film technology in surpassing the 1kW/kg barrier[236,237]. Table 6.1 lists several proposed lightweight photovoltaic cell devices for space-based solar power alongside their theorized or measured specific powers.

Photovoltaic Type	Specific Power (kW/kg)	Date	Setting
InGaP/GaAs[238]	0.090	2009	Measured under AM0
Si BSFR[239]	0.092	1991	Deployed to GEO
GaAs/Ge[239]	0.168	1993	Deployed to GEO
GaInP/GaAs/Ge Lens Concentrator[240–242]	0.180	2005	Deployed to GEO
GaInP/GaAs/Ge Parabolic Trough[228,235]	0.230	2017	Measured under AM0
InP Thin Film[236]	2.000	2009	Measured under AM0
GaInP/GaAs/GaInAs[237]	3.000	2017	Measured under AM0

Table 6.1: A table displaying various examples of previously reported space-based photovoltaic specific powers, the date of the report or publication, and the setting in which those measurements were taken.

6.2 The Case for Ultra-light LSC Devices

While decades of research and development on passive concentration techniques for space-based solar power have taken place, little to no published research exists for active concentrators. Therefore, we now turn our attention in this thesis to two topics of LSCs in relation to space-based solar power: *(i)* understanding and estimating the ultimate specific power limits for LSCs given the variety of material parameters and areal mass density form factors, and *(ii)* fabricating and launching the first-ever LSC photovoltaic device into orbit for field testing.

As discussed in chapter 2, the optical waveguide thickness, which hosts the photoluminescent material, dictates not only the amount of incident light absorption by the LSC but also the physical propagation of photons within the waveguide—thereby, the way in which we model the device (wave-optical vs ray-optical). For specific power, we must also consider the effects this parameter has on the total mass. As such, Table 6.2 breaks down the components of LSCs categorized into either ray-optical device thickness or wave-optical and provides order of magnitude estimates of the mass area density for each.

LSC Type	Component	Example Material	Approximate Mass Density (g/cm^3)	Thickness (cm)	Areal Mass Density (g/cm^2)
Wave-optical	Waveguide	PMMA	01.17	$\mathcal{O}(10^{-4})$	$< 2 \cdot 10^{-4}$
	Luminophore	$CuInS_2/ZnS$	$OD \cdot 00.46^{\dagger}$	$\mathcal{O}(10^{-4})$	$< OD \cdot 10^{-4}$
	Photovoltaic	GaAs (planar)	05.32	$1/GG \cdot \mathcal{O}(10^{-4})$	$< 1/GG \cdot 10^{-3}$
	Contacts	Ag	10.49	$\mathcal{O}(10^{-5})$	$< 10^{-4}$
	Total‡	—	—	—	$< 5 \cdot 10^{-4}$
Ray-optical	Waveguide	PMMA	1.17	$\mathcal{O}(10^{-1})$	$< 2 \cdot 10^{-1}$
	Luminophore	$CuInS_2/ZnS$	$OD \cdot 00.46$	$\mathcal{O}(10^{-1})$	$< OD \cdot 10^{-1}$
	Photovoltaic	GaAs (edge-lined)	05.32	$1/GG \cdot \mathcal{O}(10^{-1})$	$< 1/GG$
	Contacts	Cr/Au, Ag	10.49	$\mathcal{O}(10^{-5})$	$< 10^{-4}$
	Total‡	—	—	—	$< .5$

Table 6.2: Approximations for the limiting areal mass density for an LSC device. Here we distinguish between a thin (wave-optical) and thick (ray-optical) LSC device in order to quantify this limit. †: a measurement performed of a 5cm x 5cm x .01cm waveguide with .021g of $CuInS_2/ZnS$ quantum dots dispersed, yielding an optical density of approximately 0.18 at 600nm. ‡: the mass limit assuming an optical density of 1 and geometric gain of 10.

Similar to understanding the material sets and waveguide thicknesses that enable markedly higher specific powers, we must also consider the LSC parameters (Figure 2.1) that can limit device mass while enabling high power conversion efficiency. For example, the geometric gain relates the amount of cell material needed for an LSC device—and so a larger geometric may reduce overall system mass but may also decrease the power conversion efficiency performance. Therefore, to quantify the effects of system parameters on the specific power we must return to our analysis of single- and multijunction LSCs considering the AM0 irradiance spectrum.

6.3 Limits of LSCs for Aeronautical Applications

An LSC device intended for a space-based solar power application could, just as for the terrestrial case, consist of a single luminophore-cell layer (i.e., single junction) or a monolithic optical stack of multiple luminophore-cell combinations (i.e., multijunction). For the optically thick waveguide regime, we can model this system with our validated Monte Carlo ray-trace model for both realistic and hypothetical devices[243]. For thin waveguides of order photoluminesced photon wavelength, we can approximate the short-circuit current by the detailed balance limit and apply our voltage and fill factors expression as before. We build off our previous work in chapter 3 and analyze the detailed balance specific power limits of a single-junction LSC device in orbit with AM0 irradiance incident at angles normal to the waveguide top surface.

6.3.1 Specific Power Limits of Single Junctions

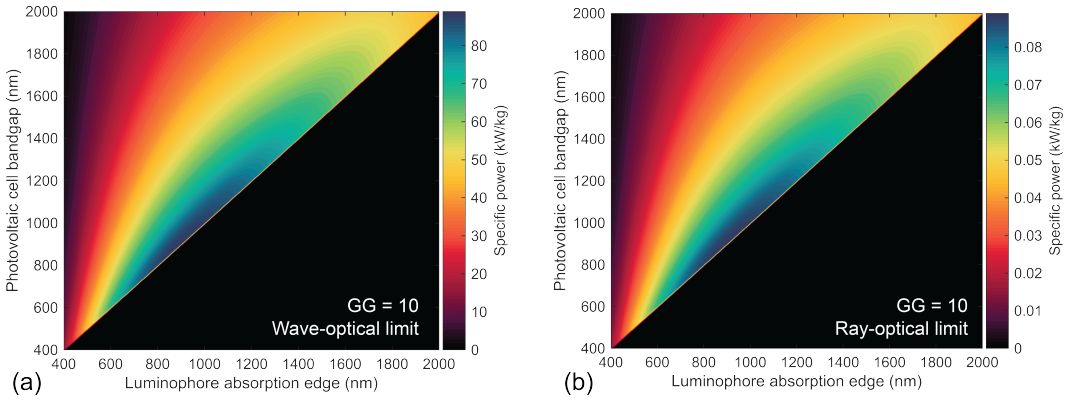

Figure 6.2: The specific power limits of an LSC from the order of magnitude mass calculations in Table 6.2 and a detailed balance model previously discussed. (a) The limits of LSC specific power (kW/kg) as a function of the luminophore absorption edge (nm) and the electronic bandgap (nm) of the coupled photovoltaic cell (also the location of the photoluminescence emission profile) for the case of a waveguide thickness of order magnitude as the photoluminesced wavelength (wave-optical limit) at a geometric gain of 10. (b) The same limits as in (a) except for a waveguide thickness much larger than a single wavelength (where we arbitrarily set the thickness at 0.10cm). In both cases, we apply the back of the envelope mass calculations as discussed in Table 6.2.

We assume an LSC device consisting of a waveguide thickness on the order of a single photoluminesced photon wavelength (i.e., between 100 and 1000nm). As stated, at this length-scale, we cannot physically apply the Monte Carlo ray-trace owing to the wave-like nature of propagating photons. Given the high absorption coefficients of emerging luminophore systems such as two-dimensional dichalcogenides[244,245], however, we can effectively apply a traditional detailed balance model to probe the upper performance limits for such LSCs in space-based solar power applications—a toy model akin to calculating the limits to multijunctions in chapter 5.1. Shown in Figure 6.2(a), we vary the luminophore bandgap together with the cell bandgap (thereby the Stokes shift as well assuming ideal photoluminescence

matching) to define the specific power limits assuming a geometric gain of 10. We can also apply this same model for the ray-optical limit case, shown in Figure 6.2(b).

As seen in Figure 6.2(a), wave-optical LSC devices hold potential to radically unseat the current record specific power devices (e.g., thin film photovoltaics on flexible substrates). While this analysis only describes the devices in their detailed balance limit (whereby we assume a 2% external radiative efficiency of the photovoltaic cell and unity photoluminescence trapping and waveguiding in the LSC), this does however demonstrate the feasibility of wave-optical LSC devices (e.g., nanophotonic waveguides) over their ray-optical counterparts (e.g., current state of the art). In the latter, we observe specific powers (kW/kg) well below .100 even in the detailed balance limit. By contrast, wave-optical LSCs can theoretically surpass well over 10kW/kg.

6.3.2 Specific Power Limits of Multijunctions

Described in chapter 5.1, LSC devices could in principle reach higher power conversion efficiencies via monolithically stacked LSC layers. Here, in order to determine if the power conversion efficiency benefit outweighs the additional mass contribution to the device, we quantify the thermodynamic limits for such an LSC stack where (from top to bottom) the energy bandgap cascades from high to low energies, respectively. Unlike the case for terrestrial photovoltaic generation, however, an increase in layers also acts to decrease the device specific power—as a greater number of layers increases the system mass.

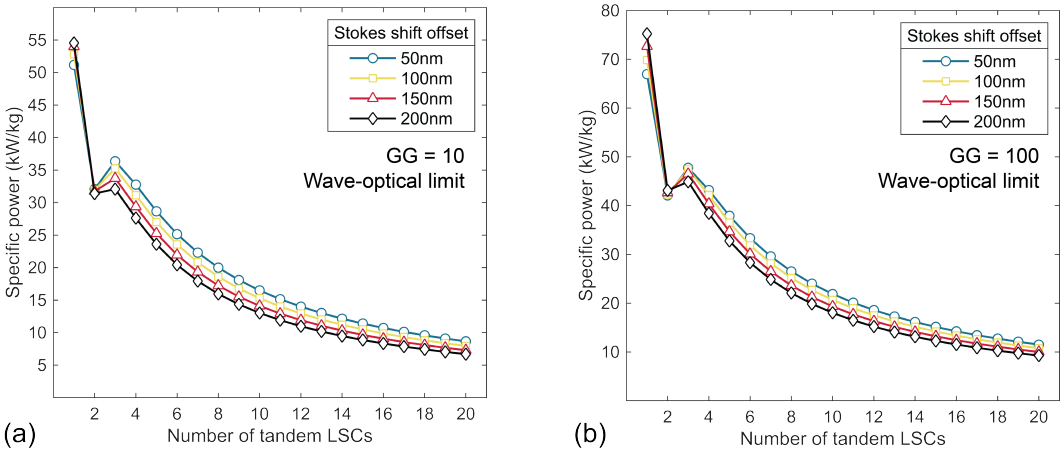

Figure 6.3: The specific power limits of a multi-layer stack LSC—with the lowest energy bandgap equal to a germanium solar cell—from the order of magnitude mass calculations in Table 6.2. Here, we look only at the wave-optical limit for waveguide thicknesses for each layer of the monolithic stack. We model the specific power (kW/kg) detailed balance and mass limits as a function of the number of LSC layers for the case where geometric gain is 10 (a) and 100(b).

Figure 6.3 illustrates the trade-off in number of LSC layers, n, versus the specific power in the wave-optical regime for each layer where we vary the Stokes shift of

the luminophore. We assume a lower energy bandgap equal to that of a germanium solar cell. For both geometric gains of 10 (a) and up to 100 (b), we find that additional LSC layers in a multijunction architecture decreases the overall specific power, whereby the additional mass of each layer outweighs the benefit of increased power conversion efficiency. However, between two and three junctions, we observe a slight increase in specific power owing to the limited number of layers (lower mass) with a relatively large increase to the power conversion efficiency. In the case for a geometric gain of 10 (a), we find an approximate lower limit of 5kW/kg for the LSC device, whereas a geometric gain of 100 (b) yields a lower limit of 10kW/kg owing to the decrease in photovoltaic mass of the system.

6.4 First Ever Space Flight of an LSC

While developing an upper bound on specific power may provide us insight into the pathway for materials and design optimization, an LSC photovoltaic device has—as of this thesis and to this author's knowledge—never been flown in outer space. Such a test not only enables us to gather the first data on the stability of a certain subset of LSC materials in orbital conditions (e.g., quantum dot stability, waveguide/cell materials, LSC form factor design), but it also introduces a new class of concentrators into the space-solar community.

Contracting with SpaceX and Momentus, our confirmed launch date for lower-earth orbit housing, among other solar cell classes, six $CuInS_2$/ZnS quantum dot waveguides coupled to edge-lined GaAs or Si photovoltaic cells is set to deliver the first power conversion efficiency measurements in space for LSCs. Figure 6.4 displays the drawing of the rocket, payload, photovoltaic cell holder, and LSC design that will launch into lower-earth orbit. This mission, while a crucial first step toward employing an LSC that delivers record specific powers, will focus solely on power conversion efficiency rather than specific power—given that we must first quantify the performance durability of these novel space materials (e.g., quantum dots).

6.4.1 Design and Optimization of Lower-Earth Orbit LSCs

With our mission to develop the first round of space field testing on high availability materials to construct optically thick LSC waveguides, Figure 6.5 shows the full, space-ready conceptualized and built LSC device. Here we choose a poly(lauryl methacrylate) waveguide material with a high optical density loading (approximately 1.0 at 450nm) of $CuInS_2$/ZnS core/shell luminophores. To prevent damage from incoming electron, proton, or ultraviolet radiation, we secure the waveguide between two glass cover-slips approximately .5mm thick.

We adhere four GaAs/Si cells onto four perimeter edges of the square slab waveguide, where we employ a space-grade and optically transparent epoxy. Figure 6.5(a) illustrates the cell configuration bordering this square, where the cells extend beyond a single waveguide edge in a pin-wheel like pattern—thereby minimizing the amount

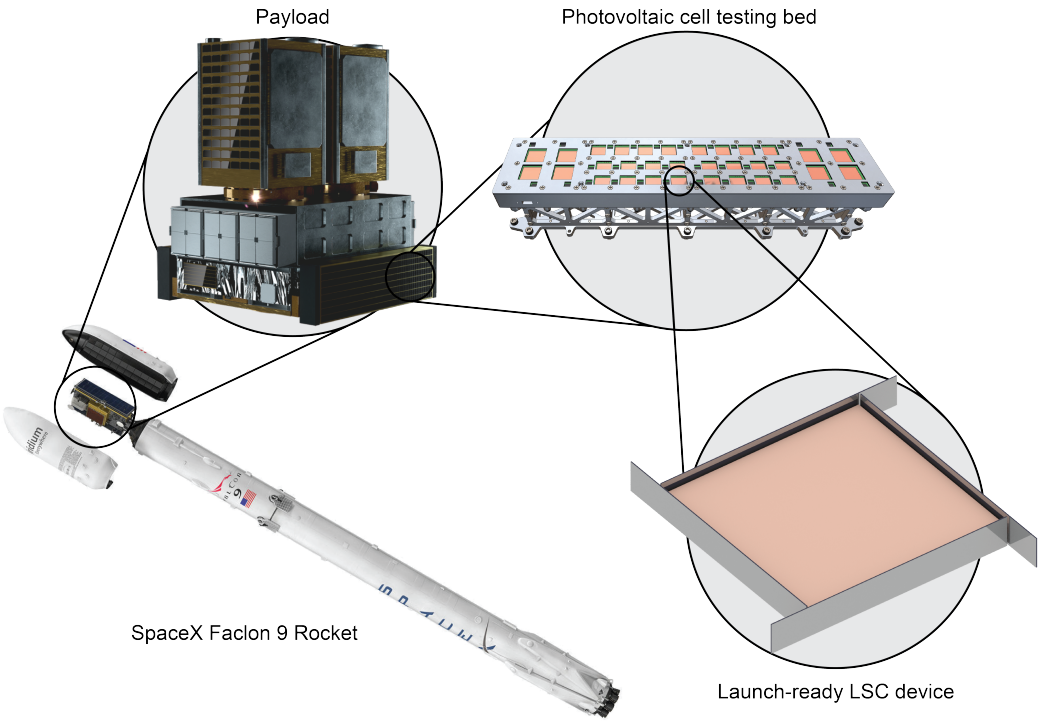

Figure 6.4: A conceptual diagram illustrating the makeup of the lower-earth orbit launch, where the LSC devices are housed on a photovoltaic holding array (with automated testing capabilities), built into the Momentus payload, and launched via a SpaceX Falcon 9 rocket.

of photoluminescence that leaks out of the corners. Similarly, we deposit a silver broadband reflector on the bottom surface of the glass substrate and an alternating high/low refractive index, aperiodic stack filter on the bottom surface of the top glass to minimize escape cone loss, shown in Figure 6.5(b). We electrically connect each cell together in series by space-grade silver epoxy, and connect the LSCs into a printed circuit board for integration into the payload operating software. Figure 6.5(c) shows a photograph of the fully assembled and electrically interconnected LSC device.

6.4.2 Flight-Ready LSC Component Fabrication

Cell Fabrication and Design

We launch three GaAs- and three Si-based LSC devices into lower earth orbit, whereby each LSC consists of four cells strung together in series. Here, we collaborate with the National Renewable Energy Laboratory (John Geisz: GaAs, Paul Stradins: Si) to design and fabricate the cells matched to our LSC device size and layer geometry. For each cell in the LSC of either type, we employ 1.0cm x .15cm active area cells to match our waveguide and mirror (top/bottom glass) layer stack. Figure 6.6 shows current-density, voltage response of the two cell types as well as the measured external quantum efficiency response of these cells. Appendices E and F

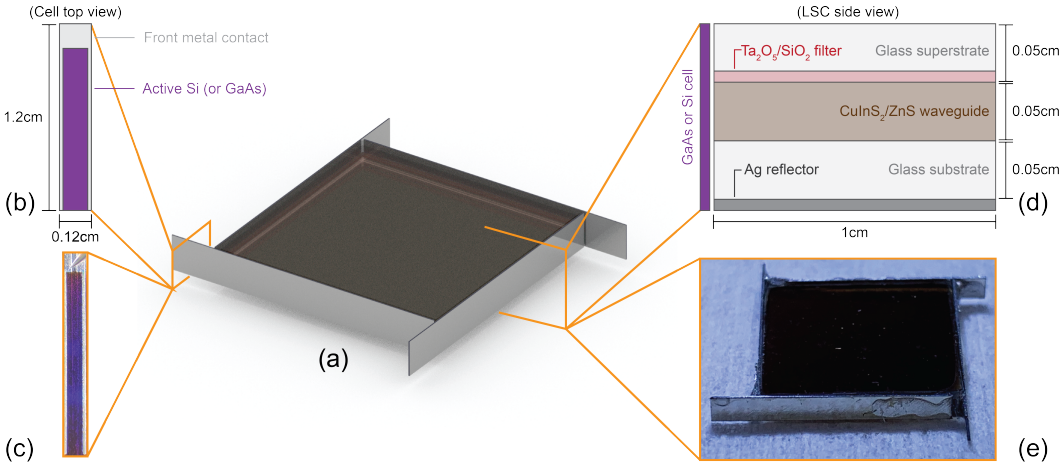

Figure 6.5: The module level design of the lower earth orbit bound LSC device. (a) A rendered three dimensional view of the LSC, where we arrange the edge-lined photovoltaic cells (GaAs or Si) in a pin-wheel configuration in order to minimize edge-escaped photoluminescence. (b),(c) A conceptual and optical microscope image, respectively, of the edge-lined Si or GaAs solar cell, when viewed from the top. (d) A two dimensional profile view of the LSC showing the approximate thicknesses of the glass and waveguide layers. (d) A photograph of the fully assembled LSC with interconnected silicon cells in series.

detail the fabrication process and cell profiles for the GaAs and Si cells, respectively.

Luminophore Waveguide Synthesis

Similar to the process outlined in chapters 3.4 and 5.3, we deposit via capillary force method an approximately .5mm-thick $CuInS_2/ZnS$ core/shell quantum dot waveguide. Appendix G describes the recipe and process of waveguide deposition in greater detail and Figure 3.16 displays the measured absorption/photoluminescence for these types of quantum dot waveguides. However, in order to bolster the optical efficiency of the LSC and deliver a higher concentration of photoluminescence to the four, edge-lining solar cells, the glass sub- and superstrates consist of a broadband silver reflector and an aperiodic dielectric stack filter. The optical density, when measured at 450nm, is optimized in this design through Monte Carlo ray-trace modeling, whereby we find an optimal value to be 1.0 and fabricate to reach this target.

Aperiodic Stack Filter Design

In order to optimize the short-pass, long-stop top filter, we model GaAs- and Si-based LSCs within our Monte Carlo ray-trace to establish the ideal reflectance and transmittance spectra. Figures 6.7(a),(b), and (c) demonstrate the results of this optimization, whereby we vary the edge-stop spectral location, short-pass transmittance, and long-stop reflectance to measure the power output under 1-sun AM0,

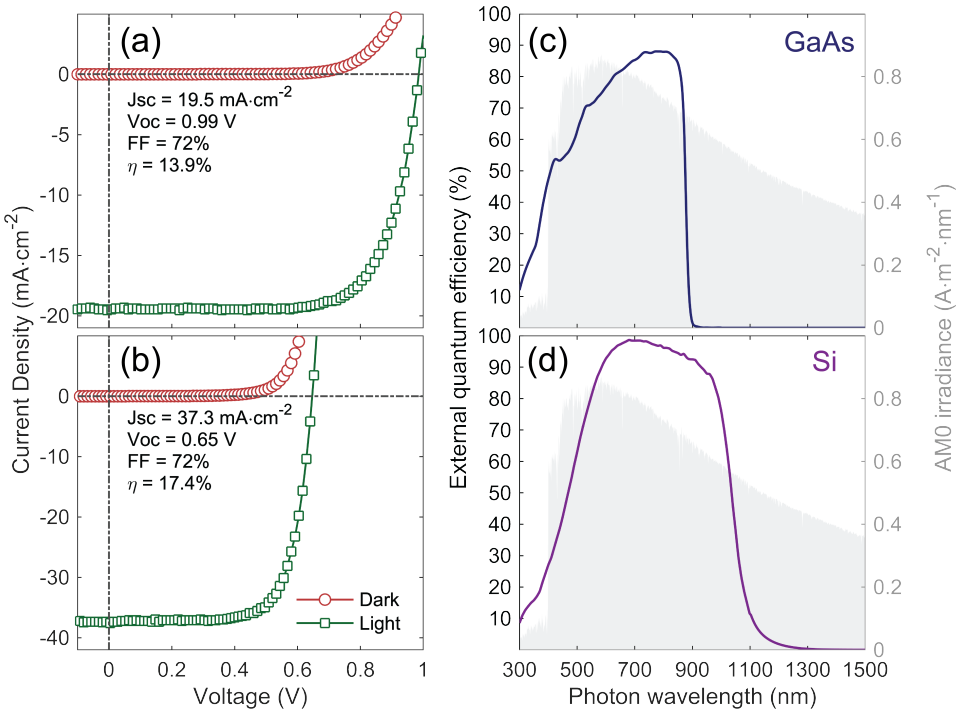

Figure 6.6: The power and spectral characteristics of two types of photovoltaic cells, GaAs (a,c) and Si (b,d), intended for use in the deployed LSC into lower-earth orbit. (a) and (b) displays the measured current density, voltage response of the device in the dark (red) and under 1-sun illumination (green). (c) and (d) give the measured external quantum efficiency response of the GaAs and Si cells, respectively, plotted against the incident AM0 radiation.

respectively.

As expected, higher transmittance and reflectance in the short-pass, long-stop spectral windows yield higher overall performance, respectively. And importantly, we identify 730nm to be the optimal band edge location given the absorption and photoluminescence profiles for these core/shell quantum dots. Armed with this target, we contract Evaporated Coatings Inc. to meet these targets via sputter deposition of Ta_2O_5/SiO_2 high/low refractive index dielectrics. Figure 6.7(d) displays the comparison between the modeled and measured short-pass, long-stop filter. We find that, while the edge location matches well between measurement and model, the short-pass transmittance/reflectance is much lower/higher (respectively) in the measured case than in the modeled.

LSC Module Layout and Assembly

With the cells, waveguides, and filter materials, we fabricate the full LSC module by first adhering the four edge-lining solar cells (either GaAs or Si) to the waveguide perimeter. Regardless of cell type, we syringe a few micro-liters of space-grade, optically transparent UV26 MasterBond epoxy to each edge of the LSC layer (one side at a time) and adhere the corresponding cell to that edge in a pinwheel configuration shown in Figures 6.5(a),(c). We cure under a 403nm ultraviolet curing

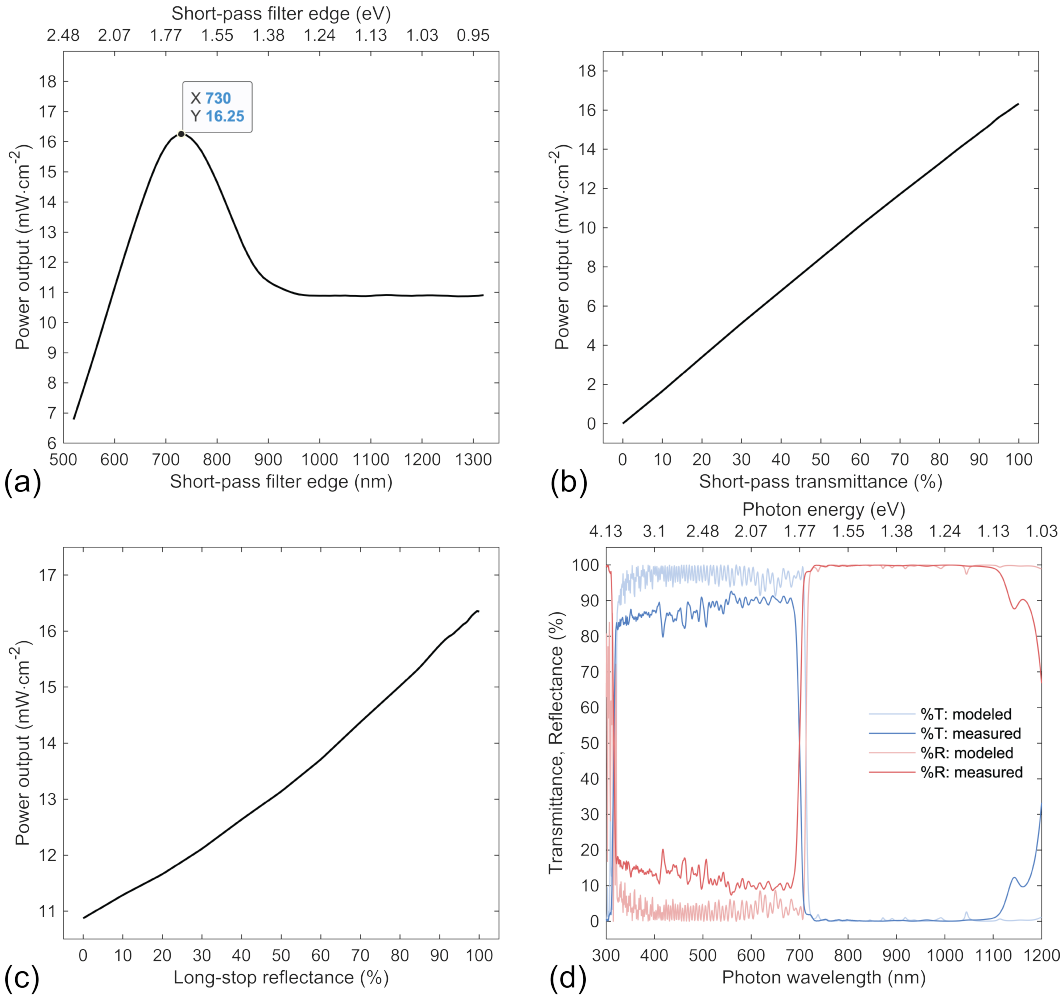

Figure 6.7: (a),(b),(c) The optimization of a short-pass, long-stop filter (via a Monte Carlo ray-trace) to enable higher amounts of photoluminescence trapping within our device architecture. We quantify the effects of filter edge location (a), short-pass transmittance (b), and long-stop reflectance (c) on the power output of the device under AM0 illumination. (d) The modeled vs. measured reflectance and transmittance of the multilayer, aperiodic stack filter consisting of alternating layers of Ta_2O_5/SiO_2.

chamber (LEDSupply) for ten mins and repeat for all four sides. Upon adhesion, we insulate adjacent cells to avoid shunting or shorting via UV26 and cure again for equal time. Finally, we connect in series three cells together (front to back contact) via a space-grade silver epoxy mixture and a pressurized syringe.

6.4.3 Preliminary Results and Analysis

Because these LSC devices are bound for lower-earth orbit, where the temperature can drastically change depending on the direct exposure to sunlight, we need to develop a sensitivity and durability analysis for temperature cycling (e.g., -100°C to $+60$°C) over many cycles at low pressures. Figures 6.8 and 6.9 show preliminary temperature cycling tests performed for each the Si- and GaAs-based LSC modules

under constant AM0 illumination, respectively. We find overall maximum power point stability over the course of testing for each of these modules—that is, no degradation in the power production over the course of the cycling. The Si-based LSC nearly attains 5mW·cm^{-2} in ideal conditions when the temperature is at its lowest (i.e., −100°C). Similarly, the GaAs-based device achieves nearly 5.5mW·cm^{-2} in ideal conditions where, for this thermal cycling test, the lowest temperature we consider is only −60°C. Of interest, we observe how, while in the Si-based LSC case current reaches a maximum for lower temperatures (presumably given by an increase in the luminophore PLQY), the same is not true for the GaAs-based LSC. In fact, we see that higher temperatures yield higher photocurrents. This remains a largely unanswered trend and warrants further study on temperature cycling of quantum dot luminophores within a waveguide.

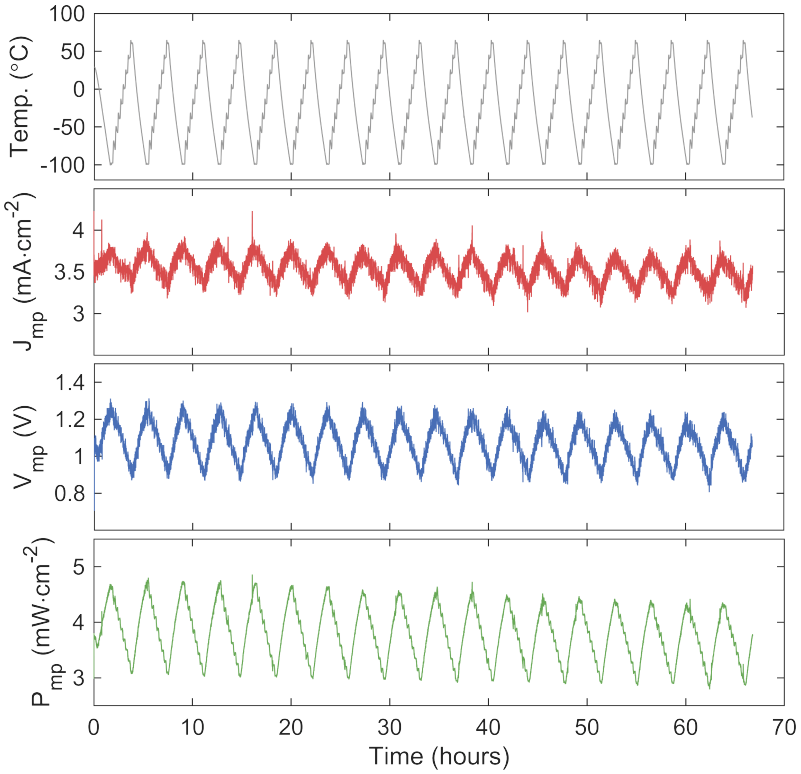

Figure 6.8: Temperature cycling studies of a first version silicon-based LSC device. Here we vary the temperature between +60°C and −100°C over many cycles (totaling over 65 hours of direct illumination under AM0 conditions). The LSC is held under vacuum. We measure the maximum power point (P_{mp}), voltage point (V_{mp}), and current point (J_{mp}).

Given our selection of materials, temperature cycling tests, and other flight-ready tests to ensure proper launch (e.g., mechanical stress testing), the LSC devices are prepared and ready for launch into lower-earth orbit. This will mark the first ever LSC flown in space and will, ideally, deliver us rich scientific insights into the performance and stability of LSCs as a candidate for space-based solar power.

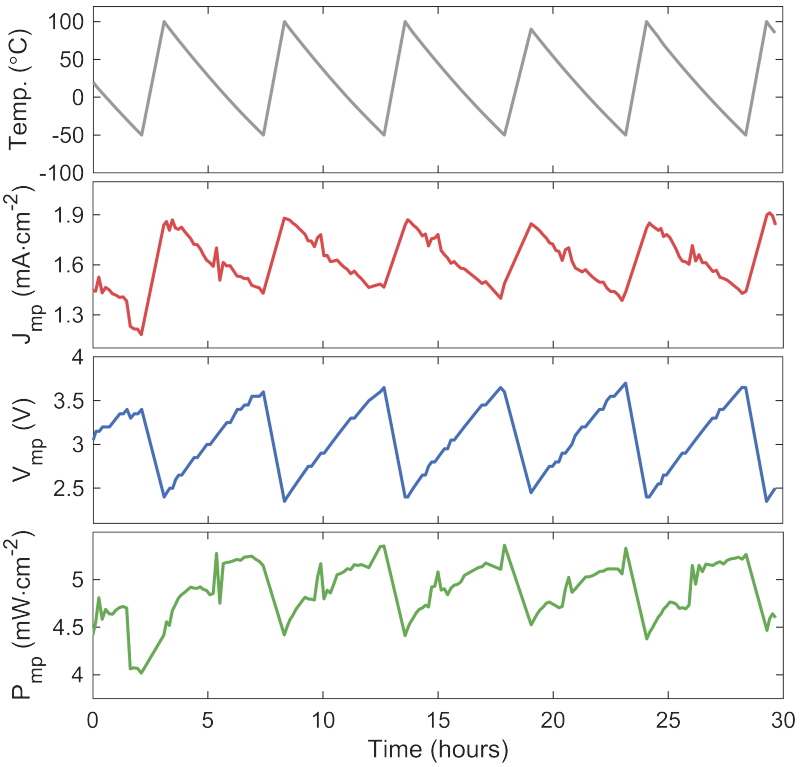

Figure 6.9: Temperature cycling studies of a first version GaAs-based LSC device. Here we vary the temperature between +100°C and −60°C over many cycles (totaling nearly 30 hours of direct illumination under AM0 conditions). The LSC is held under vacuum. We measure the maximum power point (P_{mp}), voltage point (V_{mp}), and current point (J_{mp}).

6.5 Ultra-Light, Aeronautical LSC Device Outlook

The LSC photovoltaic device offers unique advantages for ultra-lightweight solar applications—such as space-based solar power. While research in this field is early stage, the LSC (and more specifically nanophotonic waveguide structures that push the specific power to its limit) can, in its detailed balance limit, reach beyond 80kW/kg for the single junction case. In addition, we have shown a pathway for observing the durability of certain LSC material sets in lower-earth orbit. Considering such a dramatic departure from conventional LSC applications exemplifies the adaptability and flexibility of the LSC for a myriad energy generation settings.

CHAPTER 7

Conclusions & Outlook

In this thesis we have presented thermodynamic power efficiency limits, numerical modeling techniques, and experimental device fabrications and analyses for LSCs in the context of several application areas of interest.

Thermodynamically

1. We derived an expression for the dark radiative current of a general LSC.
2. We applied this expression to quantify the resulting open-circuit voltage limits.
3. We calculated the detailed balance limits (i.e., the power conversion efficiency limit via the photon flux balance given the luminophore and photovoltaic cell electronic bandgaps) for single junction, multijunction LSC, and Si/LSC tandem junction devices.

Computationally

1. We implemented a Monte Carlo ray-trace model, validated through literature base case testing and experimental comparison, versatile in its application to various form factors of LSCs.
2. We introduced an expression for calculating the probability of photoluminescence collection within a slab waveguide given the luminophore emission spatial location—whereby we supplement an existing closed-form model with this solid-angle expression.
3. We applied our models, specifically the ray-trace, to various LSC device application settings in order to unveil the effects of system and material properties on the power conversion efficiency (%) or specific power (kW/kg).
4. We described the importance of photoluminescence waveguide trapping on LSC performance, and we further developed our understanding of the potential for anisotropically emitting luminophores to enhance LSC performance.

Experimentally

1. We designed and fabricated single junction LSCs employing $CuInS_2$/ZnS or CdSe/CdS core/shell quantum dots coupled with GaAs or InGaP solar cells, respectively.

2. We assembled LSC/Si tandem modules (four terminal, optically stacked) with these two material sets and analyzed the multijunction power conversion efficiency performance within a laboratory solar simulator setting and in an outdoor testing facility.

3. We developed a hybrid concentrator system that marries luminescent and geometric concentration into a single device, and we provided preliminary insight into the concentration factor and angle of incidence characteristics.

4. We finally built an LSC employing a pin-wheel cell configuration while using space-qualified materials—intended for launch into lower-earth orbit—where we analyzed the power performance of GaAs- and Si-based devices through prolonged temperature cycling under constant AM0 exposure.

Through these efforts, we observed a world-record power conversion efficiency for a single junction LSC device approaching 10% under AM1.5g, 1-sun illumination. We also measured, for the first time, a tandem LSC/Si module with efficiencies beyond 12%. We provided quantitative roadmaps for reaching high device performance, within several application areas including: single junction, multijunction, building integrated, and space-solar photovoltaics. For the case of building integrated photovoltaics, and more specifically window or building curtain wall settings, we analyzed the technoeconomics and visual aesthetics for the case when LSCs blend into these form factors. Finally, we unveiled the effects of cell orientation within the luminescent waveguide and defined an area-scalable design where, upon increasing device sizes, the LSC maintains high efficiency given by the system geometric gain.

The Bright Future of LSCs

While this thesis detailed various physical processes, models, and application areas of LSC devices, there exist numerous topics of future research spanning myriad fields. Here, we identify only a few of these promising areas—including those venturing beyond photovoltaics.

Luminophore Anisotropy

As discussed in chapter 3.2, achieving in-plane oriented anisotropy of luminophores within the optical waveguide can lead to significant improvement in performance. While part of this thesis serves to quantify the extent of these improvements, experimental fabrication and materials optimization research stands to complement

our findings. One such approach is to fabricate photonic crystal waveguides that house periodic array elements containing the luminophore emitters, as described for example in Bauser et al.[95] and others[106,246].

As shown in Figure 7.1(a),(b),(c), we can design such a luminescent photonic crystal waveguide consisting of some high refractive index material (dielectric or semiconducting) with a certain two-dimensional repeated pattern of cylindrical holes—thereby creating a periodic perturbation in the refractive index of propagating photons. By dispersing luminophore emitters within the repeated cylindrical holes, the photonic crystal traps transverse electric and magnetic photoluminescence modes by increasing the local density of optical states[247,248]. Akin to a crystalline lattice crystal that exhibits certain allowed and forbidden electronic energies, the photonic crystal waveguide excludes certain propagation modes. Therefore, we can computationally determine the amount of photoluminescence trapping within the photonic crystal waveguide hole array, where Figure 7.1(d),(e) show the spectrally resolved amount of photoluminescence photon trapping (assuming a CdSe/CdS quantum dot emitter) and the electric field magnitude of photoluminescence within the waveguide via finite difference time domain modeling, respectively.

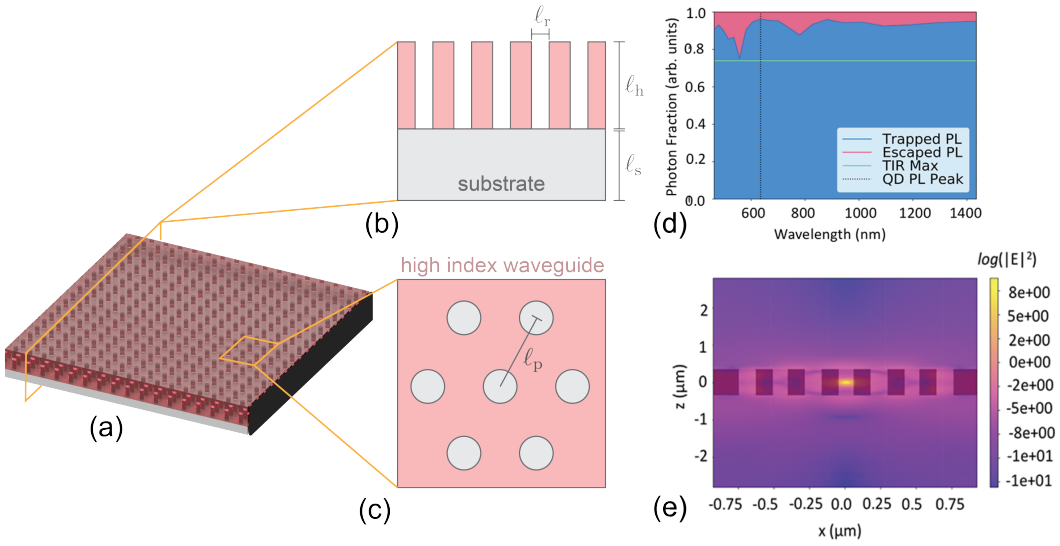

Figure 7.1: The concept of a hole-arrayed photonic crystal waveguide LSC device with a coupled photovoltaic cell on the perimeter edge. (a) A three dimensional rendering of the device with zoom-ins on the (b) profile view showing the diameter of the hole (ℓ_r), height of the high index waveguide layer (ℓ_h), and a (c) top view of the pitch between adjacent holes in a hexagonal array (ℓ_p). (d) and (e) show example finite difference time domain modeling (Lumerical) for the spectrally resolved trapping fraction of photoluminesced photons (d) and profile view of the electric field magnitude. Adapted from Bauser et al.[95].

Beyond inducing higher photoluminescence waveguide trapping efficiencies within photonic crystal waveguides, attaining anisotropic luminophore emission through spatial symmetry breaking in various organic dyes and semiconductor nanocrystals (e.g., quantum nanorods) remains an active area of research in both the LSC and liquid display fields[249–253]. Introduced in chapter 3.2 and shown conceptually in Figures 3.8 and 3.9, there exist numerous methods in order to enable preferential

emission by the luminophore into angles or waveguide modes that lie outside of the total internal reflection escape cone.

One such method that has garnered attention in areas outside of the LSC community consists of embedding luminophore emitters (e.g., quantum dot nanocrystals) within optically large dielectric spheres, termed nanojets[254–256]. Such photonic nanojets geometrically redirect incident (incident upon the dielectric sphere) or outgoing (emitted from embedded luminophore particles) photons via ray-optics and could present a novel pathway to enabling anisotropic concentration within LSCs. Figure 7.2 displays the wavelength (a),(b) and angle resolved (c),(d) spectra of an example photonic nanojet with modeled absorption and photoluminescence when a $CuInS_2/ZnS$ quantum dot is placed at the lateral edge of a 30μm diameter TiO_2 nanojet sphere.

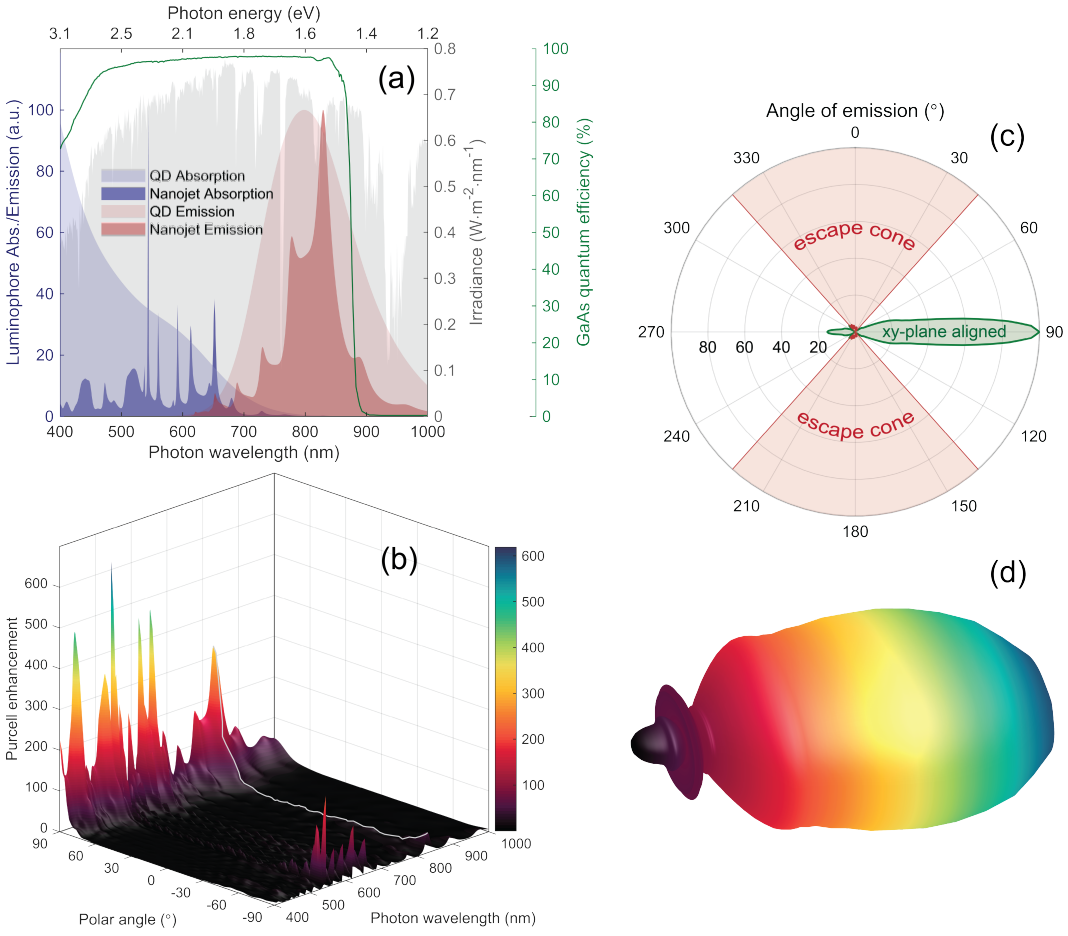

Figure 7.2: Example spectral and angular characteristics of a 30μm diameter TiO_2 nanojet sphere. (a) The wavelength resolved spectra of the photonic nanojet that employs a cluster of $CuInS_2/ZnS$ quantum dots at one edge, overlayed against an example GaAs cell spectrum for intended use in an LSC. (b) The Purcell enhancement of the emission of the photonic nanojet, quantum dot system with respect to photon wavelength and polar angle. (c),(d) A polar plot and conceptualized three dimensional emission profile of the nanojet/quantum dot system.

To obtain a preliminary analysis of how photonic nanojets hosting quantum dot luminophores could incorporate into an optical waveguide for LSC photovoltaic applications, we can apply our Monte Carlo ray-trace model employing these large spherical, directional emitters. As shown in Figure 7.3, the case when we align the nanojet photoluminescence to lie within the optical waveguide plane (xy), we achieve nearly twice as much power conversion efficiency compared to the case when we randomize the orientation of the nanojets. Future work in this area could focus on the optical consequences of aligning the nanojets within an oriented direction within the waveguide—similar to the forward emitters, decreasing the overall mean free path length of emitted photons.

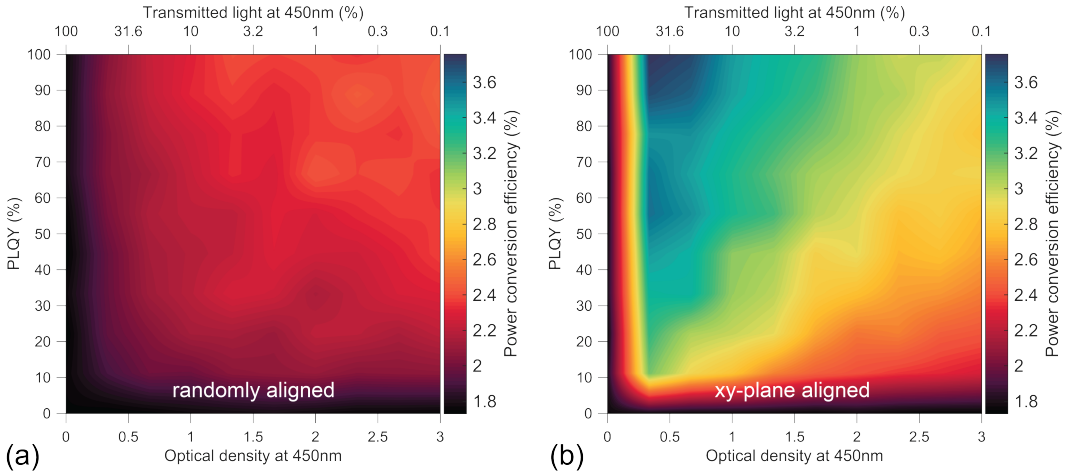

Figure 7.3: Preliminary Monte Carlo ray-trace results showing the power conversion efficiency vs optical density measured at 450nm for the (a) randomly oriented TiO_2 nanojets with embedded $CuInS_2/ZnS$ quantum dots at one edge and (b) xy-plane oriented nanojets.

Electrochromic-LSC Coupling

Chapter 4 introduced the concept of blending an LSC photovoltaic device into a conventional double pane insulated glass unit (i.e., window) for commercial high rise settings. While such building integrated photovoltaic solutions offer decreases in both the soft and balance of system costs and provide on-site electricity generation, other strategies to decrease the carbon emission footprint for commercial buildings exist. One such method involves actively tuning the visible and infrared transparency of building windows and façade. By controlling the irradiance entering into the building, heating, ventilation, and air-conditioning (HVAC) systems perform at significantly increased efficiencies and demand less energy[257–260].

Among others, electrochromic windows dynamically control the transmitted solar photon flux through manipulation of an externally controlled voltage bias[261–267]. In its most general form, an electrochromic window consists of seven layers: two outer glass panes (2), an electrically conductive layer on each pane to apply a voltage across (4), an ion storage layer (5) which hosts positively charged ions (e.g., H^+ or Li^+), an electrolyte layer through which ions can permeate under applied

voltage biasing (6), and an electrochromic layer (e.g., WO_2) where the mobilized ions and electrons from the bias combine with the metal atoms in the oxide (7). Under bias, when the ions and electrons combine with the metal oxide porous layer, the electrochromic reaches an absorptive state and, as such, appears tinted to our eye. Figure 7.4 depicts a conceptual rendering of the clear/opaque states of a double pane insulated glass unit.

Previous work describes efforts to self-power (i.e., self-bias) an electrochromic window through photovoltaic energy conversion—applying the voltage bias generated by the cell under illumination to self-powering the clear/opaque transition[268–270]. Recently it has been suggested to power these actively tunable windows through grid arrays of solar micro-cells. As shown by Potter et al.[271], the switching times decrease exponentially with the concentration of incident light onto these micro-cell arrays. As such, LSCs could offer a visually non-obtrusive method for monolithically integrating into an electrochromic window to drive this ion transport mechanism and, in so doing, decrease the switching times by orders of magnitude—shown in figure 7.4(b).

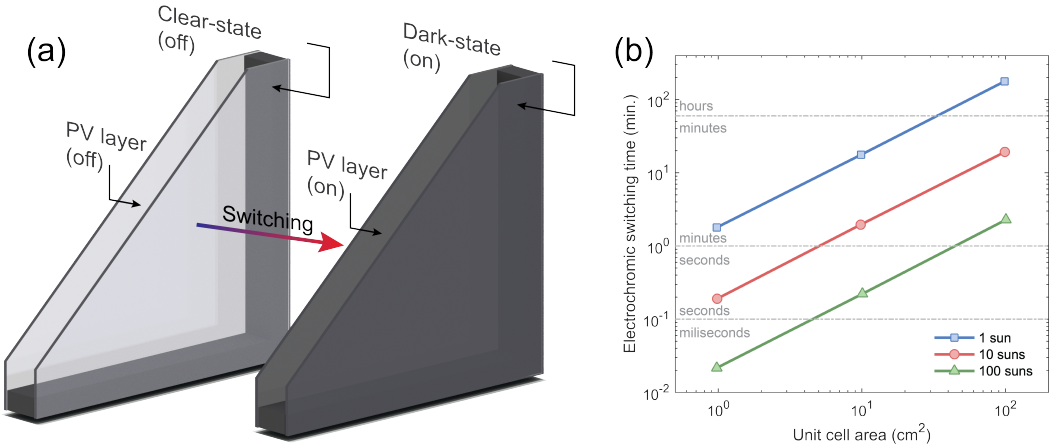

Figure 7.4: (a) A conceptual rendering of a double pane insulated glass unit employing an LSC photovoltaic device to supply the voltage bias for an electrochromic window—depicting the clear (off) and opaque (on) states. (b) The electrochromic window tinting switching times as a function of the repeated unit cell area consisting of a single solar micro-cell and the concentration of incident irradiance onto that cell for a self-powered electrochromic window. Adapted from Potter et al.[271].

Optical Étendue and the LSC

While there remain exciting research avenues for LSCs to continue developing and emerging directions that LSCs could venture into technologically, there remain unanswered thermodynamic questions concerning light management. Of significance to the photovoltaic community, the relationship between optical étendue and open-circuit voltage condition has, as of now, not been shown experimentally. In chapter 3 we developed a first-principles calculation of the dark radiative current term for a photovoltaic LSC. However, given poor photoluminescence waveguiding efficiencies,

saturation of device open-circuit voltage to the luminophore bandgap has not yet been measured.

More generally, the LSC represents a concentrating optical device that actively breaks the conservation of étendue: the solid angle of incident photons need not match the solid angle of outgoing photons owing to the Stokes shift of the luminophore. E. Yablonovitch noticed this asymmetry and, as a consequence, derived the well-known concentration factor limit for this class of optics—one whose concentration depends upon the Stokes shift (i.e., entropic heat generation) as given by Equation 1.17[99]. While provocative in theory, experiment has lagged far behind this limit. Only by increasing the waveguiding efficiency can we begin to observe these intrinsic thermodynamic advantages of the LSC.

By considering the thermodynamic consequences of étendue asymmetry, we can imagine future directions of LSC research. We could, for instance, consider the possibility of a luminescent waveguide exhibiting coherent photon emission[272]. Or we could ask about the consequences of optical étendue within nanophotonic crystal waveguides doped with aligned directional luminophores. The research topics presented in this thesis mark only but a few curiosities into the vast physical and technological phase space of the luminescent concentrator. And it is the hope of this author that such discussions catalyze further research interest within this exciting field.

APPENDIX A

A Stochastic Algorithm for LSCs

Here we provide the pseudo-code algorithm overview of the Monte Carlo ray-trace model for an LSC device, an example of the model branch tree for a variety of applications and how this code has been suited to specific settings throughout the course of this PhD, and finally a single version of the code written in Matlab/C code. To begin, algorithms 1, 2, and 3 define the Monte Carlo ray-trace pseudo-code, referred to more broadly in chapter 2. We note that R_s, R_{sh}, and n stand for the cell series and shunt resistances and ideality factor, respectively.

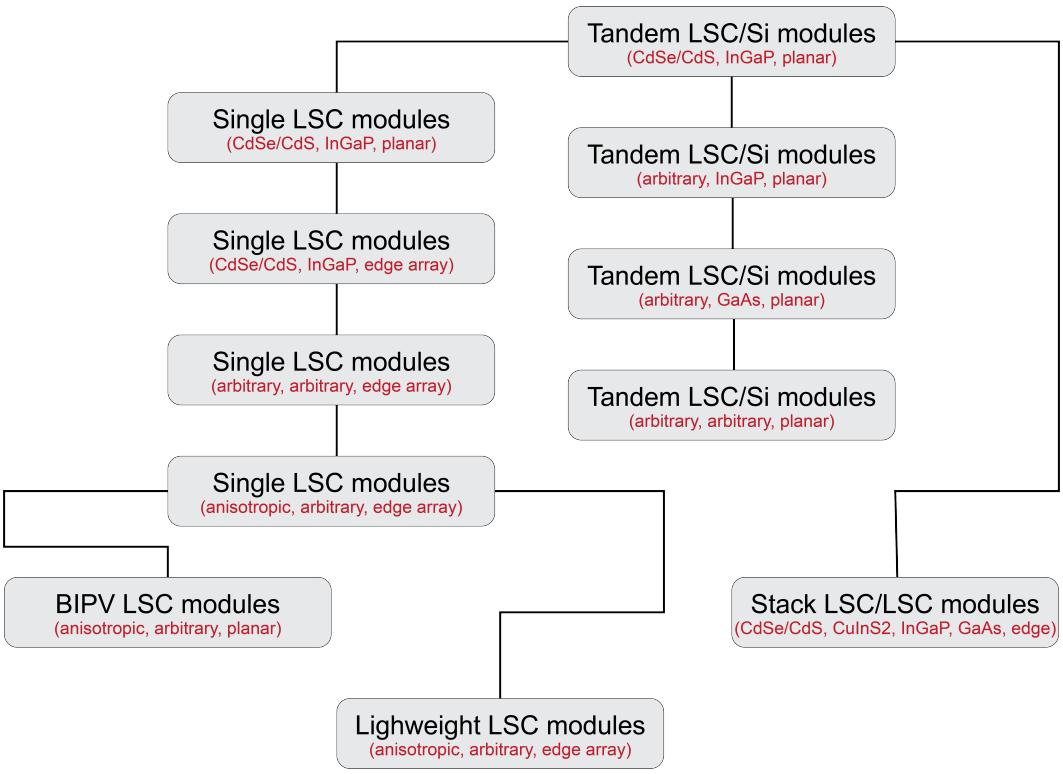

Figure A.1: An overview into how the Monte Carlo ray-trace model evolved throughout the course of this thesis given the myriad projects studied. The subtitle for each code block instance gives the luminophore, cell material, and cell orientation of that particular study.

Over the course of the thesis, the variety of LSC applications, form factors, and material types necessitated branching versions of the Monte Carlo ray-trace code. In all instances, however, the core ray-trace algorithm described remains. Figure A.1 provides a conceptual overview into the branches of the code for various projects and topics. The remainder of this appendix includes the entire implementation in Matlab/C code for an example implementation of the Monte Carlo ray-trace model.

The Main Method The following function calls the main method of the algorithm and executes the sub-functions of the model. Finally, the function saves a data file of the testing data given the parameter inputs.

```
%
%   FILE NAME:
%       mainMethod.m
%
%   FILE PURPOSE:
%       To call the sub-functions to setup the components
%       for a luminescent solar concentrator in order to
%       call the Monte Carlo ray-trace algorithm,
%       simulating how photons interact with such a device.
%-------------------------------------------------------------
function [lscCellEnergyBandgap, geometricGain,           ...
    JscTotal_lscCell, Voc_lscCell, FF_lscCell,           ...
    JscTotal_bottomCell, Voc_bottomCell, FF_bottomCell, ...
    powerEfficiency_module]                              ...
                                                         ...
= mainMethod(lumPLFileIndex, lumAbsFileIndex,            ...
    wgEdgeReflect, wgEdgeScatter, topFilterBool,         ...
    botFilterBool,lumPLQY, lumOpticalDensity,            ...
    lscCellThickness, lumScatterDistance,                ...
    wgSizeIndex, testDate, topFilterFileIndex,           ...
    botFilterFileIndex, lscCellBifacialBool,             ...
    lscCellEdgeLinedBool, lscCellNum,                    ...
    waveguideThickness, waveguideRefIndex,               ...
    percentNormal, botCellFileIndex, BlueFilterBool,     ...
    BlueFilterIndex, fracIllumIndex, anisotropicBool,    ...
    anisotropicFuncIndex, amolfAnisBool,                 ...
    amolfAnisFrac, detailedBalanceBool,                  ...
    lscCellFileIndex, ERE_lscCell, ERE_siCell,           ...
    topFilterScalingR, filterRefFactor,                  ...
    topFilterScalingT, filterTranFactor, iteration,      ...
    numIterations, incidentLightType, plTrappingMode,    ...
    plTrapping)

    %   Load all necessary data files:
    [reflect_lscCell, IQE_lscCell, reflect_bottomCell,   ...
        IQE_bottomCell, lumPLSpectrum, lumAbsSpectrum,   ...
        reflectFilterTop, transmitFilterTop,             ...
        reflectFilterBottom, transmitFilterBottom,       ...
        lumScattering, mirrorNameTop, mirrorNameBottom, ...
        reflectBlueFilter, anisotropicFunc,              ...
```

```
41          anisotropicFrac, lscCellEnergyBandgap,          ...
42          siCellEnergyBandgap, incidentLightSpectrumWatts,...
43          incidentLightSpectrumAmps,                      ...
44          incidentLightSpectrumWavelength]                ...
45                                                          ...
46      = dataLoading(lumPLFileIndex, lumAbsFileIndex,      ...
47          topFilterFileIndex, botFilterFileIndex,         ...
48          botCellFileIndex, BlueFilterIndex,              ...
49          anisotropicBool, anisotropicFuncIndex,          ...
50          amolfAnisBool, amolfAnisFrac,                   ...
51          detailedBalanceBool, lscCellFileIndex,          ...
52          topFilterScalingR, filterRefFactor,             ...
53          topFilterScalingT, filterTranFactor,            ...
54          incidentLightType);
55
56      %   Display the run number and save file header
57      %   string:
58      [prefix]                                            ...
59                                                          ...
60      = parameterDisplay(lumPLFileIndex, topFilterBool,   ...
61          botFilterBool, testDate, iteration, numIterations);
62
63      %   Load all of the constants necessary to run this
64      %   simulation:
65      [wavelengthStep, simWavelengthRange,                ...
66          dataWavelengthRange, photonStep, nAir, nGlass,  ...
67          nPolymer, wavelengthReference_450nmIndex,       ...
68          gridSize, spotSize, fractionCellCovered,        ...
69          xInject, yInject, numXPoints, numYPoints,       ...
70          numSimWavelength, xSize, ySize]                 ...
71                                                          ...
72       = constants(wgSizeIndex, fracIllumIndex,           ...
73          waveguideRefIndex);
74
75      %   Initialize the filter spectrum if applicable:
76      [reflectFilterTop_pPol, transmitFilterTop_pPol,     ...
77          reflectFilterTop_sPol, transmitFilterTop_sPol,  ...
78          reflectFilterBottom_pPol,                       ...
79          transmitFilterBottom_pPol,                      ...
80          reflectFilterBottom_sPol,                       ...
81          transmitFilterBottom_sPol]                      ...
82                                                          ...
83      = initializeFilter(reflectFilterTop,                ...
84          transmitFilterTop, reflectFilterBottom,         ...
85          transmitFilterBottom);
86
87      %   Setup PL for luminophore:
88      [lumPLSpectrumCompact]                              ...
89                                                          ...
90      = initializeLuminophore(lumPLSpectrum);
91
92      %   Set the scattering values for the polymer matrix
93      %   and the glass layer:
94      [probMatrixScatter, probGlassScatter]               ...
```

```
95                                                              ...
96      = initializeScattering(lumScattering,                   ...
97          dataWavelengthRange, lumScatterDistance,            ...
98          photonStep);
99
100     %   Set the device geometry for the LSC:
101     [geometry, plmaSize, solarCell, geometricGain,          ...
102         illuminationArea]                                   ...
103                                                             ...
104     = initializeGeometry(spotSize, xSize, ySize,            ...
105         lscCellThickness, gridSize, lscCellBifacialBool,...
106         waveguideThickness, lscCellEdgeLinedBool,           ...
107         lscCellNum);
108
109     %   Set the luminophore probability of a photon
110     %   absorbed in waveguide:
111     [probNotAbsPolymer]                                     ...
112                                                             ...
113     = luminophoreConcentration(waveguideThickness,          ...
114         lumAbsSpectrum, wavelengthReference_450nmIndex, ...
115         lumOpticalDensity, photonStep);
116
117     %   Set data structures for the monte carlo ray
118     %   trace to export to:
119     [collectPhotonOrigin_lscCell,                           ...
120         collectPhotonWavelength_lscCell,                    ...
121         collectPhotonDir_lscCell,                           ...
122         shortCircuitCurrent_lscCell,                        ...
123         collectPhotonOrigin_bottomCell,                     ...
124         collectPhotonWavelength_bottomCell,                 ...
125         collectPhotonDir_bottomCell,                        ...
126         shortCircuitCurrent_bottomCell, incidentPower,  ...
127         numFilterBounces, numLSCEdgeBounces,                ...
128         numWgModeBounces, numPLEvents, numPhotonsLost]  ...
129                                                             ...
130     = initializeOutVar(numSimWavelength, numXPoints,    ...
131         numYPoints, xInject, yInject);
132
133     %   Run the monteCarlo method.
134     parfor wavelengthIndex = 1:numSimWavelength
135         %   Start the clock for this specific iteration:
136         startTime = clock;
137         %   Call the Monte Carlo function to simulate
138         %   incident photons at the wavelengthIndex:
139         [collectPhotonOrigin_lscCell(                       ...
140             wavelengthIndex,:,:,:),                         ...
141             collectPhotonWavelength_lscCell(                ...
142             wavelengthIndex,:,:),                           ...
143             collectPhotonDir_lscCell(                       ...
144             wavelengthIndex,:,:,:,:),                       ...
145             shortCircuitCurrent_lscCell(                    ...
146             wavelengthIndex),                               ...
147             collectPhotonOrigin_bottomCell(                 ...
148             wavelengthIndex,:,:,:),                         ...
```

```
149             collectPhotonWavelength_bottomCell(         ...
150             wavelengthIndex,:,:),                       ...
151             collectPhotonDir_bottomCell(                ...
152             wavelengthIndex,:,:,:,:),                   ...
153             shortCircuitCurrent_bottomCell(             ...
154             wavelengthIndex),                           ...
155             incidentPower(wavelengthIndex),             ...
156             numPhotonsLost(wavelengthIndex,:),          ...
157             numFilterBounces(wavelengthIndex,:,:),      ...
158             numPLEvents(wavelengthIndex,:,:),           ...
159             numLSCEdgeBounces(wavelengthIndex,:,:),     ...
160             numWgModeBounces(wavelengthIndex,:,:)]      ...
161                                                         ...
162         = monteCarlo_mex(lumPLQY, solarCell,            ...
163             fractionCellCovered, xInject, yInject,      ...
164             geometry, plmaSize, probMatrixScatter,      ...
165             probGlassScatter, wavelengthIndex,          ...
166             wavelengthStep, probNotAbsPolymer,          ...
167             photonStep, reflect_lscCell, IQE_lscCell,   ...
168             reflect_bottomCell, IQE_bottomCell,         ...
169             lumPLSpectrumCompact, nAir, nGlass,         ...
170             nPolymer, topFilterBool, botFilterBool,     ...
171             reflectFilterTop_sPol,                      ...
172             transmitFilterTop_sPol,                     ...
173             reflectFilterTop_pPol,                      ...
174             transmitFilterTop_pPol,                     ...
175             reflectFilterBottom_pPol,                   ...
176             transmitFilterBottom_pPol,                  ...
177             reflectFilterBottom_sPol,                   ...
178             transmitFilterBottom_sPol,                  ...
179             wgEdgeReflect, wgEdgeScatter,               ...
180             lscCellBifacialBool, simWavelengthRange,    ...
181             dataWavelengthRange, gridSize,              ...
182             percentNormal, BlueFilterBool,              ...
183             reflectBlueFilter, anisotropicBool,         ...
184             amolfAnisBool, anisotropicFrac,             ...
185             incidentLightSpectrumWatts,                 ...
186             incidentLightSpectrumAmps,                  ...
187             incidentLightSpectrumWavelength,            ...
188             lscCellEdgeLinedBool, lscCellNum,           ...
189             plTrappingMode, plTrapping);
190         %   Stop the clock for this iteration and
191         %   calculate the toal time:
192         totalTime = clock - startTime;
193         %   Save the total time taken for this iteration:
194         timeSpent(wavelengthIndex) = 60*60*24*          ...
195             totalTime(3) + 60*60*totalTime(4) +         ...
196             60*totalTime(5) + totalTime(6);
197         %   Display the number of seconds taken to
198         %   simulate this iteration:
199         disp(strcat(num2str(simWavelengthRange(         ...
200             wavelengthIndex)),' nm light: ',            ...
201             num2str(timeSpent(                          ...
202             wavelengthIndex)),' seconds to compute;'));
```

```
203     end
204
205     %   If using the detailed balance model:
206     if detailedBalanceBool
207         %   Calculate the figures of merit:
208         [collectPhotonWavelength_lscCell,                ...
209             collectPhotonWavelength_bottomCell,          ...
210             collectPhotonRaw_lscCell,                    ...
211             collectPhotonRaw_bottomCell,                 ...
212             IscTotal_lscCell, IscTotal_bottomCell,       ...
213             JscTotal_lscCell, JscTotal_bottomCell,       ...
214             powerTotalIn, Voc_lscCell, Voc_bottomCell,   ...
215             FF_lscCell, FF_bottomCell,                   ...
216             powerTotalOut_lscCell,                       ...
217             powerTotalOut_bottomCell,                    ...
218             powerTotalOut_module,                        ...
219             powerEfficiency_module]                      ...
220                                                          ...
221         = outputVarCalc_detailedBalance(                 ...
222             collectPhotonWavelength_lscCell,             ...
223             collectPhotonWavelength_bottomCell,          ...
224             shortCircuitCurrent_lscCell,                 ...
225             shortCircuitCurrent_bottomCell,              ...
226             numSimWavelength, illuminationArea,          ...
227             incidentPower, geometricGain,                ...
228             wavelengthStep, lscCellEnergyBandgap,        ...
229             siCellEnergyBandgap, ERE_lscCell, ERE_siCell);
230     else
231         [collectPhotonWavelength_lscCell,                ...
232             collectPhotonWavelength_bottomCell,          ...
233             collectPhotonRaw_lscCell,                    ...
234             collectPhotonRaw_bottomCell,                 ...
235             IscTotal_lscCell, IscTotal_bottomCell,       ...
236             JscTotal_lscCell, JscTotal_bottomCell,       ...
237             powerTotalIn, Voc_lscCell, Voc_bottomCell,   ...
238             FF_lscCell, FF_bottomCell,                   ...
239             powerTotalOut_lscCell,                       ...
240             powerTotalOut_bottomCell,                    ...
241             powerTotalOut_module,                        ...
242             powerEfficiency_module]                      ...
243                                                          ...
244         = outputVarCalc(collectPhotonWavelength_lscCell,...
245             collectPhotonWavelength_bottomCell,          ...
246             shortCircuitCurrent_lscCell,                 ...
247             shortCircuitCurrent_bottomCell,              ...
248             numSimWavelength, illuminationArea,          ...
249             incidentPower, geometricGain, wavelengthStep);
250     end
251
252     %   Save the simulation data and workspace:
253     saveFile(prefix,simWavelengthRange,                  ...
254         dataWavelengthRange, lscCellThickness, xSize,    ...
255         ySize, spotSize, lumPLSpectrum,                  ...
256         lumAbsSpectrum, lumOpticalDensity, lumPLQY,      ...
```

```
257         lumScatterDistance, wgEdgeReflect,                ...
258         wgEdgeScatter, geometricGain,                     ...
259         collectPhotonRaw_lscCell,                         ...
260         collectPhotonRaw_bottomCell,                      ...
261         collectPhotonWavelength_lscCell, xInject,         ...
262         yInject, collectPhotonWavelength_bottomCell,      ...
263         numPhotonsLost, IscTotal_lscCell,                 ...
264         IscTotal_bottomCell, testDate,                    ...
265         topFilterFileIndex, botFilterFileIndex,           ...
266         lscCellBifacialBool, JscTotal_lscCell,            ...
267         Voc_lscCell, Voc_bottomCell, FF_lscCell,          ...
268         FF_bottomCell, JscTotal_bottomCell,               ...
269         powerTotalOut_bottomCell,                         ...
270         powerTotalOut_lscCell, powerTotalOut_module,      ...
271         powerTotalIn, powerEfficiency_module,             ...
272         collectPhotonDir_bottomCell,                      ...
273         collectPhotonDir_lscCell, numFilterBounces,       ...
274         numLSCEdgeBounces, numWgModeBounces,              ...
275         waveguideThickness, mirrorNameTop,                ...
276         mirrorNameBottom, numPLEvents,                    ...
277         probNotAbsPolymer, reflect_lscCell,               ...
278         reflect_bottomCell, IQE_lscCell, IQE_bottomCell,...
279         lumPLSpectrumCompact, reflectFilterTop_sPol,      ...
280         reflectFilterBottom_sPol, percentNormal,          ...
281         botCellFileIndex, reflectBlueFilter,              ...
282         BlueFilterBool, anisotropicBool,                  ...
283         anisotropicFuncIndex, lscCellEnergyBandgap,       ...
284         filterRefFactor, anisotropicFrac,                 ...
285         ERE_lscCell, waveguideRefIndex, anisotropicFunc);
286 end
```

The Monte Carlo For brevity, we omit the code related to the loading of input parameters/variables as well as the initialization of the layered LSC architecture. The primary method, `monteCarlo.m`, executes the algorithm outlined in 1–3. Below is one version of the implemented model.

```
1  %
2  %   FILE NAME:
3  %       monteCarlo.m
4  %
5  %   FILE PURPOSE:
6  %       To trace incident photons through the luminescent
7  %       solar concentrator device, determing if photons
8  %       are either: a) collected by a solar cell
9  %       (embedded or underyling), or b) lost/terminated
10 %       via one of the loss mechanisms.
11 %-------------------------------------------------------------
12 function [collectPhotonOrigin_lscCell,                    ...
13     collectPhotonWavelength_lscCell,                      ...
14     collectPhotonDir_lscCell,                             ...
15     shortCircuitCurrent_lscCell,                          ...
```

```
16      collectPhotonOrigin_bottomCell,                          ...
17      collectPhotonWavelength_bottomCell,                      ...
18      collectPhotonDir_bottomCell,                             ...
19      shortCircuitCurrent_bottomCell,                          ...
20      incidentPower, numPhotonsLost,                           ...
21      numFilterBounces, numPLEvents,                           ...
22      numLSCEdgeBounces, numWgModeBounces]                     ...
23                                                               ...
24  = monteCarlo(lumPLQY, solarCell, fractionCellCovered,        ...
25      xInject, yInject, geometry, plmaSize,                    ...
26      probMatrixScatter, probGlassScatter,                     ...
27      simWavelengthIndex, wavelengthStep,                      ...
28      probNotAbsPolymer, photonStep, reflect_lscCell,          ...
29      IQE_lscCell, reflect_bottomCell, IQE_bottomCell,         ...
30      lumPLSpectrum, nAir, nGlass, nPolymer,                   ...
31      topFilterBool, botFilterBool,                            ...
32      reflectFilterTop_sPol, transmitFilterTop_sPol,           ...
33      reflectFilterTop_pPol, transmitFilterTop_pPol,           ...
34      reflectFilterBottom_pPol, transmitFilterBottom_pPol,...
35      reflectFilterBottom_sPol, transmitFilterBottom_sPol,...
36      wgEdgeReflect, wgEdgeScatter, lscCellBifacialBool,       ...
37      simWavelengthRange, dataWavelengthRange, gridSize,       ...
38      percentNormal, BlueFilterBool, reflectBlueFilter,        ...
39      anisotropicBool, amolfAnisBool, anisotropicFrac,         ...
40      incidentLightSpectrumWatts,                              ...
41      incidentLightSpectrumAmps,                               ...
42      incidentLightSpectrumWavelength,                         ...
43      lscCellEdgeLinedBool, lscCellNum,                        ...
44      plTrappingMode, plTrapping)
45
46      %   Initialize the data structures for this iteration:
47      [collectPhotonOrigin_lscCell,                            ...
48          collectPhotonOrigin_bottomCell,                      ...
49          collectPhotonWavelength_lscCell,                     ...
50          collectPhotonWavelength_bottomCell,                  ...
51          shortCircuitCurrent_lscCell,                         ...
52          shortCircuitCurrent_bottomCell, incidentPower,       ...
53          numFilterBounces,                                    ...
54          numLSCEdgeBounces, numPLEvents,                      ...
55          numWgModeBounces,                                    ...
56          collectPhotonDir_lscCell,                            ...
57          collectPhotonDir_bottomCell,                         ...
58          solarCell,numPhotonsLost]                            ...
59                                                               ...
60      = initializeOutVarMonteCarlo(xInject, yInject,           ...
61      solarCell);
62      %   Import the random number generator, 'rng':
63      coder.extrinsic('rng');
64      %   Initialize the random number generator:
65      rng('shuffle');
66
67      %   BEGINNING OF THE MONTE CARLO RAY-TRACE.
68      %-------------------------------------------------------
69      %   For all x gridpoints:
```

```
70      for xPos = 1:size(xInject,2)
71          %   For all y gridpoints:
72          for yPos = 1:size(yInject,2)
73              % Termination boolean:
74              done = false;
75              %   Boolean for if photon was absorbed by
76              %   luminophores.
77              photonAbsorbed = false;
78
79
80              %   INITIALIZE THE PHOTON.
81              %-----------------------------------------------
82              %   If photon strikes at normal incidence:
83              if rand < percentNormal
84                  %   Initilize the photon's temporary
85                  %   velocity:
86                  tempVel = [0 0 -1];
87                  %   Initilize the polarization angle of
88                  %   the photon:
89                  photonPolarization = 0;
90                  %   Set the cosineFactor to 1:
91                  cosineFactor = 1;
92              else
93                  %   Generate a random value:
94                  angleGen = rand;
95                  %   Generate a random polar angle (wrt z
96                  %   axis):
97                  polarAngle = (pi/2)*angleGen + pi/2;
98                  %   Generate a random azimuthal angle
99                  %   (wrt x axis):
100                 azimuthalAngle = (2*pi)*rand;
101                 %   Now convert this into Cartesian:
102                 tempVel = [cos(azimuthalAngle)*sin(     ...
103                     polarAngle) sin(azimuthalAngle)*    ...
104                     sin(polarAngle) cos(polarAngle)];
105                 %   Initilize the polarization of the
106                 %   photon:
107                 photonPolarization = 0;
108                 %   Calculate cosine loss factor:
109                 cosineFactor = abs(cos(polarAngle));
110             end
111
112
113             %   CALCULATE SPECTRA DETAILS.
114             %-----------------------------------------------
115             %   Calculate the wavelength index for the
116             %   spectral data
117             %   (300:1500nm):
118             dataWavelengthIndex = find(                 ...
119                 simWavelengthRange(simWavelengthIndex)  ...
120                 == dataWavelengthRange);
121             %   Convert to scalar for C compatability:
122             dataWavelengthIndex = dataWavelengthIndex(1);
123             %   Incident power from this photon:
```

```
124             incidentPower(xPos,yPos)                        ...
125             = incidentPowerIntegrator(                      ...
126             simWavelengthIndex, wavelengthStep,             ...
127             simWavelengthRange, cosineFactor, gridSize,     ...
128             incidentLightSpectrumWavelength,                ...
129             incidentLightSpectrumWatts);
130
131
132             %   ASSIGN THE INITIAL POSITION FOR THE
133             %   INCOMING PHOTON.
134             %-----------------------------------------------
135             %   Assign start position directly at top
136             %   of LSC:
137             startPos = [xInject(xPos) yInject(yPos)     ...
138                 geometry(3,5)];
139             %   Update position given velocity and step:
140             tempPos = startPos + tempVel/2*photonStep;
141             %   Keep track of previous position:
142             oldPos = startPos - tempVel/2*photonStep;
143
144
145             %   CHECK IF THERE IS ANY TOP REFLECTION.
146             %-----------------------------------------------
147             %   If we are using a blue-filter:
148             if BlueFilterBool
149                 %   Calculate current polar angle:
150                 polarAngleTemp = acos(abs(tempVel(3)));
151                 %   Calculate current polar angle
152                 %   (degrees) (+1 for index):
153                 polarAngleTemp_deg = floor(             ...
154                     polarAngleTemp*180/pi) + 1;
155                 %   Calculate s-part of polarization:
156                 s_part = cos(photonPolarization)^2;
157                 %   Calculate p-part of polarization:
158                 p_part = sin(photonPolarization)^2;
159                 %   If filter reflects incident photon:
160                 if rand < (s_part * reflectBlueFilter(  ...
161                 dataWavelengthIndex,polarAngleTemp_deg) ...
162                 + p_part *  reflectBlueFilter(          ...
163                 dataWavelengthIndex, polarAngleTemp_deg))
164                     %   Add to photons lost (1 = top
165                     %   surf. loss):
166                     numPhotonsLost(1) =                 ...
167                         numPhotonsLost(1) + 1;
168                     %   Then this photon is lost:
169                     done = true;
170                 end
171             end
172             %   If there we are using a top filter:
173             if topFilterBool
174                 %   Calculate current polar angle:
175                 polarAngleTemp = acos(abs(tempVel(3)));
176                 %   Calculate current polar angle
177                 %   (degrees) (+1 for index):
```

```
178                 polarAngleTemp_deg = floor(             ...
179                     polarAngleTemp*180/pi) + 1;
180                 %   Calculate s-part of polarization:
181                 s_part = cos(photonPolarization)^2;
182                 %   Calculate p-part of polarization:
183                 p_part = sin(photonPolarization)^2;
184                 %   If filter reflects or absorbs photon:
185                 if rand > (s_part *                     ...
186                         transmitFilterTop_sPol(         ...
187                 dataWavelengthIndex,polarAngleTemp_deg) ...
188                 + p_part * transmitFilterTop_pPol(      ...
189                 dataWavelengthIndex,polarAngleTemp_deg))
190                     %   Add to photons lost (1 = top    ...
191                     %   surf. loss):
192                     numPhotonsLost(1) =                 ...
193                     numPhotonsLost(1) + 1;
194                     %   Then this photon is lost:
195                     done = true;
196                 end
197             end
198
199
200             %   LOOP THROUGH UNTIL PHOTON IS LOST OR
201             %   COLLECTED.
202             %-----------------------------------------------
203             %   While the photon is not lost:
204             while done == false
205
206
207                 %   CHECK IF PHOTON HITS SOLAR CELL(S).
208                 %---------------------------------------
209                 %   If the photon position is within the
210                 %   LSC solar cell:
211                 if tempPos(1) ≤ solarCell(1,2) &&       ...
212                    tempPos(1) ≥ solarCell(1,1) &&       ...
213                    tempPos(2) ≤ solarCell(2,2) &&       ...
214                    tempPos(2) ≥ solarCell(2,1) &&       ...
215                    tempPos(3) ≤ solarCell(3,2) &&       ...
216                    tempPos(3) ≥ solarCell(3,1) &&       ...
217                    ¬lscCellEdgeLinedBool
218                     %   If the photon strikes solar cell
219                     %   top or bottom:
220                     if oldPos(3) > solarCell(3,2) ||    ...
221                        oldPos(3) < solarCell(3,1)
222                         %   If the photon came in from
223                         %   the top:
224                         if oldPos(3) > solarCell(3,2)
225                             %   Record the photon's
226                             %   direction:
227                             collectPhotonDir_lscCell(1, ...
228                                 xPos, yPos,:) = tempVel;
229                         else
230                             %   Record the photon's
231                             %   direction:
```

```
232                         collectPhotonDir_lscCell(2, ...
233                             xPos, yPos,:) = tempVel;
234                     end
235                     %   Calculate current polar angle
236                     %   (degrees) (+1 for index):
237                     polarAngleTemp_deg = floor(     ...
238                         180/pi * acos(abs(          ...
239                         tempVel(3)))) + 1;
240                     %   If LSC cell top doesn't
241                     %   reflect photon:
242                     if rand > reflect_lscCell(      ...
243                             dataWavelengthIndex,    ...
244                             polarAngleTemp_deg) &&  ...
245                             rand >                  ...
246                             fractionCellCovered &&  ...
247                             oldPos(3) > solarCell(3,2)
248                         %   If exciton is collected:
249                         if rand < IQE_lscCell(      ...
250                                 dataWavelengthIndex,...
251                                 polarAngleTemp_deg)
252                             %   Record the position:
253                             collectPhotonOrigin_    ...
254                             lscCell(xPos,yPos,:)    ...
255                             = tempPos;
256                             %   Record the original
257                             %   wavelength:
258                             collectPhotonWave       ...
259                                 length_lscCell(xPos,...
260                                 yPos) =             ...
261                                 simWavelengthIndex;
262                             %   Calculate short
263                             %   circuit current:
264                             shortCircuitCurrent_    ...
265                                 lscCell(xPos, yPos) ...
266                                 = outputCurrent     ...
267                                 Integrator(         ...
268                                 simWavelengthIndex, ...
269                                 wavelengthStep,     ...
270                                 simWavelengthRange, ...
271                                 cosineFactor,       ...
272                                 gridSize,           ...
273                                 incidentLight       ...
274                                 SpectrumAmps,       ...
275                                 incidentLight       ...
276                                 SpectrumWavelength);
277                             %   Photon is terminated:
278                             done=true;
279                             %   Break from the while
280                             %   loop:
281                             break;
282                         %   Else is non-radiatively
283                         %   recombined:
284                         else
285                             %   Add to photons lost
```

```
286                         %   (9=lsc cell loss):
287                         numPhotonsLost(9) =     ...
288                             numPhotonsLost(9)+1;
289                         %   Photon is terminated:
290                         done = true;
291                         %   Break from the while
292                         %   loop:
293                         break;
294                     end
295                 %   If LSC cell bottom doesn't
296                 %   reflect (bifacial):
297                 elseif rand > reflect_lscCell(  ...
298                 dataWavelengthIndex,            ...
299                 polarAngleTemp_deg) &&          ...
300                 rand > fractionCellCovered &&   ...
301                 oldPos(3) < solarCell(3,1) &&   ...
302                 lscCellBifacialBool
303                     %   If exciton is collected:
304                     if rand < IQE_lscCell(      ...
305                         dataWavelengthIndex,    ...
306                         polarAngleTemp_deg)
307                         %   Record the position:
308                         collectPhotonOrigin_    ...
309                             lscCell(xPos,yPos,:)...
310                             = tempPos;
311                         %   Record the original
312                         %   wavelength:
313                         collectPhotonWavelength ...
314                             _lscCell(xPos,      ...
315                             yPos) =             ...
316                             simWavelengthIndex;
317                         %   Calculate short circuit
318                         %   current:
319                         shortCircuitCurrent_    ...
320                         lscCell(xPos, yPos)     ...
321                         = outputCurrent         ...
322                         Integrator(             ...
323                         simWavelengthIndex,     ...
324                         wavelengthStep,         ...
325                         simWavelengthRange,     ...
326                         cosineFactor,           ...
327                         gridSize,               ...
328                         incidentLightSpectrum   ...
329                         Amps,                   ...
330                         incidentLightSpectrum   ...
331                         Wavelength);
332                         %   Photon is terminated:
333                         done=true;
334                         %   Break from the while
335                         %   loop:
336                         break;
337                     %   Else is non-radiatively
338                     %   recombined:
339                     else
```

```
340                             %   Add to photons lost
341                             %   (9=lsc cell loss):
342                             numPhotonsLost(9) =     ...
343                                 numPhotonsLost(9)+1;
344                             %   Photon is terminated:
345                             done = true;
346                             %   Break from the while
347                             %   loop:
348                             break;
349                         end
350                     %   Else the photon is reflected
351                     %   from LSC cell:
352                     else
353                         %   Reflect z-velocity:
354                         tempVel(3) = -tempVel(3);
355                         %   Update the temporary
356                         %   position:
357                         tempPos(3) = tempPos(3) +   ...
358                             tempVel(3) * photonStep;
359                     end
360                 %   Photon strikes front or back:
361                 elseif oldPos(2) > solarCell(2,2) ||...
362                        oldPos(2) < solarCell(2,1)
363                     %   If the photon came in from the
364                     %   front:
365                     if oldPos(2) > solarCell(2,2)
366                         %   Record the photon's
367                         %   direction:
368                         collectPhotonDir_lscCell(3,...
369                             xPos, yPos,:) = tempVel;
370                     else
371                         %   Record the photon's
372                         %   direction:
373                         collectPhotonDir_lscCell(   ...
374                             4,xPos, yPos,:)         ...
375                             = tempVel;
376                     end
377                     %   Calculate current polar angle
378                     %   (degrees) (+1 for index):
379                     polarAngleTemp_deg = floor(180  ...
380                         /pi * acos(abs(tempVel(3))))...
381                         + 1;
382                     %   If the photon is not reflected
383                     %   by the solar cell:
384                     if rand > reflect_lscCell(      ...
385                             dataWavelengthIndex,    ...
386                             polarAngleTemp_deg)
387                         %   If exciton is collected:
388                         if rand < IQE_lscCell(      ...
389                                 dataWavelengthIndex,...
390                                 polarAngleTemp_deg)
391                             %   Record the position:
392                             collectPhotonOrigin_    ...
393                                 lscCell(xPos,yPos,:)...
```

```
394                                 = tempPos;
395                             %   Record the original
396                             %   wavelength:
397                             collectPhotonWavelength_...
398                                 lscCell(xPos,       ...
399                                 yPos) =             ...
400                                 simWavelengthIndex;
401                             %   Calculate short
402                             %   circuit current:
403                             shortCircuitCurrent_    ...
404                                 lscCell(xPos, yPos) ...
405                                 = outputCurrent     ...
406                                 Integrator(         ...
407                                 simWavelengthIndex, ...
408                                 wavelengthStep,     ...
409                                 simWavelengthRange, ...
410                                 cosineFactor,       ...
411                                 gridSize,           ...
412                                 incidentLight       ...
413                                 SpectrumAmps,       ...
414                                 incidentLight       ...
415                                 SpectrumWavelength);
416                             %   Photon is terminated:
417                             done=true;
418                             %   Break from the while
419                             %   loop:
420                             break;
421                         %   Else is non-radiatively
422                         %   recombined:
423                         else
424                             %   Add to photons lost
425                             %   (9=lsc cell loss):
426                             numPhotonsLost(9) =     ...
427                                 numPhotonsLost(9)+1;
428                             %   Photon is terminated:
429                             done = true;
430                             %   Break from the while
431                             %   loop:
432                             break;
433                         end
434                     %   Else the photon is reflected
435                     %   from LSC cell:
436                     else
437                         %   Reflect y-velocity:
438                         tempVel(2) = -tempVel(2);
439                         %   Update the temporary
440                         %   position:
441                         tempPos(2) = tempPos(2) +   ...
442                         tempVel(2) * photonStep;
443                     end
444                 %   Photon strikes left or right sides:
445                 else
446                     %   If the photon came in from
447                     %   the right side:
```

```
448                         if oldPos(1) > solarCell(2,2)
449                             %   Record the photon's
450                             %   direction:
451                             collectPhotonDir_lscCell(5, ...
452                                 xPos,yPos,:) = tempVel;
453                         else
454                             %   Record the photon's
455                             %   direction:
456                             collectPhotonDir_lscCell(   ...
457                                 6,xPos,yPos,:) = tempVel;
458                         end
459                         %   Calculate current polar angle
460                         %   (degrees) (+1 for
461                         %   index):
462                         polarAngleTemp_deg = floor(180/ ...
463                             pi * acos(abs(tempVel(3))))...
464                             + 1;
465                         %   If the photon is not reflected
466                         %   by the solar cell:
467                         if rand > reflect_lscCell(      ...
468                                 dataWavelengthIndex,    ...
469                                 polarAngleTemp_deg)
470                             %   If exciton is collected:
471                             if rand < IQE_lscCell(      ...
472                                     dataWavelengthIndex,...
473                                     polarAngleTemp_deg)
474                                 %   Record the position:
475                                 collectPhotonOrigin_    ...
476                                     lscCell(xPos,yPos,:)...
477                                     = tempPos;
478                                 %   Record the original
479                                 %   wavelength:
480                                 collectPhotonWavelength ...
481                                     _lscCell(xPos,      ...
482                                     yPos) =             ...
483                                     simWavelengthIndex;
484                                 %   Calculate short circuit
485                                 %   current:
486                                 shortCircuitCurrent_    ...
487                                     lscCell(xPos, yPos) ...
488                                 = outputCurrent         ...
489                                 Integrator(             ...
490                                 simWavelengthIndex,     ...
491                                 wavelengthStep,         ...
492                                 simWavelengthRange,     ...
493                                 cosineFactor,           ...
494                                 gridSize,               ...
495                                 incidentLightSpectrum   ...
496                                 Amps,                   ...
497                                 incidentLightSpectrum   ...
498                                 Wavelength);
499                                 %   Photon is terminated:
500                                 done=true;
501                                 %   Break from the while
```

```
                                %   loop:
                                break;
                            %   Else is non-radiatively
                            %   recombined:
                            else
                                %   Add to photons lost
                                %   (9=lsc cell loss):
                                numPhotonsLost(9) =     ...
                                    numPhotonsLost(9)+1;
                                %   Photon is terminated:
                                done = true;
                                %   Break from the while
                                %   loop:
                                break;
                            end
                        %   Else the photon is reflected
                        %   from LSC cell:
                        else
                            %   Reflect x-velocity:
                            tempVel(1) = -tempVel(1);
                            %   Update the temporary
                            %   position:
                            tempPos(1) = tempPos(1) +   ...
                                tempVel(1) * photonStep;
                        end
                    end
                end


                %   UPDATING PHOTON POSITION.
                %----------------------------------------
                %   Save old position before moving:
                oldPos = tempPos;
                %   Move photon given current velocity:
                tempPos = oldPos + photonStep*tempVel;


                %   CHECK FOR PHOTON TRAVELING THROUGH
                %   WAVEGUIDE.
                %----------------------------------------
                %   If the photon position is within LSC
                %   waveguide:
                if tempPos(1) ≥ plmaSize(1) &&          ...
                   tempPos(1) ≤ plmaSize(2) &&          ...
                   tempPos(2) ≥ plmaSize(1) &&          ...
                   tempPos(2) ≤ plmaSize(2)
                    %   Check if z lies within the
                    %   waveguide layer:
                    if tempPos(3) ≤ geometry(3,5) &&    ...
                       tempPos(3) ≥ geometry(3,4)
                        %   If the photon is absorbed by
                        %   the LSC waveguide:
                        if rand > probNotAbsPolymer(    ...
                                dataWavelengthIndex)
```

```
556                                     photonAbsorbed = true;
557                                 %   If the photon is
558                                 %   parasitically absorbed:
559                                 if rand > lumPLQY
560                                     %   Add to photons lost
561                                     %   (2 = lum. loss):
562                                     numPhotonsLost(2) =     ...
563                                     numPhotonsLost(2) + 1;
564                                     %   Photon is lost:
565                                     done = true;
566                                     %   Break from the while
567                                     %   loop:
568                                     break;
569                                 %   Else photon is emitted:
570                                 else
571                                     %   Add PL event:
572                                     numPLEvents(xPos,yPos) =...
573                                         numPLEvents(        ...
574                                         xPos,yPos) + 1;
575                                     %   Boolean for wavelength
576                                     %   emission:
577                                     reEmmited = false;
578                                     %   While searching for
579                                     %   emission:
580                                     while reEmmited == false
581                                         %   Generate a random
582                                         %   wavelength index:
583                                         newWavelengthIndex =...
584                                             ceil(rand *     ...
585                                             size(           ...
586                                             dataWavelength  ...
587                                             Range,2));
588                                         %   If PL occurs at new
589                                         %   wavelength:
590                                         if rand <           ...
591                                             lumPLSpectrum(  ...
592                                             newWavelengthIndex)
593                                             %   Update the
594                                             %   photon
595                                             %   wavelength:
596                                             dataWavelength  ...
597                                                 Index =     ...
598                                                 new         ...
599                                                 Wavelength  ...
600                                                 Index;
601                                             %   If using
602                                             %   anisotropic
603                                             %   emitter:
604                                             if anisotropicBool
605                                                 %   If
606                                                 %   using
607                                                 %   AMOLF's
608                                                 %   function:
609                                                 if amolfAnis...
```

```
610                                                 Bool
611                                                     %   PL
612                                                     %   direc
613                                                     %   tion:
614                                                     [temp   ...
615                                                     Vel,    ...
616                                                     photon  ...
617                                                     Polariz ...
618                                                     ation]  ...
619                                                             ...
620                                                     = aniso ...
621                                                     tropic  ...
622                                                     Scatter_...
623                                                     Fesc(   ...
624                                                     anisot  ...
625                                                     ropicFrac);
626                                                     %   The
627                                                     %   photon
628                                                     %   is
629                                                     %   emitt
630                                                     %   ed:
631                                                     reEmmit ...
632                                                     ed = true;
633                                                 else
634                                                     %   PL
635                                                     %   dire
636                                                     %   ction:
637                                                     [temp   ...
638                                                      Vel,   ...
639                                                      photon ...
640                                                      Polar  ...
641                                                      ization
642                                                      ]      ...
643                                                             ...
644                                                     = anisot...
645                                                     ropic   ...
646                                                     Scatter();
647                                                     %   The
648                                                     %   photon
649                                                     %   is
650                                                     %   emitt
651                                                     %   ed:
652                                                     reEmmit ...
653                                                     ed = true;
654                                                 end
655                                             %   Else using
656                                             %   isotropic:
657                                             else
658                                                 %   PL
659                                                 %   direction:
660                                                 [tempVel,   ...
661                                                 photonPolar ...
662                                                 ization]    ...
663                                                             ...
```

```
                                        = scatter();
                                        %   The photon
                                        %   is emitted:
                                        reEmmited = ...
                                        true;
                                    end
                                end
                            end
                        end
                    end
                    %   If the photon is scattered
                    %   within the waveguide:
                    if rand < probMatrixScatter(    ...
                        dataWavelengthIndex)
                        %   Scatter the photon:
                        [tempVel,                   ...
                        photonPolarization] =       ...
                        scatter();
                    end
                end
                %   Else if z lies in the glass
                %   layer (under WG):
                if tempPos(3) < geometry(3,4) &&    ...
                   tempPos(3) > geometry(3,3) &&    ...
                   rand < probGlassScatter
                    %   Scatter the photon:
                    [tempVel, photonPolarization] = ...
                        scatter();
                %   Else if z lies in the glass
                %   layer (on bottom cell):
                elseif tempPos(3) < geometry(3,2)   ...
                        && tempPos(3) >             ...
                        geometry(3,1) &&            ...
                        rand < probGlassScatter
                    %    Scatter the photon:
                    [tempVel, photonPolarization] =  ...
                        scatter();
                end
            end


            %   CHECK FOR PHOTON REACHING EDGES OF LSC.
            %-----------------------------------------
            %   If the photon hits the right side of
            %   the LSC:
            if tempPos(1) ≥ geometry(1,2)
                %   If using edge-lined PV cells and
                %   at least one cell:
                if lscCellEdgeLinedBool &&          ...
                    lscCellNum ≥ 1
                    %   Calculate current polar
                    %   angle (degrees) (+1 for
                    %   index):
                    polarAngleTemp_deg = floor(180  ...
```

```
718                         /pi * acos(abs(                 ...
719                         tempVel(3)))) + 1;
720                     %   If PV cell doesn't reflect
721                     %   photon:
722                     if rand > reflect_lscCell(          ...
723                         dataWavelengthIndex,            ...
724                         polarAngleTemp_deg) && rand     ...
725                         > fractionCellCovered
726                         %   If exciton is collected:
727                         if rand < IQE_lscCell(          ...
728                             dataWavelengthIndex,        ...
729                             polarAngleTemp_deg)
730                             %   Record the position:
731                             collectPhotonOrigin_        ...
732                                 lscCell(xPos,yPos,:)    ...
733                                 = tempPos;
734                             %   Record the original
735                             %   wavelength:
736                             collectPhotonWavelength_    ...
737                                 lscCell(xPos,yPos)      ...
738                                 = simWavelengthIndex;
739                             %   Calculate short
740                             %   circuit current:
741                             shortCircuitCurrent_        ...
742                                 lscCell(xPos, yPos)     ...
743                                 = outputCurrent         ...
744                                 Integrator(             ...
745                                 simWavelengthIndex,     ...
746                                 wavelengthStep,         ...
747                                 simWavelengthRange,     ...
748                                 cosineFactor,           ...
749                                 gridSize,               ...
750                                 incidentLight           ...
751                                 SpectrumAmps,           ...
752                                 incidentLight           ...
753                                 SpectrumWavelength);
754                             %   Photon is terminated:
755                             done=true;
756                             %   Break from the
757                             %   while loop:
758                             break;
759                         %   Else is non-radiatively
760                         %   recombined:
761                         else
762                             %   Add to photons lost
763                             %   (9=lsc cell loss):
764                             numPhotonsLost(9) =         ...
765                                 numPhotonsLost(9)+1;
766                             %   Photon is terminated:
767                             done = true;
768                             %   Break from the while
769                             %   loop:
770                             break;
771                         end
```

```
772                         %   Else the photon is reflected
773                         %   from LSC cell:
774                         else
775                             %   Reflect the x-velocity:
776                             tempVel(1) = -abs(tempVel(1));
777                             %   Move the photon through
778                             %   by one step:
779                             tempPos(1) = geometry(1,2) -...
780                                 photonStep;
781                         end
782                     %   Else we don't have a PV cell at
783                     %   the edge:
784                     else
785                         %   Add one to the number of edge
786                         %   bounces:
787                         numLSCEdgeBounces(xPos,yPos) =  ...
788                         numLSCEdgeBounces(xPos,yPos) + 1;
789                         %   If the photon is not reflected:
790                         if rand > wgEdgeReflect
791                             %   Add one to the photonsLost
792                             %   variable:
793                             numPhotonsLost(3) =         ...
794                                 numPhotonsLost(3) + 1;
795                             %   The photon is lost and
796                             %   terminated:
797                             done=true;
798                             %   Now break from the while
799                             %   loop:
800                             break;
801                         %   Else the photon is reflected
802                         %   or scattered:
803                         else
804                             %   If the photon is scattered:
805                             if rand < wgEdgeScatter
806                                 %   Scatter the photon
807                                 %   by the waveguide
808                                 %   edge:
809                                 [tempVel,               ...
810                                 photonPolarization] =   ...
811                                 backside_scatter();
812                                 %   Shift the temporary
813                                 %   velocity:
814                                 tempVel = circshift(    ...
815                                 tempVel,[1,1]);
816                             end
817                             %   Reflect the x-velocity:
818                             tempVel(1) = -abs(tempVel(1));
819                             %   Move the photon through
820                             %   by one step:
821                             tempPos(1) = geometry(1,2) -...
822                             photonStep;
823                         end
824                     end
825                 %   If the photon hits the left side of
```

```
826                     %   the LSC:
827                     elseif tempPos(1) ≤ geometry(1,1)
828                         %   If using edge-lined PV cells and
829                         %   at least two
830                         %   cells:
831                         if lscCellEdgeLinedBool &&          ...
832                             lscCellNum ≥ 2
833                             %   Calculate current polar angle
834                             %   (degrees) (+1 for
835                             %   index):
836                             polarAngleTemp_deg = floor(     ...
837                                 180/pi * acos(abs(          ...
838                                 tempVel(3)))) + 1;
839                             %   If PV cell doesn't reflect
840                             %   photon:
841                             if rand > reflect_lscCell(      ...
842                                 dataWavelengthIndex,        ...
843                                 polarAngleTemp_deg) &&      ...
844                                 rand > fractionCellCovered
845                                 %   If exciton is collected:
846                                 if rand < IQE_lscCell(      ...
847                                         dataWavelengthIndex,...
848                                 polarAngleTemp_deg)
849                                     %   Record the position:
850                                     collectPhotonOrigin_    ...
851                                         lscCell(xPos,yPos,:)...
852                                         = tempPos;
853                                     %   Record the original
854                                     %   wavelength:
855                                     collectPhotonWavelength ...
856                                     lscCell(xPos,           ...
857                                     yPos) = simWavelengthIndex;
858                                     %   Calculate short circuit
859                                     %   current:
860                                     shortCircuitCurrent_    ...
861                                         lscCell(xPos, yPos) ...
862                                     = outputCurrent         ...
863                                     Integrator(              ...
864                                     simWavelengthIndex,     ...
865                                     wavelengthStep,         ...
866                                     simWavelengthRange,     ...
867                                     cosineFactor,           ...
868                                     gridSize,               ...
869                                     incidentLightSpectrum   ...
870                                     Amps,                   ...
871                                     incidentLightSpectrum   ...
872                                     Wavelength);
873                                     %   Photon is terminated:
874                                     done=true;
875                                     %   Break from the while
876                                     %   loop:
877                                     break;
878                                 %   Else is non-radiatively
879                                 %   recombined:
```

```
880                             else
881                                 %   Add to photons lost
882                                 %   (9=lsc cell loss):
883                                 numPhotonsLost(9) =     ...
884                                     numPhotonsLost(9)+1;
885                                 %   Photon is terminated:
886                                 done = true;
887                                 %   Break from the
888                                 %   while loop:
889                                 break;
890                             end
891                         %   Else the photon is reflected
892                         %   from LSC cell:
893                         else
894                             %   Reflect the x-velocity:
895                             tempVel(1) = abs(tempVel(1));
896                             %   Move the photon through
897                             %   by one step:
898                             tempPos(1) = geometry(1,1) +...
899                             photonStep;
900                         end
901                     %   Else we don't have a PV cell at
902                     %   the edge:
903                     else
904                         %   Add one to the number of edge
905                         %   bounces:
906                         numLSCEdgeBounces(xPos,yPos) =  ...
907                         numLSCEdgeBounces(xPos,yPos) + 1;
908                         %   If the photon is not reflected:
909                         if rand > wgEdgeReflect
910                             %   Add one to the photonsLost
911                             %   variable:
912                             numPhotonsLost(4) =         ...
913                                 numPhotonsLost(4) + 1;
914                             %   The photon is lost and
915                             %   terminated:
916                             done=true;
917                             %   Now break from the while
918                             %   loop:
919                             break;
920                         %   Else the photon is reflected
921                         %   or scattered:
922                         else
923                             %   If the photon is scattered:
924                             if rand < wgEdgeScatter
925                                 %   Scatter the photon by
926                                 %   the waveguide
927                                 %   edge:
928                                 [tempVel,               ...
929                                     photonPolarization] ...
930                                     = backside_scatter();
931                                 %   Shift the temporary
932                                 %   velocity:
933                                 tempVel = circshift(    ...
```

```
934                                     tempVel,[1,1]);
935                             end
936                             %   Reflect the x-velocity:
937                             tempVel(1) = abs(tempVel(1));
938                             %   Move the photon through
939                             %   by one step:
940                             tempPos(1) = geometry(1,1) +...
941                                 photonStep;
942                         end
943                     end
944                 %   If the photon hits the back side of
945                 %   the LSC:
946                 elseif tempPos(2) ≥ geometry(2,2)
947                     %   If using edge-lined PV cells and
948                     %   at least three cells:
949                     if lscCellEdgeLinedBool &&          ...
950                             lscCellNum ≥ 3
951                         %   Calculate current polar
952                         %   angle (degrees) (+1 for
953                         %   index):
954                         polarAngleTemp_deg = floor(     ...
955                             180/pi * acos(abs(          ...
956                             tempVel(3)))) + 1;
957                         %   If PV cell doesn't reflect
958                         %   photon:
959                         if rand > reflect_lscCell(      ...
960                             dataWavelengthIndex,        ...
961                             polarAngleTemp_deg) &&      ...
962                             rand > fractionCellCovered
963                             %   If exciton is collected:
964                             if rand < IQE_lscCell(      ...
965                                 dataWavelengthIndex,    ...
966                                 polarAngleTemp_deg)
967                                 %   Record the position:
968                                 collectPhotonOrigin_    ...
969                                     lscCell(xPos,yPos,:)...
970                                     = tempPos;
971                                 %   Record the original
972                                 %   wavelength:
973                                 collectPhotonWavelength_...
974                                     lscCell(xPos,       ...
975                                     yPos) = sim         ...
976                                     WavelengthIndex;
977                                 %   Calculate short
978                                 %   circuit current:
979                                 shortCircuitCurrent_    ...
980                                     lscCell(xPos, yPos) ...
981                                 = outputCurrent         ...
982                                 Integrator(             ...
983                                 simWavelengthIndex,     ...
984                                 wavelengthStep,         ...
985                                 simWavelengthRange,     ...
986                                 cosineFactor,           ...
987                                 gridSize,               ...
```

```
                                incidentLightSpectrum   ...
                                Amps,                   ...
                                incidentLightSpectrum   ...
                                Wavelength);
                                %   Photon is terminated:
                                done=true;
                                %   Break from the while
                                %   loop:
                                break;
                            %   Else is non-radiatively
                            %   recombined:
                            else
                                %   Add to photons lost
                                %   (9=lsc cell loss):
                                numPhotonsLost(9) =     ...
                                    numPhotonsLost(9)+1;
                                %   Photon is terminated:
                                done = true;
                                %   Break from the while
                                %   loop:
                                break;
                            end
                        %   Else the photon is reflected
                        %   from LSC cell:
                        else
                            %   Reflect the y-velocity:
                            tempVel(2) = -abs(tempVel(2));
                            %   Move the photon by one
                            %   step:
                            tempPos(2) = geometry(2,2) -...
                                photonStep;
                        end
                    %   Else we don't have a PV cell at
                    %   the edge:
                    else
                        %   Add one to the number of edge
                        %   bounces:
                        numLSCEdgeBounces(xPos,yPos) =  ...
                        numLSCEdgeBounces(xPos,yPos) + 1;
                        %   If the photon is not reflected:
                        if rand > wgEdgeReflect
                            %   Add one to the photonsLost
                            %   variable:
                            numPhotonsLost(5) =         ...
                                numPhotonsLost(5) + 1;
                            %   The photon is lost and
                            %   terminated:
                            done=true;
                            %   Now break from the while
                            %   loop:
                            break;
                        %   Else the photon is reflected
                        %   or scattered:
                        else
```

```
                        %   If the photon is scattered:
                        if rand < wgEdgeScatter
                            %   Scatter the photon by
                            %   the waveguide
                            %   edge:
                            [tempVel,                ...
                            photonPolarization] =    ...
                            backside_scatter();
                            %   Shift the temporary
                            %   velocity:
                            tempVel = circshift(     ...
                            tempVel,[2,2]);
                        end
                        %   Reflect the y-velocity:
                        tempVel(2) = -abs(tempVel(2));
                        %   Move the photon by one
                        %   step:
                        tempPos(2) = geometry(2,2) -...
                            photonStep;
                    end
                end
            %   If the photon hits the front side of
            %   the LSC:
            elseif tempPos(2) ≤ geometry(2,1)
                %   If using edge-lined PV cells and
                %   at least four
                %   cells:
                if lscCellEdgeLinedBool &&           ...
                    lscCellNum ≥ 4
                    %   Calculate current polar
                    %   angle (degrees) (+1 for
                    %   index):
                    polarAngleTemp_deg = floor(      ...
                        180/pi * acos(abs(   ...
                        tempVel(3)))) + 1;
                    %   If PV cell doesn't reflect
                    %   photon:
                    if rand > reflect_lscCell(       ...
                        dataWavelengthIndex,         ...
                        polarAngleTemp_deg) && rand  ...
                        > fractionCellCovered
                        %   If exciton is collected:
                        if rand < IQE_lscCell(       ...
                            dataWavelengthIndex,     ...
                            polarAngleTemp_deg)
                            %   Record the position:
                            collectPhotonOrigin_     ...
                                lscCell(xPos,yPos,:)...
                                = tempPos;
                            %   Record the original
                            %   wavelength:
                            collectPhotonWavelength_...
                                lscCell(xPos,        ...
                                yPos) =              ...
```

```
1096                                    simWavelengthIndex;
1097                                %   Calculate short circuit
1098                                %   current:
1099                                shortCircuitCurrent_    ...
1100                                    lscCell(xPos, yPos) ...
1101                                    = outputCurrent     ...
1102                                    Integrator(         ...
1103                                    simWavelengthIndex, ...
1104                                    wavelengthStep,     ...
1105                                    simWavelengthRange, ...
1106                                    cosineFactor,       ...
1107                                    gridSize,           ...
1108                                    incidentLight       ...
1109                                    SpectrumAmps,       ...
1110                                    incidentLight       ...
1111                                    SpectrumWavelength);
1112                                %   Photon is terminated:
1113                                done=true;
1114                                %   Break from the
1115                                %   while loop:
1116                                break;
1117                            %   Else is non-radiatively
1118                            %   recombined:
1119                            else
1120                                %   Add to photons lost
1121                                %   (9=lsc cell loss):
1122                                numPhotonsLost(9) =     ...
1123                                    numPhotonsLost(9)+1;
1124                                %   Photon is terminated:
1125                                done = true;
1126                                %   Break from the
1127                                %   while loop:
1128                                break;
1129                            end
1130                        %   Else the photon is reflected
1131                        %   from LSC cell:
1132                        else
1133                            %   Reflect the y-velocity:
1134                            tempVel(2) = abs(tempVel(2));
1135                            %   Move the photon by one
1136                            %   step:
1137                            tempPos(2) = geometry(2,1) +...
1138                                photonStep;
1139                        end
1140                    %   Else we don't have a PV cell at
1141                    %   the edge:
1142                    else
1143                        %   Add one to the number of edge
1144                        %   bounces:
1145                        numLSCEdgeBounces(xPos,yPos) =  ...
1146                        numLSCEdgeBounces(xPos,yPos) + 1;
1147                        %   If the photon is not reflected:
1148                        if rand > wgEdgeReflect
1149                            %   Add one to the photonsLost
```

```
                            %   variable:
                            numPhotonsLost(6) =         ...
                                numPhotonsLost(6) + 1;
                            %   The photon is lost and
                            %   terminated:
                            done=true;
                            %   Now break from the while
                            %   loop:
                            break;
                        %   Else the photon is reflected or
                        %   scattered:
                        else
                            %   If the photon is scattered:
                            if rand < wgEdgeScatter
                                %   Scatter the photon by
                                %   the waveguide
                                %   edge:
                                [tempVel,               ...
                                photonPolarization] =   ...
                                backside_scatter();
                                %   Shift the temporary
                                %   velocity:
                                tempVel = circshift(    ...
                                    tempVel,[2,2]);
                            end
                            %   Reflect the y-velocity:
                            tempVel(2) = abs(tempVel(2));
                            %   Move the photon by one
                            %   step:
                            tempPos(2) = geometry(2,1) +...
                                photonStep;
                        end
                    end
                end


                %   CHECK FOR PHOTON MATERIALS' INTERFACE
                %   INTERACTIONS.
                %----------------------------------------
                %   Calculate temp polar angle (wrt z
                %   axis):
                polarAngleTemp = acos(abs(tempVel(3)));
                %   Calculate current polar angle
                %   (degrees) (+1 for index):
                polarAngleTemp_deg = floor(polarAngle   ...
                    Temp*180/pi) + 1;
                %   If the photon goes from Glass to    ...
                %   Polymer:
                if (tempPos(3) > geometry(3,4)) &&      ...
                    (oldPos(3) < geometry(3,4))
                    %   Change the photon velocity given
                    %   the change of
                    %   refractive index:
                    tempVel = refract( interface(nGlass,...
```

```
1204                         nPolymer, polarAngleTemp),      ...
1205                         photonPolarization, tempVel);
1206                     %   Update the position of the photon's
1207                     %   z-direction:
1208                     tempPos(3) = geometry(3,4) +        ...
1209                         photonStep*tempVel(3);
1210                 %   If the photon goes from the Polymer
1211                 %   into Air:
1212                 elseif (tempPos(3) > geometry(3,5)) &&  ...
1213                         (oldPos(3) < geometry(3,5))
1214                     %   Change the photon velocity given
1215                     %   the change of
1216                     %   refractive index:
1217                     tempVel = refract(interface(        ...
1218                         nPolymer,nAir, polarAngleTemp), ...
1219                         photonPolarization, tempVel);
1220                     %   Update the position of the photon's
1221                     %   z-direction:
1222                     tempPos(3) = geometry(3,5) +        ...
1223                         photonStep*tempVel(3);
1224                     %   If the photon reflects at the
1225                     %   Polymer's surface:
1226                     if tempPos(3) < geometry(3,5)
1227                         %   Add one to the waveguide
1228                         %   number of bounces:
1229                         numWgModeBounces(xPos,yPos) =   ...
1230                         numWgModeBounces(xPos,yPos) + 1;
1231                     end
1232                 %   If the photon is travelling in the top
1233                 %   Air of the LSC
1234                 %   device:
1235                 elseif tempPos(3) > geometry(3,6)
1236                     %   If the simulation uses a top
1237                     %   filter:
1238                     if topFilterBool
1239                         %   Define the s-polarization
1240                         %   component of the
1241                         %   photon:
1242                         s_part = cos(photonPolarization)^2;
1243                         %   Define the p-polarization
1244                         %   component of the
1245                         %   photon:
1246                         p_part = sin(photonPolarization)^2;
1247                         %   If the photon reflects off of
1248                         %   the filter:
1249                         if rand < (s_part *             ...
1250                         reflectFilterTop_sPol(          ...
1251                         dataWavelengthIndex,            ...
1252                         polarAngleTemp_deg) +           ...
1253                         p_part * reflectFilterTop_pPol( ...
1254                         dataWavelengthIndex,            ...
1255                         polarAngleTemp_deg))
1256                             %   Update the z-component of
1257                             %   the velocity to
```

```
1258                            %   reflect downward:
1259                            tempVel(3) = -abs(tempVel(3));
1260                            %   Update the z-component of
1261                            %   the position of
1262                            %   the photon:
1263                            tempPos(3) = geometry(3,6)  ...
1264                                + photonStep *          ...
1265                                tempVel(3);
1266                            %   Add one to the number of
1267                            %   photon bounces off
1268                            %   of the DBR:
1269                            numFilterBounces(xPos,yPos) ...
1270                            = numFilterBounces(         ...
1271                            xPos,yPos) + 1;
1272                        %   Else the photon passes through
1273                        %   the filter:
1274                        else
1275                            %   Add one to the photonsLost
1276                            %   variable:
1277                            numPhotonsLost(7) =         ...
1278                                numPhotonsLost(7) + 1;
1279                            %   The photon is lost and
1280                            %   terminated:
1281                            done = true;
1282                            %   Now break from the
1283                            %   while loop:
1284                            break;
1285                        end
1286                    %   Else there is no filter at all to
1287                    %   stop the photon:
1288                    else
1289                        %   If we are in PL trapping mode
1290                        %   and is trapped:
1291                        if plTrappingMode == true &&    ...
1292                                photonAbsorbed ==       ...
1293                        true && rand < plTrapping
1294                            %   Update the z-component of
1295                            %   the velocity to
1296                            %   reflect downward:
1297                            tempVel(3) = -abs(tempVel(3));
1298                            %   Update the z-component of
1299                            %   the position of
1300                            %   the photon:
1301                            tempPos(3) = geometry(3,6)  ...
1302                            + photonStep * tempVel(3);
1303                        else
1304                            %   Add one to the
1305                            %   photonsLost variable:
1306                            numPhotonsLost(7) =         ...
1307                                numPhotonsLost(7) + 1;
1308                            %   The photon is lost and
1309                            %   terminated:
1310                            done=true;
1311                            %   Now break from the
```

```
                    %   while loop:
                    break;
                end
            end
        %   If the photon goes from the top Air
        %   to the Polymer:
        elseif tempPos(3) < geometry(3,5) &&    ...
                oldPos(3) ≥ geometry(3,5)
            %   Change the photon velocity
            %   given the change of
            %   refractive index:
            tempVel = refract(interface(nAir,   ...
                nPolymer, polarAngleTemp),      ...
                photonPolarization, tempVel);
            %   Update the position of the
            %   photon's z-direction:
            tempPos(3) = geometry(3,5) +        ...
            photonStep*tempVel(3);
        %   If the photon goes from the polymer
        %   to the glass:
        elseif tempPos(3) < geometry(3,4) &&    ...
                oldPos(3) ≥ geometry(3,4)
            %   Change the photon velocity given
            %   the change of
            %   refractive index:
            tempVel = refract(interface(        ...
                nPolymer, nGlass,               ...
            polarAngleTemp), photonPolarization,...
            tempVel);
            %   Update the position of the
            %   photon's z-direction:
            tempPos(3) = geometry(3,4) +        ...
            photonStep*tempVel(3);
        %   If the photon goes from glass to
        %   the bottom air:
        elseif tempPos(3) < geometry(3,3) &&    ...
                oldPos(3) ≥ geometry(3,3)
            tempVel = refract(interface(nGlass, ...
                nAir, polarAngleTemp),          ...
                photonPolarization, tempVel);
            tempPos(3) = geometry(3,3) +        ...
                photonStep*tempVel(3);
            %   want to know how many times the
            %   photon
            %   reflects off the waveguide surface
            if tempPos(3) > geometry(3,3)
                numWgModeBounces(xPos,yPos) =   ...
                numWgModeBounces(xPos,yPos) + 1;
            end
        %   If the photon goes from the bottom air
        %   gap to the
        %   bottom glass superstrate:
        elseif tempPos(3) < geometry(3,2) &&    ...
        oldPos(3) ≥ geometry(3,2)
```

```
                    tempVel = refract(interface(nAir,     ...
                        nGlass,polarAngleTemp),           ...
                        photonPolarization, tempVel);
                    tempPos(3) = geometry(3,2) +          ...
                        photonStep*tempVel(3);
                %   If the photon is travelling in the
                %   bottom glass
                %   superstrate of the LSC device:
                elseif tempPos(3) < geometry(3,2)
                    %   If the simulation uses a bottom
                    %   filter:
                    if botFilterBool
                        %   Define the s-polarization
                        %   component of the
                        %   photon:
                        s_part = cos(photonPolarization)^2;
                        %   Define the p-polarization
                        %   component of the
                        %   photon:
                        p_part = sin(photonPolarization)^2;
                        %   If the photon reflects off
                        %   of the filter:
                        if rand < (s_part *               ...
                            reflectFilterBottom_sPol(     ...
                            dataWavelengthIndex,          ...
                            polarAngleTemp_deg) +         ...
                            p_part *                      ...
                            reflectFilterBottom_pPol(     ...
                            dataWavelengthIndex,          ...
                            polarAngleTemp_deg))
                            %   Update the z-component of
                            %   the velocity to
                            %   reflect upward:
                            tempVel(3) = abs(tempVel(3));
                            tempPos(3) = geometry(3,2)    ...
                            + photonStep * tempVel(3);
                            %   Add one to the number of
                            %   photon bounces off
                            %   of the filter:
                            numFilterBounces(xPos,yPos)   ...
                            = numFilterBounces(xPos,      ...
                            yPos) + 1;
                        %   Else if the photon passes
                        %   through:
                        elseif rand < (s_part *           ...
                        transmitFilterBottom_sPol(        ...
                        dataWavelengthIndex,              ...
                        polarAngleTemp_deg)+ p_part *     ...
                        transmitFilterBottom_pPol(        ...
                        dataWavelengthIndex,              ...
                        polarAngleTemp_deg))
                            %   Record the photon's
                            %   direction:
                            collectPhotonDir_bottomCell(...
```

```
1420                                    1,xPos,yPos,:) =        ...
1421                                    tempVel;
1422                                %   Now convert radians to
1423                                %   degrees to for the
1424                                %   z-incident angle of the
1425                                %   photon:
1426                                polarAngleTemp_deg = floor( ...
1427                                    180/pi*acos(abs(        ...
1428                                    tempVel(3))));
1429                                %   If the photon is not
1430                                %   reflected by the Si
1431                                %   solar cell:
1432                                if rand >                   ...
1433                                    reflect_bottomCell(     ...
1434                                    dataWavelengthIndex,    ...
1435                                    polarAngleTemp_deg+1)
1436                                    %   If the photon is
1437                                    %   absorbed and e-h pair
1438                                    %   is extracted:
1439                                    if rand <               ...
1440                                    IQE_bottomCell(         ...
1441                                    dataWavelengthIndex,    ...
1442                                    polarAngleTemp_deg+1)
1443                                        %   Record the position
1444                                        %   it hits at:
1445                                        collectPhotonOrigin_...
1446                                        bottomCell(xPos,    ...
1447                                        yPos,:) = tempPos;
1448                                        %   Record the
1449                                        %   wavelength it
1450                                        %   hits at:
1451                                        collectPhoton       ...
1452                                        Wavelength_         ...
1453                                        bottomCell(         ...
1454                                        xPos, yPos) =       ...
1455                                        simWavelengthIndex;
1456                                        %   Calculate the
1457                                        %   short circuit
1458                                        %   current
1459                                        %   from this photon
1460                                        %   (given the cosine
1461                                        %   factor):
1462                                        shortCircuitCurrent ...
1463                                        _bottomCell(        ...
1464                                        xPos, yPos) =       ...
1465                                        outputCurrent       ...
1466                                        Integrator(         ...
1467                                        simWavelengthIndex, ...
1468                                        wavelengthStep,     ...
1469                                        simWavelengthRange, ...
1470                                        cosineFactor,       ...
1471                                        gridSize,           ...
1472                                        incidentLight       ...
1473                                        SpectrumAmps,       ...
```

```
1474                                    incidentLight       ...
1475                                    SpectrumWavelength);
1476                                    %   The photon is
1477                                    %   absorbed and
1478                                    %   terminated:
1479                                    done=true;
1480                                    %   Now break from
1481                                    %   the while loop:
1482                                    break;
1483                                %   Else the photon is
1484                                %   absorbed and
1485                                %   non-radiatively
1486                                %   recombined:
1487                                else
1488                                    %   Count the lost
1489                                    %   photon in
1490                                    %   non-radiative
1491                                    %   recombination for
1492                                    %   Si losses:
1493                                    numPhotonsLost(10)= ...
1494                                    numPhotonsLost(10)+1;
1495                                    %   Then the photon is
1496                                    %   lost:
1497                                    done = true;
1498                                    %   Now break from the
1499                                    %   while loop:
1500                                    break;
1501                                end
1502                            %   Else the photon is
1503                            %   reflected from
1504                            %   the Si cell:
1505                            else
1506                                %   Make the z-velocity
1507                                %   travel in
1508                                %   the opposite direction:
1509                                tempVel(3) = abs(       ...
1510                                    tempVel(3));
1511                                %   Update the temporary
1512                                %   position:
1513                                tempPos(3) =            ...
1514                                    geometry(3,2) +     ...
1515                                    photonStep*tempVel(3);
1516                            end
1517                        %   Else the photon is lost due
1518                        %   to absorption
1519                        %   of the bottom filter:
1520                        else
1521                            %   Count the lost photon
1522                            %   in bottom filter
1523                            %   absorption:
1524                            numPhotonsLost(8) =         ...
1525                                numPhotonsLost(8)+1;
1526                            %   Then the photon is lost:
1527                            done = true;
```

```
1528                            %   Now break from the
1529                            %   while loop:
1530                            break;
1531                        end
1532                    %   If there is no bottom filter,
1533                    %   then the photon
1534                    %   travels through to the bottom
1535                    %   cell if not PL
1536                    %   trapped.
1537                    else
1538                        %   If we are in PL trapping
1539                        %   mode and is trapped:
1540                        if plTrappingMode == true &&    ...
1541                                photonAbsorbed ==       ...
1542                        true && rand < plTrapping
1543                            %   Update the z-component
1544                            %   of the velocity to
1545                            %   reflect downward:
1546                            tempVel(3) = -abs(tempVel(3));
1547                            %   Update the z-component of
1548                            %   the position of
1549                            %   the photon:
1550                            tempPos(3) = geometry(3,6) +...
1551                                photonStep * tempVel(3);
1552                        else
1553                            %   Record the photon's
1554                            %   direction:
1555                            collectPhotonDir_bottomCell(...
1556                                1,xPos,yPos,:) =    ...
1557                            tempVel;
1558                            %   Now convert radians to
1559                            %   degrees to
1560                            %   for the z-incident
1561                            %   angle of the
1562                            %   photon:
1563                            polarAngleTemp_deg =        ...
1564                            floor(180/pi*acos(abs(      ...
1565                            tempVel(3))));
1566                            %   If the photon is not
1567                            %   reflected by the
1568                            %   Si solar cell:
1569                            if rand > reflect_          ...
1570                                bottomCell(             ...
1571                            dataWavelengthIndex,        ...
1572                            polarAngleTemp_deg+1)
1573                                %   If the photon is
1574                                %   absorbed and e-h
1575                                %   pair is
1576                                %   extracted:
1577                                if rand < IQE_          ...
1578                                    bottomCell(         ...
1579                                    dataWavelengthIndex,...
1580                                    polarAngleTemp_deg+1)
1581                                    %   Record the position
```

```
                    %   it hits at:
                    collectPhotonOrigin ...
                    _bottomCell(xPos,   ...
                    yPos,:) = tempPos;
                    %   Record the
                    %   wavelength it hits
                    %   at:
                    collectPhotonWave   ...
                    length_bottomCell(  ...
                    xPos, yPos) =       ...
                    simWavelengthIndex;
                    %   Calculate the short
                    %   circuit current
                    %   from this photon
                    %   (given the cosine
                    %   factor):
                    shortCircuitCurrent_...
                    bottomCell(         ...
                    xPos, yPos) =       ...
                    outputCurrent       ...
                    Integrator(         ...
                    simWavelengthIndex, ...
                    wavelengthStep,     ...
                    simWavelengthRange, ...
                    cosineFactor,       ...
                    gridSize,           ...
                    incidentLight       ...
                    SpectrumAmps,       ...
                    incidentLight       ...
                    SpectrumWavelength);
                    %   The photon is
                    %   absorbed and
                    %   terminated:
                    done=true;
                    %   Now break from
                    %   the while loop:
                    break;
                %   Else the photon is
                %   absorbed and
                %   non-radiatively
                %   recombined:
                else
                    %   Count the lost
                    %   photon in non-
                    %   radiative
                    %   recombination for
                    %   Si losses:
                    numPhotonsLost(10) =...
                    numPhotonsLost(10)+1;
                    %   Then the photon
                    %   is lost:
                    done = true;
                    %   Now break from
                    %   the while
```

```
                                    %   loop:
                                    break;
                                end
                            %   Else the photon is
                            %   reflected from
                            %   the Si cell:
                            else
                                %   Make the z-velocity
                                %   travel in
                                %   the opposite direction:
                                tempVel(3) =            ...
                                abs(tempVel(3));
                                %   Update the temporary
                                %   position:
                                tempPos(3) =            ...
                                geometry(3,2) +         ...
                                photonStep*tempVel(3);
                            end
                        end
                    end
                %   If the photon goes from the bottom
                %   glass superstrate into the bottom air
                %   gap:
                elseif tempPos(3) > geometry(3,2) &&    ...
                        oldPos(3) ≤ geometry(3,2)
                    %   Change the photon velocity given
                    %   the change
                    %   of refractive index:
                    tempVel = refract(interface(nGlass, ...
                        nAir, polarAngleTemp),          ...
                        photonPolarization, tempVel);
                    %   Update the position of the photon's
                    %   z-direction:
                    tempPos(3) = geometry(3,2) +        ...
                        photonStep*tempVel(3);
                %   If the photon goes from the bottom air
                %   into the glass:
                elseif tempPos(3) > geometry(3,3) &&    ...
                        oldPos(3) ≤ geometry(3,3)
                    %   Change the photon velocity given
                    %   the change of refractive index:
                    tempVel = refract(interface(nAir,   ...
                        nGlass, polarAngleTemp),        ...
                        photonPolarization, tempVel);
                    %   Update the position of the photon's
                    %   z-direction:
                    tempPos(3) = geometry(3,3) +        ...
                    photonStep*tempVel(3);
                end
            end
        end
    end

    %   ADD UP COLLECTED CURRENTS AND INCIDENT POWER.
```

```
1690      %-------------------------------------------------------
1691      %   Now, add up the collected current by the lsc Cell:
1692      shortCircuitCurrent_lscCell = squeeze(sum(sum(      ...
1693      shortCircuitCurrent_lscCell,1),2));
1694      %   Now, add up the collected current by the bottom
1695      %   Cell:
1696      shortCircuitCurrent_bottomCell = squeeze(sum(sum(   ...
1697      shortCircuitCurrent_bottomCell, 1), 2));
1698      %   Finally, add up the incident power for this given
1699      %   wavelength:
1700      incidentPower = squeeze(sum(sum(incidentPower,1),2));
1701  end
```

Algorithm 1 MCRT: find J_{sc}, V_{oc}, FF, and η_{power}

(We first calculate J_{sc} via ray-tracing.)
Initialize $M \times M$ matrix (grid mesh), each m_x by m_y in size.
Initialize LSC device (waveguide thickness, layers, cell size, spectra, optical density, incident photon flux Φ_{in}, diffuse light probability P_{dif})
for wavelengths, $\lambda \in \Phi_{in}$ **do**
  for mesh, $m_x \in M$ **do**
    for mesh, $m_y \in M$ **do**
      if direct light **then**
        Initialize incident photon, λ, with velocity $\vec{v} = (0, 0, -1)$
      else if diffuse light **then**
        Initialize incident photon, λ, with random velocity (in $-\hat{z}$)
      end if
      if reflected off top surface **then**
        photon is lost
      end if
      move photon by step vector $|\vec{\ell}|$ (e.g., 5μm)
      if absorbed by luminophore **then**
        if emitted by luminophore (PLQY) **then**
          assign new wavelength λ_{pl}
          if anisotropic emitter **then**
            assign new velocity, v_{pl} given emission profile
          else if isotropic emitter **then**
            assign new velocity, v_{pl} randomly
          end if
        else if not emitted **then**
          photon is lost
        end if
      end if
      if incident upon solar cell **then**
        if not reflected by cell surface **then**
          if exciton is collected by contacts **then**
            photon is collected
          else if exciton recombines **then**
            if radiative recombination **then**
              emit back into waveguide at cell bandgap
            else if non-radiative recombination **then**
              photon is lost
            end if
          end if
        else if reflected by cell surface **then**
          reflect photon in opposite direction
        end if
      end if
    end for
  end for
end for

Algorithm 2 MCRT (continued):

```
for wavelengths, λ ∈ Φ_in do
  for mesh, m_x ∈ M do
    for mesh, m_y ∈ M do
      if tandem LSC/Si module then
        if photon incident upon silicon cell then
          if not reflected by cell surface then
            if exciton is collected by contacts then
              photon is collected
            else if exciton recombines then
              if radiative recombination then
                emit back into waveguide at cell bandgap
              else if non-radiative recombination then
                photon is lost
              end if
            end if
          else if reflected by cell surface then
            reflect photon in opposite direction
          end if
        end if
      end if
      if photon scattered by waveguide then
        assign random velocity
      end if
      if photon reaches waveguide top/bottom surface then
        if within waveguide escape cone then
          if external filters then
            if trapped by filter then
              reflect back into waveguide
            else if not trapped by filter then
              photon is lost
            end if
          else if no filters then
            photon is lost
          end if
        else if trapped in total internal reflection then
          reflect at boundary
        end if
      end if
    end for
  end for
end for
```

Algorithm 3 MCRT (continued):

for wavelengths, $\lambda \in \Phi_{\text{in}}$ **do**
  for mesh, $m_x \in M$ **do**
    for mesh, $m_y \in M$ **do**
      if photon reaches waveguide edges **then**
        if reflected **then**
          reflect at boundary
        else if not-reflected **then**
          photon is lost
        end if
      end if
      move photon by step ℓ
    end for
  end for
end for
J_{sc}: Sum all photons collected
Calculate J_0^{rad} via escaped photon count
Assign $J_0^{\text{non-rad}}$ via cell type
Calculate V_{oc}
Assign R_{s}, R_{sh}, n via cell type
Calculate FF
Calculate η_{power}

APPENDIX B

A Deterministic Model of LSCs

Chapter 2 describes an analytical LSC device model that combines a previous expression from Klimov et al.[39] with a geometric, solid-angle calculation between the point of photoluminescence within the optical waveguide and the collecting, edge-lined photovoltaic cell. In this model, we explicitly assume a single edge-lined LSC and further simplify the setup by assuming zero reflectance at the remaining three waveguide edges. Figure B.1 displays the architecture of this model. The included Matlab/C code below provides the implementation of this full analytical device model.

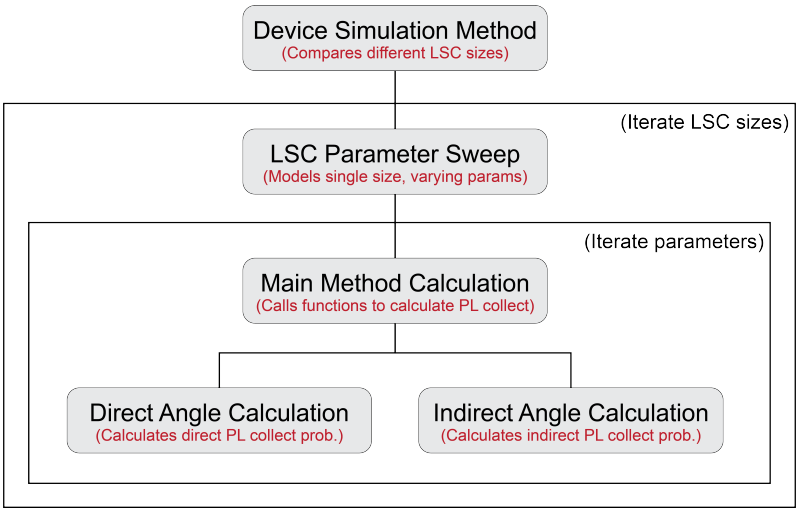

Figure B.1: A conceptualization of the analytical model architecture. The `lscDeviceSimulation.m` function calls the model by iterating through a list of LSC device sizes (shown in figure 2.5), calling the `parameterSweep.m` sub-function upon each iteration. This sub-function varies parameters such as the luminophore re-absorption coefficient (luminophore extinction factor) as well as integrates over each point of the LSC—size specified for that iteration. This function then calls the sub-sub-functions to calculate the photoluminescence collection probability for each point throughout that LSC (the `mainMethod.m`, `directSolidAngle.m` and `indirectSolidAngle.m` functions).

Device simulation call:

```
%
%   The full lsc device function for the analytical LSC
%   model.
%
%   Developed 2/24/2021 by David R. Needell
%
function [] = analyticalModel_v2_lscDeviceSimulation(   ...
    testDate)
    %   Define the range of edge lengths.
    edgeLengthArray = linspace(100e-6,1e-2,10);
    %   Set the lsc device simulation boolean to true.
    lscDeviceBool = true;
    %   Make a new folder.
    mkdir('Results/',testDate);
    %   Loop through edge lengths.
    for edgeLengthIndex = 1:size(edgeLengthArray,2)
        %   Create a new file name.
        fileName = strcat(testDate,                      ...
            '/Results_edgeLength',                       ...
            num2str(edgeLengthArray(edgeLengthIndex)));
        %   Call the simulation.
        analyticalModel_v2_parameterSweep(fileName,      ...
            lscDeviceBool, edgeLengthArray(              ...
            edgeLengthIndex));
    end
```

LSC parameter sweep call:

```
%
%   The parameter sweeping function for the analytical
%   LSC model.
%
%   Developed 2/24/2021 by David R. Needell
%
function [] = analyticalModel_v2_parameterSweep(         ...
    testingDateAndName, lscDeviceBool, edgeLengthValue)
    %   Set the parameters of the LSC.
    %-------------------------------------------------------
    %   Edge length (meters).
    edgeLength = edgeLengthValue;
    %   Waveguide thickness (meters).
    wgThickness = 500e-6;
    %   Waveguide index of refraction (unitless).
    wgIndex = 1.50;
    %   If simulating full device.
    if lscDeviceBool
        %   Define LSC coordinates in x,y,z.
```

```
20          pos_x = linspace(1e-6,edgeLength,25);
21          pos_y = linspace(-edgeLength/2,edgeLength/2,25);
22          pos_z = linspace(-wgThickness/2,wgThickness/2,25);
23      end
24
25      %   Set the parameters of the luminescence location.
26      %-------------------------------------------------------
27      if lscDeviceBool
28          %   Transform given cart to cyl.
29          pos_r = sqrt(pos_x.^2 + pos_y.^2);
30          pos_phi = atan(pos_y./pos_x);
31      else
32          %   Radial position in cylindrical coord (meters).
33          pos_r = 1e-6:500e-6:edgeLength;
34          %   Polar angle position in cylindrical coord
35          %   (degrees).
36          pos_phi = 0:1:90;
37          %   Vertical position in cylindrical coord
38          %   (meters).
39          pos_z = wgThickness/2:5e-6:wgThickness/2;
40      end
41
42      %   Set the reabsorption factor.
43      %-------------------------------------------------------
44      %   Reabsorption factor (unitless).
45      reAbs = linspace(0,10,10);
46
47      %   Collect all output data.
48      %-------------------------------------------------------
49      %   Calculate number of permutations to test.
50      numPerms = size(edgeLength,2) *                         ...
51          size(wgThickness,2) * size(wgIndex,2) *             ...
52          size(pos_r,2) * size(pos_phi,2) *                   ...
53          size(pos_z,2) * size(reAbs,2);
54      %   Initialize data matrix (7 inputs + 1 output).
55      outputData = zeros(numPerms,8);
56      %   Index the row to keep track of loop.
57      indexRow = 1;
58      %   Create a progress bar to keep track.
59      progressbar('Length','Thickness','Ref.Index',          ...
60          'r-Pos.','phi-Pos', 'z-Pos','reAbs');
61      %   Calculate output data.
62      for edgeLengthIndex = 1:size(edgeLength,2)
63          for wgThicknessIndex = 1:size(wgThickness,2)
64              for wgIndexIndex = 1:size(wgIndex,2)
65                  for pos_rIndex = 1:size(pos_r,2)
66                      for pos_phiIndex = 1:size(pos_phi,2)
67                          for pos_zIndex = 1:size(pos_z,2)
68                              for reAbsIndex = 1:size(    ...
69                                  reAbs,2)
70      %   Store all permutations and data.
71      outputData(indexRow,1) = edgeLength(edgeLengthIndex);
72      outputData(indexRow,2) = wgThickness(wgThicknessIndex);
73      outputData(indexRow,3) = wgIndex(wgIndexIndex);
```

```
74      outputData(indexRow,4) = pos_r(pos_rIndex);
75      outputData(indexRow,5) = pos_phi(pos_phiIndex);
76      outputData(indexRow,6) = pos_z(pos_zIndex);
77      outputData(indexRow,7) = reAbs(reAbsIndex);
78      outputData(indexRow,8) =                                    ...
79          analyticalModel_v2_mainMethod(                          ...
80          edgeLength(edgeLengthIndex),                            ...
81          wgThickness(wgThicknessIndex),                          ...
82          wgIndex(wgIndexIndex),[pos_r(pos_rIndex),               ...
83          pos_phi(pos_phiIndex), pos_z(pos_zIndex)],              ...
84          reAbs(reAbsIndex));
85      %   Compute fractions for progress bar.
86      fracReAbs = reAbsIndex/size(reAbs,2);
87      fracZPos = ((pos_zIndex-1)+fracReAbs)/size(pos_z,2);
88      fracPhiPos = ((pos_phiIndex-1)+fracZPos)/                   ...
89          size(pos_phi,2);
90      fracRPos = ((pos_rIndex-1)+fracPhiPos)/size(pos_r,2);
91      fracRef = ((wgIndexIndex-1)+fracRPos)/size(wgIndex,2);
92      fracThick = ((wgThicknessIndex-1)+fracRef)/                 ...
93          size(wgThickness,2);
94      fracEdge = ((edgeLengthIndex-1)+fracThick)/                 ...
95          size(edgeLength,2);
96      %   Update the progress bar.
97      progressbar(fracEdge,fracThick,fracRef,fracRPos,            ...
98          fracPhiPos,fracZPos,fracReAbs);
99      %   Increment the row index.
100     indexRow = indexRow+1;
101                             end
102                         end
103                     end
104                 end
105             end
106         end
107     end
108
109     %   Parse the data.
110     %-------------------------------------------------------
111     %   Reshape the data.
112     plottingOutputData = reshape(outputData(:,end),             ...
113         [size(reAbs,2), size(pos_z,2),size(pos_phi,2),          ...
114         size(pos_r,2),size(wgIndex,2),                          ...
115         size(wgThickness,2),size(edgeLength,2)]);
116     if lscDeviceBool
117         %   Initialize probability array.
118         collectionProbArray = zeros(size(reAbs));
119         %   Loop through the reAbs values.
120         for reAbsIndex = 1:size(reAbs,2)
121             %   Calculate net probability of device
122             %   collection.
123             currentProb = squeeze(plottingOutputData(           ...
124                 reAbsIndex,:,:,:));
125             collectionProbArray(reAbsIndex) = sum(sum(          ...
126                 sum(currentProb,3),2),1)/(size(pos_z,2)         ...
127                 *size(pos_phi,2)*size(pos_r,2));
```

```
128         end
129     end
130     %   Save the data to the results folder.
131     save(strcat('Results/',testingDateAndName,'.mat'),  ...
132         'plottingOutputData','edgeLength','wgThickness',...
133         'wgIndex','pos_r','pos_phi','pos_z','reAbs',    ...
134         'collectionProbArray');
135 end
```

Main method master function:

```
1  %
2  %   The main method function for the analytical LSC model,
3  %   calculating the solid angle of photoluminescence
4  %   within a waveguide and absorber medium.
5  %
6  %   Inputs.
7  %       - edgeLength: double 1x1 in meters
8  %       - wgThickness: double 1x1 in meters
9  %       - wgIndex: double 1x1 (no units)
10 %       - lumPosition: double 1x3 in [meters (r), degrees
11 %         (phi), meters(z)]
12 %       - reAbsorptionFactor: double 1x1 (no units: ratio
13 %         of initial absorption (assumed to be 1) to
14 %         reabsorption)
15 %
16 %   Developed 2/24/2021 by David R. Needell
17 %
18 function [collectionProb] =                              ...
19     analyticalModel_v2_mainMethod(edgeLength,            ...
20     wgThickness,wgIndex,lumPosition,reAbsorptionFactor)
21     %   Calculate direct collection solid angle.
22     omega0Norm = analyticalModel_v2_directSolidAngle(    ...
23         edgeLength, wgThickness,lumPosition,             ...
24         reAbsorptionFactor);
25     %   Calculate indirect collection solid angle.
26     omegaNorm = analyticalModel_v2_indirectSolidAngle(   ...
27         edgeLength,wgThickness,wgIndex,lumPosition,      ...
28         reAbsorptionFactor);
29     %   Calculate probability of collection.
30     collectionProb = omega0Norm+omegaNorm;
31 end
```

Direct and Indirect solid angle calculations:

```
1  %
2  %   The direct solid angle calculation function.
```

```
%
%   Developed 2/24/2021 by David R. Needell
%
function [omega0] = analyticalModel_v2_directSolidAngle(...
    edgeLength,wgThickness,lumPosition,reAbsorptionFactor)
    %   Define alpha0 term.
    alpha0 = atan((edgeLength*abs(cos(lumPosition(2)*    ...
        (pi/180))))/(2*sqrt(lumPosition(1)^2+            ...
        lumPosition(3)^2)));
    %   Define beta0 term.
    beta0 = atan((wgThickness*abs(cos(atan(              ...
        lumPosition(3)/lumPosition(1)))))/(2*             ...
        sqrt(lumPosition(1)^2+lumPosition(3)^2)));
    %   Calculate reAbsorption probability.
    reAbsorptionProb = exp(-(reAbsorptionFactor*         ...
        sqrt(lumPosition(1)^2+lumPosition(3)^2))/         ...
        wgThickness);
    %   Calculate omega0 term.
    omega0 = 4*asin(sin(alpha0)*sin(beta0))/(4*pi)*      ...
        reAbsorptionProb;
end
```

```
%
%   The integrated, direct solid angle calculation
%   function.
%
%   Developed 2/24/2021 by David R. Needell
%
function [omegaIntNorm] =                                ...
    analyticalModel_v2_indirectSolidAngle(               ...
    edgeLength,wgThickness,wgIndex,lumPosition,          ...
    reAbsorptionFactor)
    %   Calculate the escape cone angle.
    thetaCritical = asin(1/wgIndex);
    %   Define alpha term.
    alpha = @(theta) atan((edgeLength*abs(cos(           ...
        lumPosition(2)*(pi/180))))/(2*sqrt((              ...
        lumPosition(1)/(sin(theta*(pi/180)))).^2+         ...
        lumPosition(3)^2)));
    %   Define beta term.
    beta = @(theta) atan((wgThickness*abs(cos(atan(      ...
        lumPosition(3)/lumPosition(1)))))/(2*sqrt((       ...
        lumPosition(1)/(sin(theta*(pi/180)))).^2+         ...
        lumPosition(3)^2)));
    %   Calculate the reAbsorption probability.
    reAbsorptionProb = @(theta) exp(-(                   ...
        reAbsorptionFactor*sqrt((lumPosition(1)/(sin(    ...
        theta*(pi/180)))).^2+lumPosition(3)^2))/          ...
        wgThickness);
    %   Define omega term.
    omega = @(theta) 4*asin(sin(alpha(theta))*sin(beta(  ...
        theta)))*reAbsorptionProb(theta);
```

```
31      %   Calculate integrated omega term.
32      omegaInt = integral(omega,thetaCritical,pi-          ...
33          thetaCritical,'ArrayValued',true);
34      %   Define normalization function handle.
35      norm = @(x) 4*pi;
36      %   Normalize over all solid angles.
37      omegaIntNorm = omegaInt / integral(norm,             ...
38          thetaCritical,pi-thetaCritical,'ArrayValued',true);
39  end
```

APPENDIX C

Life-Cycle Assessment for Tandem LSC/Si Devices

Beyond the power conversion efficiency and even levelized cost of energy—typically used to holistically evaluate the technoeconomic competitiveness of a given energy generation technology—we should also take into account the life cycle, use, recyclability, and net carbon emissions (manufacturing, distribution, end-use, recycling, waste) from so-called cradle (the fabrication) to grave (the waste/recycling stage). These life cycle assessments enable researchers to approximate the bigger picture environmental impact of a certain technology, specifically here in the context of energy generation.

We collaborate with the Corkish group at the Australian Center for Advanced Photovoltaics at the University of New South Whales, whereby previous work has demonstrated extensive life cycle assessments for a myriad photovoltaic devices[199,273–278]. We consider a tandem LSC/Si, monolithically and optically stacked four terminal module device employing CdSe/CdS quantum dot luminophores dispersed within a waveguide polymer, poly(lauryl methacrylate), layer of approximately 50μm thickness deposited via a roll-to-roll process (e.g., doctor or draw-down blade).

We undertake the life cycle assessment for this module by estimating the necessary energy inputs and processing requirements for each of the individual components as well as for the full device integration and assembly. We model two variations for high efficiency photoluminescence trapping, top filter designs: dielectric or polymeric Bragg stack filters composed of alternating high/low refractive index materials. Such designs have shown high tunability and optimized reflectance/-transmittance characteristics[279,280]. Here, we model the layer growth via sputter deposition (dielectric) or extrusion processing (polymeric).

To collect the photoluminescence, we assume InGaP micro-cells grown via epitaxial vacuum phase deposition (e.g., MOCVD) and take into the mesa-etch process in order to isolate micro-cells of approximately 0.4 x 0.4mm in area. Via pick-and-place machining and screen printing technology, we model arranging and electrically interconnecting the micro-cells into a grid pattern, whereby the cells lie planar to the waveguide and set the geometric gain to 100. Finally, we apply a bottom AlSb high contrast grating metasurface filter for increased photoluminescence trapping

through a co-sputtering thin film deposition process. The AlSb metasurface pattern consists of cylindrical pillars in a hexagonal array defined via nanoimprint lithography followed by a dry or wet etch process. The hexagonal array of the pillars generates the desired optical properties of a reflectance peak centered about the CdSe/CdS emission—where the high transmittance of such filters in the long wavelength regime enables effective silicon subcell light collection[218].

The calculation of the environmental impacts for such a tandem LSC/SI technology is based on the area required for a solar module to produce 1 kWh of electricity (functional unit). This calculation considers an assumed efficiency and lifetime—give by our performance modeling of chapter 5—the average US insolation condition (assumed to be 1800 kWh/m[281] / year[282]), and the performance ratio (set as 0.75 for all cases). The final environmental impact results are highly sensitive to these assumptions which we choose carefully to better represent the majority of life cycle studies for photovoltaic technologies[283], in order to be relevant and applicable for further studies.

Figure C.1 presents the results for global warming potential, human and freshwater toxicity potential, freshwater eutrophication potential, and abiotic depletion potential of LSC/Si tandem modules when compared in the same model to standalone Si (in this case, passivated emitter rear contact cell type) solar modules. Through this model, we find that the tandem LSC efficiency improvement influences the environmental outputs positively, due to the lower energy usage to produce the same amount of solar-derived energy (1 kWh, which is the functional unit of this life cycle assessment) during the module lifetime, at relatively low environmental costs.

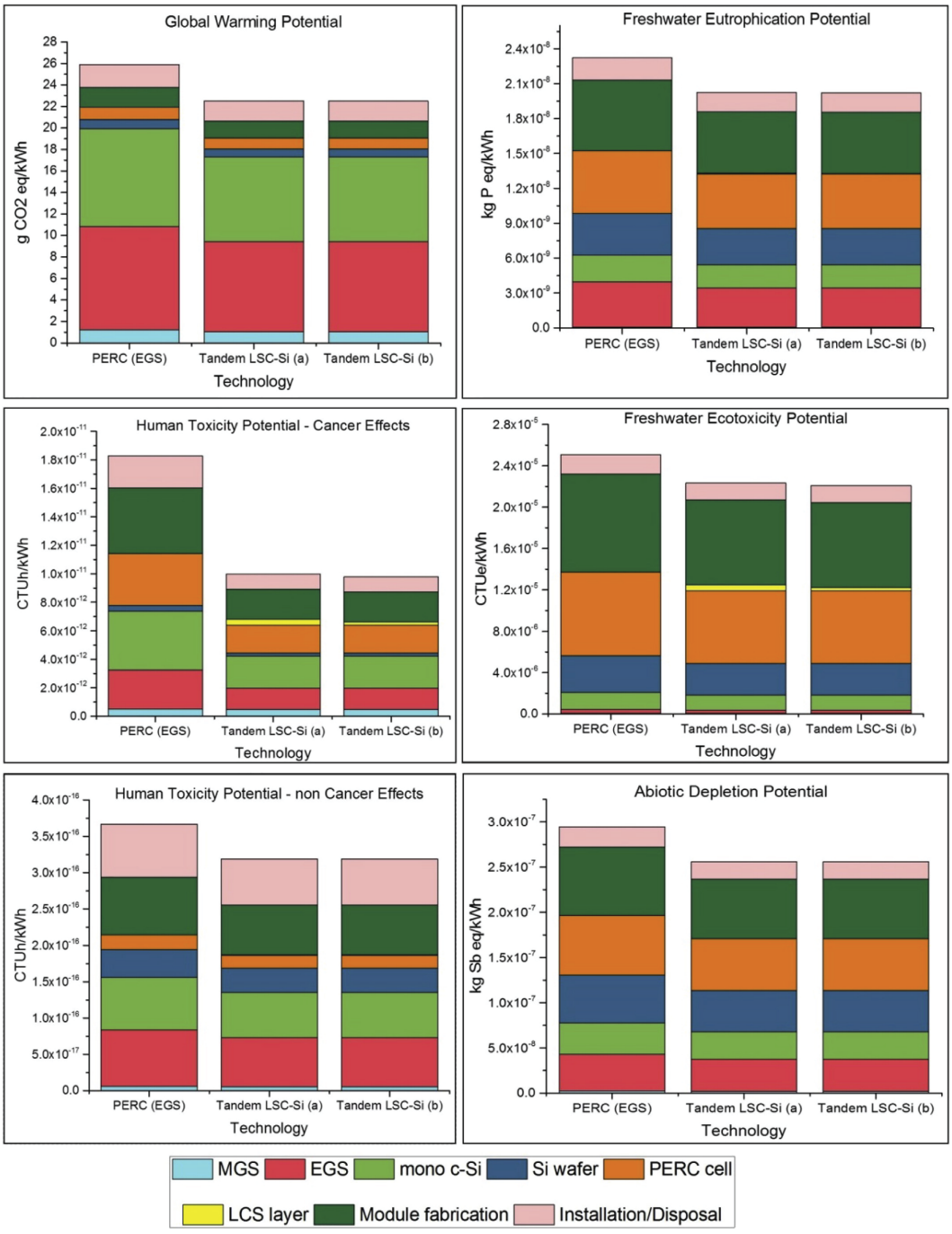

Figure C.1: Global Warming Potential (GWP), Human Toxicity Potential: Cancer and non-Cancer Potential (HTP-CE and HTP-nCE), Freshwater Eutrophication Potential (FEuP), Freshwater Ecotoxicity Potential (FEcP) and Abiotic Depletion Potential (ADP) results for the three technologies studied (PERC Si, LSC(a)/PERC Si and LSC(b)/PERC Si, where "a" represents the top filter: TiO_2/SiO_2 Stack Filter and "b" represents the top filter: PMMA Stack Filter. Adapted from Lundardi et al.[284].

APPENDIX D

Technoeconomic Analysis for Single Junction LSC Devices

Introduced in chapter 4.3, we quantify the technoeconomic cost ($) per generated direct current power (W) for a double pane, insulated glass window hosting an embedded luminescent layer coupled to a roll-to-roll manufactured two-dimensional grid array of GaAs or Si heterojunction micro-cells. Figure 4.6 conceptualizes what a single manufacturing line could look like and the example processes we assume in this model to fabricate such a building integrated photovoltaic device for an area of 1m x 1.5m.

Operating Expenditures We begin by analyze the key operating expenditures for such a manufacturing process. The following spreadsheet details the information flow, relevant values and units, and example input parameters as well as, included at the end, a list of all the raw materials and labor costs assumed for this model.

Values Legend:							
Input							
Temp Input							
Need to validate							
Units							
Calculation							
Significant Result							
ITEM	VALUE	UNITS					
OPERATING PARAMETERS							
Production Volume (PV)	*500,000.00*	windows / year					
Daily PV	2,000.00	windows / day					
Geometric Gain	150.00	unitless					
Optical Density at 450nm light	1.00	unitless					
Operating Days per Year	*250.00*	days/yr					
Operating Hours per Operating Da	*8.00*	hr/day					
Maximum Allowed Line Utilizatior	*85.0%*						
PRODUCTION OPERATIONS							
ITEM	ROCESS VALU	UNITS		CONSUMPTION/PRODUCTI(	UNITS	COST	UNITS
Stage 1a. IR-filter Deposition							
Inputs							
Window Pane	30.00	m2 / batch		6,060.61	m2 / day	9.09	$ / window
Si (sputter target)	0.081691200	kg / batch		16.50	kg / day	0.36	$ / window
Ti (sputter target)	0.465723000	kg / batch		94.09	kg / day	1.04	$ / window
Sputtering Labor (operational)	*1.0*	workers / line		101.01	person-hr / day	0.76	$ / window
Electricity	*2.00*	kWh / batch		404.04	kWh / day	0.01	$ / window
Outputs							
IR-glazed window pane (back)	10	IR-pane / batch		2,020.20	IR-panes / day		
IR-glazed window pane (front)	10	IR-pane / batch		2,020.20	IR-panes / day		
Operation							
Cycle Time	*0.50*	hours / batch					
Required Gross PV	202.02	batch / day					
Implemented No. Parallel Stations	15.00	prod lines					
Gross Production Capacity	240.00	batches / day					
Line Utilization	84.2%						
Stage 1b. Si Micro-cell Processing							
Inputs							
Full-size Si HIT cell (15.6cm x 15.6	0.066667	m2 / batch		13.60	m2 / day	13.06	$ / window
Si (sputter target)	4.97E-06	kg / batch		0.0010	kg / day	0.00002	$ / window
Ag (sputter target)	3.67E-04	kg / batch		0.0749	kg / day	0.0022	$ / window
Laser cutting labor (operational)	*1.0*	workers / line		102.03	person-hr / day	0.77	$ / window
Sputtering Labor (operational)	*1.0*	workers / line		102.03	person-hr / day	0.77	$ / window
Electricity	*1.00*	kWh / batch		204.06	kWh / day	0.01	$ / window
Outputs							
Si HIT micro-cell	266,666.67	micro cells / batch		54,416,216.03	micro cells / day		
Yield Percentage (see NOTES colu	*99.0%*						
Operation							

Cycle Time	0.50	hours / batch					
Required Gross PV	204.06	batches / day					
Implemented No. Parallel Stations	16.00	prod lines					
Gross Production Capacity	256.00	batches / day					
Line Utilization	79.7%						
Stage 2a. Micro-cell Array Printing							
Inputs							
IR-glazed window pane (back)	10.00	pane / batch		--	--	--	--
Si HIT micro-cell	266,666.67	micro cells / batch		--	--	--	--
Al paste (screen-printing)	3.49E-03	kg / batch		0.71	kg / day	0.0183	$ / window
Cu soldering tabs (bus bars)	1.01E-01	m / batch		20.36	m / day	0.0000068	$ / window
Screen printing labor (operational	0.50	workers / line		505.05	person-hr/day	3.79	$ / window
Pick-and-place labor (operational)	0.50	workers / line		505.05	person-hr/day	3.79	$ / window
Electricity	2.00	kWh / batch		404.04	kWh/day	0.01212	$ / window
Outputs							
Micro-cell Array IR-Pane	10.00	arrays / batch		2,020.20	arrays / day		
Operation							
Cycle Time	5.00	hours / batch					
Required Gross PV	202.02	batches / day		100,000.00			
Implemented No. Parallel Stations	149.00	prod lines		671.14			
Gross Production Capacity	238.40	batches / day					
Line Utilization	84.7%						
Stage 2b. QD-LMA Dipsersion							
Inputs							
InAs/InP/ZnSe QDs	1.50E+01	m2 / batch		3,030.3030	m2 / day	212.12121	$ / window
LMA	2.60E+00	kg / batch		526.0606	kg / day	4.06	$ / window
EGDMA	3.15E-01	kg / batch		63.6970	kg / day	0.73	$ / window
Trioctylphosphene	9.97E-02	kg / batch		20.1455	kg / day	0.83	$ / window
Photoinitiator	1.62E-03	kg / batch		0.3264	kg / day	0.0107	$ / window
Mixing and Sonication Labor (ope	0.50	workers/line		10.10	person-hrs/day	0.076	$ / window
Electricity	0.10	kWh / batch		20.20	kWh/day	0.00061	$ / window
Outputs							
QD-LMA Mixture	3.00E-03	m3 / batch		0.61	m3 / day		
Operation							
Cycle Time	0.10	hours / batch					
Required Gross PV	202.02	batches / day					
Implemented No. Parallel Stations	3.00	prod lines					
Gross Production Capacity	240.00	batches / day					
Line Utilization	84.2%						
Stage 3. LSC Deposition							
Inputs							
Micro-cell Array IR-Pane (back)	10.00	array / batch		--	--	--	--
QD-LMA Mixture	3.00E-03	m3 / batch		--	--	--	--
Doctor Blading Labor (operational	0.50	workers / line		10.10	person-hrs / day	0.076	$ / window
Electricity	0.05	kWh / batch		10.10	kWh / day	0.076	$ / window
Outputs							
LSC Array IR-Pane	10.00	LSC / batch		2,020.20	LSC / day		

Yield Percentage (see NOTES colu	0.99						
Operation							
Cycle Time	0.10	hours / batch					
Required Gross PV	202.02	batches / day					
Implemented No. Parallel Stations	3.00	prod lines					
Gross Production Capacity	240.00	batches / day					
Line Utilization	84.2%						
Stage 4. Front Glass Encapsulation							
Inputs							
LSC Array IR-Pane (back)	10.00	LSC / batch		--	--	--	--
IR-glazed window pane (front)	10.00	pane / batch		--	--	--	--
EVA	30.00	m2 / batch		6,000.00	m2 / day	4.61	$ / window
Vacuum Lamination Labor (operat	0.50	workers / line		5.00	person-hrs / day	0.038	$ / window
Electricity	0.50	kW / batch		100.00	kWh / day	0.0030	$ / window
Outputs							
Power Window Module	10.00	window / batch		2,000.00	window / day		
Operation							
Cycle Time	0.05	hours / batch					
Required Gross PV	200.00	batches / day					
Implemented No. Parallel Stations	2.00	prod lines					
Gross Production Capacity	320.00	batches / day					
Line Utilization	62.5%						
INDIRECT							
Labor							
Management	3.00	managers					
Engineer	3.00	engineers					
Burden Rate (for all labor)	0.50						
Maintenance	0.03						
Electricity - Factory Lighting & HV/	330.00	kWh / day				0.01	$ / window
	Totals (per unit)			**Totals (annual)**			
OPERATING EXPENDITURES	**280.02**	**$ / window**		**140,007,623.68**	**$ / year**		
Materials	245.93	$ / window		122,966,935.46	$ / year	**Cost Rates**	
Si (target)	0.36426	$ / window		182,132.19	$ / year	44.14	$ / kg
Ti (target)	1.04442	$ / window		522,209.38	$ / year	22.20	$ / kg
Pane (OEM)	9.09091	$ / window		4,545,454.55	$ / year	3.00	$ / m2
HIT Cell (OEM)	13.05989	$ / window		6,529,945.92	$ / year	1,920.00	$ / m2
Ag (target)	0.00220	$ / window		1,100.75	$ / year	58.77	$ / kg
Al (paste)	0.01833	$ / window		9,165.00	$ / year	52.00	$ / kg
Cu tabs	0.00001	$ / window		3.42	$ / year	0.0007	$ / m
InAs/InP/ZnSe QDs (OEM)	212.12121	$ / window		106,060,606.06	$ / year	140.00	$ / m2
LMA	4.06061	$ / window		2,030,303.03	$ / year	15.44	$ / kg
EGDMA	0.72727	$ / window		363,636.36	$ / year	22.84	$ / kg
Trioctylphosphene	0.82909	$ / window		414,545.45	$ / year	82.31	$ / kg
Photoinitiator	0.01067	$ / window		5,333.33	$ / year	65.37	$ / kg
EVA	4.60500	$ / window		2,302,500.00	$ / year	1.54	$ / m2
Labor	11.07280	$ / window		5,536,402.28	$ / year		

Direct	10.05280	$ / window		5,026,402.28	$ / year		*15.00*	$ / hr
Management	0.48000	$ / window		240,000.00	$ / year		*80,000.00*	$ / yr / pers
Engineer	0.54000	$ / window		270,000.00	$ / year		*90,000.00*	$ / yr / pers
Electricity	0.10973	$ / window		54,863.94	$ / year		*0.06*	$ / kWh
Maintenance	22.89884	$ / window		11,449,422.00	$ / year			

Capital Expenditures Next we must consider the initial capital investment for the plant and manufacturing components needed in order to fully fabricate each part of the final LSC window module. Below is an example of this capital expenditure cost for such a production line.

Values Legend:		
Input		
Input from 'Cost Analysis' Sheet		
Calculation		
Significant Result		
Estimated Lifetime	10 years	
ITEM	VALUE	UNITS
Stage 1a. IR-Filter Deposition		
Roll-to-roll vacuum coating system (sputterer)	*6,060,000*	$
Total as Implemented	90,900,000	$
Area per Line	*200*	sq.ft.
Stage 1b. Si Micro-Cell Processing		
Precision laser cutter	*60,000*	$
SiNx PECVD Reactor	*1,496,000*	
a-Si:H PECVD Reactor	*7,325,000*	
Total as Implemented	142,096,000	$
Area per Line	*200*	sq.ft.
Stage 2a. Micro-cell Array and Interconnection Printing		
Pick-and-Place Machine Cost	*212,000*	$
Screen Printing Cost	*353,000*	$
Total as Implemented	84,185,000	$
Area per Line	*160*	sq.ft.
Stage 2b. QD-LMA Dispersion		
QD Reactor Line	*500,000*	$
Total as Implemented	1,500,000	$
Area per Line	*100*	sq.ft.
Stage 3. LSC Deposition		
Laminator	*10,000*	$
Total as Implemented	30,000	$
Area per Line	*100*	sq.ft.
Stage 4. Front Glass Encapsulation		
Laminator	*446,000*	$
Total as Implemented	892,000	$
Area per Line	*100*	sq.ft.
Equipment Total		
Bare Equipment + Tools Sub-Total	$319,127,000	
Plant Design and Installation Cost	$63,825,400	
Equipment + Tools Installed Total	**$382,952,400**	
Building	**$570,000**	
Total Base Area (sum of stages)	760	sq.ft.
Storage	190	sq.ft.
Workflow Space Factor	*2*	
Final Area	1,900	sq.ft.
TOTAL CAPEX	**$383,522,400**	

APPENDIX E

GaAs Heterojunction Cell Fabrication Design

For many applications of the LSC within this thesis, we use a GaAs device architecture grown in vacuum phase epitaxy by our collaborator John Geisz at the National Renewable Energy Laboratory. Specifically, we grow the n-on-p upright GaAs homojunction solar cells by atmospheric pressure organometallic vapor phase epitaxy at 650°C. The Zn-doped absorber layer was approximately 2.5 μm thick and the Se-doped emitter layer was 100nm thick. Nearly lattice-matched p-GaInP was used as a back-surface-field while a 25nm thick Se-doped AlInP layer served a passivating window. Electroplated gold on the GaAs substrate formed the back contact. Front Pd/Ge/Ti/Pd/Al grids were defined by standard photolithography, deposited using e-beam evaporation, annealed at 120-140°C, and mesa isolated to form 0.02 cm^2 square devices. 80nm of ZnS deposited by thermal evaporation was used as an antireflective coating between the GaAs and the LSC waveguide. The individual devices were finally singulated with a dicing saw. Figure E.1 shows the set of shadow and etch masks used to fabricate the GaAs cell.

As seen from figure E.1, a single wafer produces over 100 individual GaAs cells for use and analysis. We perform current-density testing for each of the produced cells in order to characterize their use for the applications explored in this thesis. For example, four square GaAs cells we test sequentially after singulation and integrate into our space-based solar power prototype. Figure E.2 shows the electro-optical response for these example cells.

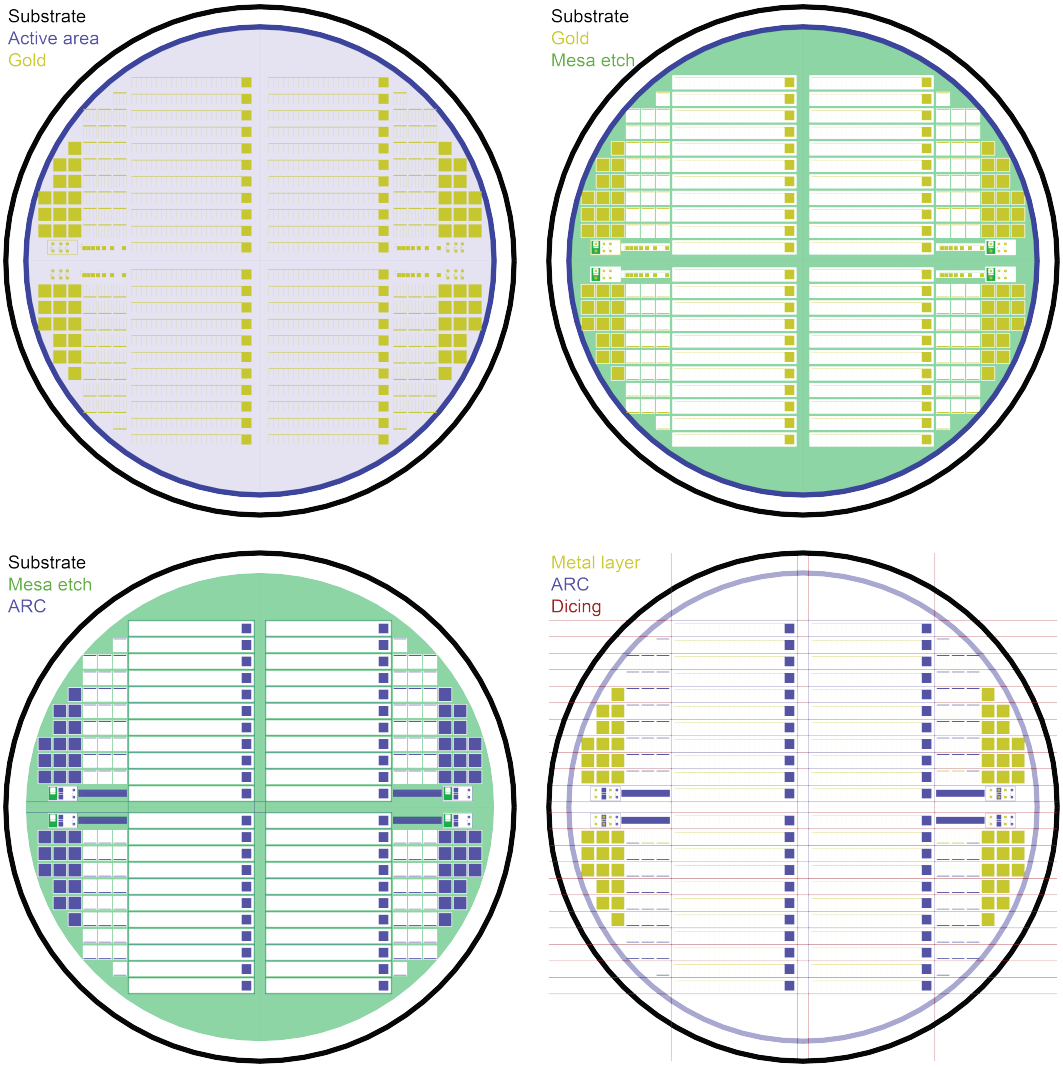

Figure E.1: The set of shadow and etch masks used to fabricate the upright n-on-p GaAs homojunction solar cells. (clockwise) The substrate (50.8mm diameter) and active area set for deposition (46.8mm diameter) and the mask to deposit the gold front contacts onto the cell for square (single junction, terrestrial project as described in chapter 3) and rectangular (single-junction, space-based project as described in chapter 6); the mesa etch mask to define individual cells on the wafer; the dicing mask showing the (red) saw lines; the antireflective coating (ARC) negative mask.

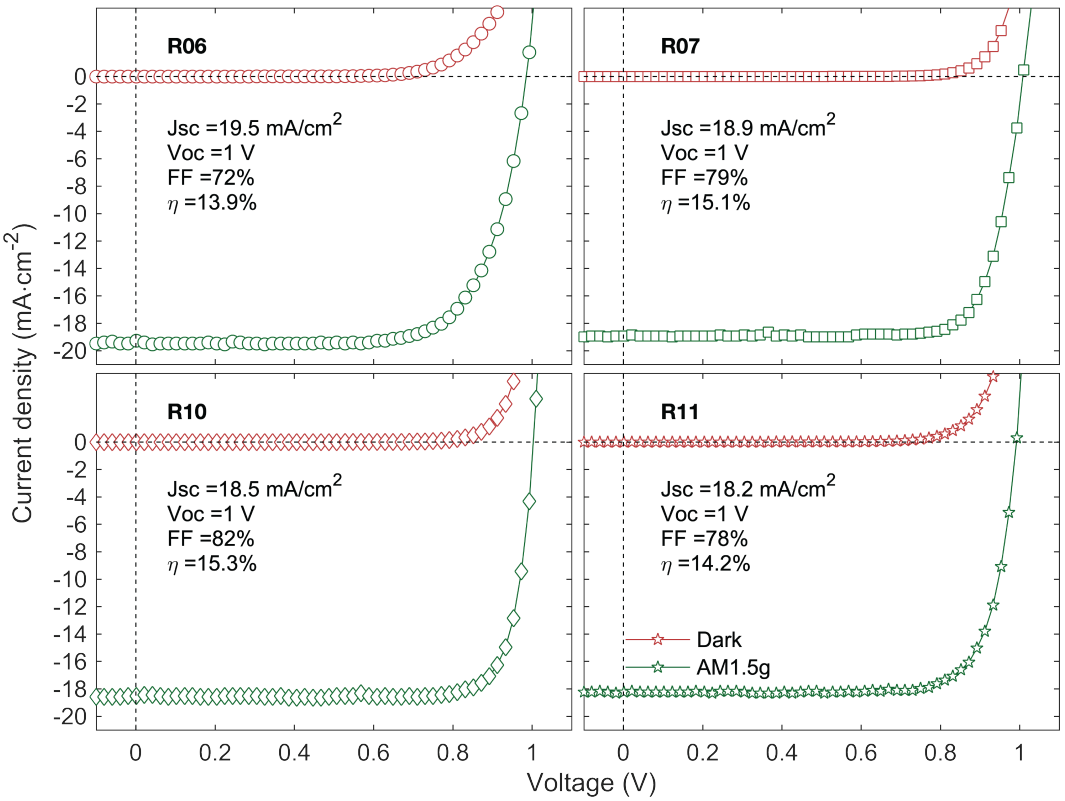

Figure E.2: Four current density ($mA{\cdot}cm^{-2}$), voltage (V) characteristic curves for four singulated GaAs rectangular (1.2cm x .12cm) cells under AM1.5g exposure (green) and in the dark at 300°C (red). For each we record the short-circuit current, open-circuit voltage, fill factor, and power conversion efficiency.

APPENDIX F

Passivated Contact Si Cell Design and Analysis

For the case of a tandem LSC/Si four terminal module, only the long wavelength light (for $CuInS_2$/ZnS: >800nm, for CdSe/CdS: >700nm) transmits through the top LSC component to reach the underlying silicon subcell. Here we discuss the optical coupling and performance of a highly efficient passivated contact silicon bottom cell—where the open circuit voltage maintains above 700mV under, for example, the CdSe/CdS quantum dot based LSC spectrum[114]. These measurements are compared against the performance of a Si cell under a 1μm InGaP filter to mimic the prototypical spectrum incident upon a Si cell in a conventional III-V/Si tandem (monolithic stack). Finally, we compare the performance of the passivated contact Si cell against the p-type passivated emitter rear contact (p-PERC) Si cell provided by our industrial partner, Jinko cells, under the spectrum passing though the LSC top module. Both types of cell suffer similar percentage loss in short circuit current due to reduced incident light intensity but a higher performance is observed for the passivated contact Si cell because of the high Voc, which makes the passivated contact Si cell a more efficient bottom cell compared to the p-PERC cell and the choice of cell which we use in chapter 5.

Our passivated contact Si cell is a rear junction front/back oppositely doped poly-Si/SiO_x layers deposited on an n-Cz Si wafer. A single side textured n-Cz wafer is cleaned using standard RCA recipe, and then approximately 1.5 nm thick low temperature thermal SiO_x is grown on the wafer in a furnace. 50 nm of p/n a-Si:H is then grown on top of this oxide layer using plasma-enhanced chemical vapor deposition and the sample is placed inside the furnace at 850°C for 30 mins to crystallize the a-Si to poly Si and also diffuse the dopants. Additional hydrogenation is provided by depositing 15 nm of alumina oxide using atomic layer deposition and then annealing the sample at 400°C in a forming gas environment. This process provides excellent surface passivation with very low J_0 values of about 10 fA·cm^{-2} and cells with implied open circuit voltages (no series or shunt losses) of greater than 730 mV have been obtained. Metal contacts are made by thermally evaporating aluminum through shadow masks for both front grid and back blanket metal. Finally, SiN_x anti-reflection coating is deposited on the front of the cell. In the resulting Si passivated contact solar cells, we achieve close to 720 mV in Voc at 1

sun, and above 700 mV under the 1 μm InGaP filter, which transmits less light to Si than the LSC top structure.

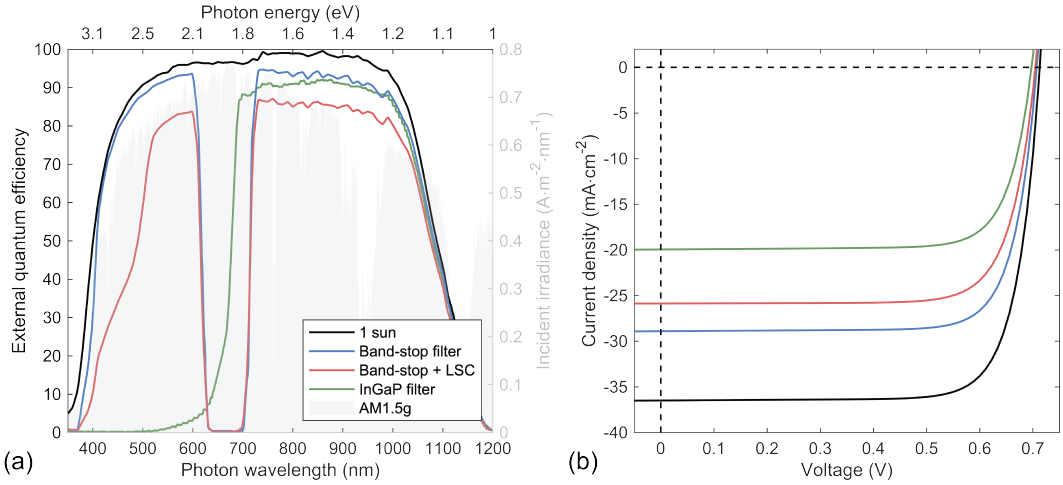

Figure F.1: The external quantum efficiency (a) and current density, voltage response (b) curves for the passivated contact silicon cell under a variety of irradiance operating conditions.

We measure the passivated contact Si bottom cell under the spectrum passing through a stack of CdSe/CdS QD waveguide and the band-pass filter (spectra for these layers shown in figure 5.9) or 1μm thick InGaP filter as shown in the inset of figure F.1. A separate measurement shows that supplying an additional top filter will decrease the silicon subcell power conversion efficiency by approximately 0.2%. The shadow loss from 0.5% area coverage of the planar LSC photovoltaic cells, and nearly 2.5% area coverage of the interconnects and busbar for the LSC could further reduce the short-circuit current density of the Si cell by nearly 1mA·cm^{-2}, which could result in an additional 0.6% loss in efficiency. However, the shadow loss associated with the InGaP cell array interconnects and busbar can be further minimized.

Figures F.1(a),(b) show the evolution of the Si cell current-voltage response curves, external quantum efficiency, and the cell parameters as different layers of the top module are stacked on top of the Si cell. Under one sun illumination, the passivated contact Si cell demonstrates a 20.4% power conversion efficiency with a high Voc of 716mV. Short-circuit current density reaches 36.4mA·cm^{-2}—lower than a typical Si cell given the lack of front metal optimization to minimize grid shadow loss. In addition, the cell also exhibits parasitic absorption loss in the n-poly silicon layer as seen in the quantum efficiency curve in figure F.1(b). This low blue response, however, will not significantly affect the Si subcell performance under an LSC monolithic stack since CdSe/CdS quantum dots absorb photons within this wavelength range. When the bottom filter is optically stacked on top of the Si cell, we see a slight drop in Voc from 716 to 709 mV; this is to be expected due to lower incident light intensity as the filter reflects photons between 620–700nm back onto the top module, allowing more energy to be harvested by the higher voltage InGaP cells. The current density of the Si cell is then reduced to 28.9mA·cm^{-2} as we see a

drop in quantum efficiency response within 600–720 nm. This results in the Si cell efficiency of 16.1%.

When the CdSe/CdS QD waveguide is placed on top of the bottom filter, open-circuit voltage is further decreased to 707 mV and the short-circuit current falls to 25.9mA·cm^{-2}, as the absorption from CdSe/CdS quantum dot layer and parasitic absorption in the PLMA waveguide further reduce the incident light on the Si cell. This is seen by the decrease in red quantum efficiency curve of Si cell and an overall power conversion efficiency of 14.2% is obtained for the Si subcell. We finally measure the same Si cell under 1μm of InGaP filter to estimate and compare the cell performance for a typical III-V/Si tandem structure. The InGaP filter has greater than 90% transmission for wavelengths longer than 680nm. Open-circuit voltage of the Si cell maintains above 700 mV, however, short-circuit current density of the cell reduces to 19.9mA·cm^{-2} as the InGaP filter cuts off photons below 680 nm; in an LSC configuration, there is approximately 0.5% area coverage of InGaP cell arrays—depending on the system geometric gain—which allows greater incident spectrum from short wavelength to pass through to the Si bottom cell.

APPENDIX G

CdSe/CdS Synthesis and Waveguide Recipe

Materials Hexanes (mixture of isomers, anhydrous 95%, Sigma Aldrich), toluene (anhydrous 99.5%, Sigma Aldrich), methyl acetate (anhydrous 99.5%, Sigma Aldrich), cadmium oxide (CdO, 99.99%, Sigma Aldrich), n-octadecylphosphonic acid (ODPA, 99%, PCI Synthesis), tri-n-octylphosphine oxide (TOPO, 99%, Sigma Aldrich), tri-n-octylphosphine (TOP, 97%, Strem), selenium (Se, 99.999%, Sigma Aldrich), 1-octanethiol (OctSH, 99%, Sigma Aldrich), 1-octadecene (ODE, 90% technical grade, Sigma Aldrich), and oleic acid (OA, 90% technical grade, Sigma Aldrich) were all purchased and used without further purification.

Recipe The synthesis of wurtzite phase CdSe quantum dot cores were synthesized following previously reported[285] synthetic procedures with minor modifications. Briefly, 60 mg CdO, 280 mg ODPA, and 3 g TOPO were added to a round bottom flask and connected to a Schlenk line. The mixture was heated to 150°C and degassed under high vacuum for 1.5 hours. Afterwards, the reaction mixture was placed under inert argon gas and heated to 320°C. The mixture was maintained at this temperature until the reaction mixture became clear and the complexation of $Cd(ODPA)_2$ completes, typically taking nearly 2 hours. During the complexation of $Cd(ODPA)_2$, a solution of 58 mg Se powder dissolved into 360 mg TOP was prepared inside an argon glovebox by stirring the solution at room temperature until the powder dissolved (typically around 1 hour). Following the complexation of $Cd(ODPA)_2$, the reaction mixture was heated to 372°C and 1.5 g TOP was injected into the mixture. Once the temperature stabilized at 372°C, a syringe with the complexed TOP:Se (58 mg Se dissolved in 360 mg TOP) was swiftly injected into the reaction mixture. The reaction mixture was then allowed to react for about 30-60 seconds until the desired CdSe core size was reached and then the reaction was cooled rapidly to room temperature using forced air. After cooling to around 100°C, 3 mL of toluene was injected to slow the precipitation of TOPO. Typically, the preceding reaction was scaled up 2-5 times to produce sufficient quantities of cores for a larger number of reactions. The CdSe cores were isolated from the reaction mixture by adding methyl acetate as an anti-solvent, followed by centrifugation at around 8000 G for 6 mins. The colorful precipitate was re-suspended in hexanes

and the supernatant was discarded, with this process repeated twice more. The isolated CdSe cores were stored inside a glovebox for further use.

Next, the previously synthesized CdSe cores were shelled with CdS to achieve the desired CdSe/CdS quantum dots following previously reported[285] synthetic procedures. Briefly, prior to the shelling reaction a 0.2 M solution of $Cd(Oleate)_2$ with ODE was prepared by: adding a 10:1 molar ratio of OA:CdO into a round bottom flask, diluted with ODE to 0.2 M, degassed at 110°C for two hours, heated to 160°C under inert argon atmosphere until complexation of $Cd(Oleate)_2$ was completed, and stored within a glovebox for further use. The typical scale for the shelling reaction was 100 nanomoles, determined by optical characterization of the CdSe core solution using a reported size-dependent absorbance curve[286]. For these shelling reactions, 6 mL of ODE was added to a round bottom flask and degassed at 110°C before adding 100 nanomoles of CdSe quantum dots and removing the hexane solvent. Afterwards, the reaction flask was placed under argon and heated to 240°C. At 240°C, a syringe pump was used to slowly inject a syringe containing 0.2 M $Cd(Oleate)_2$ and a syringe with an equal volume of 0.2 M OctSH in ODE at a rate of 3 mL/hr. The volume of precursors needed to achieve a specific shell thickness was estimated assuming a shelling reaction with a perfect conversion, however the non-quantitative nature of the shelling reaction results in slightly thinner CdS shells. After the slow injection was started, the temperature was increased to 310°C for the remainder of the shelling reaction. After the prespecified volume was injected, the mixture was allowed to react for an additional 10 mins to consume any remaining precursors. The resulting CdSe/CdS core/shell quantum dots were isolated in a similar manner to the CdSe cores using methyl acetate as an antisolvent and resuspending in hexanes. The processed was repeated 6-8 times to remove residual ODE, OA, and $Cd(Oleate)_2$ that might be problematic when creating optically transparent polymeric waveguides. The resulting CdSe/CdS core/shell quantum dots were maintained in an inert atmosphere glovebox for further use.

Optical Characterization The steady state absorbance spectra were acquired with a Shimadzu UV-3600 double beam spectrometer operating with 1 nm slit widths at the second slowest scanning setting. Solution phase photoluminescence measurements were taken using a calibrated Horiba Jobin-Yvon Fluorolog steady-state scanning PMT spectrofluorometer. Samples were prepared by diluting the quantum dot stock solution until reaching an appropriate optical density for measurements.

Photoluminescence quantum yields were collected by using a home-built integrating sphere setup, described more completely elsewhere[116]. For the home-built integrating sphere setup, a Fianium SC450 pulsed supercontinuum laser provides a bright collimated white light source that is monochromated through two monochromators, an Acton Research SP150 and Acton Research SP275. The monochromatic light is passed through a beam-splitter and a fraction of the light is collected with a calibrated power meter while most of the light enters a Spectralon integrating sphere. Within the integrating sphere, samples are held using a custom-milled Spectralon holder directly in the beam path. Light exiting the integrating sphere is focused

onto the entrance of a SP2300 monochromator and collected using a thermoelectrically cooled Princeton Instruments PIXIS 440B silicon CCD. The setup is corrected for both spectral positions using a combination of neon and mercury wavelength calibration lamps, as well as corrected for sensitivity using a NIST-traceable radiometric calibration lamp from Ocean Optics. An integrating sphere setup can measure PLQYs with uncertainties approaching ±2.5% depending on the spectral position of the PL spectrum.

TEM Characterization Samples for TEM analysis were prepared by diluting the quantum dot stock solution in toluene (OD < 0.1) and then drop-casting approximately 8 μL of the dilute solution onto a TEM grid. All TEM images were taken on a FEI Tecnai T20 S-Twin TEM operating at 200 kV with a LaB6 filament and a Gatan Orius SC200 camera.

Waveguide Fabrication Under inert atmosphere, mix lauryl methacrylate (LMA, Sigma-Aldrich, inhibitor removed with a column), ethylene glycol dimethacrylate (EGDMA, Sigma-Aldrich, inhibitor removed), trioctylphosphine (TOP, Sigma-Aldrich), 2-Hydroxy-2-methylpropiophenone (Darocur 1173, Sigma-Aldrich) at a volume ratio of 100:10:4:0.05. Disperse CdS/CdSe quantum dots in solution and remove volatile solvent by placing under vacuum. Place soda lime glass spacers (SPI) between the substrate and a repel-silane (GE Healthcare) treated quartz plate. Inject monomer/QD solution between the glass plates and cure under 365 nm UV. The quartz plate can be removed after curing as surface treatment prevents it from strongly bonding to the LSC.

Photocurrent Mapping Photocurrent mapping of optical performance of PL within the LSC waveguide, as shown in figure 5.14(a), was measured using a spatially resolved laser beam (NKT SuperK Extreme 20W white laser) aligned with a monochromator (Oriel 77770 1/4m) to enable wavelength selection. For this experiment, a wavelength of 490nm was used, as it is within the absorption spectrum of the CdSe/CdS quantum dots. A 5x objective lens was used to allow for a beam spot size of <10μm and improve precision. Photocurrent collection was measured for a single 0.16mm^2 InGaP cell with a 25mm x 25mm CdSe/CdS waveguide, of optical density 0.3 at 450nm, deposited atop—translating to a GG of 625. The sample measured was exposed during the full week of outdoor testing in Golden, CO at NREL, and was kept in the same testing conditions as the LSC/Si tandem module. To perform the photocurrent mapping, the beam spot began its scan from the corner of the micro-cell to eliminate photocurrent collection from direct illumination of the cell, and extended the scan into a spatial quadrant away from this corner point. The beam moved in 60μm increments during the 2D scan, extending 5mm from the origin in each the x and y spatial coordinates. This led to a total of 6,561 measurements in the scanned 25mm^2 area.

APPENDIX H

Diffuse Trench Reflector Design and Fabrication

As discussed in chapters 3 and 5, to test a planar configuration for the GaAs-based LSC devices employing $CuInS_2Zn/S$ core/shell quantum dot waveguides we place the devices within a diffuse trench reflector. By doing so, we effectively achieve periodic boundary conditions of the waveguide—thereby emulating the device performance for an infinite array of planar photovoltaic cells within the waveguide. Figure H.1 illustrates the diffuse trench reflector structure.

We begin with stock aluminum and mill the top and bottom pieces of the reflector to size. For the bottom component, we cut a 5.91 inch by 5.91 inch square base and mill trenches approximately 3.94 inches by 3.94 inches at a depth of .13 inches to expose a stage of approximately 1.97 inches by 1.97 inches. For the complementary top component, we cut a matched 3.94 inch square at a thickness of .50 inches and mill the interior to create a shell of depth .39 inches with shelled area slightly greater than the bottom stage. We finally mill a top aperture to allow incident light through at an area of 1.97 inches by 1.97 inches.

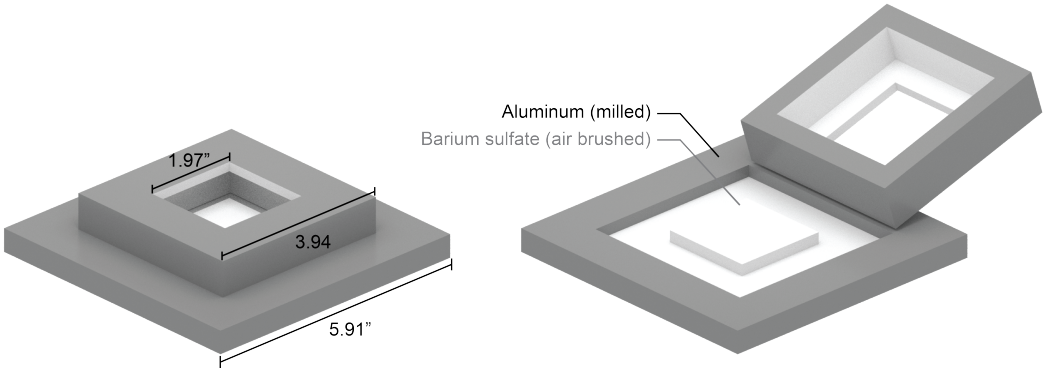

Figure H.1: The design and rendering of the diffuse trench reflector used for measured planar LSC devices. (Left) The diffuse trench reflector in its final arrangement, where a 1.97 inch square entrance aperture allows solar simulator irradiance through to reach the stage. (Right) An exploded view of the two pieces of the trench reflector, where we paint (via air brush) barium sulfate onto the stage and top component interior to attain high diffuse reflectance.

Next, tape all sides to remain aluminum coated (i.e., any side that will not have the Lambertian reflector deposited) and sand blast the remaining area in order to increase the surface roughness to allow greater adhesion between the aluminum surface and the paint. We mix barium sulfate paint (Avian Technologies) and deposit no fewer than 20 layers onto the exposed surfaces of our aluminum trench in order to achieve high diffuse reflectance within the 300nm to 1200nm wavelength range.

APPENDIX I

Characterization of LSC Samples under Illumination

To measure the power conversion efficiency of the LSC device under an ABET solar simulator (Model 11044 Sun 2000), we first calibrate the lamp to the 1000 W/m^2. To accomplish this, we use a silicon reference response cell (PV Measurements Inc., PVM311), whose short-circuit current (applied voltage across the cell is zero) yields 132 mA under 1000 W/m2. Figure I.1(a) shows the measured response curve of the reference cell, after approximately six hours of lamp warmup time in order to ensure irradiance stability of the simulator. However, we vary the entrance aperture of the diffuse trench reflector with an attached optical iris (Thorlabs ID25) in order to quantify the effect of geometric gain on the LSC device performance. Since the source of the solar simulator is not a perfectly collimated lamp, we apply the same aperture across our reference cell (no diffuse trench reflector) and vary the iris diameter in order to measure the corresponding short-circuit current density. Therefore, we can estimate (with uncertainty given by the measurement of the iris diameter) the total irradiance that passes through the iris. Figure I.1(b) shows the trends of this irradiance (mW/cm^2) measurement with respect to iris aperture diameter (i.e., geometric gain given our cell area of 1.4mm x 1.4mm).

To calculate the input irradiance for a given aperture as well the resulting short-circuit current of the LSC and silicon (if applicable) photovoltaic components, we must measure the iris diameter with a set of calipers. Therefore, we have uncertainty associated with the read out of the calipers, where we record measurements of our aperture (from 1.5mm diameter up to 9mm diameter) and record an uncertainty of .05mm for each measurement. We calculate the uncertainty of the aperture area in quadrature to estimate the total short-circuit current density at a given illumination area and geometric gain. Similarly, we measure the area of the embedded GaAs photovoltaic cell within the LSC via optical microscopy and assume an uncertainty of .01mm, again calculating error in quadrature to determine the overall LSC geometric gain. We note that the power conversion efficiency is area normalized by the overall illuminated waveguide top surface area (i.e., the aperture) rather than the GaAs photovoltaic cell area—thereby giving the power conversion efficiency of the entire LSC device.

We measure the current-voltage relationship with a Keithley 2440 sourcemeter,

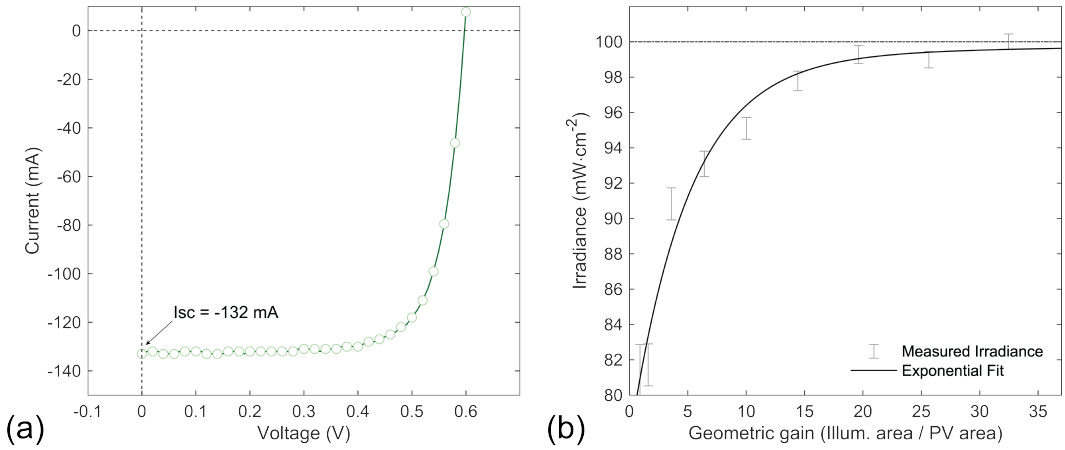

Figure I.1: The solar simulator measurement setup for quantifying the irradiance and calibration of the ABET solar simulator. (a) The calibration response curve of the reference silicon cell under full illumination of the solar simulator, where -132mA denotes 100 mW/cm^2 for the AM1.5g spectrum. (b) The irradiance response curve for varying illumination aperture area. Here we observe a decreased power density of incident light for smaller values of the geometric gain. For the reported efficiencies in the main text, we use this calibration curve (exponential fit) to calculate the power conversion efficiency of the LSC (single, on-silicon tandem) devices.

where we vary the voltage from -0.1V to 1.2V for both the LSC and silicon subcell components in discrete step intervals with 101 steps. We measure the cells at room temperature (300K) in air. When in the tandem configuration, we perform the current-voltage analysis of one device component (either the silicon or LSC) while holding the other at open-circuit voltage.

APPENDIX J

Market Research of Luminescent Solar Concentrators

Market Research Findings

Despite decades of device research and product development, the amount of installed building integrated photovoltaic (e.g., windows) technology has not experienced the same growth, or even the same trend, as its utility photovoltaic counterpart (figure J.1). Moreover, research into how to further integrate photovoltaic windows into the commercial buildings market remains an active area of study in both academia and industry[174,287–289]. One possible reason is that such window modules have not yet achieved sufficiently high power conversion efficiency and annualized energy production in order to meaningfully offset building electrical loads. Yet, despite advances in photovoltaic efficiency and durability, power-generating window adoption remains limited in this commercial, high-rise market. This could indicate that conversion efficiency is not the sole driving factor for widespread photovoltaic window adoption. A second possibility is that the customer needs and associated value propositions for the photovoltaic window market significantly differ from those of the utility-scale photovoltaic market, such that the same norms do not apply. If such is the case, then power conversion efficiency and average visible transparency of the window module alone may not be sufficient to meet customer needs.

In order to assess how photovoltaic window technology could enter into the commercial glass and building market, we must first develop a comprehensive understanding of the value chain for a traditional window—a double-pane insulated glass unit—from cradle (i.e., initial manufacturing) to end-use (i.e., use in a commercial high-rise building). While the building load electrical generation for photovoltaic windows is applicable for all building sizes, in this chapter we specifically address a sub-segment of the commercial market, considering only large-scale ($\geq$100,000 ft^2), high-rise buildings[179]. Such large-scale high-rises typically exhibit larger window-to-wall ratios than other commercial building market sub-segments[290]. We trace this window cradle-to-end-use value chain (figure J.2) by conducting nearly 150 in-person interviews across the commercial building value chain during the fall of 2019. We categorize these 150 interviews as: 37% within the glass and window manufacturing

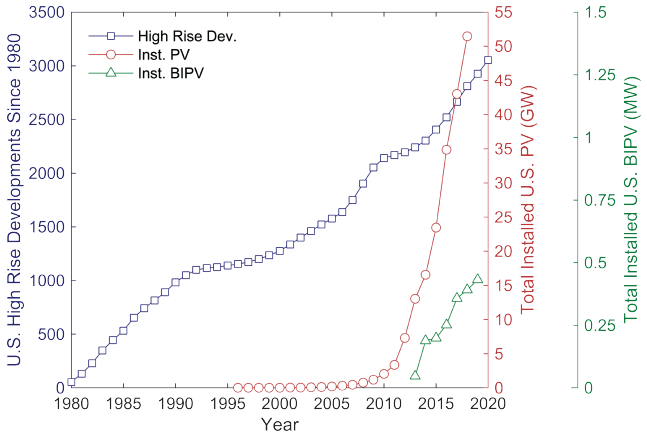

Figure J.1: A comparison of the number of U.S. high-rise developments since 1980 (left y-axis, blue) against the total installed U.S. PV capacity (right y-axis, red) in gigawatts (GW) and the total installed U.S. BIPV capacity (far right y-axis, green) in megawatts (MW). Adapted from Needell et al.[167].

chain; 15% from suppliers and distributors; 28% from real estate developers, architects, engineers, and contractors (general and sub-); 12% from city and building regulators; and 8% from building occupants and end-users.

The cradle-to-end-use value chain of a double-pane window describes how solar powered windows would be transferred from photovoltaic window manufacturers, to window suppliers and distributors, to large-area building developers, and eventually to the end-users—either as the building owners or occupants. We can subcategorize roles of the various parties within this value chain as the direct economic buyer(s) of photovoltaic window coating technologies; decision maker(s) who determine whether or not to adopt a particular IGU product; influencer(s) that can sway buyers or decision makers; and saboteur(s) that can impede or prevent BIPV window technology from entering into the market.

From our collected data, we can identify a singular economic buyer within the first stage of the value chain—photovoltaic window manufacturing. We also find that key decision makers, window influencers, and emerging window technology saboteurs all occupy distinct roles within the third stage of the value chain, building development. In contrast, none of these roles (e.g., economic buyer, key decision maker, influencer) exists within the end-use stages (e.g., ownership or occupancy) for such a photovoltaic window process flow.

Within the value chain, we identify specific needs for each of the major roles that impact market adoption for photovoltaic window technology—influencers, key decision makers, and economic buyers. Influencers (in this case architects) are motivated to create aesthetically attractive building designs to increase project acquisition. As such, photovoltaic windows need to meet the aesthetic needs (material, color, clarity, flexibility) of architects. The key decision makers (here commercial real estate developers) are motivated by an increased return on investment (ROI) to turn a greater profit[291]. For a real estate developer, the primary purpose for a window simplifies to increasing the availability of natural daylight, allowing unob-

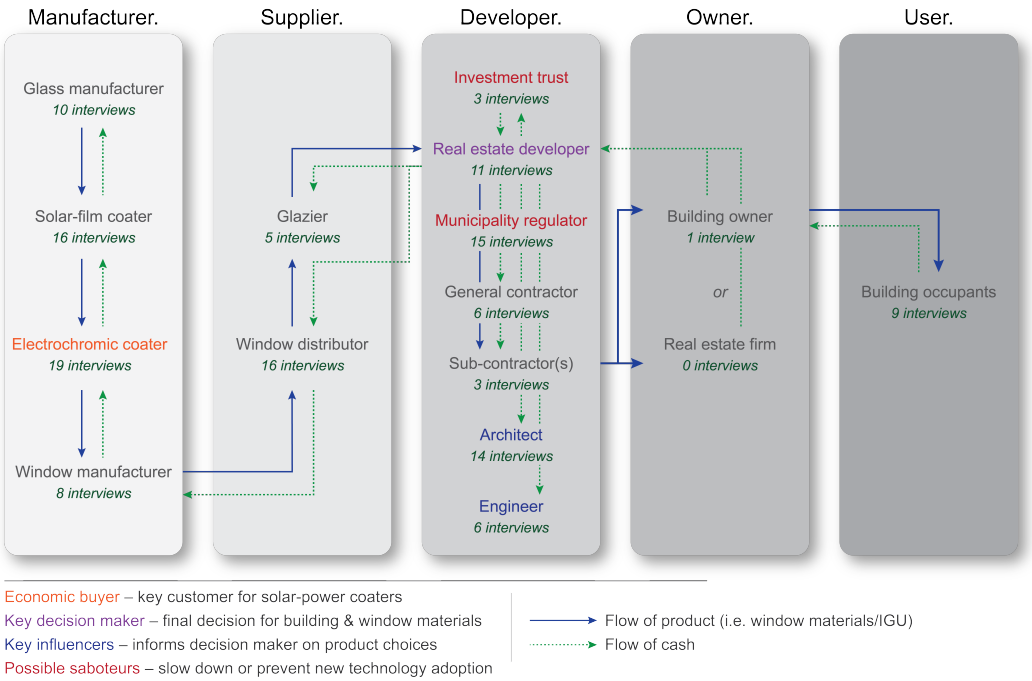

Figure J.2: A conceptual diagram of the commercial window and glass ecosystem, tracing both the flow of product (i.e., window materials, IGU, etc.) and flow of cash through the five primary divisions and specific roles within each division. Here we also identify roles within the ecosystem: economic buyer, key decision maker, influencers, and possibly saboteurs to the adoption of new window technology. Below each specific role we give the number of interviews conducted with an employee at a firm/company that corresponds to that role. Adapted from Needell et al.[167].

structed views, and enabling comfort through temperature control, all in order to attain higher building occupancy rates and therefore heightened ROIs. Finally, the economic buyers (window manufacturers) are incentivized to maintain the status quo; i.e., to produce windows whose production costs and installation procedures and costs do not disrupt the current practice of window production and installation. Therefore, electrically connected windows, which incur additional installation costs, are intrinsically at odds with the economic buyers' primary need.

While electricity generated by photovoltaic windows may appear to be the most obvious added value for high-rise buildings, this value is only appreciable to the end-user (building occupant or owner), who occupies the top stage of a value chain pyramid and accordingly has no significant decision making role in the value chain. Moreover, the real estate developer's greatest need (i.e., increased ROI) does not necessarily align with that of the building occupant's or end-user's. From nearly 150 qualitative interviews, large-scale building developers most commonly rely upon higher degrees of comfort, increased views, or other "soft" values to attract more tenants. While lower utilities costs may attract a certain number of tenants, our interviews show currently most developers rely upon other methods (e.g., soft values) to achieve increased ROI.

Given the disparity between the power-production capabilities of current pho-

tovoltaic window concepts and the market needs (identified through this interview process) of high-rise building developers and window manufacturers in the United States, we identify several strategies to enable power-generating window technology to meet such market needs. One strategy, as has been discussed by previous studies[292–295], involves an increase in policy and regulation of required on-site solar production and energy efficiency of such building markets in order to create a demand for the key decision makers. As introduced in the previous section, another such strategy could be to align building developers' current needs of increased ROI with photovoltaic window technology. From interviews conducted throughout this study, dynamic windows (e.g., electrochromic, discussed in chapter 7) represent one such technology that provides the "soft" values needed for increased occupancy rates. An example of how to introduce photovoltaic window technologies could be to hybridize dynamically transparent windows with power-generating components[166,258,260,267,296–301].

Interview Background and Data

To collect this data, we participated in the National Science Foundation (NSF) Innovation Corps (I-Corps) program in fall 2019. The I-Corps program is a seven week intensive program, aimed at bridging the information gap between basic scientific research and technological commercialization. Each team accepted to this program conducts over 100 in-person interviews with professionals in the chosen industry and searching for commonly cited market needs across interviews. In order to reduce potential biases in our own discovery process, we omit mention of solar-powered BIPV window technology from the interview process. Instead, we focus on the commercial building industry as a whole—from window and glass manufacturing to building development to end-users—in order to understand current needs in this market.

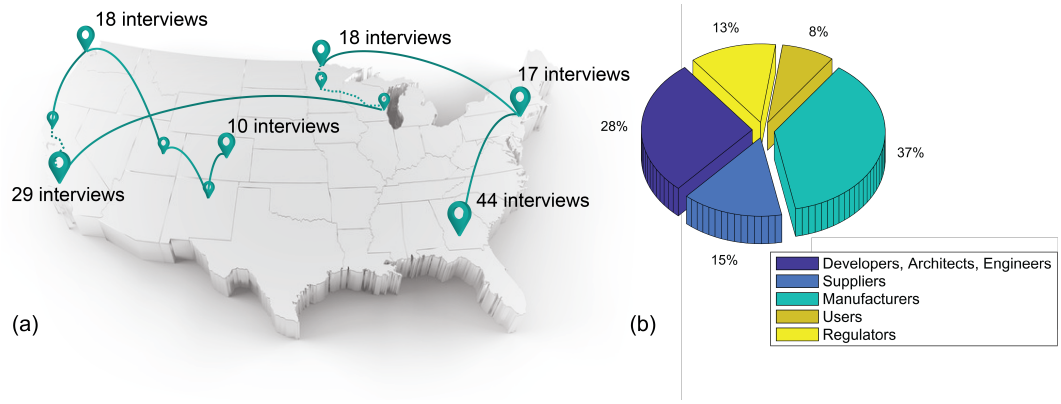

Figure J.3: (a) a geographical depiction of the interview trip across the United States (international interviews not shown here). (b) a breakdown of a total of 142 interviews with respect to the role of the interviewee within the commercial window market. Adapted from Needell et al.[167].

As shown in figure J.3(a), we conduct nearly 150 customer interviews across four countries, 14 US states, and 41 cities. Given the size and complexity of the

commercial building market, as detailed in figure J.2, we arrange our interviews to cover each step of the window value chain. Figure J.3(b) illustrates the breakdown of our discovery interviews during this seven week timeframe (October 20$^{\text{th}}$ through December 5$^{\text{th}}$, 2019): 37% of our total interviews come from manufacturers in this glass and window ecosystem; 15% from suppliers; 28% from the real estate developers, architects, engineers, and contractors; 12% from regulators; and 8% from building occupants and end-users.

References

[1] Enerdata, "Global Energy Statistical Yearbook," *Online Access*, 2019.

[2] IEA, "World Energy Balances 2019," Tech. Rep. 1, 2019.

[3] IPCC, "2019: Summary for Policymakers," *IPCC Special Report on Climate Change, Desertification, Land Degradation, Sustainable Land Management, Food Security, and Greenhouse gas fluxes in Terrestrial Ecosystems*, 2019.

[4] IPCC, "2018: Summary for Policymakers," *IPCC Special Report on the impacts of global warming of 1.5°C above pre-industrial levels and related global greenhouse gas emission pathways, in the context of strengthening the global response to the threat of climate change,*, 2018.

[5] S. N. Gosling and N. W. Arnell, "A global assessment of the impact of climate change on water scarcity," *Climatic Change*, vol. 134, no. 3, pp. 371–385, 2016.

[6] J. F. Mercure, H. Pollitt, N. R. Edwards, P. B. Holden, U. Chewpreecha, P. Salas, A. Lam, F. Knobloch, and J. E. Vinuales, "Environmental impact assessment for climate change policy with the simulation-based integrated assessment model E3ME-FTT-GENIE," *Energy Strategy Reviews*, vol. 20, pp. 195–208, 2018.

[7] BP, "BP Statistical Review of World Energy," tech. rep., 2019.

[8] J. Tsao, N. Lewis, and G. Crabtree, "Solar FAQs," *US department of Energy*, no. 1, pp. 1–24, 2006.

[9] H. Moaveni, D. K. Click, R. H. Meeker, R. M. Reedy, and A. Pappalardo, "Quantifying solar power variability for a large central PV plant and small distributed PV plant," *Conference Record of the IEEE Photovoltaic Specialists Conference*, vol. 2, pp. 969–972, 2013.

[10] S. B. Darling, F. You, T. Veselka, and A. Velosa, "Assumptions and the levelized cost of energy for photovoltaics," *Energy and Environmental Science*, vol. 4, no. 9, pp. 3133–3139, 2011.

[11] J. Perlin, *From space to earth: the story of solar electricity.* Earthscan, 1999.

[12] D. S. Philips and W. Warmuth, "Photovoltaics Report," Tech. Rep. March, 2019.

[13] G. Kavlak, J. McNerney, and J. E. Trancik, "Evaluating the causes of cost reduction in photovoltaic modules," *Energy Policy*, vol. 123, no. October, pp. 700–710, 2018.

[14] NREL, "Best Research Cell Efficiencies," 2018.

[15] A. Arons and M. Peppard, "Einstein's proposal of the photon concept - a translation of the Annalen der Physik paper of 1905," *American Journal of Physics1*, vol. 33, no. 5, pp. 367–374, 1965.

[16] C. Z. N. Peidong Yang, L. Dou, and P. Yang, "Bandgap engineering in semiconductor alloy nanomaterials with widely tunable compositions," *Nature Reviews Materials*, vol. 2, pp. 1–15, 2017.

[17] J. R. Chelikowsky and M. L. Cohen, "Electronic structure of silicon," *Physical Review B*, vol. 10, no. 12, pp. 5095–5107, 1974.

[18] M. A. Green and S. P. Bremner, "Energy conversion approaches and materials for high-efficiency photovoltaics," *Nature Materials*, vol. 16, pp. 23–34, jan 2017.

[19] W. Shockley and H. J. Queisser, "Detailed balance limit of efficiency of p-n junction solar cells," *Journal of Applied Physics*, vol. 32, no. 3, pp. 510–519, 1961.

[20] C. H. Henry, "Limiting efficiencies of ideal single and multiple energy gap terrestrial solar cells," *Journal of Applied Physics*, vol. 51, no. 8, pp. 4494–4500, 1980.

[21] T. O. M. Tiedje, E. L. I. Yablonovitch, G. D. Cody, and B. G. Brooks, "Limiting Efficiency of Silicon Solar Cells," *IEEE Transactions on Electron Devices*, vol. 31, no. 5, pp. 711–716, 1984.

[22] L. Tous, *Nickel/Copper Plated Contacts as an Alternative to Silver Screen Printing for the Front Side Metallization of Industrial High Efficiency Silicon Solar Cells*. Doctor of engineering, KU Leuven, 2014.

[23] R. Fu, D. Feldman, and R. Margolis, "U.S. Solar Photovoltaic System Cost Benchmark: Q1 2018, NREL/TP-6A20-72399.," *Technical Report: NREL/TP-6A20-72399*, no. November, 2018.

[24] A. Polman and H. A. Atwater, "Photonic design principles for ultrahigh-efficiency photovoltaics," *Nature Materials*, vol. 11, no. 3, pp. 174–177, 2012.

[25] M. A. Green, Y. Hishikawa, E. D. Dunlop, D. H. Levi, J. Hohl-Ebinger, M. Yoshita, and A. W. Ho-Baillie, "Solar cell efficiency tables (Version 53)," *Progress in Photovoltaics: Research and Applications*, vol. 27, no. 1, pp. 3–12, 2019.

[26] J. F. Geisz, R. M. France, K. L. Schulte, M. A. Steiner, A. G. Norman, H. L. Guthrey, M. R. Young, T. Song, and T. Moriarty, "Six-junction III–V solar cells with 47.1% conversion efficiency under 143 Suns concentration," *Nature Energy*, vol. 5, no. 4, pp. 326–335, 2020.

[27] K. A. Horowitz, T. W. Remo, B. Smith, and A. J. Ptak, "A Techno-Economic Analysis and Cost Reduction Roadmap for III-V Solar Cells," *Technical Report*, pp. NREL/TP–6A20–72103, nov 2018.

[28] S. P. Philipps, A. W. Bett, K. Horowitz, S. Kurtz, J. Peng, J. J. Wu, X. Li, Y. Zhou, Z. Yu, Y. Guo, J. J. Wu, Y. Lin, Z. Li, X. Wu, C. Wu, Y. Xie, S. P. Philipps, A. W. Bett, K. Horowitz, and S. Kurtz, "Current Status of Concentrator Photovoltaic (CPV) Technology," *National Renewable Energy Laboratory*, vol. 139, pp. 1–25, 2015.

[29] F. Meinardi, F. Bruni, and S. Brovelli, "Luminescent solar concentrators for building-integrated photovoltaics," *Nature Reviews Materials*, vol. 2, pp. 1–9, 2017.

[30] B. P. Jelle and C. Breivik, "State-of-the-art Building Integrated Photovoltaics," *Energy Procedia*, vol. 20, no. 1876, pp. 68–77, 2012.

[31] A. K. Shukla, K. Sudhakar, and P. Baredar, "A comprehensive review on design of building integrated photovoltaic system," sep 2016.

[32] B. P. V. Heiz, Z. Pan, L. Su, S. T. Le, and L. Wondraczek, "A Large-Area Smart Window with Tunable Shading and Solar-Thermal Harvesting Ability Based on Remote Switching of a Magneto-Active Liquid," *Advanced Sustainable Systems*, vol. 2, no. 1, p. 1700140, 2018.

[33] H. Li, K. Wu, J. Lim, H.-J. Song, and V. I. Klimov, "Doctor-blade deposition of quantum dots onto standard window glass for low-loss large-area luminescent solar concentrators," *Nature Energy*, vol. 1, no. December, p. 16157, 2016.

[34] N. Aste, M. Buzzetti, C. Del Pero, R. Fusco, F. Leonforte, and D. Testa, "Triggering a large scale luminescent solar concentrators market: The smart window project," *Journal of Cleaner Production*, vol. 219, pp. 35–45, 2019.

[35] R. J. Yang and P. X. Zou, "Building integrated photovoltaics (BIPV): costs, benefits, risks, barriers and improvement strategy," *International Journal of Construction Management*, vol. 16, pp. 39–53, jan 2016.

[36] B. Norton, P. C. Eames, T. K. Mallick, M. J. Huang, S. J. McCormack, J. D. Mondol, and Y. G. Yohanis, "Enhancing the performance of building integrated photovoltaics," *Solar Energy*, vol. 85, no. 8, pp. 1629–1664, 2011.

[37] G. Smestad, H. Ries, R. Winston, and E. Yablonovitch, "The thermodynamic limits of light concentrators," *Solar Energy Materials*, vol. 21, no. 2-3, pp. 99–111, 1990.

[38] A. Rabl, "Comparison of solar concentrators," *Solar Energy*, vol. 18, no. 2, pp. 93–111, 1976.

[39] V. I. Klimov, T. A. Baker, J. Lim, K. A. Velizhanin, and H. McDaniel, "Quality Factor of Luminescent Solar Concentrators and Practical Concentration Limits Attainable with Semiconductor Quantum Dots," *ACS Photonics*, vol. 3, no. 6, pp. 1138–1148, 2016.

[40] S. Kurtz, "Opportunities for development of a mature concentrating photovoltaic power industry," *2009 International Conference on Compound Semiconductor Manufacturing Technology, CS MANTECH 2009*, no. July, 2009.

[41] B. Mendewala, K. Nikolaidou, C. Hoffman, S. Sarang, J. Lu, B. Ilan, and S. Ghosh, "The potential of scalability in high efficiency hybrid perovskite thin film luminescent solar concentrators," *Solar Energy*, vol. 183, pp. 392–397, 2019.

[42] W. H. Weber and J. Lambe, "Luminescent greenhouse collector for solar radiation," *Applied Optics*, vol. 15, no. 10, p. 2299, 1976.

[43] W. G. van Sark, "Luminescent solar concentrators – A low cost photovoltaics alternative," *Renewable Energy*, vol. 49, pp. 207–210, jan 2013.

[44] T. Wang, B. Yu, B. Chen, Z. Hu, Y. Luo, G. Zou, and Q. Zhang, "A theoretical model of a cylindrical luminescent solar concentrator with a dye-doping coating," *Journal of Optics*, vol. 15, no. 5, 2013.

[45] B. C. Rowan, L. R. Wilson, and B. S. Richards, "Advanced material concepts for luminescent solar concentrators," *IEEE Journal on Selected Topics in Quantum Electronics*, vol. 14, no. 5, pp. 1312–1322, 2008.

[46] J. S. Batchelder, "The Luminescent Solar Concentrator," 1982.

[47] L. R. Bradshaw, K. E. Knowles, S. McDowall, and D. R. Gamelin, "Nanocrystals for luminescent solar concentrators," *Nano Letters*, vol. 15, no. 2, pp. 1315–1323, 2015.

[48] I. Coropceanu and M. G. Bawendi, "Core/shell quantum dot based luminescent solar concentrators with reduced reabsorption and enhanced efficiency," *Nano Letters*, vol. 14, no. 7, pp. 4097–4101, 2014.

[49] M. G. Debije and V. A. Rajkumar, "Direct versus indirect illumination of a prototype luminescent solar concentrator," *Solar Energy*, vol. 122, pp. 334–340, 2015.

[50] M. Fisher, C. Ippen, D. Farrell, R. Walters, M. González, K. Trautz, J. Tischler, J. Morseman, A. Büchtemann, and A. Chatten, "Flexible luminescent solar concentrators utilizing bio-derived tandem fluorophores," *Conference Record of the IEEE Photovoltaic Specialists Conference*, vol. 610, pp. 3333–3338, 2012.

[51] X. Hu, R. Kang, Y. Zhang, L. Deng, H. Zhong, B. Zou, and L.-J. Shi, "Ray-trace simulation of CuInS(Se)2 quantum dot based luminescent solar concentrators.," *Optics express*, vol. 23, no. 15, pp. A858–67, 2015.

[52] Y. Zhao, G. A. Meek, B. G. Levine, and R. R. Lunt, "Near-infrared harvesting transparent luminescent solar concentrators," *Advanced Optical Materials*, vol. 2, pp. 606–611, jul 2014.

[53] J. S. Batchelder, a. H. Zewail, and T. Cole, "Luminescent solar concentrators . 1 : Theory of operation and techniques for performance evaluation," *Applied optics*, vol. 18, no. 18, pp. 3090–110, 1979.

[54] Z. Hu, X. Wang, W. Wu, Y. Luo, G. Zou, L. Wang, Q. Zhang, J. Zhang, T. Wang, and W. Ma, "Luminescent solar concentrator employing rare earth complex with zero self-absorption loss," *Solar Energy*, vol. 85, no. 11, pp. 2571–2579, 2011.

[55] Z. Krumer, W. G. van Sark, R. E. Schropp, and C. de Mello Donegá, "Compensation of self-absorption losses in luminescent solar concentrators by increasing luminophore concentration," *Solar Energy Materials and Solar Cells*, vol. 167, pp. 133–139, 2017.

[56] N. Aste, M. Buzzetti, C. Del Pero, and F. Leonforte, "Glazing's techno-economic performance: A comparison of window features in office buildings in different climates," *Energy and Buildings*, vol. 159, pp. 123–135, 2018.

[57] B. Rowan, S. McCormack, J. Doran, and B. Norton, "Quantum dot solar concentrators: an investigation of various geometries," *High and Low Concentration for Solar Electric Applications II*, vol. 6649, p. 66490A, sep 2007.

[58] H. Zhao, D. Benetti, L. Jin, Y. Zhou, F. Rosei, and A. Vomiero, "Absorption Enhancement in Giant Core/Alloyed-Shell Quantum Dots for Luminescent Solar Concentrator," *Small*, vol. 12, no. 38, pp. 5354–5365, 2016.

[59] Y. Zhou, D. Benetti, Z. Fan, H. Zhao, D. Ma, A. O. Govorov, A. Vomiero, and F. Rosei, "Near Infrared, Highly Efficient Luminescent Solar Concentrators," *Advanced Energy Materials*, vol. 6, no. 11, pp. 1–8, 2016.

[60] J. Bomm, A. Büchtemann, A. J. Chatten, R. Bose, D. J. Farrell, N. L. A. Chan, Y. Xiao, L. H. Slooff, T. Meyer, A. Meyer, W. G. J. H. M. Van Sark, and R. Koole, "Fabrication and full characterization of state-of-the-art quantum dot luminescent solar concentrators," *Solar Energy Materials and Solar Cells*, vol. 95, no. 8, pp. 2087–2094, 2011.

[61] J. S. Batchelder, a. H. Zewail, and T. Cole, "Luminescent solar concentrators. 2: Experimental and theoretical analysis of their possible efficiencies.," *Applied optics*, vol. 20, no. 21, pp. 3733–3754, 1981.

[62] A. Hermann, "Luminescent Solar Concentrators – A Review," *Solar Energy*, vol. 29, no. 4, pp. 323–329, 1982.

[63] F. Meinardi, A. Colombo, K. A. Velizhanin, R. Simonutti, M. Lorenzon, L. Beverina, R. Viswanatha, V. I. Klimov, and S. Brovelli, "Large-area luminescent solar concentrators based on /'Stokes-shift-engineered/' nanocrystals in a mass-polymerized PMMA matrix," *Nat Photon*, vol. 8, no. 5, pp. 392–399, 2014.

[64] M. Rafiee, S. Chandra, H. Ahmed, and S. J. McCormack, "An overview of various configurations of Luminescent Solar Concentrators for photovoltaic applications," *Optical Materials*, vol. 91, no. March, pp. 212–227, 2019.

[65] L. H. Slooff, E. E. Bende, A. R. Burgers, T. Budel, M. Pravettoni, R. P. Kenny, E. D. Dunlop, and A. Büchtemann, "A luminescent solar concentrator with 7.1% power conversion efficiency," *physica status solidi (RRL) - Rapid Research Letters*, vol. 2, pp. 257–259, dec 2008.

[66] M. Mani, B. Reddy, M. Sreenath, S. Lokabhiraman, and N. Anandrao, "Modelling the Effect of Device Geometry on Concentration Ratios of Quantum Dot Solar Concentrators," *ISES World Congress 2007*, no. November, p. Solar Energy and Human Settlement, 2009.

[67] F. Meinardi, S. Ehrenberg, L. Dhamo, F. Carulli, M. Mauri, F. Bruni, R. Simonutti, U. Kortshagen, and S. Brovelli, "Highly Efficient Luminescent Solar Concentrators based on Ultra-Earth-Abundant Indirect Band Gap Silicon Quantum Dots," *Nature Photonics*, vol. 11, no. 3, pp. 177–185, 2017.

[68] H.-J. Song, B. G. Jeong, J. Lim, D. C. Lee, W. K. Bae, and V. I. Klimov, "Performance Limits of Luminescent Solar Concentrators Tested with Seed/Quantum-Well Quantum Dots in a Selective-Reflector-Based Optical Cavity," *Nano Letters*, vol. 18, pp. 395–404, jan 2018.

[69] J. R. Albani, *Structure and Dynamics of Macromolecules: Absorption and Fluorescence Studies*. Elsevier, 2004.

[70] A. Bagga, P. K. Chattopadhyay, and S. Ghosh, "Origin of Stokes shift in InAs and CdSe quantum dots: Exchange splitting of excitonic states," *Physical Review B - Condensed Matter and Materials Physics*, vol. 74, no. 3, pp. 1–7, 2006.

[71] P. Reiss, M. Protière, and L. Li, "Core/shell semiconductor nanocrystals," jan 2009.

[72] L. Desmet, A. J. M. Ras, D. K. G. de Boer, and M. G. Debije, "Monocrystalline silicon photovoltaic luminescent solar concentrator with 42% power conversion efficiency," *Optics Letters*, vol. 37, no. 15, p. 3087, 2012.

[73] M. G. Debije, P. P. Verbunt, P. J. Nadkarni, S. Velate, K. Bhaumik, S. Nedumbamana, B. C. Rowan, B. S. Richards, and T. L. Hoeks, "Promising fluorescent dye for solar energy conversion based on a perylene perinone," *Applied Optics*, vol. 50, no. 2, pp. 163–169, 2011.

[74] G. V. Shcherbatyuk, R. H. Inman, C. Wang, R. Winston, and S. Ghosh, "Viability of using near infrared PbS quantum dots as active materials in luminescent solar concentrators," *Applied Physics Letters*, vol. 96, no. 19, pp. 13–16, 2010.

[75] R. Sumner, S. Eiselt, T. B. Kilburn, C. Erickson, B. Carlson, D. R. Gamelin, S. McDowall, and D. L. Patrick, "Analysis of Optical Losses in High-Efficiency CuInS2-Based Nanocrystal Luminescent Solar Concentrators: Balancing Absorption versus Scattering," *Journal of Physical Chemistry C*, vol. 121, no. 6, pp. 3252–3260, 2017.

[76] F. Meinardi, H. McDaniel, F. Carulli, A. Colombo, K. A. Velizhanin, N. S. Makarov, R. Simonutti, V. I. Klimov, and S. Brovelli, "Highly efficient large-area colourless luminescent solar concentrators using heavy-metal-free colloidal quantum dots," *Nature Nanotechnology*, vol. 10, no. 10, pp. 878–885, 2015.

[77] H. Wijaya, D. Darwan, K. R. G. Lim, T. Wang, K. H. Khoo, and Z. K. Tan, "Large-Stokes-Shifted Infrared-Emitting InAs-In(Zn)P-ZnSe-ZnS Giant-Shell Quantum Dots by One-Pot Continuous-Injection Synthesis," *Chemistry of Materials*, vol. 31, no. 6, pp. 2019–2026, 2019.

[78] M. Amani, P. Taheri, R. Addou, G. H. Ahn, D. Kiriya, D.-H. H. Lien, J. W. Ager, R. M. Wallace, and A. Javey, "Recombination Kinetics and Effects of Superacid Treatment in Sulfur- and Selenium-Based Transition Metal Dichalcogenides," *Nano Letters*, vol. 16, pp. 2786–2791, apr 2016.

[79] H. Fang, C. Battaglia, C. Carraro, S. Nemsak, B. Ozdol, J. S. Kang, H. A. Bechtel, S. B. Desai, F. Kronast, A. A. Unal, G. Conti, C. Conlon, G. K. Palsson, M. C. Martin, A. M. Minor, C. S. Fadley, E. Yablonovitch, R. Maboudian, and A. Javey, "Strong interlayer coupling in van der Waals heterostructures built from single-layer chalcogenides," *Proceedings of the National Academy of Sciences*, vol. 111, no. 17, pp. 6198–6202, 2014.

[80] A. Sanguineti, A. Monguzzi, G. Vaccaro, F. Meinardi, E. Ronchi, M. Moret, U. Cosentino, G. Moro, R. Simonutti, M. Mauri, R. Tubino, and L. Beverina, "NIR emitting ytterbium chelates for colourless luminescent solar concentrators," *Physical Chemistry Chemical Physics*, vol. 14, no. 18, pp. 6452–6455, 2012.

[81] C. S. Erickson, L. R. Bradshaw, S. McDowall, J. D. Gilbertson, D. R. Gamelin, and D. L. Patrick, "Zero-reabsorption doped-nanocrystal luminescent solar concentrators," *ACS Nano*, vol. 8, no. 4, pp. 3461–3467, 2014.

[82] W. Shurcliff and C. R. Jones, "The Trapping of Fluorescent Light Produced within Objects of High Geometrical Symmetry," *Journal of the Optical Society of America*, vol. 39, no. 1, pp. 912–916, 1949.

[83] D. R. Needell, Z. Nett, O. Ilic, C. R. Bukowsky, J. He, L. Xu, R. G. Nuzzo, B. G. Lee, J. F. Geisz, A. P. Alivisatos, and H. A. Atwater, "Micro-optical Tandem Luminescent Solar Concentrator," in *2017 IEEE 44th Photovoltaic Specialist Conference (PVSC)*, pp. 1737–1740, IEEE, jun 2017.

[84] D. R. Needell, O. Ilic, C. R. Bukowsky, Z. Nett, L. Xu, J. He, H. Bauser, B. G. Lee, J. F. Geisz, R. G. Nuzzo, A. P. Alivisatos, and H. A. Atwater, "Design Criteria for Micro-Optical Tandem Luminescent Solar Concentrators," *IEEE Journal of Photovoltaics*, vol. 8, pp. 1560–1567, nov 2018.

[85] D. R. Needell, C. R. Bukowsky, S. Darbe, H. Bauser, O. Ilic, and H. A. Atwater, "Spectrally Matched Quantum Dot Photoluminescence in GaAs-Si Tandem Luminescent Solar Concentrators," *IEEE Journal of Photovoltaics*, vol. 9, pp. 397–401, mar 2019.

[86] J. Gutmann, H. Zappe, and J. C. Goldschmidt, "Quantitative modeling of fluorescent emission in photonic crystals," *Physical Review B - Condensed Matter and Materials Physics*, vol. 88, no. 20, 2013.

[87] J. Gutmann, H. Zappe, and J. C. Goldschmidt, "Predicting the performance of photonic luminescent solar concentrators," *IEEE Journal of Photovoltaics*, pp. 1864–1868, 2013.

[88] J. C. Goldschmidt, M. Peters, A. Bösch, H. Helmers, F. Dimroth, S. W. Glunz, and G. Willeke, "Increasing the efficiency of fluorescent concentrator systems," *Solar Energy Materials and Solar Cells*, vol. 93, no. 2, pp. 176–182, 2009.

[89] T. S. Parel, C. Pistolas, L. Danos, and T. Markvart, "Modelling and experimental analysis of the angular distribution of the emitted light from the edge of luminescent solar concentrators," *Optical Materials*, vol. 42, 2015.

[90] Y. Shen, Y. Jia, X. Sheng, L. Shen, J. A. Rogers, and N. C. Giebink, "Non-imaging Optical Gain in Luminescent Concentration through Photonic Control of Emission Étendue," *ACS Photonics*, vol. 1, no. 8, pp. 746–753, 2014.

[91] N. D. Bronstein, L. Li, L. Xu, Y. Yao, V. E. Ferry, A. P. Alivisatos, and R. G. Nuzzo, "Luminescent Solar Concentration with Semiconductor Nanorods and Transfer-Printed Micro-Silicon Solar Cells," *ACS Nano*, vol. 8, pp. 44–53, jan 2014.

[92] M. G. Debije and P. P. C. Verbunt, "Thirty Years of Luminescent Solar Concentrator Research: Solar Energy for the Built Environment," *Advanced Energy Materials*, vol. 2, pp. 12–35, jan 2012.

[93] A. G. Curto, G. Volpe, T. H. Taminiau, M. P. Kreuzer, R. Quidant, and N. F. V. Hulst, "Unidirectional Emission of a Quantum Dot Coupled to a Nanoantenna," *Science*, vol. 20, no. August, pp. 930–933, 2010.

[94] A. G. Curto, T. H. Taminiau, G. Volpe, M. P. Kreuzer, R. Quidant, and N. F. van Hulst, "Multipolar radiation of quantum emitters with nanowire optical antennas," *Nature Communications*, vol. 4, p. 1750, 2013.

[95] H. C. Bauser, C. R. Bukowsky, M. Phelan, W. Weigand, D. R. Needell, Z. C. Holman, and H. A. Atwater, "Photonic Crystal Waveguides for >90% Light Trapping Efficiency in Luminescent Solar Concentrators," *ACS Photonics*, vol. 7, pp. 2122–2131, aug 2020.

[96] H. C. Bauser, D. R. Needell, and H. A. Atwater, "AlSb as a material for high index contrast nanophotonics," *Optical Materials Express*, vol. 11, p. 1334, may 2021.

[97] H. Bauser, C. R. Bukowsky, M. Phelan, W. Weigand, D. R. Needell, Z. C. Holman, and H. A. Atwater, "Luminescent solar concentrators with high concentration using photonic crystal waveguides," in *High Contrast Metastructures X* (J. A. Fan, C. J. Chang-Hasnain, and W. Zhou, eds.), p. 13, SPIE, mar 2021.

[98] U. Rau, U. W. Paetzold, and T. Kirchartz, "Thermodynamics of light management in photovoltaic devices," *Physical Review B - Condensed Matter and Materials Physics*, vol. 90, 2014.

[99] E. Yablonovitch, "Thermodynamics of the Fluorescent Planar Concentrator," *Journal of the Optical Society of America*, vol. 70, no. 11, pp. 1362–1363, 1980.

[100] C. Tummeltshammer, A. Taylor, A. J. Kenyon, and I. Papakonstantinou, "Losses in luminescent solar concentrators unveiled," *Solar Energy Materials and Solar Cells*, vol. 144, 2016.

[101] A. Kerrouche, D. A. Hardy, D. Ross, and B. S. Richards, "Luminescent solar concentrators: From experimental validation of 3D ray-tracing simulations to

coloured stained-glass windows for BIPV," *Solar Energy Materials and Solar Cells*, vol. 122, pp. 99–106, 2014.

[102] P. Shirley, "Time complexity of Monte Carlo radiosity," *Computers & Graphics*, vol. 16, pp. 117–120, jan 1992.

[103] I. Papakonstantinou and C. Tummeltshammer, "Fundamental limits of concentration in luminescent solar concentrators revised: the effect of reabsorption and nonunity quantum yield," *Optica*, vol. 2, no. 10, p. 841, 2015.

[104] D. J. Farrell and M. Yoshida, "Operating regimes for second generation luminescent solar concentrators," *Progress in Photovoltaics: Research and Applications*, vol. 20, pp. 93–99, jan 2012.

[105] I. Fujieda, Y. Tsutsumi, K. Yunoki, and Y. Yamada, "Simple analytical model for optical efficiency of an energy-harvesting projector," in *Nonimaging Optics: Efficient Design for Illumination and Solar Concentration XVI* (R. Winston and E. Yablonovitch, eds.), no. September 2019, p. 17, SPIE, sep 2019.

[106] I. Rousseau and V. Wood, "Nanophotonic luminescent solar concentrators," *Applied Physics Letters*, vol. 103, no. 13, 2013.

[107] K. Kunz, *The Finite Difference Time Domain Method for Electromagnetics*. 2018.

[108] A. R. Kutayiah, S. Kumar, R. Ratnaweera, K. Easwaran, and M. Sheldon, "Markov Chains for Modeling Complex Luminescence, Absorption, and Scattering in Nanophotonic Systems," *arXiv*, dec 2020.

[109] N. Metropolis, *The Beginning of the Monte Carlo Method*. 1987.

[110] L. G. Polgar and J. R. Howell, "Directional Thermal-Radiative Properties of Conical Cavities," *Nasa Tn D-2904*, pp. 1–28, 1965.

[111] D. Sahin, B. Ilan, and D. F. Kelley, "Monte-Carlo simulations of light propagation in luminescent solar concentrators based on semiconductor nanoparticles," *Journal of Applied Physics*, vol. 110, no. 3, p. 033108, 2011.

[112] M. Kennedy, S. J. McCormack, J. Doran, and B. Norton, "Ray-trace modelling of reflectors for quantum dot solar concentrators," in *High and Low Concentration for Solar Electric Applications II* (M. Symko-Davies, ed.), vol. 6649, p. 664905, sep 2007.

[113] M. A. Green, "Accuracy of Analytical Expressions for Solar Cell Fill Factors," *Solar Cells*, vol. 7, no. 1, pp. 337–340, 1983.

[114] S. Theingi, D. R. Needell, H. C. Bauser, M. E. Phelan, W. Nemeth, D. Findley, H. Su, B. A. Koscher, Z. Nett, O. Ilic, C. R. Bukowsky, R. G. Nuzzo, A. P. Alivisatos, J. F. Geisz, P. Stradins, and H. A. Atwater, "Luminescent Solar Concentrator Tandem-on-Silicon with above 700mV Passivated Contact Silicon Bottom Cell," in *2019 IEEE 46th Photovoltaic Specialists Conference (PVSC)*, pp. 0747–0749, IEEE, jun 2019.

[115] L. H. Slooff, R. Kinderman, A. R. Burgers, A. Büchtemann, R. Danz, T. B. Meyer, A. J. Chatten, D. Farell, K. W. J. Barnham, and J. A. M. van Roosmalen, "The luminescent concentrator illuminated," *Photonics for Solar Energy Systems*, vol. 6197, no. Lc, p. 61970K, 2006.

[116] N. D. Bronstein, Y. Yao, L. Xu, E. O'Brien, A. S. Powers, V. E. Ferry, A. P. Alivisatos, R. G. Nuzzo, E. O'Brien, A. S. Powers, V. E. Ferry, A. P. Alivisatos, and R. G. Nuzzo, "Quantum Dot Luminescent Concentrator Cavity Exhibiting 30-fold Concentration," *ACS Photonics*, vol. 2, no. 11, pp. 1576–1583, 2015.

[117] M. Phelan, D. R. Needell, H. Bauser, H. Su, M. Deceglie, S. Theingi, B. Koscher, Z. Nett, C. R. Bukowsky, O. Ilic, P. Stradins, J. Geisz, R. Nuzzo, A. P. Alivisatos, and H. A. Atwater, "Outdoor performance of a tandem InGaP/Si photovoltaic luminescent solar concentrator," *Solar Energy Materials and Solar Cells*, vol. 223, no. October 2020, p. 110945, 2021.

[118] N. J. Zaluzec, "Analytical formulae for calculation of X-ray detector solid angles in the scanning and scanning/transmission analytical electron microscope," *Microscopy and Microanalysis*, vol. 20, no. 4, pp. 1318–1326, 2014.

[119] T. Markvart, "Detailed balance method for ideal single-stage fluorescent collectors," *Journal of Applied Physics*, vol. 99, no. 2, 2006.

[120] U. Rau, F. Einsele, and G. C. Glaeser, "Efficiency limits of photovoltaic fluorescent collectors," *Applied Physics Letters*, vol. 87, no. 17, pp. 1–3, 2005.

[121] G. C. Glaeser and U. Rau, "Collection and conversion properties of photovoltaic fluorescent collectors with photonic band stop filters," *Proceedings of SPIE*, vol. 6197, pp. 61970L–61970L–11, 2006.

[122] C. G. Knott, "Life and scientific work of Peter Guthrie Tait," in *Cambridge University Press*, pp. 213–215, 1911.

[123] H. Ries, G. P. Smestad, and R. Winston, "Thermodynamics of light concentrators," in *Nonimaging Optics: Maximum Efficiency Light Transfer* (R. Winston and R. L. Holman, eds.), vol. 1528, pp. 7–14, oct 1991.

[124] A. Arakengy, "Liouville's Theorem and the Intensity of Beams," *American Journal of Physics*, vol. 25, no. 8, pp. 519–525, 1957.

[125] S. Sandhu, Z. Yu, and S. Fan, "Detailed balance analysis of nanophotonic solar cells," *Optics Express*, vol. 21, no. 1, p. 1209, 2013.

[126] W. G. J. H. M. V. Sark, Z. Krumer, C. D. M. Donegá, and R. E. I. Schropp, "Luminescent Solar Concentrators : the route to 10 % efficiency," *IEEE Journal of Photovoltaics*, pp. 2276–2279, 2014.

[127] F. Meinardi, Q. A. Akkerman, F. Bruni, S. Park, M. Mauri, Z. Dang, L. Manna, and S. Brovelli, "Doped Halide Perovskite Nanocrystals for Reabsorption-Free Luminescent Solar Concentrators," *ACS Energy Letters*, vol. 2, no. 10, pp. 2368–2377, 2017.

[128] P. Moraitis, D. K. de Boer, P. T. Prins, C. de Mello Donegá, K. Neyts, and W. G. van Sark, "Should Anisotropic Emission or Reabsorption of Nanoparticle Luminophores Be Optimized for Increasing Luminescent Solar Concentrator Efficiency?," *Solar RRL*, vol. 4, p. 2000279, oct 2020.

[129] J. C. Martin, R. J. Ratnaweera, S. Kumar, J.-r. Wen, A. R. Kutayiah, and M. T. Sheldon, "Detailed balance efficiencies for luminescent solar concentrators with aligned semiconductor nanorods: the benefits of anisotropic emission," *Journal of Photonics for Energy*, vol. 10, p. 1, may 2020.

[130] D.-H. Lien, S. Z. Uddin, M. Yeh, M. Amani, H. Kim, J. W. Ager, E. Yablonovitch, and A. Javey, "Electrical suppression of all nonradiative recombination pathways in monolayer semiconductors," *Science*, vol. 364, pp. 468–471, may 2019.

[131] A. F. Rigosi, H. M. Hill, Y. Li, A. Chernikov, and T. F. Heinz, "Probing Interlayer Interactions in Transition Metal Dichalcogenide Heterostructures by Optical Spectroscopy: MoS2/WS2 and MoSe2/WSe2," *Nano Letters*, vol. 15, no. 8, pp. 5033–5038, 2015.

[132] H.-L. Liu, T. Yang, J.-H. Chen, H.-W. Chen, H. Guo, R. Saito, M.-Y. Li, and L.-J. Li, "Temperature-dependent optical constants of monolayer MoS_2, $MoSe_2$, WS_2, and WSe_2: spectroscopic ellipsometry and first-principles calculations," *Scientific Reports*, vol. 10, p. 15282, dec 2020.

[133] S. J. Byrnes, "Multilayer optical calculations," pp. 1–20, mar 2016.

[134] Y. Li, A. Chernikov, X. Zhang, A. Rigosi, H. M. Hill, A. M. van der Zande, D. A. Chenet, E.-M. Shih, J. Hone, and T. F. Heinz, "Measurement of the optical dielectric function of monolayer transition-metal dichalcogenides: MoS2, MoSe2, WS2, and WSe2," *Physical Review B*, vol. 90, p. 205422, nov 2014.

[135] Y. Chen, J. Vela, H. Htoon, J. L. Casson, J. Donald, D. a. Bussian, V. I. Klimov, J. a. Hollingsworth, and D. J. Werder, "" Giant " Multishell CdSe Nanocrystal Quantum Dots with Suppressed Blinking " Giant " Multishell CdSe Nanocrystal Quantum Dots with Suppressed Blinking," *Journal of Americal Chemical Society*, vol. 130, no. 15, pp. 5026–5027, 2008.

[136] K. Wu, H. Li, and V. I. Klimov, "Tandem luminescent solar concentrators based on engineered quantum dots," *Nature Photonics*, vol. 12, pp. 105–110, feb 2018.

[137] A. Carlson, A. M. Bowen, Y. Huang, R. G. Nuzzo, and J. A. Rogers, "Transfer printing techniques for materials assembly and micro/nanodevice fabrication," *Advanced Materials*, vol. 24, no. 39, pp. 5284–5318, 2012.

[138] J. Yoon, L. Li, A. V. Semichaevsky, J. H. Ryu, H. T. Johnson, R. G. Nuzzo, and J. A. Rogers, "Flexible concentrator photovoltaics based on microscale silicon solar cells embedded in luminescent waveguides," *Nature Communications*, vol. 2, no. 1, 2011.

[139] X. Feng, M. A. Meitl, A. M. Bowen, Y. Huang, R. G. Nuzzo, and J. A. Rogers, "Competing Fracture in Kinetically Controlled Transfer Printing," *Langmuir*, vol. 23, pp. 12555–12560, dec 2007.

[140] B. Furman, E. Menard, A. Gray, M. Meitl, S. Bonafede, D. Kneeburg, K. Ghosal, R. Bukovnik, W. Wagner, J. Gabriel, S. Seel, and S. Burroughs, "A high concentration photovoltaic module utilizing micro-transfer printing and surface mount technology," in *2010 35th IEEE Photovoltaic Specialists Conference*, pp. 000475–000480, IEEE, jun 2010.

[141] T.-H. Kim, A. Carlson, J.-H. Ahn, S. M. Won, S. Wang, Y. Huang, and J. A. Rogers, "Kinetically controlled, adhesiveless transfer printing using microstructured stamps," *Applied Physics Letters*, vol. 94, p. 113502, mar 2009.

[142] M. A. Meitl, Z.-T. Zhu, V. Kumar, K. J. Lee, X. Feng, Y. Y. Huang, I. Adesida, R. G. Nuzzo, and J. A. Rogers, "Transfer printing by kinetic control of adhesion to an elastomeric stamp," *Nature Materials*, vol. 5, pp. 33–38, jan 2006.

[143] J. Yoon, A. J. Baca, S. I. Park, P. Elvikis, J. B. Geddes, L. Li, R. H. Kim, J. Xiao, S. Wang, T. H. Kim, M. J. Motala, B. Y. Ahn, E. B. Duoss, J. A. Lewis, R. G. Nuzzo, P. M. Ferreira, Y. Huang, A. Rockett, and J. A. Rogers, "Ultrathin silicon solar microcells for semitransparent, mechanically flexible and microconcentrator module designs," *Nature Materials*, vol. 7, no. 11, pp. 907–915, 2008.

[144] M. R. Bergren, N. S. Makarov, K. Ramasamy, A. Jackson, R. Guglielmetti, and H. McDaniel, "High-Performance CuInS2 Quantum Dot Laminated Glass Luminescent Solar Concentrators for Windows," *ACS Energy Letters*, vol. 3, no. 3, pp. 520–525, 2018.

[145] Y. Zhou, D. Benetti, X. Tong, L. Jin, Z. M. Wang, D. Ma, H. Zhao, and F. Rosei, "Colloidal carbon dots based highly stable luminescent solar concentrators," *Nano Energy*, vol. 44, no. August 2017, pp. 378–387, 2018.

[146] R. Fu, D. Feldman, R. Margolis, M. Woodhouse, K. Ardani, R. Fu, D. Feldman, R. Margolis, M. Woodhouse, and K. Ardani, "U.S. Solar Photovoltaic System and Energy Storage Cost Benchmark: Q1 2020," *National Renewable Energy Laboratory*, no. September, pp. 1–120, 2021.

[147] K. Ardani, J. J. Cook, R. Fu, and R. M. Margolis, "Cost-Reduction Roadmap for Residential Solar Photovoltaics (PV), 2017–2030," Tech. Rep. NREL/TP-6A20-70748, National Renewable Energy Laboratory, 2018.

[148] T. James, A. Goodrich, M. A. Woodhouse, R. M. Margolis, and S. Ong, "Building-Integrated Photovoltaics (BIPV) in the Residential Sector: An Analysis of Installed Rooftop System Prices," Tech. Rep. NREL/TP-6A20-53103, National Renewable Energy Laboratory, 2011.

[149] C. J. Traverse, R. Pandey, M. C. Barr, and R. R. Lunt, "Emergence of highly transparent photovoltaics for distributed applications," *Nature Energy*, vol. 2, no. November, pp. 1–12, 2017.

[150] "Energy Information Administration (EIA)- Commercial Buildings Energy Consumption Survey (CBECS) Data."

[151] "Residential Energy Consumption Survey (RECS) - Data - U.S. Energy Information Administration (EIA)."

[152] Y. Li, X. Guo, Z. Peng, B. Qu, H. Yan, H. Ade, M. Zhang, and S. R. Forrest, "Color-neutral, semitransparent organic photovoltaics for power window applications," *Proceedings of the National Academy of Sciences*, vol. 117, no. 35, p. 202007799, 2020.

[153] R. R. Lunt and V. Bulovic, "Transparent, near-infrared organic photovoltaic solar cells for window and energy-scavenging applications," *Applied Physics Letters*, vol. 98, p. 113305, mar 2011.

[154] K. S. Chen, J. F. Salinas, H. L. Yip, L. Huo, J. Hou, and A. K. Jen, "Semitransparent polymer solar cells with 6% PCE, 25% average visible transmittance and a color rendering index close to 100 for power generating window applications," *Energy and Environmental Science*, vol. 5, pp. 9551–9557, nov 2012.

[155] T. D. Lee and A. Ebong, "Thin film solar technologies: a review," in *2015 12th International Conference on High-capacity Optical Networks and Enabling/Emerging Technologies (HONET)*, pp. 1–10, IEEE, dec 2015.

[156] J. L. H. Chau, R.-T. Chen, G.-L. Hwang, P.-Y. Tsai, and C.-C. Lin, "Transparent solar cell window module," *Solar Energy Materials and Solar Cells*, vol. 94, pp. 588–591, mar 2010.

[157] D. Fraga, T. Stoyanova Lyubenova, R. Martí, I. Calvet, E. Barrachina, and J. Carda, "Ecologic ceramic substrates for CIGS solar cells," *Ceramics International*, vol. 42, pp. 7148–7154, may 2016.

[158] L. Zhu, J. Zhang, D. Wang, R. Wang, Y. Sun, and C. Wu, "Optimal design and photoelectric performance study of micro-lens light trapping structure for CIGS thin film solar cell in BIPV," *Renewable Energy*, vol. 177, pp. 1356–1371, nov 2021.

[159] T. D. Lee and A. U. Ebong, "A review of thin film solar cell technologies and challenges," *Renewable and Sustainable Energy Reviews*, vol. 70, pp. 1286–1297, apr 2017.

[160] M. Saifullah, S. Ahn, J. Gwak, S. Ahn, K. Kim, J. Cho, J. H. Park, Y. J. Eo, A. Cho, J.-S. Yoo, and J. H. Yun, "Development of semitransparent CIGS thin-film solar cells modified with a sulfurized-AgGa layer for building applications," *Journal of Materials Chemistry A*, vol. 4, no. 27, pp. 10542–10551, 2016.

[161] Q. Xue, R. Xia, J. Brabec, H.-l. L. Yip, C. J. Brabec, and H.-l. L. Yip, "Recent advances in semi-transparent polymer and perovskite solar cells for power generating window applications," *Energy and Environmental Science*, vol. 11, no. 7, pp. 1688–1709, 2018.

[162] J. Burschka, N. Pellet, S. J. Moon, R. Humphry-Baker, P. Gao, M. K. Nazeeruddin, and M. Grätzel, "Sequential deposition as a route to high-performance perovskite-sensitized solar cells," *Nature*, vol. 499, no. 7458, pp. 316–319, 2013.

[163] E. H. Jung, N. J. Jeon, E. Y. Park, C. S. Moon, T. J. Shin, T. Y. Yang, J. H. Noh, and J. Seo, "Efficient, stable and scalable perovskite solar cells using poly(3-hexylthiophene)," *Nature*, vol. 567, no. 7749, pp. 511–515, 2019.

[164] C. Roldán-Carmona, O. Malinkiewicz, R. Betancur, G. Longo, C. Momblona, F. Jaramillo, L. Camacho, and H. J. Bolink, "High efficiency single-junction semitransparent perovskite solar cells," *Energy and Environmental Science*, vol. 7, pp. 2968–2973, aug 2014.

[165] S. Mirershadi and S. Ahmadi-Kandjani, "Efficient thin luminescent solar concentrator based on organometal halide perovskite," *Dyes and Pigments*, vol. 120, 2015.

[166] A. Cannavale, G. E. Eperon, P. Cossari, A. Abate, H. J. Snaith, and G. Gigli, "Perovskite photovoltachromic cells for building integration," *Energy & Environmental Science*, vol. 8, no. 5, pp. 1578–1584, 2015.

[167] D. R. Needell, M. E. Phelan, J. T. Hartlove, and H. A. Atwater, "Solar power windows: Connecting scientific advances to market signals," *Energy*, vol. 219, p. 119567, 2021.

[168] T. E. Kuhn, C. Erban, M. Heinrich, J. Eisenlohr, F. Ensslen, and D. H. Neuhaus, "Review of technological design options for building integrated photovoltaics (BIPV)," *Energy and Buildings*, p. 110381, sep 2020.

[169] E. Yablonovitch, T. Gmitter, and B. Bagley, "As2S3/GaAs, a new amorphous/crystalline heterojunction for the III-V semiconductors," *Applied Physics Letters*, vol. 57, no. 21, pp. 2241–2243, 1990.

[170] H. Fardi, M. Jan, and B. Van Zeghbroeck, "Design and simulation of Multi-Quantum-Well GaAs/AlGaAs single junction p-i-n with back surface DBR reflector," *Conference Record of the IEEE Photovoltaic Specialists Conference*, pp. 785–788, 2012.

[171] M. M. Sanfacon and S. P. Tobin, "Analysis of AlGaAs/ GaAs Solar Cell Structures by Optical Reflectance Spectroscopy," *IEEE Transactions on Electron Devices*, vol. 37, no. 2, pp. 450–454, 1990.

[172] S. A. Ringel, J. A. Carlin, C. L. Andre, M. K. Hudait, M. Gonzalez, D. M. Wilt, E. B. Clark, P. Jenkins, D. Scheiman, A. Allerman, E. A. Fitzgerald, and C. W. Leitz, "Single-junction InGaP/GaAs solar cells grown on Si substrates with SiGe buffer layers," *Progress in Photovoltaics: Research and Applications*, vol. 10, pp. 417–426, sep 2002.

[173] N. D. Arora and J. R. Hauser, "Antireflection layers for GaAs solar cells," *Journal of Applied Physics*, vol. 53, no. 12, pp. 8839–8846, 1982.

[174] M. Kryszak and L. W. Wang, "The value of aesthetics in the BIPV roof products segment: a multiperspective study under European market conditions," *Energy Sources, Part A: Recovery, Utilization, and Environmental Effects*, pp. 1–22, aug 2020.

[175] C. Yang and R. R. Lunt, "Limits of Visibly Transparent Luminescent Solar Concentrators," 2017.

[176] Z. Song, C. L. McElvany, A. B. Phillips, I. Celik, P. W. Krantz, S. C. Watthage, G. K. Liyanage, D. Apul, and M. J. Heben, "A technoeconomic analysis of perovskite solar module manufacturing with low-cost materials and techniques," *Energy and Environmental Science*, vol. 10, no. 6, pp. 1297–1305, 2017.

[177] J. Xiao, *Technoeconomic Analysis of Perovskite Photovoltaic Manufacturing for Powering Telecommunications*. Master of engineering, Massachussets Institute of Technology, 2017.

[178] J. Jean, J. Xiao, R. Nick, N. Moody, M. Nasilowski, M. Bawendi, and V. Bulović, "Synthesis cost dictates the commercial viability of lead sulfide and perovskite quantum dot photovoltaics," *Energy and Environmental Science*, vol. 11, no. 9, pp. 2295–2305, 2018.

[179] A. M. Shirazi, Z. S. Zomorodian, and M. Tahsildoost, "Techno-economic BIPV evaluation method in urban areas," *Renewable Energy*, vol. 143, pp. 1235–1246, dec 2019.

[180] K. A. Horowitz, M. Woodhouse, H. Lee, and G. P. Smestad, "A bottom-up cost analysis of a high concentration PV module," *AIP Conference Proceedings*, vol. 1679, no. September 2015, 2015.

[181] A. Louwen, W. Van Sark, R. Schropp, and A. Faaij, "A cost roadmap for silicon heterojunction solar cells," *Solar Energy Materials and Solar Cells*, vol. 147, pp. 295–314, 2016.

[182] S. Razza, F. Di Giacomo, F. Matteocci, L. Cinà, A. L. Palma, S. Casaluci, P. Cameron, A. D'Epifanio, S. Licoccia, A. Reale, T. M. Brown, and A. Di Carlo, "Perovskite solar cells and large area modules (100 cm 2) based on an air flow-assisted PbI 2 blade coating deposition process," *Journal of Power Sources*, vol. 277, pp. 286–291, mar 2015.

[183] Z. Yang, C.-C. Chueh, F. Zuo, J. H. Kim, P.-W. Liang, and A. K. Jen, "High-Performance Fully Printable Perovskite Solar Cells via Blade-Coating Technique under the Ambient Condition," *Advanced Energy Materials*, vol. 5, p. 1500328, jul 2015.

[184] K. Burrows and V. Fthenakis, "Glass needs for a growing photovoltaics industry," *Solar Energy Materials and Solar Cells*, vol. 132, pp. 455–459, 2015.

[185] M. Yamaguchi, "Super-high efficiency III–V tandem and multijunction cells," in *Clean electricity from photovoltaics*, pp. 347–375, 2nd ed., 2001.

[186] M. Yamaguchi, T. Takamoto, A. Khan, M. Imaizumi, S. Matsuda, and N. J. Ekins-Daukes, "Super-high-efficiency multi-junction solar cells," *Progress in Photovoltaics: Research and Applications*, vol. 13, pp. 125–132, mar 2005.

[187] R. R. King, D. C. Law, K. M. Edmondson, C. M. Fetzer, G. S. Kinsey, H. Yoon, D. D. Krut, J. H. Ermer, R. A. Sherif, and N. H. Karam, "Advances in High-Efficiency III-V Multijunction Solar Cells," *Advances in OptoElectronics*, vol. 2007, pp. 1–8, dec 2007.

[188] R. R. King, D. Bhusari, D. Larrabee, X.-Q. Liu, E. Rehder, K. Edmondson, H. Cotal, R. K. Jones, J. H. Ermer, C. M. Fetzer, D. C. Law, and N. H. Karam, "Solar cell generations over 40% efficiency," *Progress in Photovoltaics: Research and Applications*, vol. 20, pp. 801–815, sep 2012.

[189] E. Jackson, "Areas for improvement of the semiconductor solar energy converter," in *Trans. Intern Conf. on the Use of Solar Energy-The Scientific Basis*, p. 122, 1955.

[190] M. A. Green, M. J. Keevers, I. Thomas, J. B. Lasich, K. Emery, and R. R. King, "40% efficient sunlight to electricity conversion," *Progress in Photovoltaics: Research and Applications*, vol. 23, pp. 685–691, jun 2015.

[191] B. Mitchell, G. Peharz, G. Siefer, M. Peters, T. Gandy, J. C. Goldschmidt, J. Benick, S. W. Glunz, A. W. Bett, and F. Dimroth, "Four-junction spectral beam-splitting photovoltaic receiver with high optical efficiency," *Progress in Photovoltaics: Research and Applications*, vol. 19, pp. 61–72, jan 2011.

[192] J. D. McCambridge, M. A. Steiner, B. L. Unger, K. A. Emery, E. L. Christensen, M. W. Wanlass, A. L. Gray, L. Takacs, R. Buelow, T. A. McCollum, J. W. Ashmead, G. R. Schmidt, A. W. Haas, J. R. Wilcox, J. Van Meter, J. L. Gray, D. T. Moore, A. M. Barnett, and R. J. Schwartz, "Compact spectrum splitting photovoltaic module with high efficiency," *Progress in Photovoltaics: Research and Applications*, vol. 19, pp. 352–360, may 2011.

[193] A. Antonini, M. A. Butturi, P. D. Benedetto, P. Zurru, D. Sartore, E. Milan, D. Uderzo, and A. Parretta, "Mirror Based Spectral Splitting CPV System," *25th European Photovoltaic Solar Energy Conference*, vol. 39, no. 0, pp. 20–24, 2010.

[194] W. Ma, W. Li, R. Liu, M. Cao, X. Zhao, and X. Gong, "Carbon dots and AIE molecules for highly efficient tandem luminescent solar concentrators," *Chemical Communications*, vol. 55, no. 52, pp. 7486–7489, 2019.

[195] J. Wang, J. Wang, Y. Xu, J. Jin, W. Xiao, D. Tan, J. Li, T. Mei, L. Xue, and X. Wang, "Controlled Synthesis of Long-Wavelength Multicolor-Emitting Carbon Dots for Highly Efficient Tandem Luminescent Solar Concentrators," *ACS Applied Energy Materials*, p. acsaem.0c02265, nov 2020.

[196] L. Zdražil, S. Kalytchuk, K. Holá, M. Petr, O. Zmeškal, Š. Kment, A. L. Rogach, and R. Zbořil, "A carbon dot-based tandem luminescent solar concentrator," *Nanoscale*, vol. 12, no. 12, pp. 6664–6672, 2020.

[197] M. Yamaguchi, K.-H. Lee, K. Araki, and N. Kojima, "A review of recent progress in heterogeneous silicon tandem solar cells," *Journal of Physics D: Applied Physics*, vol. 51, p. 133002, apr 2018.

[198] K. A. Bush, A. F. Palmstrom, Z. J. Yu, M. Boccard, R. Cheacharoen, J. P. Mailoa, D. P. Mcmeekin, R. L. Z. Hoye, C. D. Bailie, T. Leijtens, I. M. Peters, M. C. Minichetti, N. Rolston, R. Prasanna, S. Sofia, D. Harwood, W. Ma, F. Moghadam, H. J. Snaith, T. Buonassisi, Z. C. Holman, S. F. Bent, and M. D.

Mcgehee, "23.6%-efficient monolithic perovskite/silicon tandem solar cells with improved stability," *Nature Energy*, vol. 2, no. February, pp. 1–7, 2017.

[199] M. Monteiro Lunardi, A. Wing Yi Ho-Baillie, J. P. Alvarez-Gaitan, S. Moore, and R. Corkish, "A life cycle assessment of perovskite/silicon tandem solar cells," *Progress in Photovoltaics: Research and Applications*, vol. 25, no. 8, pp. 679–695, 2017.

[200] P. S. Schulze, A. J. Bett, M. Bivour, P. Caprioglio, F. M. Gerspacher, Ö. Kabaklı, A. Richter, M. Stolterfoht, Q. Zhang, D. Neher, M. Hermle, H. Hillebrecht, S. W. Glunz, and J. C. Goldschmidt, "25.1% High-Efficiency Monolithic Perovskite Silicon Tandem Solar Cell with a High Bandgap Perovskite Absorber," *Solar RRL*, vol. 4, no. 7, pp. 1–10, 2020.

[201] S. R. Kurtz, P. Faine, and J. M. Olson, "Modeling of two-junction, series-connected tandem solar cells using top-cell thickness as an adjustable parameter," *Journal of Applied Physics*, vol. 68, no. 4, pp. 1890–1895, 1990.

[202] R. Oshima, Y. Shoji, K. Makita, A. Ubukata, and T. Sugaya, "Evaluation of GaAs solar cells grown under different conditions via hydride vapor phase epitaxy," *Journal of Crystal Growth*, vol. 537, no. March, p. 125600, 2020.

[203] A. Onno, J. Wu, Q. Jiang, S. Chen, M. Tang, Y. Maidaniuk, M. Benamara, Y. I. Mazur, G. J. Salamo, N.-P. Harder, L. Oberbeck, and H. Liu, "Al0.2Ga0.8As Solar Cells Monolithically Grown on Si and GaAs by MBE for III-V/Si Tandem Dual-junction Applications," *Energy Procedia*, vol. 92, pp. 661–668, aug 2016.

[204] A. L. Greenaway, B. F. Bachman, J. W. Boucher, C. J. Funch, S. Aloni, and S. W. Boettcher, "Water-Vapor-Mediated Close-Spaced Vapor Transport Growth of Epitaxial Gallium Indium Phosphide Films on Gallium Arsenide Substrates," *ACS Applied Energy Materials*, vol. 1, pp. 284–289, feb 2018.

[205] J. Geisz, J. Olson, M. Romero, C. Jiang, and A. Norman, "Lattice-mismatched GaAsP Solar Cells Grown on Silicon by OMVPE," in *2006 IEEE 4th World Conference on Photovoltaic Energy Conference*, vol. 1, pp. 772–775, IEEE, may 2006.

[206] A. Augusto, P. Balaji, H. Jain, S. Y. Herasimenka, and S. G. Bowden, "Heterojunction solar cells on flexible silicon wafers," *MRS Advances*, vol. 1, pp. 997–1002, mar 2016.

[207] A. Augusto, P. Balaji, J. Karas, and S. G. Bowden, "Impact of substrate thickness on the surface passivation in high performance n-type solar cells," in *2018 IEEE 7th World Conference on Photovoltaic Energy Conversion (WCPEC)*, pp. 2792–2794, IEEE, jun 2018.

[208] A. Augusto, S. Y. Herasimenka, R. R. King, S. G. Bowden, and C. Honsberg, "Analysis of the recombination mechanisms of a silicon solar cell with low bandgap-voltage offset," *Journal of Applied Physics*, vol. 121, p. 205704, may 2017.

[209] A. Augusto, J. Karas, P. Balaji, S. G. Bowden, and R. R. King, "Exploring the practical efficiency limit of silicon solar cells using thin solar-grade substrates," *Journal of Materials Chemistry A*, vol. 8, pp. 16599–16608, aug 2020.

[210] A. Augusto, E. Looney, C. del Cañizo, S. G. Bowden, and T. Buonassisi, "Thin silicon solar cells: Pathway to cost-effective and defect-tolerant cell design," *Energy Procedia*, vol. 124, pp. 706–711, sep 2017.

[211] A. Augusto, K. Tyler, S. Y. Herasimenka, and S. G. Bowden, "Flexible Modules Using ¡70 μm Thick Silicon Solar Cells," *Energy Procedia*, vol. 92, pp. 493–499, 2016.

[212] P. Balaji, S. Bowden, and A. Augusto, "Studying edge losses in silicon heterojunction solar cells," in *2020 47th IEEE Photovoltaic Specialists Conference (PVSC)*, vol. 2020-June, pp. 2203–2206, IEEE, jun 2020.

[213] P. Balaji, W. J. Dauksher, S. G. Bowden, and A. Augusto, "Improving surface passivation on very thin substrates for high efficiency silicon heterojunction solar cells," *Solar Energy Materials and Solar Cells*, vol. 216, p. 110715, oct 2020.

[214] S. Essig, C. Allebé, T. Remo, J. F. Geisz, M. A. Steiner, K. Horowitz, L. Barraud, J. S. Ward, M. Schnabel, A. Descoeudres, D. L. Young, M. Woodhouse, M. Despeisse, C. Ballif, and A. Tamboli, "Raising the one-sun conversion efficiency of III-V/Si solar cells to 32.8% for two junctions and 35.9% for three junctions," *Nature Energy*, vol. 2, no. 9, 2017.

[215] J. F. Geisz, M. A. Steiner, I. García, S. R. Kurtz, D. J. Friedman, I. Garc??a, S. R. Kurtz, and D. J. Friedman, "Enhanced external radiative efficiency for 20.8% efficient single-junction GaInP solar cells," *Applied Physics Letters*, vol. 103, no. 4, 2013.

[216] C. Dagdeviren, T.-i. Kim, M. J. Kim, J. A. Rogers, S. J. Cho, Z. Ma, H.-j. Chung, A. Ameen, A. Carlson, S. H. Jin, Y. H. Jung, K. J. Yu, H. A. Pao, and H. Jang, "Thin Film Receiver Materials for Deterministic Assembly by Transfer Printing," *Chemistry of Materials*, vol. 26, no. 11, pp. 3502–3507, 2014.

[217] R. Nuzzo, I. L. Us, E. Menard, and N. C. Us, "Optical Systems Fabricated By Printing-Based Assembly," *US Patent*, vol. 2, no. 12, 2015.

[218] H. C. Bauser, D. R. Needell, C. R. Bukowsky, O. Ilic, Z. Nett, B. G. Lee, J. F. Geisz, A. P. Alivisatos, and H. A. Atwater, "Metasurfaces as Wavelengths Selective Mirros in Tandem Luminescent Solar Concentrators," in *2018 IEEE 45th Photovoltaic Specialist Conference (PVSC)*, 2018.

[219] O. Ilic, P. Bermel, G. Chen, J. D. Joannopoulos, I. Celanovic, and M. Soljačić, "Tailoring high-temperature radiation and the resurrection of the incandescent source," *Nature Nanotechnology*, vol. 11, no. 4, pp. 320–324, 2016.

[220] N. A. DiOrio, N. J. Blair, J. M. Freeman, A. M. Habte, E. M. Elqvist, M. G. Deceglie, D. Jordan, A. Nag, and C. A. Deline, "Solar System Modeling at NREL," *National Renewable Energy Lab.*, no. NREL/PR-6A20-72547, 2018.

[221] R. An, F. Zhang, X. Zou, Y. Tang, M. Liang, I. Oshchapovskyy, Y. Liu, A. Honarfar, Y. Zhong, C. Li, H. Geng, J. Chen, S. E. Canton, T. Pullerits, and K. Zheng, "Photostability and Photodegradation Processes in Colloidal CsPbI3 Perovskite Quantum Dots," *ACS Applied Materials and Interfaces*, vol. 10, no. 45, pp. 39222–39227, 2018.

[222] T. Aubert, S. J. Soenen, D. Wassmuth, M. Cirillo, R. Van Deun, K. Braeckmans, and Z. Hens, "Bright and stable CdSe/CdS@SiO2nanoparticles suitable for long-term cell labeling," *ACS Applied Materials and Interfaces*, vol. 6, no. 14, pp. 11714–11723, 2014.

[223] E. F. Fernández, F. Almonacid, P. M. Rodrigo, and P. J. Pérez-Higueras, "CPV systems," in *McEvoy's Handbook of Photovoltaics: Fundamentals and Applications*, pp. 931–985, Elsevier Inc., jan 2018.

[224] D. Fleischman, K. T. Fountaine, C. R. Bukowsky, G. Tagliabue, L. A. Sweatlock, and H. A. Atwater, "High Spectral Resolution Plasmonic Color Filters with Subwavelength Dimensions," *ACS Photonics*, vol. 6, pp. 332–338, 2019.

[225] H. Y. Kim, D. E. Yoon, J. Jang, G. M. Choi, D. C. Lee, and B. S. Bae, "Quantum dot/siloxane composite film exceptionally stable against heat and moisture," *Digest of Technical Papers - SID International Symposium*, vol. 48, no. 1, pp. 452–454, 2017.

[226] Y. J. Choi, D. Hwang, H. Chung, D. Y. Kim, and D. Y. Kim, "Controlling the spatial distribution of quantum dots in nanofiber for light-harvesting devices," *NPG Asia Materials*, vol. 7, pp. e202–7, jul 2015.

[227] O. Chen, J. Zhao, V. P. Chauhan, J. Cui, C. Wong, D. K. Harris, H. Wei, H.-S. Han, D. Fukumura, R. K. Jain, and M. G. Bawendi, "Compact high-quality CdSe-CdS core-shell nanocrystals with narrow emission linewidths and suppressed blinking.," *Nature materials*, vol. 12, no. 5, pp. 445–51, 2013.

[228] M. D. Kelzenberg, P. Espinet-Gonzalez, N. Vaidya, T. A. Roy, E. C. Warmann, A. Naqavi, S. P. Loke, J.-S. Huang, T. G. Vinogradova, A. J. Messer, C. Leclerc, E. E. Gdoutos, F. Royer, A. Hajimiri, S. Pellegrino, and H. A. Atwater, "Design and Prototyping Efforts for the Space Solar Power Initiative Michael," in *2017 IEEE 44th Photovoltaic Specialist Conference, PVSC 2017*, pp. 558–561, 2017.

[229] P. E. Glaser, "Power from the Sun: Its Future," *Science*, vol. 162, no. 3856, pp. 857–861, 1968.

[230] P. E. Glaser, O. E. Maynard, J. Mackovciak, and E. L. Ralph, "Feasability study of a satellite solar power station," Tech. Rep. February 1974, 1974.

[231] P. Jaffe and J. McSpadden, "Energy conversion and transmission modules for space solar power," *Proceedings of the IEEE*, vol. 101, no. 6, pp. 1424–1437, 2013.

[232] M. O'Neill, A. McDanal, M. Piszczor, P. George, M. Eskenazi, M. Botke, D. Edwards, D. Hoppe, and H. Brandhorst, "Recent progress on the stretched lens array (sla)," in *18th Space Photovoltaic Research and Technology Conference*, 2005.

[233] M. O'Neill, A. McDanal, H. Brandhorst, K. Schmid, P. LaCorte, M. Piszczor, and M. Myers, "Recent space pv concentrator advances: More robust, lighter, and easier to track," in *2015 IEEE 42nd Photovoltaic Specialist Conference (PVSC)*, pp. 1–6, IEEE, 2015.

[234] T. Stern, "Interim results of the slats concentrator experiment on lips-ii (space vehicle power plants)," in *Conference Record of the Twentieth IEEE Photovoltaic Specialists Conference*, pp. 837–840, IEEE, 1988.

[235] M. D. Kelzenberg, P. Espinet-Gonzalez, N. Vaidya, E. C. Warmann, A. Naqavi, S. P. Loke, P. Saive, T. A. Roy, T. G. Vinogradova, C. Leclerc, E. E. Gdoutos, F. Royer, A. Fikes, F. Bohn, B. Abiri, M. R. Hashemi, M. Gal-Katziri, A. Hajimiri, S. Pellegrino, and H. A. Atwater, "Ultralight Energy Converter Tile for the Space Solar Power Initiative," in *Photovoltaic Specialist Conference (PVSC), 2018 IEEE 45th*, pp. 3357–3359, 2018.

[236] K.-T. Shiu, J. Zimmerman, H. Wang, and S. R. Forrest, "Ultrathin film, high specific power InP solar cells on flexible plastic substrates," *Applied Physics Letters*, vol. 95, p. 223503, nov 2009.

[237] D. Cardwell, A. Kirk, C. Stender, A. Wibowo, F. Tuminello, M. Drees, R. Chan, M. Osowski, and N. Pan, "Very high specific power elo solar cells (¿ 3 kw/kg) for uav, space, and portable power applications," in *2017 IEEE 44th Photovoltaic Specialist Conference (PVSC)*, pp. 3511–3513, IEEE, 2017.

[238] K. Shimazaki, Y. Kobayashi, M. Takahashi, M. Imaizumi, T. Takamoto, T. Ito, and Y. Nozaki, "Development status of ultra-lightweight solar panel using space solar sheet," in *2009 34th IEEE Photovoltaic Specialists Conference (PVSC)*, pp. 002457–002461, IEEE, 2009.

[239] P. A. Jones, S. F. White, T. J. Harvey, and B. S. Smith, "A high specific power solar array for low to mid-power spacecraft," in *NASA. Lewis Research Center, Proceedings of the 12th Space Photovoltaic Research and Technology Conference (SPRAT 12)*, 1993.

[240] M. O'Neill, A. McDanal, M. Piszczor, P. George, M. Eskenazi, M. Botke, D. Edwards, D. Hoppe, and H. Brandhorst, "Recent progress on the stretched lens array (sla)," in *18th Space Photovoltaic Research and Technology Conference*, 2005.

[241] M. O'Neill, A. McDanal, H. Brandhorst, K. Schmid, P. LaCorte, M. Piszczor, and M. Myers, "Recent space pv concentrator advances: More robust, lighter, and easier to track," in *2015 IEEE 42nd Photovoltaic Specialist Conference (PVSC)*, pp. 1–6, IEEE, 2015.

[242] M. J. O'Neill, "1,000 W/kg Solar Concentrator Arrays for Far-Term Space Missions," in *AIP Conference Proceedings*, vol. 699, pp. 875–882, AIP, 2004.

[243] D. R. Needell, H. Bauser, M. Phelan, C. R. Bukowsky, O. Ilic, M. D. Kelzenberg, and H. A. Atwater, "Ultralight Luminescent Solar Concentrators for Space Solar Power Systems," in *2019 IEEE 46th Photovoltaic Specialists Conference (PVSC)*, pp. 2798–2801, IEEE, jun 2019.

[244] D. Jariwala, A. R. Davoyan, J. Wong, and H. A. Atwater, "Van der waals materials for atomically-thin photovoltaics: promise and outlook," *Acs Photonics*, vol. 4, no. 12, pp. 2962–2970, 2017.

[245] D. Jariwala, A. R. Davoyan, G. Tagliabue, M. C. Sherrott, J. Wong, and H. A. Atwater, "Near-unity absorption in van der waals semiconductors for ultrathin optoelectronics," *Nano letters*, vol. 16, no. 9, pp. 5482–5487, 2016.

[246] M. Peters, J. C. Goldschmidt, P. Löper, B. Bläsi, and A. Gombert, "The effect of photonic structures on the light guiding efficiency of fluorescent concentrators," *Journal of Applied Physics*, vol. 105, no. 1, pp. 1–10, 2009.

[247] J. D. Joannopoulos, S. G. Johnson, J. N. Winn, and R. D. Meade, "Molding the flow of light," *Princeton Univ. Press, Princeton, NJ [ua]*, 2008.

[248] Y. Ding and R. Magnusson, "Band gaps and leaky-wave effects in resonant photonic-crystal waveguides," *Optics Express*, vol. 15, no. 2, p. 680, 2007.

[249] G. H. Heilmeier and L. Zanoni, "guest-host interactions in nematic liquid crystals. a new electro-optic effect," *Applied Physics Letters*, vol. 13, no. 3, pp. 91–92, 1968.

[250] R. Van Ewyk, I. O'connor, A. Mosley, A. Cuddy, C. Hilsum, C. Blackburn, J. Griffiths, and F. Jones, "Anisotropic fluorophors for liquid crystal displays," *Displays*, vol. 7, no. 4, pp. 155–160, 1986.

[251] R. Pinol, J. Lub, M. P. Garcia, E. Peeters, J. L. Serrano, D. Broer, and T. Sierra, "Synthesis, properties, and polymerization of new liquid crystalline monomers for highly ordered guest- host systems," *Chemistry of Materials*, vol. 20, no. 19, pp. 6076–6086, 2008.

[252] C. Nobile, L. Carbone, A. Fiore, R. Cingolani, L. Manna, and R. Krahne, "Self-assembly of highly fluorescent semiconductor nanorods into large scale smectic liquid crystal structures by coffee stain evaporation dynamics," *Journal of Physics: Condensed Matter*, vol. 21, no. 26, p. 264013, 2009.

[253] A. Montali, C. Bastiaansen, P. Smith, and C. Weder, "Polarizing energy transfer in photoluminescent materials for display applications," *Nature*, vol. 392, no. 6673, pp. 261–264, 1998.

[254] A. Heifetz, S. C. Kong, A. V. Sahakian, A. Taflove, and V. Backman, "Photonic nanojets," *Journal of Computational and Theoretical Nanoscience*, vol. 6, no. 9, pp. 1979–1992, 2009.

[255] Z. Chen, A. Taflove, and V. Backman, "Photonic nanojet enhancement of backscattering of light by nanoparticles: a potential novel visible-light ultramicroscopy technique," *Optics Express*, vol. 12, no. 7, p. 1214, 2004.

[256] M. Schmid and P. Manley, "Nano- and microlenses as concepts for enhanced performance of solar cells," *Journal of Photonics for Energy*, vol. 5, no. 1, p. 057003, 2014.

[257] Y. Wang, E. L. Runnerstrom, and D. J. Milliron, "Switchable materials for smart windows," *Annual Review of Chemical and Biomolecular Engineering*, vol. 7, no. 1, pp. 283–304, 2016. PMID: 27023660.

[258] N. DeForest, A. Shehabi, J. O'Donnell, G. Garcia, J. Greenblatt, E. S. Lee, S. Selkowitz, and D. J. Milliron, "United States energy and CO2 savings potential from deployment of near-infrared electrochromic window glazings," *Building and Environment*, vol. 89, pp. 107–117, jul 2015.

[259] B. A. Korgel, "Composite for smarter windows," *Nature*, vol. 500, pp. 278–279, aug 2013.

[260] N. C. Davy, M. Sezen-Edmonds, J. Gao, X. Lin, A. Liu, N. Yao, A. Kahn, and Y.-L. Loo, "Pairing of near-ultraviolet solar cells with electrochromic windows for smart management of the solar spectrum," *Nature Energy*, vol. 2, no. 8, p. 17104, 2017.

[261] S. K. Deb, "A Novel Electrophotographic System," *Applied Optics*, vol. 8, p. 192, jan 1969.

[262] S. Deb, "Optical and photoelectric properties and colour centres in thin films of tungsten oxide," *Philosophical Magazine*, vol. 27, no. 4, pp. 801–822, 1973.

[263] J. R. Platt, "Electrochromism, a possible change of color producible in dyes by an electric field," *The Journal of Chemical Physics*, vol. 34, no. 3, pp. 862–863, 1961.

[264] B. Faughnan, "Display devices," *Topics in applied physics*, vol. 39, p. 181, 1980.

[265] A. Schuster, D. Nguyen, and O. Caporaletti, "Solid state electrochromic infrared switchable windows," *Solar Energy Materials*, vol. 13, no. 2, pp. 153–160, 1986.

[266] C. Bechinger, J. N. Bullock, J.-G. Zhang, C. E. Tracy, D. K. Benson, S. K. Deb, and H. M. Branz, "Low-voltage electrochromic device for photovoltaic-powered smart windows," *Journal of applied physics*, vol. 80, no. 2, pp. 1226–1232, 1996.

[267] M.-H. Cui, J.-S. Guo, H.-Q. Xie, Z.-H. Wu, and S.-C. Qiu, "All-solid-state complementary electrochromic windows based on the oxymethylene-linked polyoxyethylene complexed with liclo4," *Journal of Applied Polymer Science*, vol. 65, no. 9, pp. 1739–1744, 1997.

[268] L.-M. Huang, C.-W. Hu, C.-Y. Peng, C.-H. Su, and K.-C. Ho, "Integration of polyelectrolyte based electrochromic material in printable photovoltaic electrochromic module," *Solar Energy Materials and Solar Cells*, vol. 145, pp. 69–75, 2016. Eleventh International Meeting on Electrochromism (IME-11).

[269] A. Ghosh, B. Norton, and A. Duffy, "First outdoor characterisation of a pv powered suspended particle device switchable glazing," *Solar Energy Materials and Solar Cells*, vol. 157, pp. 1–9, 2016.

[270] A. L. Dyer, R. H. Bulloch, Y. Zhou, B. Kippelen, J. R. Reynolds, and F. Zhang, "A vertically integrated solar-powered electrochromic window for energy efficient buildings," *Advanced Materials*, vol. 26, no. 28, pp. 4895–4900, 2014.

[271] M. M. Potter, M. A. Yoder, A. Petronico, S. E. Lehman, B. G. Nicolau, M. J. Enright, M. Phelan, J. He, H. A. Atwater, and R. G. Nuzzo, "Autonomous Light Management in Flexible Photoelectrochromic Films Integrating High Performance Silicon Solar Microcells," *ACS Applied Energy Materials*, vol. 3, no. 2, pp. 1540–1551, 2020.

[272] J.-t. Shen and S. Fan, "Coherent photon transport from spontaneous emission in one-dimensional waveguides," *Optics letters*, vol. 30, no. 15, pp. 2001–2003, 2005.

[273] M. Monteiro Lunardi, A. Wing Yi Ho-Baillie, J. P. Alvarez-Gaitan, S. Moore, and R. Corkish, "A life cycle assessment of perovskite/silicon tandem solar cells," *Progress in Photovoltaics: Research and Applications*, vol. 25, no. 8, pp. 679–695, 2017.

[274] M. M. Lunardi, S. Moore, J. Alvarez-Gaitan, C. Yan, X. Hao, and R. Corkish, "A comparative life cycle assessment of chalcogenide/si tandem solar modules," *Energy*, vol. 145, pp. 700–709, 2018.

[275] M. M. Lunardi, J. P. Alvarez-Gaitan, N. L. Chang, and R. Corkish, "Life cycle assessment on hydrogenation processes on silicon solar modules," in *2018 IEEE 7th World Conference on Photovoltaic Energy Conversion (WCPEC) (A Joint Conference of 45th IEEE PVSC, 28th PVSEC 34th EU PVSEC)*, pp. 2452–2457, 2018.

[276] M. M. Lunardi, J. P. Alvarez-Gaitan, J. I. Bilbao, and R. Corkish, "Comparative life cycle assessment of end-of-life silicon solar photovoltaic modules," *Applied Sciences*, vol. 8, no. 8, 2018.

[277] M. M. Lunardi, J. Alvarez-Gaitan, N. L. Chang, and R. Corkish, "Life cycle assessment on perc solar modules," *Solar Energy Materials and Solar Cells*, vol. 187, pp. 154–159, 2018.

[278] M. M. Lunardi, P. R. Dias, R. Deng, and R. Corkish, *Life Cycle Environmental Assessment of Different Solar Photovoltaic Technologies*, ch. Chapter 5¡x xml:space="preserve"¿ ¡/x¿, pp. 5–1–5–34.

[279] C. S. Torres, D. Chigrin, J. Vivas, A. Goldschmidt, S. Zankovych, P. Ferrand, and S. Romanov, "Polymer-based photonic crystals," in *Proceedings of 2003 5th International Conference on Transparent Optical Networks, 2003.*, vol. 1, pp. 190–vol, IEEE, 2003.

[280] S. Tibuleac and R. Magnusson, "Reflection and transmission guided-mode resonance filters," *J. Opt. Soc. Am. A*, vol. 14, pp. 1617–1626, Jul 1997.

[281] B. Burger, K. Kiefer, C. Kost, S. Nold, S. Philipps, R. Preu, J. Rentsch, T. Schlegl, G. Stryi-Hipp, G. Willeke, *et al.*, "Photovoltaics report," *Freiburg: Fraunhofer Institute for Solar Energy Systems*, 2016.

[282] J. A. Otkin, M. C. Anderson, J. R. Mecikalski, and G. R. Diak, "Validation of goes-based insolation estimates using data from the us climate reference network," *Journal of Hydrometeorology*, vol. 6, no. 4, pp. 460–475, 2005.

[283] S. Gerbinet, S. Belboom, and A. Léonard, "Life cycle analysis (lca) of photovoltaic panels: A review," *Renewable and Sustainable Energy Reviews*, vol. 38, pp. 747–753, 2014.

[284] M. M. Lunardi, D. R. Needell, H. Bauser, M. Phelan, H. A. Atwater, and R. Corkish, "Life Cycle Assessment of tandem LSC-Si devices," *Energy*, vol. 181, pp. 1–10, aug 2019.

[285] D. A. Hanifi, N. D. Bronstein, B. A. Koscher, Z. Nett, J. K. Swabeck, K. Takano, A. M. Schwartzberg, L. Maserati, K. Vandewal, Y. van de Burgt, A. Salleo, and A. P. Alivisatos, "Redefining near-unity luminescence in quantum dots with photothermal threshold quantum yield," *Science*, vol. 363, pp. 1199–1202, mar 2019.

[286] J. Jasieniak, L. Smith, J. van Embden, P. Mulvaney, and M. Califano, "Re-examination of the size dependent absorption properties of CdSe quantum dots," *Journal of Physical Chemistry C*, vol. 113, pp. 19468–19474, 2009.

[287] S. Attia, S. Bilir, T. Safy, C. Struck, R. Loonen, and F. Goia, "Current trends and future challenges in the performance assessment of adaptive façade systems," *Energy and Buildings*, vol. 179, pp. 165–182, nov 2018.

[288] M. Meir, "State-of-the-art and SWOT analysis of building integrated solar envelope systems," tech. rep., IEA Solar Heating and Cooling Programme, nov 2019.

[289] P. Macé, B. Stridh, D. Frieden, S. Woess-Gallasch, D. Frederiksen, Kenn (Kenergy, S. Larsson, David (Solkompaniet, N. van Oorschot, John (ZuydUniversity, S. Benson, Jessica (RISE, S. Román, Eduardo (Tecnalia, and F. Burgun, Françoise (CEA, "Development of BIPV Business Cases - Guide for stakeholders," tech. rep., IEA PVPS, 2020.

[290] D. W. Winiarski, M. A. Halverson, W. Jiang, and U. S. D. of Energy, "Analysis of Building Envelope Construction in 2003 CBECS," Tech. Rep. June, 2007.

[291] P. H. Shaikh, N. B. M. Nor, P. Nallagownden, I. Elamvazuthi, and T. Ibrahim, "A review on optimized control systems for building energy and comfort management of smart sustainable buildings," jun 2014.

[292] H. C. Curtius, "The adoption of building-integrated photovoltaics: barriers and facilitators," *Renewable Energy*, vol. 126, pp. 783–790, oct 2018.

[293] A. B. Jaffe and R. N. Stavins, "The energy paradox and the diffusion of conservation technology," *Resource and Energy Economics*, vol. 16, pp. 91–122, may 1994.

[294] R. Wüstenhagen and M. Bilharz, "Green energy market development in Germany: effective public policy and emerging customer demand," *Energy Policy*, vol. 34, pp. 1681–1696, sep 2006.

[295] M. Aguirre and G. Ibikunle, "Determinants of renewable energy growth: A global sample analysis," *Energy Policy*, vol. 69, pp. 374–384, jun 2014.

[296] M. G. Debije, "Solar Energy Collectors with Tunable Transmission," *Advanced Functional Materials*, vol. 20, pp. 1498–1502, apr 2010.

[297] A. Shehabi, N. Deforest, A. McNeil, E. Masanet, J. Greenblatt, E. S. Lee, G. Masson, B. A. Helms, and D. J. Milliron, "U.S. energy savings potential from dynamic daylighting control glazings," *Energy and Buildings*, vol. 66, pp. 415–423, nov 2013.

[298] S. K. Deb, S. H. Lee, C. Edwin Tracy, J. Roland Pitts, B. A. Gregg, and H. M. Branz, "Stand-alone photovoltaic-powered electrochromic smart window," *Electrochimica Acta*, vol. 46, pp. 2125–2130, apr 2001.

[299] J. R. Platt, "Electroehromism, a possible change of color producible in dyes by an electric field," *The Journal of Chemical Physics*, vol. 34, pp. 862–863, mar 1961.

[300] A. P. Schuster, D. Nguyen, and O. Caporaletti, "Solid state electrochromic infrared switchable windows," *Solar Energy Materials*, vol. 13, pp. 153–160, feb 1986.

[301] Y. Wang, E. L. Runnerstrom, and D. J. Milliron, "Switchable Materials for Smart Windows," *Annual Review of Chemical and Biomolecular Engineering*, vol. 7, no. 1, pp. 283–304, 2016.